

**DESIGN AND MODELLING OF A PHOTOVOLTAIC DRIVEN FAN
SOLAR AIR HEATER FOR DRYING WOODCHIP IN SCOTLAND**

ANDRES CLEMENTE

Industrial Engineer

A thesis submitted in partial fulfilment of the requirements of Edinburgh
Napier University for the degree of Doctor of Philosophy

January 2011

ABSTRACT

In the wood fuel supply chain, the water contained in the product determines one aspect of the quality of the wood. It is necessary to reduce the moisture content (MC) of the wood in order to reduce transport and storing costs and also to increase the heating value of the wood. In this thesis a solar thermal application has been developed to dry woodchips using exclusively solar energy.

The novel solar woodchip dryer comprises a small woodchip dryer and a solar air thermal system (SATS) to increase the temperature of the drying air. The particularity of this woodchip dryer is that the input air flow is governed by a photovoltaic driven fan. Based on the experimental results obtained, the woodchip dryer and the SATS thermal performance were modelled and a simulation tool for predicting the dried woodchip production during a period of time has been developed.

Two small capacity dryers, a thin and a thick layer dryer, have been designed and built to dry woodchip based on the flow capacity of the SATS. The drying performances are studied for both configurations comparing the drying times, drying rates and efficiencies at different test conditions. The drying curves obtained from each test are modelled as a function of key parameters, temperature and velocity employing the Page model equation. Based on the experimental results, a drying model has been successfully developed to predict the MC when the woodchip dryer operates within a range of drying conditions.

A quantitative and qualitative analysis of the SATS thermal performance has been conducted employing various solar air collector configurations under Scottish weather conditions. The pneumatic characteristics of the solar dryer including the dryer are determining for the analysis of the system performance. Because of the PV driven fan electrical characteristics, the SATS presents a unique operation regime in which air flow depends exclusively on solar radiation. Thus the SATS thermal performance has been successfully modelled as a function of irradiance. The study necessarily includes the effect of environmental factors such as wind and cloudiness in the transient regime.

The potential of using a solar woodchip dryer has been assessed based on the results obtained from modelling the dryer and the SATS together. The feasibility and employability of using the solar dryer for drying woodchips is discussed considering the productivity, the energy savings, costs and integration.

DECLARATION

I hereby declare that the work presented in this thesis was solely carried out by myself at Napier University, Edinburgh, except where due acknowledgement is made, and that it has not been submitted for any other degree.

.....

ANDRES CLEMENTE (Candidate)

.....

Date

ACKNOWLEDGEMENTS

I would like first to thank my supervisory team, Thomas Grassie, Douglas Henderson, and Jorge Kubie for their great support and helpful discussions. I am most grateful to the opportunity they have offered to me with this project.

I would like also to thank the technical staff: Ian Campbell, Kevin McCann, Bill Campbell, Willy Laing, Derek Cogle, Bill Young and all the others that with their effort have contributed to the project and have made my time happier in the university.

I would like to thank all the other students from Napier University that have been along with me during all this time and have shared with me the experience of the PhD and living in Scotland. Many especial thanks to Naren, Smuga, Zurine, Gracia, Eneko, Celine, Carlitos, Gillespie and of course to Elena that has given to me strength when I needed it. Thanks to all the friends that I have met during this period of time.

I would also like to thank my family for their support and their unconditional encouragement throughout my years living far from them. Feeling that they were always there made me feel safe to move confident through this time.

Finally, I would like to thank my office colleagues, Haroon, Hoil, Naren, Peter, Celine, Tham, Wahid, Ahmad, Yasher, Aymeric and Muneer. I wish you all the best in your present studies and future careers.

CONTENT

ABSTRACT	ii
DECLARATION	iii
ACKNOWLEDGEMENTS	iv
CONTENT	v
LIST OF TABLES	xiii
NOMENCLATURE.....	xv
1. INTRODUCTION	1
1.1 Woodchip resources	1
1.1.1 Introduction	1
1.1.2 Wood fuel in Scotland.....	3
1.1.3 Woodchips	7
1.1.4 Moisture content in wood fuel	9
1.1.5 Drying woodchip	11
1.2 Solar energy	14
1.2.1 Introduction	14
1.2.2 Photovoltaic technology.....	15
1.2.3 Solar air heater.....	15
1.2.4 Transpired solar collectors	17
1.2.5 Solar dryers	18
1.3 Project.....	19
1.3.1 Description	19
1.3.2 Aims and objectives.....	21
1.3.3 Thesis outline	22
2. LITERATURE REVIEW OF PREVIOUS WORK.....	25
2.1 Thermal drying process	25
2.1.1 Introduction	25
2.1.2 Moisture content and equilibrium moisture content.....	26
2.1.3 Drying wood.....	27
2.1.4 Thin layer dryer	28
2.1.5 Deep bed dryers.....	29
2.1.6 Modelling drying process.....	31
2.2 Solar air thermal systems.....	35
2.2.1 Introduction	35
2.2.2 Solar air collectors.....	35
2.2.2.1 Design of the solar air collector.....	35
2.2.2.1.1 Absorber plate.....	36
2.2.2.1.2 Glazing cover.....	37
2.2.2.1.3 Back insulation	38
2.2.2.1.4 Solar air heater angles	38
2.2.2.2 Analysis and modelling of solar air collectors	39
2.2.2.3 Transpired air collector	42
2.2.2.3.1 Thermal performance of a SATPC.....	42
2.2.2.3.2 Air flow in SATPC.....	44
2.2.3 PV driven fan systems	46
2.2.3.1 PV modules	46
2.2.3.2 Fan and motor coupling	48
2.2.3.3 PV fan and motor coupling	48
2.2.3.4 Flow modelling in PV-driven systems	49

2.3 Drying woodchip.....	51
3. WOODCHIP DRYER	53
3.1 Introduction.....	53
3.2 Methodology.....	53
3.2.1 Introduction.....	53
3.2.2 Dryer design and construction.....	53
3.2.2.1 Dryer design.....	53
3.2.2.2 Dryer parts.....	55
3.2.2.2.1 Air Flow control unit.....	55
3.2.2.2.2 The drying facility.....	55
3.2.2.3 Instrumentation.....	57
3.2.2.3.1 Power input measurements.....	58
3.2.2.3.2 Weighing scale.....	58
3.2.2.3.3 Flow meter.....	58
3.2.2.3.4 Humidity sensor.....	59
3.2.2.3.5 Thermocouples	59
3.2.2.3.6 Data logger	60
3.2.2.3.7 Error analysis methodology.....	60
3.2.3 Woodchip characteristics	60
3.2.4 Testing procedure.....	63
3.2.4.1 Parameters to control	63
3.2.4.2 Air flow in the dryer.....	64
3.2.4.3 Mass /energy balance	65
3.2.4.4 Tests	66
3.3 Results	67
3.3.1 Introduction	67
3.3.2 Thin layer dryer result.....	68
3.3.2.1 Moisture content.....	69
3.3.2.2 Drying rates and efficiencies.....	71
3.3.2.3 Test Comparison: 57% MC and 52% MC woodchips.	75
3.3.2.4 Comparison of drying 3kg and 4kg of 52% MC woodchip	77
3.3.3 Thick layer dryer results	80
3.3.4 Mass and energy balance	85
3.4 Modelling.....	90
3.4.1 Introduction	90
3.4.2 Modelling a drying test.....	90
3.4.3 Page model.....	94
3.4.4 Drying macro model.....	96
3.4.4.1 Modelling a drying data set.....	96
3.4.4.2 The error analysis of the drying macro model.....	97
3.4.4.3 Number of tests.....	100
3.4.4.4 Modelling the thick layer dryer	103
3.4.4.5 Validation of the results.....	105
3.5 Summary.....	105
4. SOLAR AIR THERMAL SYSTEM.....	108
4.1 Introduction.....	108
4.2 Methodology.....	108
4.2.1 Solar air collector design	108
4.2.1.1 Introduction	109
4.2.1.2 Absorber plate.....	109

4.2.1.3 Glazing cover	111
4.2.1.4 Wooden case	111
4.2.1.5 Flat plate collector configuration.....	113
4.2.2 PV driven fan design.....	114
4.2.3 Instrumentation.....	116
4.2.3.1 Pyranometer.....	116
4.2.3.2 Thermocouple.....	117
4.2.3.3 Relative humidity sensors	117
4.2.3.4 Flow meter.....	117
4.2.3.5 Anemometer	117
4.2.3.6 Pitot tube installation	118
4.2.3.7 Error analysis methodology	119
4.2.4 Testing procedure.....	120
4.2.4.1 Pneumatic characteristics	120
4.2.4.2 SATS thermal testing	125
4.2.4.2.1 SATS tests	125
4.2.4.2.2 SATS testing rig.....	127
4.2.4.2.3 Collector time constant	128
4.2.4.2.4 Solar data processing	129
4.3 Results	130
4.3.1 Introduction	130
4.3.2 Pneumatic performance	130
4.3.2.1 PV driven fan electrical connection.....	130
4.3.2.2 Fan Characteristics.....	132
4.3.2.3 Pneumatic characteristics in the woodchip dryer	133
4.3.2.4 Pressure drop in the solar air collector.....	134
4.3.2.5 Total pressure drop in the system	136
4.3.2.6 Modelling the air flow	138
4.3.3 SATS thermal performance results	141
4.3.3.1 Time constant	142
4.4.3.2 SATS thermal performance	145
4.4.3.2.1 SATS with a TPC thermal performance.....	145
4.4.3.2.2 Difference between 2mm and 3mm TPC.....	148
4.4.3.2.3 Flat plate - fabric collector performance.....	149
4.4.3.2.4 SATS thermal performance when working along with dryer 2.....	150
4.4 SATS thermal model	157
4.4.1 Modelling the collector outlet temperatures	157
4.4.2 Error and Validation of the model	159
4.5 Heat loss modelling.....	165
4.6 Summary.....	166
5 SOLAR WOODCHIP DRYER	169
5.1 Introduction.....	169
5.2 Solar dryer macro model	170
5.2.1. Introduction	170
5.2.2 SDMM structure.....	171
5.3 SDMM results.....	174
5.3.1 Solar dryer tests validation.....	174
5.3.1.1 Solar dryer validation results.....	175
5.3.1.2 The error analysis	177
5.4.2 SDMM simulation	179
5.4.3 SDMM results for daily weather data.....	179

5.4.4 SDMM results for annual weather data	182
5.4.4.1 Solar dryer 1 annual production	182
5.4.4.2 Solar dryer with a SATS comprising a 3mm TPC	183
5.4.4.3 SDMM annual simulations for two woodchip types.	184
5.5 Evaluation of the solar woodchip dryer.....	185
5.5.1 Solar dryer effectiveness	185
5.5.2 Energy saving	186
5.5.3 Study of feasibility.....	187
5.5.3.1 Volume of woodchip.	188
5.5.3.2 Quality of the initial and final product.....	189
5.5.3.3 Drying season.	189
5.5.3.4 Drying times	190
5.5.3.5 Economical analysis	190
5.5.3.6 Conclusions from the study of feasibility.....	192
5.6 Solar wall for drying woodchip	193
5.6.1 Solar wall drying model.....	193
5.6.2 Solar wall dryer results	195
5.6.2.1 Case 1: Small solar wall dryer: 20m ²	196
5.6.2.2 Case 2: Large solar wall dryer: 100m ²	198
5.6. Summary.....	199
6. CONCLUSION AND FURTHER WORK.....	201
6.1 Introduction.....	201
6.2 Summary of conclusions	202
6.2.1 Drying woodchips.....	202
6.2.2 PV driven fan flow modelling.....	203
6.2.3 SATS thermal performance	203
6.2.4 Solar woodchip dryer.....	204
6.3 Contribution to knowledge	206
6.4 Further work	208
6.4.1 Drying woodchip.....	208
6.4.2 SATS	208
6.4.3 Solar woodchip dryer.....	208
REFERENCES	210
APPENDIX.....	220
Appendix A.....	219
Appendix A1: Drying data test processing	220
Appendix A2: Modelling drying test data	221
Appendix A3: Mass and Energy balance.....	223
Appendix A4: SATS	227
Appendix A5: SDMM	229
Appendix A6: SWDM	229
Appendix B.....	233

LIST OF FIGURES

Figure 1.1: Plantation of Sitka spruce in a Scottish forest.....	3
Figure 1.2: Timber factory in Scotland.	5
Figure 1.3: Wood chipper machine in operation.	8
Figure 1.4: Boiler efficiency as a function of MC for a 50kW boiler, Helin (2005).	10
Figure 1.5: Wood drying seasoning next to the road.....	13
Figure 1.6: Solar air systems for preheating air in a garage.	16
Figure 1.7: Roof mounted Solarwall installation.	18
Figure 1.8: Solar dryer applications, Malnutrition Matters (2008).	19
Figure 2.1: Deep bed drying illustration.....	30
Figure 2.2: Solar air thermal system lab tester, Ion et al. (2006).	40
Figure 2.3: Equivalent heat flow circuit of a flat plate collector, Matuska et al. (2009).....	42
Figure 2.4: The velocity field in a local hole of the SATPC, Deans <i>et al.</i> (2008).	46
Figure 2.5: IV curve of a PV module.	47
Figure 2.6: IV curves of a PV module at different ambient conditions.	48
Figure 2.7: IV characteristic of a PV driven fan connection.....	49
Figure 2.8: IV characteristic of a PV driven fan.	50
Figure 2.9: Fresh woodchip being dried with force air ventilation.	52
Figure 3.1.a: Schematic diagram of the thin layer dryer.....	54
Figure 3.1.b: Schematic diagram of the thick layer dryer.....	54
Figure 3.2: Dryer 1 prototype, apparatus and instrumentation.	56
Figure 3.3: Dryer 2 prototype, apparatus and instrumentation.	57
Figure 3.4.a: Fresh sample of the first type of woodchip.	61
Figure 3.4.b: Dried sample of the second type of woodchip.	61
Figure 3.5.a: MC curves for 4 drying tests at 22°C.....	70
Figure 3.5.b: MC curves for 4 drying tests at 31°C.....	70
Figure 3.5.c: MC curves for 4 drying tests at 40.5°C.....	70
Figure 3.6.a and Figure 3.6.b: Drying rate vs time and Drying rate vs MC for 3 tests with a drying velocity of 0.19 m/s.	72
Figure 3.7.a and Figure 3.7.b: Drying rate vs time and Drying rate vs MC for 4 tests at 30°C.....	72
Figure 3.8.a: Dryer efficiency curves for 3 tests with a drying velocity of 0.19 m/s.....	74
Figure 3.8.b: Dryer efficiencies curves for 4 tests at 30°C.....	74
Figure 3.9.a: MC curves from drying tests at 0.19m/s, employing the first and the second woodchip sample.....	76
Figure 3.9.b: MC curves obtained from the first and the second sample drying at the same temperature..	76
Figure 3.10.a: Drying rate curves obtained from the 3kg and 4 kg drying tests.	79
Figure 3.10.b: Drying rate vs. MC curves obtained from the 3kg and 4 kg drying tests.	79
Figure 3.11: Data measurements obtained from a test with a 20cm woodchip layer.....	82
Figure 3.12: MC curves obtained from 5 drying tests with a 30cm deep bed dryer.....	82
Figure 3.13.a: Drying rate vs time curves obtained from 5 drying tests with a 30cm deep bed dryer.....	84

Figure 3.13.b: Drying rate vs MC curves obtained from 5 drying tests with a 30cm deep bed dryer.....	84
Figure 3.14: Psychrometric diagram of 2 drying tests.....	86
Figure 3.15.a: Mass balance obtained from 3 drying tests with a drying velocity of 0.1875 m/s.	87
Figure 3.15.b: Mass balance obtained from 4 drying tests with a temperature of 30°C.....	87
Figure 3.16: Energy balance for a drying test with a drying velocity of 0.1875 m/s and a temperature of 30°C.....	90
Figure 3.17: Measured and Page modelled MR curves obtained from 4 drying tests at 30°C.....	94
Figure 3.18.a: Representation of k values.....	95
Figure 3.18.b: Representation of n values.	95
Figure 3.19.a: Predicted and experimental MC curves at 21°C for the first woodchip sample.....	98
Figure 3.19.b: Predicted and experimental MC curves at 30°C for the first woodchip sample.	98
Figure 3.19.c: Predicted and experimental MC curves at 40.5°C for the first woodchip sample.....	98
Figure 3.20: Predict vs experimental MC data for 12 drying tests with the first wood sample.	99
Figure 3.21.a and 3.21.b: Drying model tests selection graphics.....	102
Figure 3.22: Predict vs experimental MC data for 15 drying tests data obtained from the thick layer dryer.	104
Figure 3.23: Validation of the drying model with a drying test set at 50°C with a drying velocity of 0.5m/s.	105
Figure 4.1.a and figure 4.1.b: Drawing of a transpired plate collector (left). Drawing of a flat plate solar air collector (right).....	109
Figure 4.2: Details of the aluminium transpired plates.	110
Figure 4.3: Wooden frame details, holding the absorber plates and fan location at the back.....	112
Figure 4.4: Solar collector testing rig on the roof.	112
Figure 4.5.a: 5W PV module fan electrical characteristics.....	114
Figure 4.6: Pyranometer instrument employed to measure the solar radiation.....	116
Figure 4.5.b: 10 W PVmodule fan electrical characteristics.....	114
Figure 4.7: Pitot tube configurations for measuring pressure in fluid systems. Perry et al. (1984).....	118
Figure 4.8: Inclined manometer tube to measure pressure.	119
Figure 4.9: Pitot tube installation for measuring the pressure drop in the system.....	122
Figure 4.10: Effect of the density on the pneumatic curves, Clarage (2008).....	125
Figure 4.11: PV driven fan voltages as a function of irradiance measured in winter and in summer.	131
Figure 4.12: Characteristic curves of the fan at 7 voltages.....	132
Figure 4.13: ΔP - Q curves obtained from the thin layer dryer, dryer 1.	133
Figure 4.14: ΔP - Q curves obtained from the thick layer dryer, dryer 2.....	133
Figure 4.15: ΔP - Q curves obtained from 6 solar air collector configurations in solar dryer 1.....	135
Figure 4.16: Predicted and experimental ΔP - Q curves from 2 unglazed TPCs.....	136
Figure 4.17: ΔP - Q curves obtained from 6 solar air collector configurations with dryer 1.	137
Figure 4.18: ΔP - Q curves obtained from 2 solar air collector configurations with dryer 2.	137
Figure 4.19.a: Flow vs irradiance curve for 3mm TPC in solar dryer 1.	139
Figure 4.19.b: Irradiance data and predicted air flow values in solar dryer 1 during a test.	140

Figure 4.20.a: Flow vs irradiance curve for 3mm TPC in solar dryer 2.....	140
Figure 4.20.b: Irradiance data and predicted air flow values in solar dryer 2 during a test	141
Figure 4.21.a: Heat transfer transient due to a step increase in irradiance for a SATS with 3mm TPC....	143
Figure 4.21.b: Heat transfer transient due to a step decrease in irradiance for a SATS with 3mm TPC...	143
Figure 4.22.a and figure 4.22.b: Thermal performance of SATS with 2mm unglazed TPC.	146
Figure 4.23.a and figure 4.23.b: Thermal performance of SATS with 2mm TPC using glazing cover. ...	146
Figure 4.24.a and figure 4.24.b: Thermal performance of SATS with 3mm unglazed TPC.	147
Figure 4.25.a and figure 4.25.b: Thermal performance of SATS with 3mm TPC using glazing cover. ...	147
Figure 4.26.a and figure 4.26.b: Thermal performance of the SATS with a flat plate made of fabric.	150
Figure 4.27.a and figure 4.27.b: Thermal performance of the SATS with a flat plate collector made of fabric and with glazing cover.....	150
Figure 4.28.a and figure 4.28.b: Thermal performance of the SATS with 3mm TPC operating with 10cm woodchip layer in solar dryer 2.	152
Figure 4.29.a and figure 4.29.b: Thermal performance of the SATS with glazed 3mm TPC operating with 10cm woodchip layer in solar dryer 2.....	152
Figure 4.30.a and figure 4.30.b: Thermal performance of the SATS with 3mm TPC operating with 20cm woodchip layer in solar dryer 2.	152
Figure 4.31.a and figure 4.31.b: Thermal performance of the SATS with glazed 3mm TPC operating with 20cm woodchip layer in solar dryer 2.....	153
Figure 4.32.a and figure 4.32.b: Thermal performance of the SATS with 3mm TPC operating with 30cm woodchip layer in solar dryer 2.	153
Figure 4.33.a and figure 4.33.b: Thermal performance of the SATS with glazed 3mm TPC operating with 30cm woodchip layer in solar dryer 2.....	153
Figure 4.34.a and figure 4.34.b: Thermal efficiencies for the SATS with 2mm TPC with and without glazing.....	154
Figure 4.35: SATS with 3mm TPC performance in a windy day.....	156
Figure 4.36: ΔT model obtained from the performance of SATS with 3mm glazed TPC.	158
Figure 4.37: Predicted and experimental collector outlet temperatures obtained from the SATS with 2mm glazed TPC operating in solar dryer 1.....	160
Figure 4.38: Predicted and experimental collector outlet temperatures obtained from the SATS with 3mm TPC operating in solar dryer 1.....	160
Figure 4.39: Predicted and experimental collector outlet temperatures obtained from the SATS with 3mm TPC operating in solar dryer 2 with 30cm woodchip layer.	161
Figure 4.40: (left) Modelled vs predicted temperatures in SATS with 2mm TPC no covered and dryer 1.	163
Figure 4.41: (right) Modelled vs predicted temperatures in SATS with 2mm TPC covered and dryer 1.	163
Figure 4.42: (left) Modelled vs predicted temperatures in SATS with 3mm TPC no covered and dryer 1.	163
Figure 4.43: (right) Modelled vs predicted temperatures in SATS with 3mm TPC covered and dryer 1.	163
Figure 4.44: (left) Modelled vs predicted temperatures in SATS with 3mm TPC no covered and dryer 2.	163
Figure 4.45: (right) Modelled vs predicted temperatures in SATS with 3mm TPC covered and dryer 2.	163

Figure 5.1: Solar dryer 1 installed on the roof of the university.	170
Figure 5.2: SDMM modules diagram.	173
Figure 5.3: Diagram of SDMM simulations conducted	175
Figure 5.4: Solar dryer validation test in a sunny day.	176
Figure 5.5: Solar dryer validation test in a warm overcast day.	177
Figure 5.6: Solar dryer validation test in a cloudy/ sunny warm day.	177
Figure 5.7: Drying process simulation results for 3 solar dryer configurations operating at same weather conditions.	179
Figure 5.8: SDMM simulation of solar dryer 1 operating on 6 days at different weather conditions.	180
Figure 5.9: SDMM simulation of solar dryer 2 operating on 6 days at different weather conditions.	181
Figure 5.10: SDMM annual simulation for solar dryer 1.	182
Figure 5.11: Comparison of the annual operation for solar dryer 1 and dryer 2 employing the SATS with a 3mm TPC covered and uncovered.	183
Figure 5.12: SDMM annual simulation for the solar dryer 1 drying two woodchip samples.	184
Figure 5.13: Solar wall collector performance.	195
Figure 5.14: Drying capacity of the solar wall dryer using different heating inputs.	196

LIST OF TABLES

Table 1.1: Estimated annual heat energy consumption	5
Table 1.2: Comparison of characteristic values for different fuels	8
Table 1.3: Comparison of fuel prices for domestic consumers.....	9
Table 1.4: Low heating value in wood as a function of MC.....	10
Table 2.1: Mathematical drying models.	32
Table 3.1: Quantities to be measured, instrumentation and measurement errors.....	60
Table 3.2: Characteristics of the drying tests set that corresponds to the first wood sample.....	68
Table 3.3: Drying times from 57% MC to 30% MC for first woodchip sample.....	71
Table 3.4: Drying efficiencies when drying woodchip from 57% to 30% MC in the thin layer dryer.	74
Table 3.5: Weight, water content and water evaporated in two samples of woodchips.....	75
Table 3.6: Drying times obtained from the second woodchip sample tests.....	77
Table 3.7: Characteristics of the 3 kg and the 4 kg drying tests.....	78
Table 3.8: Weight, water content and water evaporated in 3 kg and 4 kg of woodchips.....	78
Table 3.9: Characteristics of the drying tests conducted with the thick layer dryer.	81
Table 3.10: Results obtained from the drying tests conducted with the thick layer dryer	83
Table 3.11: k values associated to each drying tests conducted with the first woodchip sample.	91
Table 3.12: Statistical results from the drying test models.	93
Table 3.13: Page model values for the constants.	94
Table 3.14: Statistical indicator obtained when comparing measured and modelling MC in the first woodchip sample being dried with the thin layer dryer.	100
Table 3.15: Model equations obtained from the thin layer dryer performance with the second woodchip sample.	101
Table 3.16: Statistical indicator values obtained from modelling the thin layer dryer performance when drying the second woodchip sample.	102
Table 3.17: Model equations obtained from the thick layer dryer performance for different woodchip layers.	103
Table 3.18: Statistical indicator values obtained from modelling the thick layer dryer performance with different woodchip layers.	104
Table 4.1: Absorber plate characteristics	110
Table 4.2: Quantities to be measured, instrumentation and measurement errors.....	120
Table 4.3: Air flow in solar dryer 1 with 6 collector configurations	138

Table 4.4: Air flow in solar dryer 2 with 2 collector configurations	138
Table 4.5: $\tau_{\text{collector}}$ test results for a 3mm TPC covered and uncovered.....	144
Table 4.6: Maximum collector efficiencies registered in the tests.	155
Table 4.7: ΔT modelling curves for SATS with various collector configurations operating with solar dryer 1.....	158
Table 4.8: ΔT modelling curves for SATS with 3mm TPC configurations operating with solar dryer 2.	159
Table 4.9: Statistical values of the linear correlation between predicted and measured data	164
Table 5.1: Climate conditions observed for the 6 days considered for the daily analysis.	171
Table 5.2: Annual dried woodchip production in solar dryer 1.....	183
Table 5.3: Monthly woodchip drying production and solar dryer effectiveness.....	186
Table 5.4: Energy collected by the SATS and average solar collector efficiencies in a year.	187
Table 5.5: Heat demand in 4 cases.	188
Table 5.6: Natural drying sample results after 1 day drying.....	190
Table 5.7: Solar dryer component costs	191
Table 5.8: Performance of 20m ² solar dryer at different flow rates.	197
Table 5.9: Performance of 20m ² solar dryer operating with an approaching air velocity of 100m ³ /h m ²	198
Table 5.10: Performance of 100m ² solar dryer at different flow rates.	199
Table 5.11: Performance of 3 solar dryers operating at the same air flow rate.....	199

NOMENCLATURE

a	y-axis intersection	
A	Area	m^2
A_{duct}	Area of the duct	m^2
A_{tray}	Area of the tray	m^2
b	Line slope	
$\cos \varphi$	Power factor	
C_p	Specific calorific heat	$kJ/kg\ K$
D_H	Hydraulic diameter	m
f	Friction factor	m
F_R	Heat removal factor	
g	Gravity constant	m/s^2
$G_{threshold}$	Solar radiation threshold	W/m^2
G_T	Solar radiation	W/m^2
H	Height of the collector	m
h_{amb}	Ambient air enthalpy	kJ/kg
h_i	Inlet air enthalpy	kJ/kg
$h_{conv,plate-amb}$	Convection heat coefficient from plate to ambient	$kW/m^2\ K$
I	Current	A
I_G	Irradiance	W/m^2
I_m	PV module current at maximum power	A
I_{SC}	PV module short circuit current	A
k	Drying process characteristic	$1/s$
K	Pressure drop coefficient	
K'	Humidity transport resistance	
K''	Moisture content gradient resistance	
k_{duct}	Ducting conductivity	$W/m\ K$
L	Solar collector length	m
L_{duct}	Length of the duct	m
\dot{m}	Mass flow	kg/s
MC	Moisture content on a wet basis	$\%$
MC_{eq}	Equilibrium moisture content	$\%$
MC_t	Moisture content at any time	$\%$
MC_0	Initial moisture content	$\%$
MR	Moisture ratio	
MR_{exp}	Moisture ratio experimental	

MR_{pre}	Moisture ratio predicted	
n	Number of constants in the equation	
N	Number of data	
Nu	Nusselt number	%
ΔP	Pressure drop	Pa
ΔP_{total}	Total pressure drop	Pa
$\Delta P_{absorber}$	Pressure drop in the absorber	Pa
$\Delta P_{acceleration}$	Pressure drop due to the fluid acceleration	Pa
$\Delta P_{buoyancy}$	Pressure drop due to the gradient of density	Pa
ΔP_{plenum}	Pressure drop in the plenum	Pa
P_{input}	Power input of the heater	W
Pr	Prandtl number	
P_v	Partial water pressure in the product	Pa
P_{va}	Partial water pressure in the air	Pa
Q	Volumetric air flow rate	m^3/h
$Q_{conv,coll-amb}$	Convection heat losses from collector to ambient	W
$Q_{rad,coll-amb}$	Radiant heat losses from collector to ambient	W
Q_u	Useful heat gained	W
R^2	Regression parameter	
Ra	Rayleigh number	
RH	Relative humidity	%
RH_0	Initial relative humidity	%
RH_{amb}	Ambient relative humidity	%
RH_{dry}	Drying relative humidity	%
t	Time	s
$Time_{drying}$	Drying time	s
T_a	Ambient air temperature	$^{\circ}C$
T_i	Input air temperature	$^{\circ}C$
T_{inlet}	Inlet air temperature	$^{\circ}C$
T_{drying}	Drying air temperature	$^{\circ}C$
T_o	Output air temperature	$^{\circ}C$
T_{outlet}	Outlet air temperature	$^{\circ}C$
ΔT	Increment of temperature	$^{\circ}C$
U_L	Heat loss coefficient	$W/m^2 K$
V	Voltage	V
$V_{anemometer}$	Air velocity across the anemometer	m/s

V_{dry}	Drying velocity	m/s
V_{drying}	Drying air velocity	m/s
V_m	PV voltage at maximum power	V
V_{max}	Maximum velocity in the collector	m/s
V_{OC}	PV open voltage	V
V_S	Velocity of air approaching to collector	m/s
$V_{suction}$	Suction velocity	m/s
V_{wind}	Wind velocity	m/s
w	Humidity in air	g water/ kg air
w_i	Humidity in the inlet air	g water/kg air
w_o	Humidity in the outlet air	g water/kg air
w_{sat}	Humidity in the air at saturation conditions.	g water/kg air
W	Mass of product	g
$Water_0$	Initial mass of water in the product	g
W_0	Initial mass of the product	g
W_{dried}	Mass of dried product	g
$W_{evaporated}$	Mass of water evaporated from the product	g
W_{time}	Mass of product at any time	g
$w.b.c$	Water binding capacity	g
X^2	Reduced chi squared	

Symbols

α	Collector absorptivity	
α_{air}	Air thermal conductivity	W/m K
β	Inverse of the temperature	1/°K
ε	Collector emissivity	
ε_{duct}	Emissivity of the ducting material	
ξ	Dimensionless pressure	
η_{drying}	Drying efficiency	%
$\eta_{collector}$	Collector efficiency	%
$\eta_{solar\ dryer}$	Solar dryer efficiency	%
μ	Dynamic viscosity	kg/m.s
ρ	Density	kg/m ³

$\Delta\rho$	Density difference	kg/m^3
σ	Stefan Boltzmann constant	$5.669 \cdot 10^{-8} \text{ W/m}^2 \cdot \text{K}^4$
$\sigma_{\text{collector}}$	Collector porosity	%
τ	Collector transmittance	
$\tau_{\text{collector}}$	Collector time constant	sec
ν	Kinematic viscosity	m^2/s
ω	Angular speed	rad/s

Abbreviations

CFD	Computational fluid dynamics
LHV	Low heating value
MBE	Mean bias error
MC	Moisture content
PV	Photovoltaic
RMSE	Root mean square error
SAC	Solar air collector
SATPC	Solar air transpired plate collector
SATS	Solar air thermal system
SDMM	Solar dryer macro model
SWDM	Solar wall drying model
TPC	Transpired plate collector

1. INTRODUCTION

The introduction chapter presents the background to the content of the thesis. This chapter reviews the prospects of two types of renewable energy involved in the project: biomass and solar energy. A description of the wood fuel resources shows the relevance of reducing the moisture content of the product before it is burnt. Further, the solar energy resources for drying applications are presented briefly, which includes the potential of using transpired plate collector and photovoltaic technologies. This chapter also summarises the project, the objectives of the research and provides an outline for the thesis.

1.1 Woodchip resources

1.1.1 Introduction

Wood fuel is any energetic product that comes from woody resources including sawmill residues and forestry, thinning operations and short rotation energy plantation products. As a bioenergy product, wood fuel is burnt to obtain heat and also to produce electricity.

Wood, as a fuel was the main source of energy in all civilizations and empires until the industrial revolution in the nineteenth century and the consequent growth in the consumption of fossil fuels. In addition, past civilizations flourished and were supported by forest and food producing areas. Wood resources had a decisive influence on the societies that remained. In fact, in the nineteenth century, the development of Europe and the United States would probably have not been possible without abundant wood supplies. Furthermore, the industrial revolution was initially only possible due to the availability of biomass resources: wood fuel and charcoal, Schubert (1967).

In the twentieth century, the socio-economical frame was based on the development of fossil fuel technologies which was detrimental to more sustainable resources. Woodchips, briquettes and pellets were only introduced to the market of various countries as a response to the fossil fuel crisis of the 1970s. However, despite the initial movement towards the development of wood fuel as an alternative energy resource, any interest in this fuel market lessened when oil prices decreased, Björheden (2006). Only a small number of countries with high forestry resources, like Finland and

Austria, kept progressing in this direction to become leaders in the development of wood fuel technology and also as a reference for the management of wood fuel resources.

For decades fossil fuel resources have covered most of energy demand and consumption in industrial countries. However, in many developing countries traditional biomass continues to be the main source of energy, providing on average 35% of the energy needs of three-quarters of the world's population. This rises to between 60% and 90% in the poorest developing countries. Modern biomass energy applications are increasing rapidly in both industrial and developing countries. Further, for the majority of the world's people, biomass will continue to be the prime source of energy for the foreseeable future, Criqui et al. (2000).

Wood fuel, as any biomass product, is considered to be carbon neutral and hence a renewable resource because of the potential to reduce CO₂ emissions. Biomass when burned, releases CO₂ that is largely balanced by the CO₂ that has been captured in its own growth over a much shorter period of time. Conversely, fossil fuels release the CO₂ that was captured by photosynthesis millions of years ago. Consequently, the displacement of fossil fuels with biomass would result in significantly lower net carbon emissions being released into the atmosphere. Indeed, biomass can also be viewed as a way of storing solar energy. The energy from the sun is captured and stored via the process of photosynthesis in growing material.

Traditional uses of biomass are often inefficient, wasting much of the energy available. They are also associated with a significant negative environmental impact. Modern applications replace traditional uses, particularly in industrialised countries. This requires capital, technology, skills, market structure and a certain level of development. The development of wood fuel resources depends on the cooperation between the government, the forest industries and related institutions. The creation of a wood fuel market could bring remarkable socio-economic benefits:

- Wood fuel is considered carbon neutral if neglecting the emissions due to local transport. The usage of this source then helps to reduce global emissions and tackle climate change.
- Consuming wood fuel resources helps to reduce the importation of fossil fuels, and therefore reduces a country's energy bill and reduces its economic dependence on unstable countries.

- The management of the forest to produce wood fuel benefits a wide range of other forest functions, such as biodiversity.
- Wood fuel provides opportunities for new companies and opens a potential energy market, especially in rural areas.

1.1.2 Wood fuel in Scotland

In recent years Scotland and the UK have benefited from cheap and abundant coal, oil and gas. Nowadays, the policy drivers are changing as fossil fuel reserves decrease and new threats such as climate change and energy security arise. In order to harness renewable resources it is essential to confront these new threats and biomass is a potential source of energy. Scotland has a large number of available renewable resources that can be used to fulfil commitments in order to develop a low carbon economy. New initiatives to promote renewable energy have focussed largely on electricity generation. However one third of the primary energy in the UK is to produce heat and therefore using biomass resources for heating may imply a reduction in overall energy resources.



Figure 1.1: Plantation of Sitka spruce in a Scottish forest.

Wood fuel in Scotland, despite its potential, has not been developed in the same way as it has in other countries in Europe such as Austria, Sweden or Finland which

have been working on forestry resources for decades. In the EU, Biomass represents around 64% of renewable energy production and wood fuel alone provides around half of it. For instance, the Swedish energy agency estimates the total energy consumption to be 405 TWh, 45% of which came from renewable energy resources and of that 25% came from biomass, Ljungdell (2005).

Scotland has some of the most important forest resources within the UK. Many years ago most of the country was covered by broad-leaved trees such as oak, birch, and conifers like the Scottish pine. However, the large number of trees cut down for timber, the coal industry and metallurgic applications meant the woodland area was only 5% by the early 20th century. Thereafter, Scottish forestry policies boosted afforestation, with the majority of the trees being planted during the 1960s and 1970s. Sitka spruce, originally from Alaska, which is suitable for the Scottish climate constitutes 70% of trees planted nowadays, Blackburn et al. (1997). The Forestry Commission estimates that woodland covers more than 1.3 million hectares, which is approximately 17% of the land in Scotland.

The timber industry plays an important role in the country. The Scottish forestry industries cluster, SFIC, has assessed the current situation of the timber industry in Scotland. The results show that there are 80 sawmills which produce around 1 million m³ per year of sawn wood. This is approximately 10% of the UK's timber demand. Timber production is set to rise over the next 20 years by over 65%, to reach a production peak in 2020 due to the large-scale conifer planting previously mentioned. With regards to the production of wood fuel, it is estimated that from every 100 tonnes processed by the softwood sawmill, 45 tonnes of by-product, sawdust, bark and woodchips is produced, SFIC (2007).

The Biomass Energy Group, BEG, estimated that wood fuel in Scotland has the capacity to produce electricity of up to 450 MWe. However, In the Forum for Renewable Energy Development in Scotland (FREDS), the Biomass Energy group (BEG) highlighted that the primary role of biomass in Scotland should be in the heating sector rather than the electricity sector, BEG (2005). Heat energy can be produced very efficiently from biomass and can considerably reduce greenhouse gas emissions. The Sustainable Development Commission, in the report *Wood fuel for warmth*, SDC (2005), claimed that at best, wood fuel resources in the Scottish forests was up to 1 million oven dried tonnes per year. This would be able to supply 3.4 TWh for heating.



Figure 1.2: Timber factory in Scotland.

The Renewable Heat Group (RHG) assessed the potential of the heat resources to cover the heat demand in the country. Table 1.1 shows the estimated annual heat energy consumption in Scotland, RHG (2008). It shows that more than half of the total energy consumption goes to the domestic sector. Conversely, wood fuel resources are estimated to be 3.4 TWh per year which would cover 9% of the domestic heat demand. Viewed another way, if in Scotland there are around 2.4 million households, who use an average of 20 MWh per year, it means that wood fuel would heat around 200,000 homes.

Table 1.1: Estimated annual heat energy consumption, RHG (2008).

	Total energy consumption (TWh/year)	Estimated heat energy for space heating (TWh/year)	Estimated heat energy for industrial processes (TWh/year)	Estimated heat demand for heat water (TWh/year)	Estimated total heat demand (TWh/year)	Electricity used as heat (TWh/year)
Industry	35	4	23	2	27	2
Domestic	56	36		11	47	5
Service & public	27	15		2	17	4
TOTAL	118				91	

In Scotland, heating supplies depend heavily on fossil fuel resources and only a small percentage comes from renewable energies. In addition, there are areas in the

North West of the country that are off the gas grid and have no access to the main gas supply. The result is a reliance on fuels such as oil, coal, liquefied petroleum gas or electric storage heating. This fact makes the wood fuel market particularly interesting with regards to partially covering the heat demands of the country.

The wood fuel market can be classified depending on the size of the installation. Thus, there are three categories that describe the installations:

- Small scale: Domestic wood fuel burners and boilers in the 5 – 25 kW output range are used in rural dwellings which are often sited near woodlands and may not have a main gas supply. On this scale, the requirements of both processing and burning equipment are low and cheap.
- Medium scale: The capacities of the boiler system is in the 20–500 kW output range of systems and are suited to community heating projects and district heating schemes, such as large country homes, farms, schools and medium commercial and industrial facilities.
- Large scale: The capacity of the boilers is over 500 kW and their purpose is to heat and produce electricity that is appropriate for large heat consumers such as hospitals, blocks of flats or major industrial processes. The development of purpose-built biomass electricity plants or the burning of biomass in combination with coal, co-firing in existing power stations can generate electricity on a large scale. These facilities can combine electricity production with heat generation.

In Scotland the late development of forestry resources has limited the production and demand for wood fuel. There has always been a regular consumption of wood fuel despite the availability of coal and oil, for example burning wood logs in stoves. It was only during the oil crisis in the 1970s that people became interested in the alternatives to wood fuel and new products such as woodchips were introduced into the market. By 2005, SDC (2005) reported that there was a demand for pellets but no producers, so the majority of them were shipped from Nordic countries. During the last decade wood fuel was mainly limited to woodchips. In 2005, there were only 50 automated and semi-automated wood fuel heating schemes registered in Scotland, with an estimated heat output of 4.6 MW. Regarding electricity production using biomass, the same studies estimated that there were 55 MW_e installed throughout the country, SDC (2005).

Presently, the biggest project that uses woodchips to produce electricity and heat is a power plant in Lockerbie, which has a maximum capacity of 44 MW_e.

1.1.3 Woodchips

Woodchips are a mechanically shredded woody material obtained from products such as whole trees, coppices and timber and forestry residues. It is a cheap, bulky fuel which is easy to handle that can be fed to a boiler automatically. Wood chips have a great surface-volume ratio and can burn very efficiently in a stove. The product is characterised by its:

- Wood origin.
- Particle size distribution.
- Moisture content.
- Energy density.
- Ash content.

Woodchips are a bulky material with a non-uniform distribution of physical properties. Parts of the tree have different wood properties and the particle size of the chips and their shape depend on the chipper's characteristics and the way it operates. Size and moisture content are key factors when burning woodchips. Therefore, combustion systems and the storage-feed mechanism are designed to work with specific types of woodchip. Small power installations and automated systems require a product that is of higher quality with lower moisture content. The classes of woodchip are very diverse, so the woodchip as a product has been classified in terms of quality. The European standards working group published a table of standards for the grading of woodchips, DD CENT TS 14961:2005 Solid Biofuels – Fuel Specifications and Classes. These are the standards that UK is expected to adopt in the future, Alakangas et al. (2006).

The energy content or heating value of the woodchip is the amount of energy released per kilogram of product burned and is used to compare fuels. Low Heating Value, LHV, is usually taken as the energy value for the woodchip and it refers to the energy that is actually available from combustion after accounting for the energy losses from water evaporation in the product. The LHV woodchip depends on the tree's origin and moisture content level. Hardwood tree species like oak and beech have higher LHV

than soft wood trees like pine, poplar and willow. However, despite having lower LHV, soft woods have higher growth rates and therefore soft wood trees are more suitable for short rotation coppice plantations.



Figure 1.3: Wood chipper machine in operation.

Wood fuels are a good alternative to conventional fossil fuels because of their sustainable characteristics. Table 1.2 shows a comparison of the energetic characteristics of the 30% MC woodchip with other conventional fuels resources. Although, woodchips have lower LHV than other fuel resources, LHV levels in woodchips are close to the coal values. The energy density of the woodchip is clearly low in comparison to the oil and coal values. This fact makes the costs of fuel transportation high. Even though the CO₂ emissions in woodchips are as high as in other fuel resources, the gases emitted by the combustion can be considered neutral because of the short carbon cycle in trees.

Table 1.2: Comparison of characteristic values for different fuels, Cotton (2005).

Fuel	Low Heating Value (MWh/tonne)	Energy density (MWh/m ³)	CO ₂ emissions (kgCO ₂ /MWh)
Coal	7.7	50.0	31.3 *
Oil	11.6	34.0	27.7 *
Natural gas	15.2	0.04	18.4 *
Softwood chips @30%MC	4.1	10.0	21.3

(*) Data from Greenhouse gas conversion factors published by DEFRA (2009)

The woodchip prices are variable and depend on the costs involved in the supply chain. Transportation from the forest to the boiler involves harvesting, forwarding, transportation, storage and drying. These are all operations that affect the final fuel price. Wood fuel prices are relatively high in comparison with other fuels. However, wood fuel products are becoming more competitive because of fossil fuel decadence.

Table 1.3 shows a comparison of fuel prices for domestic consumers in Scotland, published by SDC (2005) in Scotland. Woodchip prices usually oscillate between £25 and £60 per dried oven tonne. Wood fuel burners are expensive, as the total cost including the price per kW installed plus the equipment maintenance and the woodchip prices are much more costly than single gas boiler. Thus, many wood fuel installations require the support of funding schemes and grants. The success of the wood fuel market depends on schemes which involve producers, companies and consumers to promote the sector.

Table 1.3: Comparison of fuel prices for domestic consumers, Forestry Commission (2010).

Type of fuel	£ pence/ kWh
Heating oil	6.3
LPG	7.9
Electricity	13.0
Natural gas	3.9
Woodchips at 30% MC	2.3, £70 to £100 per tonne delivered
Wood pellets at 5% MC	3.9, £185 per tonne delivered
500mm logs	1.92, £50 per tonne delivered

1.1.4 Moisture content in wood fuel

The moisture content, MC, indicates the amount of water in the fuel and it is defined as the mass percentage of water in the wood. Kofman (2006) studied the MC in various samples of wood and found that freshly felled trees or green wood have a MC range of between 40% to 65%. Fresh hardwood species usually have a minimum of 50% MC, while softwoods species store more water and the MC is higher than 55%. These levels of MC indicate that more than half of the fresh wood mass is water. Moisture in the wood is not desirable and it causes several inconveniences at the time of dealing with wood fuel products. These are the main drawbacks of keeping water in the wood:

- Water in the wood means it is an extra load to be transported and handled and therefore this increases haulage costs, energy consumption and emissions.
- High MC is not desired when storing wood because it accelerates the biological degradation of the material. Fungal activity may cause significant dry matter losses.
- Heating values are reduced by the MC. Furthermore, water in the wood implies low thermal efficiencies in the combustion which could cause an increment in emissions.

Table 1.4 shows the relationship between the low heating value and the moisture content for hard and soft woods. The heating values of the woodchip present a linear dependence with moisture content.

Table 1.4: Low heating value in wood as a function of MC, Houdson (2006).

	0% MC	10% MC	35% MC	50% MC
Conifer whole tree	4.92 MWh/tonne	4.36 MWh/tonne	2.96 MWh/tonne	2.12 MWh/tonne
Hardwood whole tree	5.04 MWh/tonne	4.47 MWh/tonne	3.03 MWh/tonne	2.18 MWh/tonne

When burning dried wood in a stove, less energy is used to evaporate the moisture. Therefore, flame temperature is higher and this is usually more appropriate for having a better combustion. For each boiler design, there is an optimum woodchip MC value in which the burning efficiency reaches the maximum. Figure 1.4 shows how the efficiency of the boiler varies with the moisture content of the woodchip for a boiler design of 50 kW, Helin (2005).

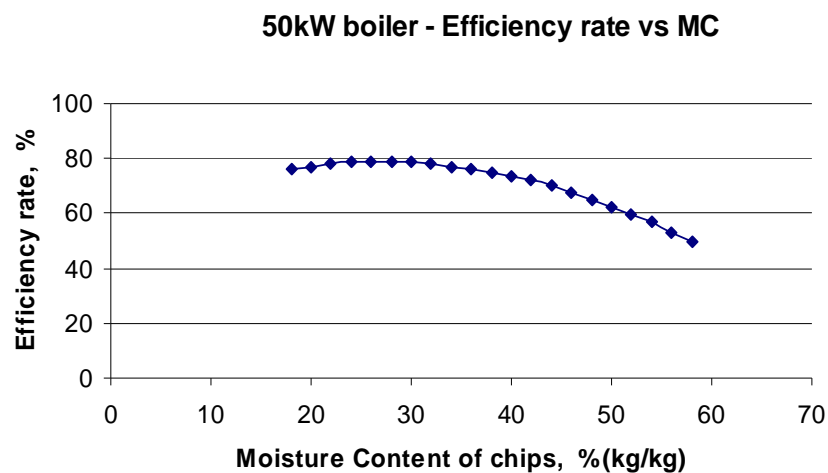


Figure 1.4: Boiler efficiency as a function of MC for a 50kW boiler, Helin (2005).

The quality of the wood to burn depends on the size of the boiler installation. Small wood fuel installations are designed to work with a low fuel load and the quality requirements are usually high, especially in automatic feed systems. Although the lower the MC the better, 30% MC is commonly accepted as a maximum MC reference value. Medium and large boilers are more tolerant of the MC, of levels up to 55%, and can handle a coarser woodchip than small boilers, Kofman (2006). Finally, the boiler efficiencies depend on the correct design and management of the installation, the quality of the woodchip employed and the boiler maintenance.

1.1.5 Drying woodchip

In the previous section the negative effect of the MC in the woodchip and the importance of removing water from the product before burning it in a boiler were highlighted. Having high levels of MC is not convenient and drying is an essential step in the woodchip supply chain.

Large-scale woodchip installation implies high levels of investment in expensive and large dryer installations in order to maximise woodchip production. Drying systems operate at high temperatures and high air volume flow rates. They usually employ heat recovered from the main burning process and have to deal with environmental security, Amos (1998). There are many types of dryer. The most commonly used in large power installations are rotatory dryers, flash dryers and superheated steam dryers, which are classified by the way the water is removed through evaporation and by the way the woodchip is in contact with the air flow, Castleman (1994).

The priority of medium- and small-scale woodchip producers is to reduce drying costs, to achieve a product of adequate quality in a reasonable period of time. There are diverse techniques of drying wood fuel that depend on the following productive factors:

- Quality of the wood, initial and final MC levels of the product.
- Volume of production and supply times.
- Environmental conditions.
- Space and storage facilities.

Drying is a process that needs time and energy, therefore conditioning the woodchip for burning increases the fuel prices. There are different possibilities when dealing with wood fuel which can be classified into two main categories. The first is

natural drying in which the wood is dried slowly and influenced by the surrounding environmental conditions. The second is forced drying which involves the usage of power to circulate air through the wood and the usage of heat to speed up the thermal process. In the latter, a small percentage of dried woodchips can be burnt to provide the thermal input.

- Natural drying 'in situ'.
- Natural drying open/covered roadside drying.
- Force air drying.
- Force hot air drying.

Wood, when harvested, is normally left to dry 'in situ' or moved into piles on the roadside for a period of time. When piled, the timber may be placed into bales and either exposed to the weather conditions or covered with plastic to protect it from rain and snow. The MC usually decreases with time, it may drop to 15% of the initial MC, but the final MC values depend on the local weather and the season in which the wood is harvested and collected. In high latitude countries like Scotland, timber may be left to season for a minimum period of a year before it is collected to be processed. Natural drying takes longer to reach acceptable levels of MC and drying is usually complemented using forced ventilation.

However, when storing woodchips outdoors, the drying process is much slower than storing wood in log piles. Moreover, chipping increases the active surface for the growth of microbia, bacteria and fungi that may bring negative consequences. It is important to reduce the water content to minimise the fungal activity that may produce large matter losses and which may also have significant health risks. Important research is being conducted in several Northern countries, especially in Finland where climate conditions for drying are unfavourable. Tahvanainen (2006) and Laitila (2006) reported problems when drying and storing forest woodchip outdoors and they discussed the ineffectiveness of natural drying.

Storing wood in sheds makes it possible to use forced air ventilation in order to reduce the drying times. The drying cost increases as the power supply is required to run the fan. The level of moisture is reduced depending on the quantity and quality of the wood that is being dried, the air flow and the climate conditions. The final moisture content values achieved usually range between 20% to 30% MC, Reeb (2006). This

drying method is better adapted to the demand for a specific quality product, since the drying conditions can usually be controlled.



Figure 1.5: Wood drying seasoning next to the road.

In order to enhance the drying process the forced air can be pre-heated. The heat source may come from the same wood product or from solar energy. The operation costs depend on the operational drying temperature and power for the fan. The drying process can be optimised using a combination of air temperature and flow rate.

Kiln drying is a pre-heated forced air application in which wood is dried under controlled humidity and temperature conditions, Reeb (2006). Kiln dryers are particularly used for timber products since the wood tends to shrink, break and lose its structural integrity if moisture is removed in an incorrect manner.

It is not necessary to have specific requirements in order to dry woodchip for fuel, for example the way the wood dries, therefore commercial dryers are less sophisticated. Installations are simpler in order to minimise the handling costs and woodchip dryers may be adapted so the installations can be employed for other agricultural products.

The cost of drying woodchip varies according to the technique used. Drying costs depend on the installation, the equipment needed, the manpower required and the energy consumption. For instance, McGovern (2007) estimated the price of the

woodchip between £20 and £30 per dried tonne when using a pre-heated forced air dryer.

1.2 Solar energy

1.2.1 Introduction

Like biomass resources, the utilisation of solar energy for domestic and industrial use has become an important area of research due to its high availability. Solar energy is the major energy source on the Earth's surface. Every day, the sun delivers 4.176×10^6 TWh of energy to the Earth and just a very small portion of that is transformed or used in human activity applications. It is estimated that the solar energy that falls on the surface of Earth in one hour is comparable to the world's fuel consumption during the whole year, Muneer (2004). In addition, even in cloudy Northern countries there is more than enough solar energy to meet the demand during certain periods of the year.

In recent years, new technological advances and the new socio-economical context have created new prospects for solar energy. Widespread use of solar technology can reduce fossil fuel consumption and can therefore dramatically reduce the CO₂ emissions from heat and electricity production.

MacGregor et al. (1984) showed that solar energy can play an important role in partially covering the heat demand of the domestic sector in Scotland. The amount of solar energy available at higher latitudes is less than that generally available at locations closer to the equator. Page et al. (1986) reported that for the UK, the average annual irradiation falling on a South facing surface tilted at 45° is approximately 1000 kWh/m², while for locations near the equator, the annual solar radiation may reach up to 2500 kWh/m². However, Scotland is a Northern country and has a cold climate where daily temperatures are generally low and consequently heating seasons are long; around nine or ten months. Thereby, solar heating can still have a significant import at higher latitudes.

In Scotland, solar thermal systems have been developed to suit many applications. There are many cases in which solar energy is considered in architectural designs. For instance, solar ventilation and passive solar systems such as sunspaces may be found in sustainable constructions.

During the past few years, solar water heating technologies have been developed and solar water collectors for sanitary water have been widely employed. This is shown by the increment in the number of commercial manufacturers and installers accredited by the Scottish Community and Householder Renewable Initiative, SCHRI (2008).

1.2.2 Photovoltaic technology

Photovoltaic systems convert sunlight into electricity by means of semi conductor materials that form the photovoltaic cells which are arranged together in PV modules and PV arrays.

Over the past few decades, PV technology has been increasingly developed. In the early 1990s, growing concerns for the environment and global warming as a result of fossil fuel emissions led many governments to review their energy policies in order to promote the use of solar energy for the production of electricity. While in 1997 the global PV production was estimated to be 114 MW_P, five years later the photovoltaic industry quadrupled the production to 505 MW_P, Green (2004).

In Scotland, photovoltaic applications are particularly advantageous in remote, rural areas or off-grid locations where it is expensive to supply electricity, Scottish Solar Energy Group (2001). In these cases, an electrical installation requires complementary equipment including batteries and an inverter, in order to adapt the power generated to the electrical appliances.

Conversely, in common dwellings with an electrical connection to the grid it is also possible to have a PV system interconnected to the mains power supply with no need for batteries. Further, when PV modules generate more electricity than is required the surplus can be transported to the grid.

1.2.3 Solar air heater

Solar air heaters, SAH, are economical and reliable heating applications which are used to heat building spaces and pre-heat industrial applications such as dryers and air conditioning systems. The SAH uses the solar energy collected by an absorber plate to increase the inlet air temperature. Using air as a working fluid limits the thermal performance of the solar air heater due to the low density, small heat conductivity and the small volumetric heat capacity, Pottler et al. (1999). As a consequence:

- Storing heat using air is difficult as it requires a large volume.

- SAHs have a quick response to irradiance changes.
- Contrarily to solar water systems, there are no problems associated with freezing and boiling.
- Possible air leakages decrease the thermal performance but do not disable the whole system.

The air in the solar air heaters normally needs to be powered to circulate around the system. Thus, active installations use fans to blow and control the air through the ducts, while passive air systems like chimneys use natural thermal mechanisms, such as the buoyancy pressure to move the air. In any case, the optimisation of the SAH system should address both the rate of heat transfer and the pressure drop with flow rate.



Figure 1.6: Solar air systems for preheating air in a garage.

SAH systems provide a free source of energy which can be effectively utilised for preheating air. Solar energy applications are an easy way to save energy consumption and reduce CO₂ emissions. In architectural designs, SAH systems are normally integrated in the building façade or structure of the construction as this decreases the costs. Further, SAHs are easy to maintain. Large industrial installations employ the most favourable side of the building to integrate the solar collectors. Double façades and perforated unglazed plates are the most common collectors used for solar pre-heating air in buildings.

1.2.4 Transpired solar collectors

Within the solar thermal systems, the unglazed transpired plate collector represents a cheap and efficient technology for preheating air applications. Transpired plate collectors, TPC, consist of a dark perforated metal plate installed over a building's south-facing wall or on the roof, forming an air space between the wall and the new façade. As air passes through the holes in the collector, it is warmed. A fan or blower creates negative pressure in the wall cavity to draw ventilated air through the holes and deliver it into the building.

Transpired solar collector, TPC, is a technology that has been developed over the last few decades in the USA and Canada. It was in the 1990s when a Canadian company called Conservation Engineering Inc. invented the Solarwall, Figure 1.7, a successful commercial product, widely used in the U.S. and Canada for both residential and commercial buildings. It was recognised by R&D Magazine in 1995 as one of the 100 most important technological innovations.

The TPC is a simple application which is highly reliable, economical and commonly used for pre heating air in buildings with large wall surfaces like offices, storage space, garages and schools. Moreover, TPCs are proven to have a satisfactory performance in industrial and agricultural purposes as drying crops.

The manufacturing costs of the TSC are relatively low and they do not require any maintenance, as there are no moving parts apart from the fan and therefore the payback of the installations are usually low. For instance, Solarwall can capture as much as 80% of the available solar energy, reducing annual heating costs by £7 to £40 per square metre of wall installed and thus reducing CO₂ emissions. Furthermore, TPC may also be used in summer cooling when the building wall is passively cooled by solar thermo-siphoning.

Recently, the most current technology innovation has integrated the performance of a PV array with a TPC. The hybrid system performed very efficiently. The combination of the PV module with a solar air heater that removes the heat from the cell increases the PV efficiency by up to 10%. When using the hybrid thermal PV system, the total solar efficiency increased to over 50%, compared to the typical 10 to 15% for PV modules alone, Hollick et al. (2007).



Figure 1.7: Roof mounted Solarwall installation.

1.2.5 Solar dryers

Solar drying technology involves practical techniques that use solar energy for drying purposes. There are many uses for solar drying, although the main applications are in the agricultural industries. In many countries around the world, drying SAHs have been used to conserve food such as fruits, crops and leaves because it is a practical, economical and environmentally sustainable application.

Drying is one of the oldest techniques employed for food preservation. Since agricultural products are usually stored, drying enhances the product's life, minimises losses and also saves on shipping and transportation costs. Every year, millions of tonnes of food products are lost through spoilage. Thus, drying technology is important for the economy of some producer countries, especially for the developing ones in the third world. In some areas, if drying production was widely implemented, significant savings would be made for farmers and this could help to strengthen the economic situation as well as change the nutritional conditions in these regions Brenndorfer (1985). As an example, Figure 1.8 shows a project where a solar dryer application was used for drying fruit and vegetables in a remote location in South Africa. This project was carried out by a non-profitable organisation, Malnutrition Matters (2008).

Solar drying is also employed in small-scale industrial applications, for example wood drying kilns, ceramic or building material storages. The feasibility of using solar

energy for drying depends on many factors: volume of production, climatic conditions and the final product quality required.



Figure 1.8: Solar dryer applications, Malnutrition Matters (2008).

1.3 Project

1.3.1 Description

Nowadays, the new socio-economical situation forces governments to address important challenges like tackling climate change. There is a growing interest in developing sustainable technologies and using available clean renewable resources like solar energy and biomass. This work presents a practical application that contributes to the development of both solar energy and wood fuel technologies: A PV driven solar transpired plate for drying woodchips.

The project consisted of a study of a cheap novel solar dryer, designed for drying woodchip on a small-scale under Scottish weather conditions. The work included the study of a small capacity dryer and a novel solar air thermal system, SATS, which has been developed to heat the drying air. The SATS considered worked exclusively with solar radiation and consisted of an innovative PV driven fan solar collector whose

performance was governed by environmental factors such as solar radiation, ambient temperature and wind. Thus, the SATS utilised solar energy in two ways: both to generate heat and power. The SATS had a particular operation regime, as both rate of heat removal and air flow rate depended mostly on the solar radiation values and the pneumatic characteristics of the system.

Various solar collector configurations were tested in order to compare their performance and draw conclusions about the SATS design. The main SATS configuration was comprised of a 1.8 m² solar transpired plate collector and a PV module that supplied electricity to the fan. The way the heat collected by the absorber plate was transferred to the air and sucked into the system implied high collector efficiencies. The air was blown in and conveyed to the dryer by the PV driven fan situated on the back plate of the collector.

The capacity of the woodchip dryer was designed based on the experimental results obtained from the solar air collector. In order to find an optimal configuration for drying woodchips using the SATS air flow, two different configurations were tested: a thin layer and a thick layer dryer. The performance of both dryers was studied by drying a small amount of woodchip using various testing conditions.

The effectiveness of the solar woodchip dryers was judged by the total production for certain weather conditions. The best system configuration was the one that maximised the amount of dried woodchip delivered in a given period of time. The performance of the solar dryer depended on three subsystems interconnected by the pneumatic characteristics of the components:

- PV driven fan.
- Transpired plate collector.
- Woodchip dryer.

Both the transpired plate and the woodchip dryer introduced a pressure drop in the system which defined the range of air flow in the system. At the same time, the thermal performance of the SATS depended on the air flow delivered by the PV driven fan. The modelling of these subsystems leads to the prediction of flow rate and the outlet temperature as a function of the environmental factors, in addition to the PV module, fan and solar collector specifications. The woodchip dryer performance was modelled to estimate the amount of woodchips that would dry as a function of drying parameters, including the quality of the woodchip, temperature and drying velocities.

The solar dryer macro model, SDMM, was an application that combined the subsystem models to simulate the solar dryer performance as a function of environmental parameters. SDMM simulation results were taken into account in the viability study of the solar woodchip dryer prototype.

1.3.2 Aims and objectives

The aims of the project can thus be summarised as follows:

1. To study the parameters and factors that govern the performance of a solar woodchip dryer through the literature review, including drying principles, solar transpired plate theory and PV–fan connection.
2. To design and build a small capacity woodchip dryer. To test the dryer in laboratory conditions in order to analyse the drying process and evaluate the dryer performance.
3. To characterise the drying of woodchip. This necessitates consideration of key parameters, including chip quality, drying air temperature and relative humidity, and air velocities.
4. To develop a drying macro model able to predict the drying rates and moisture content curves when a woodchip dryer operates in a wide range of drying conditions.
5. To design and build the SATS, and, hence, to field test under real weather conditions, allowing performance analysis for various collector configurations.
6. To study the pneumatic characteristics of the solar dryer, including the PV driven fan electrical characteristics. To test the pressure drop in both dryer and solar air collector configurations and the PV driven fan performance in the field.
7. To develop an empirical model that predicts the air flow in each solar woodchip dryer configuration as a function of the relevant environmental parameters.
8. To develop an empirical model that describes the collector outlet temperatures of the SATS as a function of the environmental parameters for various solar air collector configurations.

9. To develop a solar dryer macro model to predict the dried woodchip production during a period of time as a function of the climate conditions and the woodchip quality.
10. To determine the feasibility of the solar woodchip dryer prototype, including an evaluation of the energy savings and an economical assessment.
11. To estimate the benefits of employing a solar air collector in Scotland to back up a large scale woodchip dryer.

1.3.3 Thesis outline

Chapter 1 provides the background to this research work and presents the objectives and structure of this thesis. It presents the project starting from a brief introduction of the wood fuel resources in Scotland to the importance of drying woodchips before they are burned. A short review of the solar energy resources is included, emphasising the solar dryer as an alternative technology for drying woodchip.

Chapter 2 considers current literature covering key aspects found in the project, namely the body of work related to drying woodchip and solar drying. The first part necessarily includes a review about drying woodchip as a thermal process. The second part covers the reviewed work on solar air collectors, particularly on solar transpired plates. The third part offers a reviewed work of PV driven fan technology. The last part shows practical examples of woodchip dryers.

Chapter 3 deals with the woodchip dryer analysis. The methodology describes the dryer experimental setup in the lab and the testing procedure. The results of two dryer configurations, thin and thick layer configuration, are presented. Thus, drying curves, efficiencies and drying rates are evaluated as a function of the key parameters that govern the drying process. The dryer performance is modelled based on the experimental results. A macro model that predicts the drying rates was obtained. A statistical analysis of modelled system outputs is used to evaluate the accuracy of the dryer model.

Chapter 4 deals with the SATS analysis. The chapter integrates the study of two systems that are interconnected: the solar air collector and the PV driven fan that form the SATS. The methodology includes a description of the SATS experimental setup and the testing procedure. The results are presented separately. Firstly, the pneumatic study of the solar dryer in order to model the air flow is given, and secondly the results of the

SATS thermal performance for various collector configurations are analysed and modelled. The validity of the SATS thermal model is considered through comparison of predicted and experimental results.

Chapter 5 integrates the woodchip dryer and the SATS model in a solar dryer macro model, SDMM, which predicts the amount of woodchip that can be dried during a period of time. Annual and daily simulations are considered in order to evaluate the potential of using this novel solar dryer for drying woodchip on a small scale. A feasibility and viability study included the economical and practical aspects of the prototype. The chapter also introduces an estimation for the potential of drying woodchip using a solar transpired plate collector in a large-scale production.

Chapter 6 draws important conclusions from each aspect of the presented work and also discusses the potential for future work.

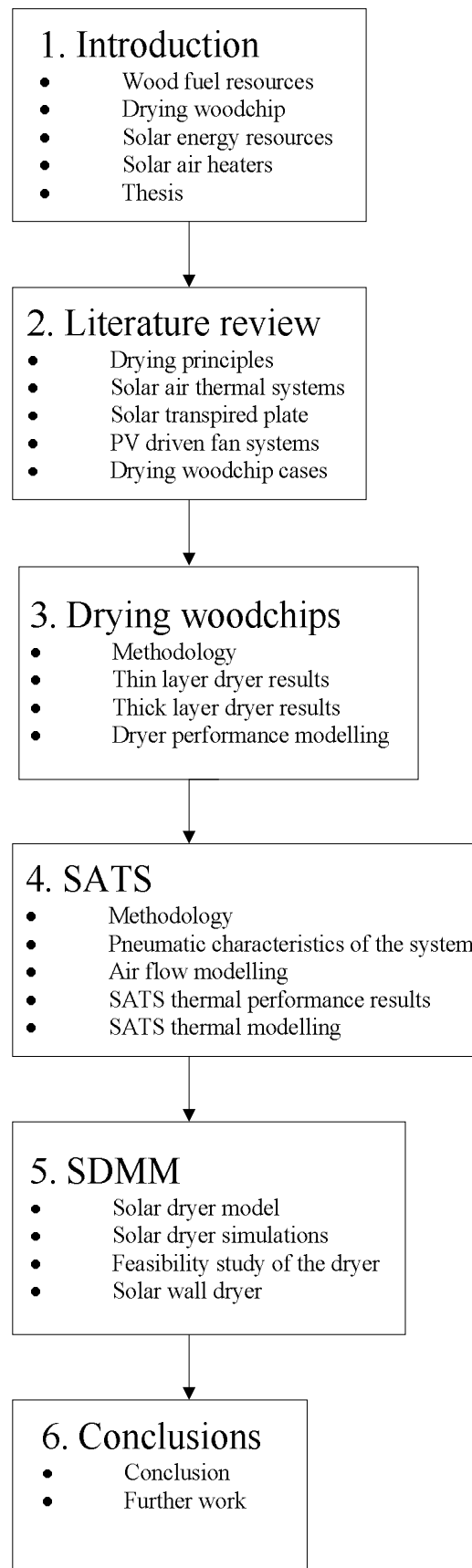


Figure 1.9: Structure of the thesis.

2. LITERATURE REVIEW OF PREVIOUS WORK

2.1 Thermal drying process

2.1.1 Introduction

Drying is defined as the process of removing water from a product. There are various drying methods which depend on the characteristics of the product to be dried. Drying techniques commonly found in the industry are chemical drying with desiccants, freeze drying, absorption processes, mechanical processes and thermal drying. Kudra *et al.* (2002) classified a range of industrial applications that use drying technology to obtain products such as fertilizer, detergents and manufacturing materials like polymers, ceramics and timber. Thermal drying is widely used for drying agricultural products and food preservation.

Ekechukwu (1999) defined thermal drying as a heat and mass transfer process. This involves water diffusion phenomena within the product to the surface and a subsequent evaporation. The sensible heat of the air is reduced as it is utilised to evaporate the moisture in the product. Thus, the total heat content in the air remains constant since the loss of sensible heat is regained as latent heat of vaporisation.

Water diffusion and evaporation are the drying mechanisms governed by the difference in partial vapour pressures. During a thermal drying process, the water content in the product moves towards a state of equilibrium in which partial vapour pressures in the product and the ambient air are close. Vapour pressure in the air varies with relative humidity and temperature. Therefore, the point of equilibrium also depends on these psychometric parameters. Drying implies the extraction of moisture from the product by passing air around it. Air flow carries the free water vapour away until moisture in the product reaches a state of equilibrium.

Drying with air ventilation at an ambient temperature is a slow drying process that implies long drying times. Pre-heating the drying air using a heat source, such as solar energy, accelerates the process. When drying with a solar dryer, the useful solar energy transferred to the fluid raises the air temperature, increases the energy available to evaporate the water near the woodchip, and hence increases the drying rates. Moreover, heating helps the water diffusion in the woodchip and increases the saturation vapour

pressure of the air, and hence the difference between this and the vapour pressure at the woodchip surface.

2.1.2 Moisture content and equilibrium moisture content

The proportion of water in a product is called moisture content. As is shown in equation 2.1, moisture content is commonly represented on a wet basis, $MC_{\text{wet basis}}$, dividing the mass of the water contained by the total mass of product, W :

$$MC_{\text{wet basis}} = \frac{W - W_{\text{dried}}}{W} \quad \text{Equation 2.1}$$

When a product is exposed to a stream of air, the difference in water vapour pressure between the product surface and air determines whether the product absorbs or desorbs moisture. The equilibrium moisture content, EMC, indicates the MC in the product after having been exposed to a particular environment for an indefinitely long period of time. At equilibrium conditions, the vapour pressure held within the product equals the vapour pressure of the surrounding air.

The energy employed to evaporate water from a product depends on its level of MC, air temperature and relative humidity. Thus, the higher the air temperature or the lower the RH, the less energy is required to evaporate the water. Likewise, with identical drying conditions, the closer the product is to its EMC, the higher is the energy required to evaporate the water bounded to the product surface, Ekechukwu (1999). The EMC values depend on the physical properties of the product, ambient temperature and air humidity. The curves that describe the EMC as a function of the RH for a constant temperature are called sorption isotherms. Products describe two different sorption isotherm curves: desorption isotherm curves when a product dries and adsorption isotherm curves when the product gains water. These sorption curves form a hysteresis cycle which is caused because the water disposition in the inner structure of the product has changed, Van Arsdel *et al.* (1967). Sorption isotherm curves are important in order to control the quality of the final dried product, especially in corn and crop drying. Theoretical models have been developed by Langmuir (1918), Henderson (1952) and Gregg *et al.* (1967) to estimate the sorption isotherms.

2.1.3 Drying wood

Wood is a hygroscopic material like any vegetable matter. Water forms part of the material and it is bound to the walls of the structure. Wood contains water in both liquid and vapour phase trapped in the cells and capillaries of the material. Moreover, there is a portion of free water in the capillarity network. When drying wood, the water content in the interior of the product moves to the surface. There are two main transport mechanisms of water migration within the product: diffusion and capillary forces. The structural properties of the material as cavities in the walls, and the tortuosity and porosity of the fibres affect the water migration in the material, Keey (1972).

The water migration in hygroscopic materials has been described using the principles of diffusion theory in solids that embrace the mass and heat transfer theory. Luikov (1966) developed a study in transport phenomena and described the flux of moisture proportional to the gradient of water concentration, the gradient of temperature in the body and a diffusion coefficient. The diffusion coefficient, which is called diffusivity, depends on the physical properties of the material such as porosity, permeability and chemical composition.

In the first drying stages, the free water moves easily from the interior to the surface. As the woody matter gets dried, more effort is required for the water to migrate. There is a transition point called fibre saturation point which indicates a change in the drying rate because the remaining water has a high boundary degree. Beyond this point, reducing the moisture content requires more energy as the water migration affects the structure of the capillaries and vessels. Rowell (2005) studied the fibre saturation point for various types of wood and found that for soft woods the fibre saturation point values were between 27 and 31% and for hard wood species the values were between 28% and 32% MC.

In addition, when wood dries below the fibre saturation point, the physical properties of the material change. Important shrinkage phenomena could be caused by interstitial tensions in the walls, producing defects such as checks, splits and warping. These may seriously affect the quality of the wood. It is essential to control the wood drying process, especially for timber applications, in order to achieve a product of the required quality. However, defects derived from shrinkage do not affect the final quality of the product when drying wood for fuel.

In conclusion, drying wood implies two phases in the drying process. Initially, there is a period of constant drying rate where the free water migration is sufficiently high to maintain the surface in a wet condition. Under these circumstances, the drying rate is controlled by the rate of the vaporisation of water from the wood surface. This rate depends on the water binding capacity of the air flow. Secondly, there is a critical point, related to the fibre saturation point in which the drying rate begins to fall. The internal water diffusion mechanism, which depends on the wood MC and temperature gradients, predominates. Thus, drying rates gradually decrease until the equilibrium is reached.

2.1.4 Thin layer dryer

Thin layer drying analysis is a common way to describe a wide range of simple and small dryers that deal with a relatively small amount of product and which operate with a large volume of air. The product that is to be dried is placed in the cabinet and spread on a tray, forming a thin layer. Air flow is abundant and its relative humidity depends on the moisture content in the product, Ekechukwu (1999). Thus, the drying rates are heavily dependent on:

- The nature of the product and its characteristic dimensions.
- Initial moisture content.
- Air temperature and relative humidity.
- Drying velocity.

As solar dryer applications with forced ventilation usually imply drying on a low scale, many solar dryers are studied based on the thin layer dryer analysis. Extensive research, especially in food engineering, has been carried out in order to describe the drying process of agricultural products and to model dryer performances. For instance, wheat drying by Mohapatra *et al.* (2005) in India and rough rice drying by Abe *et al.* (1997) in Turkey are examples of the various types of work undertaken on thin layer drying.

From the water diffusion and vaporisation theory, a differential equation was developed in order to describe the drying rates of the thin layer dryer, equation 2.2. The water evaporated, w , in an interval of time is directly proportional to a constant and the vapour pressure difference between the air and wet surface of the product. The constant K' is characteristic of the process and represents the product's resistance to transport

moisture and the drying conditions which includes product size, physical properties, air flow temperature and velocities.

$$\frac{dw}{dt} = -K'(P_v - P_{va}) \quad \text{Equation 2.2}$$

Where P_v is the vapour pressure in the product and P_{va} is the pressure vapour pressure in the air. $P_v - P_{va}$ represents the external driving force of the drying process. So, when P_v is bigger than P_{va} then drying takes place and when P_v is lower than P_{va} this implies the re-absorption of water by the product. The negative sign in the equation indicates the decrease in moisture content over time.

Assuming a linear relationship between P_v and the MC in the product and also assuming that P_{va} is proportional to the relative humidity in the equilibrium, which becomes proportional to the equilibrium moisture content, MC_{eq} , then equation 2.2 can be rewritten as:

$$\frac{dMC}{dt} = -K''(MC - MC_{eq}) \quad \text{Equation 2.3}$$

Solving the differential equation for an interval of time, given the initial conditions of moisture content and equilibrium moisture content for the drying conditions, the drying process for a product under certain conditions is described as equation 2.4.

$$MR = \frac{(MC - MC_{eq})}{(MC_0 - MC_{eq})} = e^{-kt} \quad \text{Equation 2.4}$$

A relationship denominated as moisture ratio, MR, was defined as a function of the MC_{eq} and initial moisture content, MC_0 . This variable and therefore MC shows an exponential behaviour with time during the drying process. MR is commonly used to model the drying performance.

2.1.5 Deep bed dryers

Deep bed drying is a way of drying in which the volume of product to dry is large in comparison to the air flow circulating the system. The deep bed dryer consists of a

drying chamber where the product to be dried is placed, forming a thick layer. Air flow has a longer path length or longer residence time to pick up moisture from the product.

A deep layer of a product may cause a high pressure drop in the system and therefore solar air collector applications may be not suitable for deep bed drying. Nonetheless, a few cases were found such as drying cocoa beans by Fagunwa *et al.* (2009) in Nigeria and drying rough rice by Bala *et al.* (1994) in Bangladesh.

In deep bed dryers, air goes from the bottom to the top, forming a drying zone in the product where the drying process occurs. This zone is limited by the bottom layer, where the product is in equilibrium conditions, and where the top layer of the air flow is completely saturated. Thus, the drying zone moves upwards in the bed as the product becomes dry, creating a MC distribution in the product to be dried, as shown in Figure 2.1. In shallow bed drying, the drying zone may cover the entire depth of the product, while in very deep bed drying, some regions may be over dried at the bottom of the dryer.

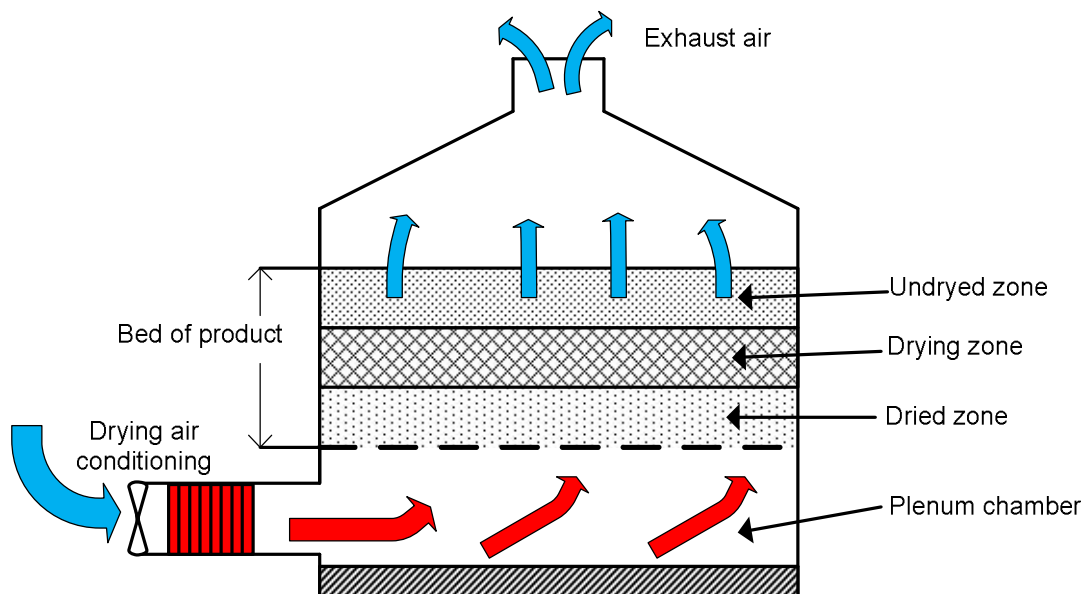


Figure 2.1: Deep bed drying illustration.

The deep bed drying process can be separated into two periods. Firstly, is the period of constant rate in which the drying rate is maximum as the outlet air leaves the dryer fully saturated. During this period, the drying rate depends solely on the water binding capacity of the air. Secondly, the decreasing rate period describes the drying process once the drying front has reached the top of the deep bed and air leaves no longer saturated. During this period, the drying performance can be analysed in a similar way to that of the thin layer dryer operation, Ekechukwu (1999).

2.1.6 Modelling drying process

The study of the drying process of different agricultural products has been a subject of interest to various researchers. Mathematical models have been employed in order to describe drying rates and to predict the performance of dryers as a function of the drying conditions.

Normally, the drying process is modelled using theoretical and semi theoretical models based on the thin layer dryer analysis. Equation 2.4 shows a mathematical expression of the MR suggested by Lewis (1921), which is commonly called the Newton model.

$$MR = e^{-kt} \quad \text{Equation 2.4}$$

Equation 2.4 shows an exponential behaviour of the MR which is variable with time. k is the characteristic parameter of the function and indicates the velocity of the drying process. Thus k is a parameter that depends on the dryer configuration, product characteristics and drying conditions such as temperature, relative humidity and drying velocity.

Due to its simplicity, the Newton model has been widely used to describe the drying of different types of crops by Ayensu (1997) and Sabbath *et al.* (1979). However, the equation provides results with limited precision. Therefore, researchers have developed a series of semi-theoretical expressions in order to increase the accuracy of the model. Menges *et al.* (2006) has compiled a total of 16 drying models with different mathematical expressions.

Henderson and Pabis (1961) obtained a modified drying expression, equation 2.5, to introduce a new parameter to the Newton model equation. This equation has been used to model drying grain by the above mentioned authors, and also various agricultural products by Pal *et al.* (1997). Likewise, in order to overcome the shortcomings of the previous models, Page (1949) cited by Diamante *et al.* (1993) suggested a new drying model, equation 2.6. This equation has been widely used by researchers to describe thin layer drying rates: for crops by Abe *et al.* (1997) and various vegetables by Prabhanjan *et al.* (1995). Other semi-theoretical expressions commonly employed and based on the thin layer analysis is the logarithmic model proposed by Ertekin *et al.* (2004), equation 2.7.

Moreover, another set of model expressions were obtained from Fick's theory of mass diffusion in solids. Sharaf-Eldeen *et al.* (1980) introduced the two-term exponential model, equation 2.8, and Midilli (2002) developed his own drying model expression, equation 2.9, which is commonly employed to describe the drying rates. Table 2.1 shows the model equations associated with each drying model.

Table 2.1: Mathematical drying models.

Model name	Model expression	Equation
Newton	$MR = \exp(-kt)$	Equation 2.4
Henderson & Pabis	$MR = a \cdot \exp(-kt)$	Equation 2.5
Page	$MR = \exp(-kt^n)$	Equation 2.6
Logarithmic	$MR = a \cdot \exp(-kt) + b$	Equation 2.7
Two term exponential	$MR = a \cdot \exp(-kt) + (1-a) \cdot \exp(-a \cdot kt)$	Equation 2.8
Midilli	$MR = a \cdot \exp(-kt^n) + bt$	Equation 2.9

When studying the drying performance, researchers approximate each MR curve of each test, in a set of drying tests, employing the above presented model equations using the least square method. The accuracy of the mathematical model obtained from each single test with N data is evaluated by means of statistical parameters, equations 2.10 to 2.12. The coefficient of correlation, R^2 , is usually the primary criterion for selecting the best model equation to define the drying curves. Root mean square error, (RMSE) is another statistical parameter used to determine the quality of the fit, Torul *et al.* (2002). Some other authors, like Ertekin *et al.* (2004), employ the reduced chi squared, X^2 , that also considers the number of parameters of the model equation, n , in the RMSE expression.

$$R^2 = 1 - \frac{\sum_{i=1}^N (MR_{\text{exp},i} - MR_{\text{pre},i})^2}{\sum_{i=1}^N (\overline{MR}_{\text{exp},i} - MR_{\text{exp},i})^2} \quad \text{Equation 2.10}$$

$$RMSE = \frac{1}{N} \left(\sum_{i=1}^N (MR_{\text{exp},i} - MR_{\text{pre},i})^2 \right)^{\frac{1}{2}} \quad \text{Equation 2.11}$$

$$X^2 = \frac{1}{N - n} \left(\sum_{i=1}^N (MR_{\text{exp},i} - MR_{\text{pre},i})^2 \right) \quad \text{Equation 2.12}$$

The final purpose of modelling the MR variable is to develop a general model that includes all the information collected from various drying tests. Based on the most suitable mathematical model selected to describe the MR curve of each test and the study of the model equation parameters obtained from each test, a general mathematical expression is developed to describe the drying rates as a function of the controlled drying conditions: temperature and drying velocity. Thus, researchers have typically created drying models for any product to estimate the drying curves at any given drying condition.

In this thesis, the predicted results obtained from modelling the drying and the SATS performance were compared with experimental values. The goodness of the models developed has been assessed employing regression technique including the analysis of various statistical indicators:

- Slope of the best-fit line.
- Coefficient of correlation, R^2 .
- Mean bias error, MBE.
- Root mean square error, RMSE.
- Skewness
- Kurtosis

Experimental results can be plotted against modelled data in a unique graphic. By least squares regression, an equation commonly named \hat{y} , equation 2.13, minimises the sum of the squares of the errors can be obtained. The slope, b , of the best-fit line between the computed and measured variable is desirably equal to one. When the slope exceeds the unity indicates over estimation for high values and underestimation for low values and vice versa. While the y-intercept of the regression line, a , is desirable to be the origin of coordinates.

$$\hat{y} = a + bx \quad \text{Equation 2.13}$$

Where x represents the experimental values.

The coefficient of correlation, R^2 , is the ratio of explained variation to the total variation. It lies between zero and one. A high value of R^2 indicates a lower variation and is desirable. R^2 is often used to judge the adequacy of a regression model but it should not be the only criterion for choosing a particular model.

$$R^2 = \frac{\sum_{i=1}^N (y_i - \bar{y})^2}{\sum_{i=1}^N (y_i - \hat{y}_i)^2} \quad \text{Equation 2.14}$$

Where: y_i is the modelled value

\bar{y} is the mean value

\hat{y}_i is the predicted value (regression line value)

The mean bias error, MBE, provides a measure of the trend of the model, whether it has a tendency to under-predict or over-predict its modelled values. Positive values of MBE indicate under-estimation while negative values imply over-estimation by the proposed model. A MBE nearest to zero is desired. It is given by the following equation:

$$MBE = \frac{1}{N} \left(\sum_{i=1}^N (y_i - x_i) \right) \quad \text{Equation 2.15}$$

Where: N = number of points

The root mean square error, RMSE, gives a value of the level of scatter that the model produces by providing a comparison of the actual deviation between the predicted and the measured values. Since it is a measure of the absolute deviation, RMSE is always positive. A lower absolute value of RMSE indicates a better model.

$$RMSE = \left(\frac{\sum_{i=1}^N (y_i - \hat{y}_i)^2}{N - 2} \right)^{1/2} \quad \text{Equation 2.16}$$

Skewness, equation 2.17, is a measure of symmetry, or more precisely, the lack of symmetry. A distribution is symmetric if it looks the same to the left and right of the center point. Negative values for the skewness indicate data that are skewed left and

positive values for the skewness indicate data that are skewed right. By skewed left, the left tail is long relative to the right tail and skewed right means that the right tail is long relative to the left tail.

$$Skewness = \frac{\sum_{i=1}^N (\hat{y}_i - \bar{y})^3}{s^3(N-1)} \quad \text{Equation 2.17}$$

Where s^2 is the standard deviation defined as in equation 2.18.

$$s^2 = \frac{1}{N-1} \left(\sum_{i=1}^N (y_i - \bar{y})^2 \right) \quad \text{Equation 2.18}$$

Kurtosis, equation 2.19, is a measure of whether the data are peaked or flat relative to a normal distribution. That is, data sets with high kurtosis tend to have a distinct peak near the mean, decline rather rapidly, and have heavy tails. Data sets with low kurtosis tend to have a flat top near the mean rather than a sharp peak. A uniform distribution, with kurtosis equal to 0, is the extreme case.

$$Kurtosis = \frac{\sum_{i=1}^N (\hat{y}_i - \bar{y})^4}{s^4(N-1)} - 3 \quad \text{Equation 2.19}$$

2.2 Solar air thermal systems

2.2.1 Introduction

The solar air thermal system, SATS, considered for the design of the solar woodchip dryer is a combination of photovoltaic and thermal solar energy applications. This section contains a review of previous research work on solar air collector technology and PV driven fan applications.

2.2.2 Solar air collectors

2.2.2.1 Design of the solar air collector

Solar air collectors, SAC, are radiative heat exchangers that transform solar radiant energy into heat. Their operation is generally simple: the working fluid is

brought into contact with an absorbing dark surface which absorbs the solar radiation and causes the air temperature to rise. The design, construction materials and construction methods for solar air heaters have been slowly developed compared to liquid based collectors. The efficiency of SAC is lower because of the low thermal capacity of the air and low heat transfer coefficients between the air and absorber plate Duffie *et al.* (1985). No freezing or leaking problems are the most important advantages of solar air collectors.

SAC can be classified into concentration collectors and flat plate type collectors which operate with high and low temperature increments respectively. Ekechukwu *et al.* (1999) reviewed the solar applications for drying and concluded that flat plate collectors were more suitable for drying and air conditioning applications. Flat plate collectors can provide the required drying temperatures and they are more economical than the more complex concentrating collectors.

Within the flat plate collector, unglazed plate SAC are the simplest and cheapest configuration that is widely used for crop drying and preheating operations. Corrugated sheets on building roofs or facades are frequently converted into this type of collectors. Brenndorfer *et al.* (1985) suggested that bare plate collectors are suitable for applications in which temperature increments of lower than 10°C are required. Since heat losses from the absorber may be considerable, bare plate collectors are adequate when operating at high air velocities.

For a greater rise in temperature and higher collector efficiencies, it is necessary to limit the heat losses. As the sides and the back of the collector can be insulated adequately, the major heat losses of the collector are from the front plate which must be exposed to solar radiation and to the ambient. The use of a glazing cover is a common practice to minimise convective heat losses in the collector and it permits air to circulate over the absorber plate. Parker *et al.* (1993) compared the performance of three different SAC designs using a glazing cover: with air flow over, under and on both sides of the absorber.

2.2.2.1.1 Absorber plate

The absorber plate is the most important part of the collector. It has a double thermal function since solar radiation is transformed to thermal energy on it and, thereafter this the heat is transferred to the air. Appropriate absorber plate is characterised by having good radiation properties in its surface: High absorptance of

short wave length radiation and low emissivity of thermal radiation for long wavelength, Duffie *et al.* (1985). Absorber plates normally have relatively high thermal conductivity and are thermally stable under the temperature regimes encountered during operation and stagnation. They should be durable, have a low weight per unit area and be cheap.

The low thermal conductivity of air, $0.025\text{W/m}\cdot\text{K}$, implies comparatively poor heat transfer coefficients from the metallic absorber to flowing air. Various absorber plate designs have been developed in order to alter the flow geometry and thus enhance the heat transfer. Kutscher *et al.* (1993) introduced and modelled the transpired plate collector performance, which is shown in detail in section 2.3.4. Metwally *et al.* (1997) proposed to modify the absorber flat plate for corrugated and v-shape geometries in order to introduce turbulences into the flow. Garg *et al.* (1991) introduced an absorber plate with fins attached and developed a model to study the performance when modifying the collector characteristics. Yeh *et al.* (2000) reported a considerable improvement in the flat plate solar collector efficiency when collectors are constructed with plain fins attached to baffles to create air turbulence.

In addition, packed-bed solar air heaters absorb the solar radiation in depth and have a high ratio of heat transfer area to air volume. They operate with a high heat transfer capability, resulting in a relatively low absorber temperature. This will decrease the heat losses from the absorber to ambient air and, hence, result in an increase in the thermal efficiency. Mohamad (1997) suggested a porous absorber plate and Sharma *et al.* (1991) proposed a solid matrix. Choundhury *et al.* (1988) conducted a comparative theoretical parametric analysis of SACs with and without packing different materials, shapes and sizes in the flow passage above the back plate.

In the design of the collector, both the thermal and pneumatic characteristics of the SAC have to be considered. The absorber may generate a notable pressure drop; especially in packed bed systems and consequently this may imply a high consumption of electrical power required to move the air.

2.2.2.1.2 Glazing cover

Duffie *et al.* (1991) and Smyth *et al.* (2006) established that the use of one or more transparent covers reduced thermal losses by convection by restricting air movement. Furthermore, covers protect the absorber plate from harm, dirt, rain and other environmental factors. The material must have a high transmittance in the visible

range and low transmittance to infrared radiation in order to effectively trap the re-radiated heat from the absorber plate. Other qualities of a good cover material include low heat absorptivity, stability at operating and stagnation temperatures, resistance to breakage, durability under adverse weather conditions and low cost. Glass or plastic sheets are the most common materials used for glazing covers.

Glass has been used very widely as a cover material due to its high transmittance to visible light, durability and stability to high temperatures. However glass is expensive and has low shatter resistance and relatively high weight per unit area.

Plastics, like polycarbonate, are being used increasingly, but their major limitations are the relatively low stability at higher collector operating temperatures and their low durability in bad weather conditions, particularly degradation under ultra-violet radiation. However, some treated plastics show high transmittance to visible light and equally low transmittance to infrared. Moreover, the weight of a plastic cover is about 10% of a glass cover of the same area, Duffie *et al.* (1985).

2.2.2.1.3 Back insulation

Depending on the solar thermal application, it may be necessary to reduce the heat losses across the back plate in order to enhance the collector efficiencies. Muneer *et al.* (2006) explained that the insulation of the collector was essential to protect it from conduction and convection heat losses across the back of the plate. The thickness of the insulation is usually between 25mm and 150mm and ideally it would have a reflective foil to reflect thermal radiation back to the absorber. Common insulation materials for solar air heaters are high-temperature resistant fibreglass blanket and extruded polyurethane foam with high thermal resistance. Insulation should have a low thermal expansion coefficient and should not melt or outgas at collector stagnation temperatures.

2.2.2.1.4 Solar air heater angles

The location and orientation of the collector with respect to the sun is an important aspect that needs to be considered in the design and siting of the SACs. In the absence of full analytical facilities, a rule of thumb is to design the solar air heater for the peak of production in the most favourable conditions. The solar collector is designed such that it is perpendicular to the solar radiation at solar noon, Hastings *et al.* (2000).

The inclination angle of the incident solar radiation depends on the latitude of the site where the solar collector is located. There are several authors that justify different

values for the optimum angle inclination of an installed solar collector. Following the indications established by Duffie *et al.* (1985), an optimal angle is 0.9 times the latitude of the location. Thus, in the case of Edinburgh where the latitude is 55° , the collector tilt would be 49.5° . Regarding the solar water heater research, Buchberg *et al.* (1974) showed that systems in higher Northern latitudes are often optimised for winter collection and are therefore tilted 5 to 10° more than the angle of latitude. A CFD study conducted by Henderson *et al.* (2007), in Edinburgh, showed that an integrated solar water heater would perform better at 50° than at 35° as higher Nusselt numbers were obtained, implying better heat transfer coefficients.

These values should be taken as a reference for designers, however, in practical situations, the angles that affect the incident radiation, i.e. the tilt angle and azimuth angle of the solar air heaters, usually are adjusted to the facilities. In building installations, solar collectors can either be integrated on the façade with a tilt angle similar to 90° or on the roof with a tilt angle adapted to the roof slope. The azimuth angle is usually defined by the orientation of the building.

2.2.2.2 Analysis and modelling of solar air collectors

Much research has been done on SACs systems. Authors have analysed and modelled the thermal performance of experimental solar prototypes. The study of the collector efficiencies and pressure drop as a function of the key parameters that characterises the system is essential in order to optimise the SAC designs.

Due to the large variety of SAC types available, there was a need to set a common criterion to measure the effectiveness of SACs. Thus, the experimental testing procedures are normally subjected to the standards presented by the ASHRAE Standard 93-86 and European Standard EN 12975-2:2006. For instance, Figure 2.2 illustrates a lab SAC simulator for testing, developed by Ion *et al.* (2006), which is in agreement with the standards set by ASHRAE.

The experimental testing results, obtained following the standards, allow for the direct comparison of different solar collector performances. For this, it is common practice to present the collector performance in a plot that shows the collector efficiencies, $\eta_{collector}$, against values of $\Delta T / I$, where I is the average solar radiation on the collector and ΔT is the increment of air temperature between inlet and outlet.

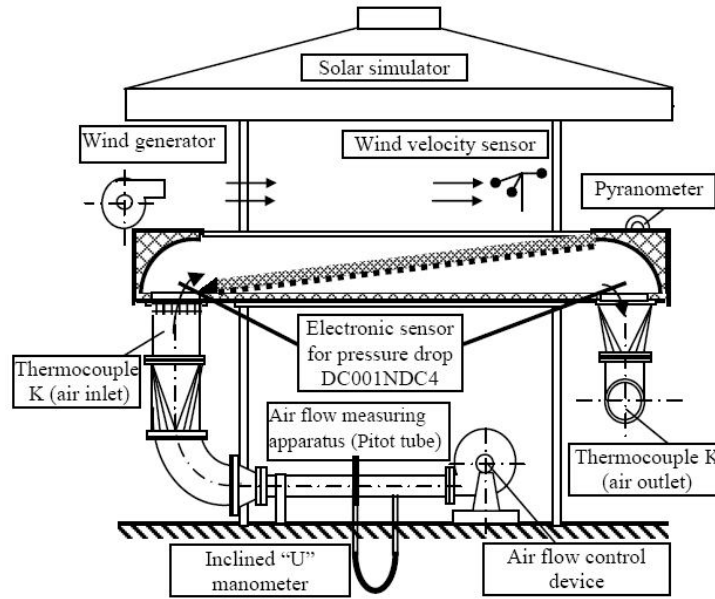


Figure 2.2: Solar air thermal system lab tester, Ion et al. (2006).

The steady state regime of solar collector performance can be evaluated by an energy balance applied to the collector system. The useful heat obtained by the collector is the heat gained by the air flow. It is calculated as the increment of sensible heat of the inlet air, equation 2.20.

$$Q_u = \dot{m} \cdot C_p \cdot (T_o - T_i) \quad \text{Equation 2.20}$$

Likewise, the amount of heat transferred by the collector to the air flow or useful heat gain, Q_u , can be estimated, as in equation 2.21, where the first term represents the heat absorbed by the collector and the second term the heat losses. F_R is the heat removal factor and U_L the heat loss coefficient, Duffie *et al.* (1985).

$$Q_u = A \cdot F_R \cdot [G_T \cdot (\tau \cdot \alpha) - U_L \cdot (T_i - T_a)] \quad \text{Equation 2.21}$$

The efficiency of the solar collector is calculated as the rate of utile heat per unit of solar radiation received by the collector, equation 2.22.

$$\eta = \frac{Q_u}{G_T \cdot A} \quad \text{Equation 2.22}$$

Thus Hottel *et al.* (1955), as presented in equation 2.23, is a linear relationship between various parameters which are characteristics of solar thermal performance.

This analysis is commonly employed to determine the heat loss coefficient, U_L , and the optical efficiency, $(\alpha \cdot \tau)$, by knowing the slope and the intercept of the efficiency curve.

$$\eta = F_R \cdot (\tau \cdot \alpha) - F_R \cdot U_L \frac{(T_i - T_a)}{G_T} \quad \text{Equation 2.23}$$

Many researchers have worked on developing theoretical models in order to simulate solar air collector performance. Two main ways of thermal analysis have been encountered in the research review. In the first group, efforts have been made to combine the key factors into a system of equations and thus formulate a mathematical model which describes the thermal performance of the collector. Pottler *et al.* (1999) and Moumimi *et al.* (2004) have developed macro theoretical models that solve the heat transfer equations by employing adequate correlations in the calculation of the required heat transfer coefficients. Further, there is a second group that uses computational fluid dynamics, CFD, which uses a finite volume procedure to solve the Navier-Stokes equations for the solar collector fluid systems. The advantage of using CFD is the versatility of working with complex geometries and the possibility of visualising the flow and temperature fields.

The heat transfer analysis of the solar collector can be represented as a thermal network that presents the equivalent heat flow circuit collector, including heat losses. Each solar collector prototype has a particular diagram with similar equations that govern the heat transfer in the collector.

Figure 2.3 represents the heat flow circuit showing all the thermal interactions between the parts of the single flat plate solar collector with a glazing cover. Further, conduction and radiation heat transfer are calculated in a similar manner for most of the solar collectors. The convection heat transfer also implies knowledge of the nature of the air flow in the system. The convection heat coefficients are calculated as a function of the Nusselt number, air thermal conductivity and hydraulic diameter. Nusselt numbers, which describe the character of the heat transfer, are calculated by a specific correlation that depends on the fluid characteristics. In forced convection, correlation values are dependent on Reynolds and Prandtl numbers, while in natural convection the Rayleigh numbers are pertinent.

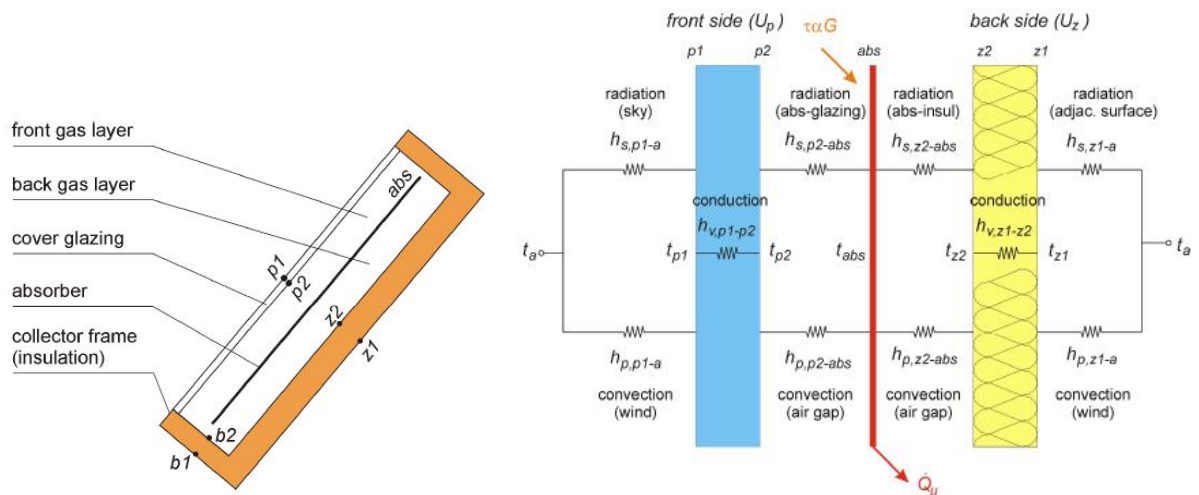


Figure 2.3: Equivalent heat flow circuit of a flat plate collector, Matuska et al. (2009).

2.2.2.3 Transpired air collector

Within the SACs, there is a particular configuration which effectively transfers the collected heat from a perforated absorber plate to the air. The principle of work of the solar air transpired plate collectors, SATPC, is different to the conventional solar plates. The transpired plate consisted of a dark perforated absorber plate, usually a metal sheet fixed to another parallel surface or wall. Ambient air is pulled through the holes on the plate surface by a fan. Thus, the surrounding air efficiently takes the heat gained by the absorber and is delivered into the collector.

2.2.2.3.1 Thermal performance of a SATPC

The geometry of the SATPC absorber implies favourable operating conditions which cause an improvement in the thermal performance compared to the flat plate collectors. Kutscher *et al.* (1993) demonstrated that the transpiration in a SATPC serves to enhance the convective heat transfer coefficient between the absorber and the air stream. Since suction occurs on the surface, the boundary layer is blown in. This means a significant reduction in convective heat losses and also implies relatively low plate temperatures and a consequent reduction in radiation losses. Thus, the design allows the elimination of the glazing with its associated costs.

A review of the heat loss theory applied to the transpired collector was presented by Kutscher *et al.* (1993). The heat transfer mechanism of the unglazed transpired collector was modelled by assuming a flat plate collector with homogenous suction. A simple energy balance on the collector can be utilised to describe the SATPC performance, equation 2.24. The heat gained by the inlet air is equal to the heat

absorbed by the plate, minus the radiant and convection heat losses between the collector and ambient.

$$C_p \cdot \dot{m} \cdot (T_o - T_i) = G_T \cdot (\tau \cdot \alpha) - Q_{rad, coll-amb} - Q_{conv, coll-amb} \quad \text{Equation 2.24}$$

Homogenous suction causes the thicknesses of the fluid and thermal boundary layers to remain practically constant over the length of the plate. The fluid boundary layer depends on the suction velocity, while the free stream velocity over the plate is the wind. At the plate edge, the boundary layer thickness asymptotically approaches this constant value. Kutscher *et al.* (1993) showed that, in no wind conditions, the convective heat losses were only occurring in the starting length of the plate where the boundary layer has not reached the asymptotic region. In the other part of the plate, the asymptotic region, where the boundary layers reach constant thicknesses, there are no net fluxes of heat from the absorber plate into the boundary layer because the boundary layer is sucked in through the plate. Therefore, there are no convective heat losses in this region; they are only at the starting length of the plate. They concluded that for the high suction velocities used in transpired collectors, the laminar asymptotic boundary layer assumption was also valid.

Based on this analytical study, Kutscher *et al.* (1993) showed that the natural convective heat losses to the ambient were negligible compared to the forced convective heat losses. They expressed the convective heat loss coefficient from the collector to the ambient, equation 2.25, as a function of the ratio between wind and suction velocities, the ambient air properties and the length of the collector.

$$h_{conv, plate-amb} = 0.82 \cdot \left(\frac{V_{wind}}{V_{suction}} \right) \cdot \frac{\rho \cdot v \cdot C_p}{L} \quad \text{Equation 2.25}$$

Kutscher *et al.* (1993) developed the heat transfer theory that describes the SATPC performance. Their work reported the characteristics of the fluid in the collector, estimating the total pressure drop in the collector and obtained a Nusselt correlation as a function of the hole diameter, pitch and porosity.

Kutscher (1994) measured the heat exchange effectiveness on thin and thick transpired plates with circular holes on a square or triangular layout over a range of parameters. They presented a correlation for heat exchange effectiveness based on the measured data. Thus, SATPC efficiency results were correlated with equations

involving dimensionless groups such as the Reynolds number, the ratio of approach velocity to wind velocity and the hole pitch to diameter ratio.

Numerous researchers have used computational tools to analyse the flow and the thermal performance of the SATPC. Arulanandam *et al.* (1999) obtained a correlation for heat exchange effectiveness using a CFD model for a plate with circular holes on a square layout, under no-wind conditions. Van Decker *et al.* (2001) investigated thick and thin plates with circular holes on a square or triangular layout over a range of approach velocities and wind speeds, and presented a relationship for heat exchange effectiveness. Gunnewiek *et al.* (2002) developed a CFD code to assess the effect of the wind on the flow distribution in the SATPC and quantified the minimum negative pressure for air suction.

Leon *et al.* (2007) developed a modelling tool based on previous works in transpired collectors to design and optimise its performance. The results compared efficiencies and temperature increments as a function of the SATPC key parameters such as perforation diameter and pitch, absorber porosity, approaching velocity and optical characteristics of the absorber plate.

2.2.2.3.2 Air flow in SATPC

Unlike in the flat plate collectors, the SATPC air flow rates are not constant in each cross section as there is a net flow in each hole of the transpired plate. This fact complicates the thermal analysis of the collector and increases the complexity in modelling the performance with a simple system of equations. The local air velocities can be estimated from the local pressure values. Kutscher *et al.* (1993) also developed a complete study in pneumatics in the SATPC. They showed that the pressure drop in any cross section of the collector can be calculated as the sum of pressure drop contributions in the plenum and across the collector plate, as is described in equation 2.26.

$$\Delta P_{total} = \Delta P_{absorber} + \Delta P_{plenum} - \Delta P_{buoyancy} + \Delta P_{acceleration} \quad \text{Equation 2.26}$$

- $\Delta P_{absorber}$ due to the friction caused by the air crossing the absorber plate, equation 2.27. It is calculated as a function of the approaching velocity, V_s , the porosity of the TPC, $\sigma_{collector}$, and the Reynolds number, Re_D .

$$\Delta P_{absorber} = \xi \cdot \frac{1}{2} \rho \cdot v_s^2 \quad \text{where: } \xi = 6.82 \cdot \left(\frac{1 - \sigma_{collector}}{\sigma_{collector}} \right)^2 \cdot Re_D^2 \quad \text{Equation 2.27}$$

- ΔP_{plenum} due to the frictional losses developed between the air flows and the plenum wall, equation 2.28. Friction losses are calculated as a function of the friction factor, f , and the length, L , and hydraulic diameter of the collector, D_H .

$$\Delta P_{\text{plenum}} = f \cdot \frac{1}{2} \rho \cdot \frac{L}{D_H} v_s^2 \quad \text{Equation 2.28}$$

- $\Delta P_{\text{buoyancy}}$ is due to buoyancy forces that are developed because the air in the plenum is warmer and lighter than the ambient air and it tends to push the plenum air up, equation 2.29. It is proportional to the variation of density, $\Delta\rho$, the gravity, g , and the height of the collector, H .

$$\Delta P_{\text{buoyancy}} = \Delta\rho \cdot g \cdot H \quad \text{Equation 2.29}$$

- $\Delta P_{\text{acceleration}}$ is due to the air acceleration in the plenum. The quantity of air increases as it flows through the plenum. Thus, as the area of the plenum is constant, the bulk flow velocity increases. Bernoulli's equation for energy conservation leads to the development of a pressure drop term due to the acceleration. This term is calculated in proportion to the maximum plenum velocity, V_{max} , equation 2.30.

$$\Delta P_{\text{acceleration}} = \rho \cdot \frac{1}{2} V_{\text{max}}^2 \quad \text{Equation 2.30}$$

The aforementioned authors have modelled these equations to calculate the air flow in the collector and then obtained the thermal performance of the SATPC.

Further analysis with CFD modelling has allowed for a detailed analysis of the flow in the SATPC. Deans *et al.* (2008) visualised the profile of air velocities when air is crossing a hole in the SATPC, as shown in Figure 2.4. Zhao *et al.* (2006) studied the buoyancy effect in the flow distribution in a SATPC when working with natural ventilation and they also analysed the relationship between air flow and heat transfer effectiveness for various flow rates. Gawlik (1999) analysed the air flow and the thermal performance of the SATPC near one hole of the absorber plate, and concluded that low cost and low conductivity materials can be used successfully as transpired absorber plates.

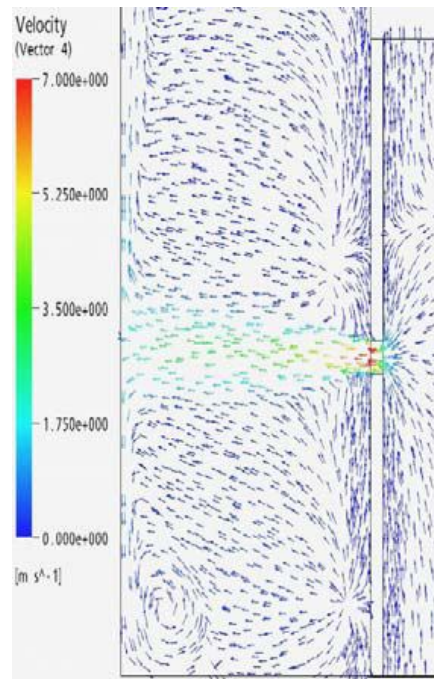


Figure 2.4: The velocity field in a local hole of the SATPC, Deans *et al.* (2008).

2.2.3 PV driven fan systems

2.2.3.1 PV modules

The photovoltaic system converts sunlight to electricity by means of semi-conductors embedded within the PV cells. Silicon and Germanium are the common semi-conducting elements that allow the electrons or electric current to move. The operation of the PV cell is like the electronic diode when excited by a certain index of luminosity. PV cells are usually connected in series, forming PV modules that supply power at higher voltages. The efficiency of the PV cells depends on the manufacturing technology. In the 1990s, lab produced cells were reported as having efficiencies of over 30%. Nowadays, labs are close to obtaining concentrator cells with efficiencies of up to 40%, Green *et al.* (2006).

Commercial silicon PV cells are either monocrystalline, polycrystalline or amorphous. Most commercially available PV modules are manufactured from polycrystalline silicon wafers that have lower production costs and lower efficiencies.

The assessment of the design and operation of the solar PV module performance is based on the electrical output. Each PV module is characterised by the current-voltage curves that describe the electrical performance for a constant solar radiation and constant PV module temperature.

Figure 2.5 shows the characteristics of an I-V curve of a PV module obtained experimentally when the PV module is connected to a variable electrical resistance. The main features of a typical I-V curve are the short circuit current, I_{sc} , the open voltage, V_{oc} , and the maximum power point, P_m . The last one can only be evaluated after the I-V curve has been determined and it is the maximum result of the I·V product in the curve. I_m and V_m are the current and voltage at maximum power respectively.

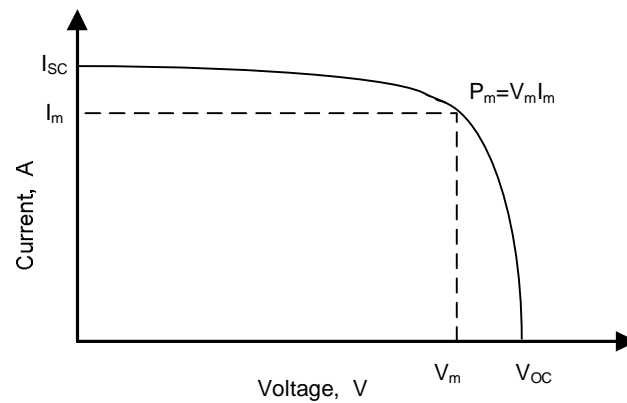


Figure 2.5: IV curve of a PV module.

The PV module performance is affected mainly by three environmental factors: levels of irradiance, temperature and wind speed. Figure 2.6 shows the I-V curves for a PV module operating at three different conditions. As irradiance increases, I_{sc} increases linearly, while V_{oc} increases logarithmically, Buresch (1983) and Mallick *et al.* (2004). An increment in PV module temperature results in a slight increment in the I_{sc} and a significant decrement in the V_{oc} . Although I_{sc} increases with temperature, the maximum power available from the PV module has decreased due to the larger decrease in voltage. Thus, the effect of temperature on the PV panel cannot be neglected for the production of electricity. Van Dyk *et al.* (2004) reported that at ambient temperatures of 25°C, PV modules operate at a higher temperature and they can lose up to 14% of their potential production.

Considering that temperature effect on current and irradiance effect on voltage are rather small, when modelling the PV module performance, various researchers have simplified their work by ignoring one or both of these effects. Jacobson *et al.* (2000) neglected the effect of temperature on I_{sc} and that of irradiance on V_{oc} . Conversely, Chamberlin *et al.* (1995) ignored the temperature effect on current but included a linear rather than logarithmic term for the effect of irradiance on V_{oc} .

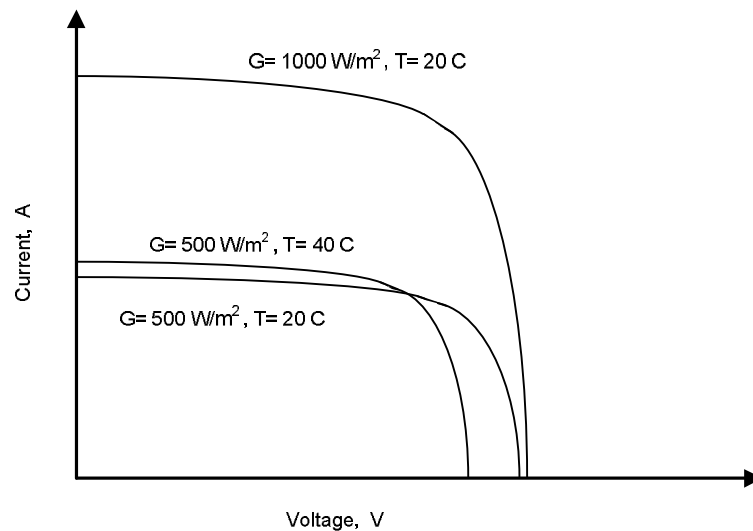


Figure 2.6: IV curves of a PV module at different ambient conditions.

2.2.3.2 Fan and motor coupling

The fan is powered by the motor connected to the PV panel. There are two main types of motors, namely AC and DC motors. The latter are most extensively used for PV applications as they can be coupled directly to the PV module. Newborough et al. (1990) reported several advantages of DC motors over AC motors as higher efficiencies, large starting torque and simpler means for regulating rotational speed. However, DC motors usually have higher manufacturing costs and a shorter life expectancy than AC motors.

2.2.3.3 PV fan and motor coupling

Within the DC motors, the permanent magnet brushless, PMBLDC, motors were found to be the most suitable for solar applications. Singh et al. (1998) stated that PMBLDC motors in water pumping applications working with PV arrays are widely used because of their high operating efficiency and the free maintenance operation due to the brushless construction. Langridge et al. (1996) reported that, due to their high torque to weight ratio, mechanical-electrical conversion efficiencies for this type of motor can reach values of up to 90%.

The analysis of the PV module and fan connection is fundamental in order to use the power yielded by the PV panel. The electrical characteristics of both components determine the final voltage and therefore the angular velocity of the fan. The operational point is calculated as the intersection of the I-V curves of both the PV module and fan

motor. Figure 2.7 represents the IV characteristics of a fan motor coupled with a PV module.

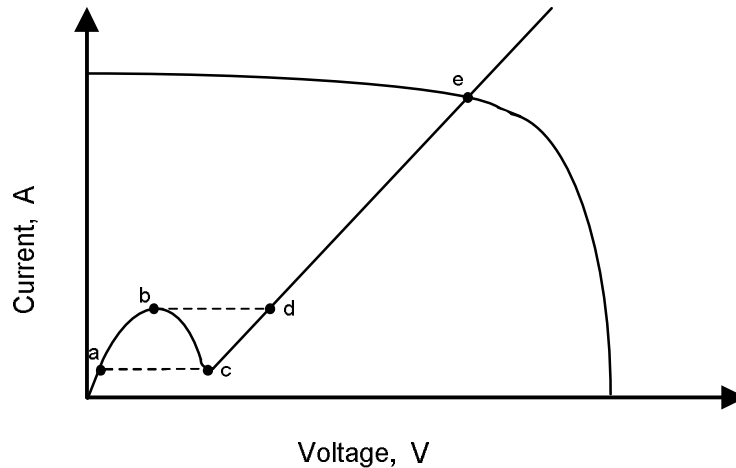


Figure 2.7: IV characteristic of a PV driven fan connection.

The IV curve of the fan motor in Figure 2.7 shows the common electrical behaviour of a permanent magnet motor. For low irradiance levels the motor is under stall conditions as the rotor remains blocked. The induced electro-motive force in the rotor is not enough to overcome the starting torque, point *a*. There is a threshold level of irradiance in which the PV module delivers enough current to the armature inducing sufficient electro-motive force, point *b*, and hence a torque to start the rotor. From this point *b*, the PV motor operational point moves directly to point *d*. A further increment in irradiance implies a higher operational point voltage, point *e*. When irradiance decreases to low levels, the motor operational points follows the motor characteristic curve down to point *c*. At this point, the motor stalls and the operational point jumps to point *a*. Thus, the electrical PV driven motor characteristic describes a hysteresis cycle at stall conditions.

2.2.3.4 Flow modelling in PV-driven systems

Modelling of flow rate in PV-driven systems requires knowledge of the electrical and pneumatic characteristics of the parts that comprises the system. In the previous section, the principal characteristics of the electrical connection between the PV module and fan motor have been discussed. The study of the pneumatic characteristics of the system involves knowledge of the pressure drop and flow characteristic and ΔP - Q curves of both the fan and pneumatic system.

A single ΔP - Q curve is usually supplied by manufacturers for the specific operating conditions of angular speed and fluid temperature. The performance of other

operating conditions can be obtained experimentally, although it is usually obtained through the affinity laws.

Odeh *et al.* (2006) approximated the axial fan ΔP curve at constant speed as a function of flow rate by a third grade polynomial expression. Meanwhile, Grassie (2007) used a fourth order polynomial curve to describe the ΔP - Q curves of the axial fan obtained previously in the lab.

Pressure drop in the system with turbulent flow has a quadratic dependence with flow, as shown in equation 2.31. The coefficient K is a function of the duct properties or the geometric characteristics of the system and air density.

$$\Delta P = K \cdot Q^2 \quad \text{Equation 2.31}$$

Many authors have obtained expressions based on the theory of viscous flow. Thus, knowing the roughness, the diameter and the length of the duct, in addition to the fluid density and viscosity, Darcy's equation and Colebrook's equation can be used to determine ΔP as an analytical function of flow, Odeh *et al.*, (2006) and Grassie, (2007).

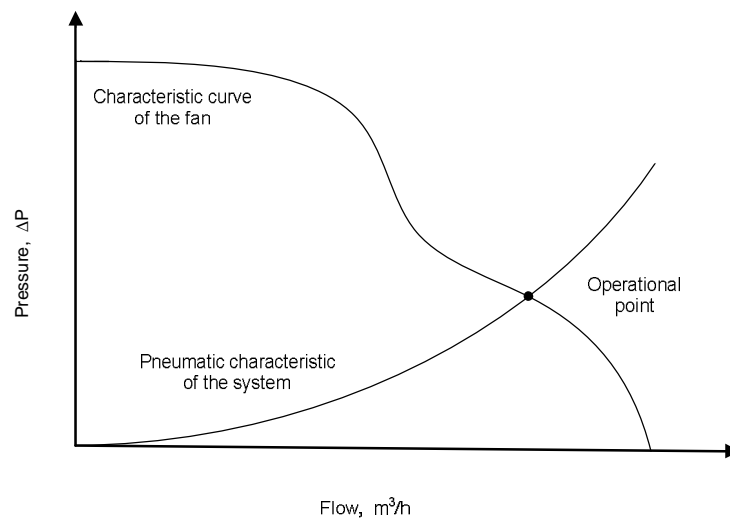


Figure 2.8: IV characteristic of a PV driven fan.

In the analysis and design of the fan-duct systems, it is useful to study the ΔP - Q system characteristics and fan characteristics in the same graphic, as shown in Figure 2.8. The operating points are the intersection of the system and the fan curves.

Most available literature regarding the flow rate modelling of PV-driven systems is on water pumping applications. The empirical relationships of flow rate as a function of irradiance at different pumping heads were developed and the coefficients of these

quadratic relationships were further expressed as functions of head pressure. Bione *et al.* (2004) also showed a quadratic relationship between flow rate and irradiance in a PV-driven water-pumping system. Eckstein *et al.* (1990) and Betka *et al.* (2004) described the pump pressure as a function of flow rate and pump rotational speed.

With regards to solar air thermal applications, Odeh *et al.* (2006) studied a PV driven roof slate based ventilation for pre-heating. The author separately modelled the electrical and pneumatic performance of all the components of the system using theoretical based equations. A macro model predicted the system air flow rates in various weather conditions.

Grassie (2007) studied the pneumatics of a solar transpired plate application for pebble bed stores where the fan was driven by a PV module. The author modelled the air flow operational points as a function of solar irradiance, employing a quadratic equation.

2.3 Drying woodchip

As was discussed in the introduction chapter, drying is an essential step in the woodchip chain supply. Due to the importance of drying wood, many researchers, especially in high latitude countries, have studied the advantages of various experimental drying methods. However, most of them address the difficulties when storing and naturally drying large amount of product for electricity generation. Kofman *et al.* (1997) concluded that it is complicated to store willow chips harvested from short rotation coppice. Small chips are not suitable for storage over prolonged periods of time, for example for more than 2 months. Fine chips lose a large amount of dry matter, which implies a consequent decrement in their heat value. Garstang *et al.* (2002), from Yorkshire, studied the factors that affected mass losses of a non-ventilated bulk storage of woodchips and provided recommendations regarding the best storage practice for large-scale production.

Studies were also conducted for the study of small-scale installations for drying wood fuel. Thus, Gigler *et al.* (2000) compared the drying performance of various types of willow woodchip of different sizes and also willow chunks using a small drying application. They studied the negative effect of the high pressure drop over a product bed that causes high energy costs and found that piles of wood chunks required much less energy than chips. Gigler *et al.* (2000) conducted natural wind drying experiments

for different wood species. They showed that large piles of wood chunks generally dried well, microbial activity was negligible, and dry matter losses were low and the drying rate in a pile largely depended on the dimensions of the chunks.

Using drying installations for drying agricultural, forced ventilation systems has been tested for drying woodchip in a deep bed. Gigler *et al.* (2000) assessed the drying suitability of a farm facility for storing potatoes, including the study of the pressure drop. They analysed the performance of a 1m deep willow chip bed dryer when using forced ventilation with 25,000 m³/h to dry 1440kg of willow chips.

Kielder Forest Products Ltd (2001) conducted various storing-drying trials in order to calculate the viability of using a force ventilation batch dryer instead of natural drying. The area of the dryer was 120m² and the high capacity fan operated with 50,000m³/h flow to dry 0.5, 1 and 1.5m deep woodchip bed. The drying costs were £4 per tonne of wet woodchip which is an important contribution to the total price of the woodchip.



Figure 2.9: Fresh woodchip being dried with forced air ventilation.

Similarly, Mc Govern (2007), in Aberdeen, conducted several tests to dry woodchips with hot air ventilation, using a high capacity batch grain dryer, Figure 2.9. The study consisted of the optimisation of the fuel resources to reduce the drying costs. The analysis considered the dryer performance operating on two days with 1m and 1.5m woodchip bed depths. The costs of the woodchip production were estimated to be approximately £14 to £20 per wet tonne dried.

3. WOODCHIP DRYER

3.1 Introduction

The study of the novel solar dryer requires the full understanding of the drying principles and the key factors which are involved in the process of drying woodchip. Considering the capacity of the solar air thermal system that comprises the novel woodchip solar dryer, two different dryer configurations have been designed, built and tested in order to study the operation of drying woodchip using low flow rates at low temperatures.

The chapter presents the experimental methodology including the construction of the dryer prototypes and testing procedure. The results obtained from the tests are discussed showing the influence of the key factors on the drying rates, drying times and dryer efficiencies. Finally the woodchip dryer performance is modelled using a simple mathematical expression that describes the drying process within a range of operation conditions.

3.2 Methodology

3.2.1 Introduction

This section summarizes the main aspects of the design and operation of the dryer prototypes. The initial prototype was based on thin layer configuration designs typically employed for solar drying. The dryer was built and its performance tested and analysed. Later using a similar methodology a second dryer based on other deep bed drying models was also built and tested.

3.2.2 Dryer design and construction

3.2.2.1 Dryer design

The dryer must be designed to guarantee the final product quality and to satisfy the production requirements. The main aim of the present woodchip solar dryer is to dry the maximum amount of woodchip using exclusively the air generated by the solar air thermal system proposed.

In the dryer design, the pressure drop caused by the product being dried has to be taken into consideration. Woodchip presents an important resistance to the air flow circulation. Depending on how the woodchip was laid in the dryer, two possible dryer configurations were analysed: Thin and thick layer dryers, the latter being the configuration which introduced the higher pressure drop in the system.

The dryer was designed to work with the output of the SATS prototype presented in the introduction chapter. Thus, the maximum possible air flow delivered by the SATS PV driven fan was $250\text{m}^3/\text{h}$. And the maximum possible heat input expected to be collected by the SATS was 1440 W in the most favourable case: 1.8 m^2 solar collector working at $1000\text{ W}/\text{m}^2$ solar radiation with a maximum efficiency of 80%.

The dryer consisted of two parts: a flow control unit which regulated the air flow rate and its temperatures, and the drying facility where the drying process takes part. During the tests, thin layer and thick dryer configurations used the same flow unit control while the drying facility was completely different. Figure 3.1.a and figure 3.1.b shows a schematic diagram of both dryer 1 and dryer 2 designs respectively.

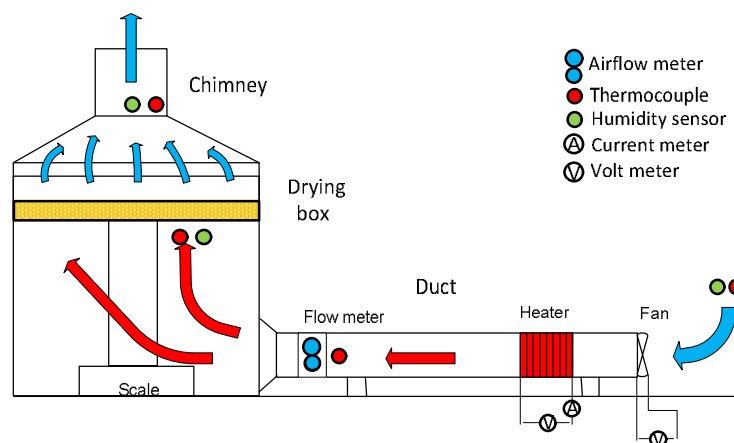


Figure 3.1.a: Schematic diagram of the thin layer dryer.

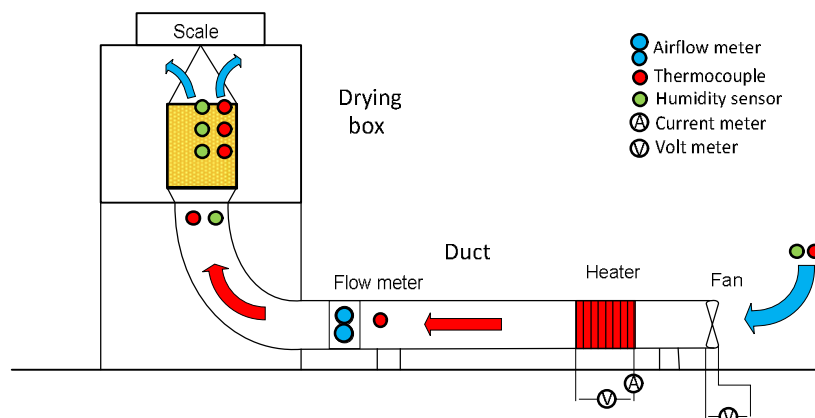


Figure 3.1.b: Schematic diagram of the thick layer dryer.

3.2.2.2 Dryer parts

3.2.2.2.1 Air Flow control unit

The air flow control unit is the part of the dryer used to adjust the air flow and drying temperature. Air from the surroundings was delivered into the system by a fan at ambient temperature and warmed up by a heater. Three components comprised the delivery system: the ducting, a fan and a heater.

The ducting consisted of a long rigid aluminium pipe of 140 mm diameter. It was used for fixing the apparatus and the instrumentation. The fan was located at one of the sides of the pipe and the heating element was installed at the centre of the pipe. On the other side, a round to square aluminium adaptor was attached to the pipe to help the air to flow at the entrance of the drying chamber. Wedges were attached to the tube oriented to different directions in order to mix the cold and hot air flow and ensure a homogeneous flow temperature.

The fan employed for the drying tests had the same capacity as the fan initially selected for the SATS. The model of the fan employed was PAPST 12VDC, 135mm diameter and 9,5W. During the drying tests, the fan was connected to a DC power source and air flow rate was regulated by the output voltage.

The thermal input was provided by an electrical resistance obtained from a tumble dryer appliance that generated heat when electric current passes through it. As a resistive element, the electric power was transformed totally into heat proportional to the voltage and the current.

3.2.2.2.2 The drying facility

The drying chamber is the place where the drying process takes place. Pre-heated air was driven from the pipe into the bottom of the drying box, and from below to the top, passing across the tray, removing the water from the woodchips.

Dryer 1: thin layer dryer

The model design of the drying chamber was based on various prototypes developed by other researchers, including Ayensu (1997) for crop drying and Akpinar (2006) for vegetable and fruits drying. The dryer chamber comprised a wooden box, a scale, a tray and a chimney. The scale lay at the base of the box and held the tray using a tower stand. A sealed wooden box around the tray forced the air through the woodchip tray. However, following the same methodology of other researchers such as Yaldiz *et*

al.(2003) and Togrul *et al.* (2002), the drying facility was not required to have heat insulation as the purpose of this project was not to build an optimal dryer but to study the drying process under controlled conditions. Appropriate instrumentation was located at several points in the drying cabinet to measure humidity and temperature. A chimney was also built in order to collect the outlet air and then measure its psychrometric properties. Figure 3.2 shows the dryer prototype 1 mounted in the lab.

- The tray had a square form with sides of 510 mm long and it was located 900 mm above the base of the chamber.
- The base of the tray was made of a plastic mesh that allowed the air to pass through and supported the woodchip at the same time.
- Attached parts were well sealed to minimize the air losses
- Air flow velocities in the box were not uniform because of the dryer configuration.
- Air was mixed in the box and the difference between maximum and minimum temperature was observed to be less than 1°C.



Figure 3.2: Dryer 1 prototype, apparatus and instrumentation.

Dryer 2: thick layer dryer

The thick layer dryer, shown in Figure 3.3, had a small section area and it was designed to operate with high drying temperatures. The design of this dryer

configuration was based on Menges *et al.* (2006) prototype used to study the drying characteristics of many products. The woodchip sample was placed in a box suspended from a scale hook located at the top of the system. The flow control unit was connected to the dryer through a flexible pipe and the pre-heated air entered the box and crossed the woodchip from below.

- The square tray was a thin plastic mesh that had an area of 170x170 mm².
- The box was attached to the base and it was well sealed avoiding any air leakage.
- Drying air temperatures were measured at the bottom of the box and they were observed to be stable and constant during the test.



Figure 3.3: Dryer 2 prototype, apparatus and instrumentation.

3.2.2.3 Instrumentation

The drying tests were characterised by air flow rates and drying temperatures regulated by the respective power sources. In order to control the operation of the dryer, drying parameters were monitored during the process. The weight of the sample, air flow rate and air properties in several points of the dryer were measured every 1 minute during the drying test.

3.2.2.3.1 Power input measurements

The heat input was provided by a resistive element that delivered heat proportional to the electric current. The heat received by the system was calculated as the active power consumed by the device defined in equation 3.1. The power was estimated as the product of the current and voltage as the inductive effect was negligible, Alonso & Finn (1974).

$$P = V \cdot I \cdot \cos \varphi \quad \text{Equation 3.1}$$

The power supplied to the system was controlled by an AC variac transformer. The heat input that determined the final drying temperatures for the tests was within a range of 0 to 1500W. The electrical measurements for both voltage and current were taken with a digital multimeter, Data Precision 1351 Digital Multimeter. The voltage meter and current meter employed had a precision of $\pm 0.01V$ and $\pm 0.001A$ respectively. The instrument display introduced a reading error of $\pm 0.1V$ for the voltage measurement and $\pm 0.01A$ for the current measurement.

3.2.2.3.2 Weighing scale

Due to the interest in tracking the changes in the sample weight, a high precision scale that included internal software for recording weighing data at any interval of time was employed. The weighing scale utilised was a A&D GX 6100 0.01 model. The weighing measurements were logged periodically into a computer using a specific software, WinCT that allowed communication between scale and PC to import weight data into an EXCEL spreadsheet. The scale had a lab precision with ± 0.01 gram of tolerance in the range of measurements and the reading error was ± 0.01 gram for all the range of measurements. However the scale introduced a design limitation as the maximum weight permitted was limited to 6.1kg.

3.2.2.3.3 Flow meter

The air flow velocity was constant for each test and it was measured using a ducting airflow meter. The model was an Airflow TM AV6 digital hand held vane anemometer of 100 mm diameter. It consisted of an axial turbine that generated a torque proportional to the air flow that crossed the instrument area. The instrument, calibrated by the manufacturer, had a tolerance in the airflow measurement of 1% for all the range of measurement. The reading error was ± 0.01 m/s.

3.2.2.3.4 Humidity sensor

Humidity sensors were employed to measure the relative humidity of the air at different points of the drying process. The humidity sensors employed were electronic devices which had resistive electrical behaviour sensitive to the relative humidity. The sensors employed were Honeywell HIH 4003 model calibrated in the factory. They had an operational error of $\pm 4\%$ points across the measurement range, 0% to 100%. Humidity sensors were connected to the power source and their signal was registered into the data logger. Relative humidity values were converted from the voltage readings using a linear correlation provided by the manufacturer. The uncertainty due to the transduction from voltage to RH was included in the tolerance range.

3.2.2.3.5 Thermocouples

The thermocouples were employed for measuring the air temperature at different points of the dryer: especially the ambient air and inlet and outlet air flow temperatures. Because the flow was not completely uniform, there were at least two thermocouples at each measuring point. The thermocouples employed were k-type. They were chromel-alumel alloys that generate a voltage proportional to the temperature difference between the hot and the cold junctions. Thus, two wires produced a differential of voltage proportional to the temperature. The thermocouples were calibrated in the laboratory following a methodical assessment of calibration used for the study of other solar thermal systems as solar water heaters, (Junaidi, 2007). The construction and calibration of the thermocouples were fulfilled for the degree of confidence required. Two tests were conducted for each sensor: A cold test in which the cold junction of the thermocouple sensor was placed in a thermos flask filled with ice at 0°C. The thermocouple measurements were recorded by the data logger until the stabilisation of the voltage. To verify the measurements, a reference British Standard thermometer of range 0-10°C was placed in the ice. And a hot test in which the thermocouple hot junction was placed in a hot bath with boiling water at 100° C. The thermocouple temperature readings were recorded by the data logger until the stabilisation of the voltage. Reference British Standard thermometers of range 70-100°C were positioned in the hot bath to calibrate the thermocouples.

The accuracy of the thermocouples was $\pm 0.5^\circ\text{C}$ in the range of working temperatures. The thermocouples, employed in the tests, were all connected directly to a data logger that automatically converted the voltage signal into temperatures.

3.2.2.3.6 Data logger

Data loggers were used for recording the temperatures and the relative humidity voltages. The instrument utilised was a Grant Instrument Squirrel 2020 series, type 1F8. The data logger converted automatically the voltage signal into temperatures using a polynomial relationship defined by the British Standards for k-type thermocouples. The 12 Bit data loggers have a sensitivity specification of 0.1°C.

Table 3.1: Quantities to be measured, instrumentation and measurement errors

Measurement	Unit	Instrument	Instrument precision	Reading error
Voltage	V	Multimeter	± 0.01 V	± 0.1 V
Current	A	Multimeter	± 0.001 A	± 0.01 A
Relative humidity	%	Humidity sensor	± 4 % points	-
Temperature	°C	k-type thermocouples	± 0.5 C	± 0.1 C
Air flow velocity	m/s	Velocimeter	± 1 %	± 0.01 m/s
Weight	g	Weighing machine	± 0.01 g	± 0.01 g

3.2.2.3.7 Error analysis methodology

In Table 3.1, the errors caused in each of the readings due to instrument tolerance are given. These values are used to calculate errors in the predicted values through propagation of error. This type of calculation is difficult since some equations have to be solved iteratively. The approach taken here is to run the model developed, not only for the measured values but also for their lower and upper limits. For example, for a measured temperature of 20°C, the model is tested for 19.4 °C, 20 °C and 20.6 °C. Thus, the three predicted values for the drying rates are used to calculate error in the drying model.

Throughout this thesis, whenever predicted values are compared to measurements, the calculated errors are simply a representation of how far the calculated value is from measurements. So errors are calculated as the difference divided by the measured value.

3.2.3 Woodchip characteristics

Within all the variety of trees planted in Scotland, Sitka spruce was selected for testing material, as there is a large forest production of this type of wood. Two samples of woodchip with different qualities were employed in the drying tests.

The first collection of woodchip was taken in February 2007. The woodchip was donated by the Forestry Commission from Queen Elizabeth forest park located near Aberfoyle. 150 kg of woodchip was obtained from the trunk of fresh spruce trees which had been shredded using a chipper machine.



Figure 3.4.a: Fresh sample of the first type of woodchip.



Figure 3.4.b: Dried sample of the second type of woodchip.

Woodchip fuel is a product with a distribution of material quality with different characteristics that depend on the type of wood, the chipper machine and the chipping process. The size distribution in the sample was not uniform and there were chips with different geometries and shapes. A high percentage of woodchip had characteristic

dimensions defined by the blade of the chipper, 10 mm. The woodchip sample also contained pieces of bark, needles and large chips which were removed manually in order to keep a uniform material for testing. Figure 3.4.a shows a picture of the first woodchip sample used in the drying tests.

Sitka spruce is a soft wood and its properties depend on the season of the year. The wood sample when harvested show MC levels of $60\% \pm 2\%$ when dried in an oven. The bulk density of the wood employed depends on the MC and was found to be between 400 to 450 kg/m^3 when measured. The sample was always found wet by touch and initial MC was maintained in levels around 58% MC by storing the wood in sealed plastic bags to minimise the water content losses. The stored woodchip initially preserved its quality and structural composition as the appearance of the sample remained the same. However after a prolonged storing time, signs of decay were found in the woodchip as the microbial activity increased because of the high MC levels.

The second woodchip collection was taken in January 2008. 150 kg of woodchip was donated by Pentlands Plants Ltd, a local company that was consolidating its position in the wood fuel market as woodchip producers. Their chipper machine operated with a blade of 20 mm and therefore, most of the wood chips had this characteristic dimension. Again, there was a noticeable distribution of shapes and sizes of woodchips, although chips were more uniform than in the first sample as the chipper machine had a screen with a characteristic dimension of 20 mm. The wood tree was Sitka spruce and this time the moisture content in the sample was lower, $54\% \pm 2\%$. MC and the bulk density of the woodchip was measured $400 \text{ kg/m}^3 \pm 20 \text{ kg/m}^3$. Like the first sample, the product was also sealed in plastic bags keeping the moisture in during the testing period. Figure 3.4.b shows the aspect of the second type of woodchip after being dried in the oven.

After the testing period of the second sample, the woodchip remaining was left to dry naturally under the weather conditions during a prolonged period of time and then stored in a bag with a low MC. In further experimental work, this sample of woodchip was available but with a lower MC than required. Thus the woodchip sample was re-wetted to 60 % MC and 50%, obtaining a third woodchip sample with similar quality as the one of the fresh woodchip sample. Although it must be considered that possible modifications in the internal structure may have occurred, implying changes in the water migration phenomena within the woodchips.

3.2.4 Testing procedure

The dryer testing and analysis was divided in two set of experiments associated with each dryer configuration. The performance of the thin layer dryer was the first to be studied and modelled. Secondly, following a similar methodology, the thick layer dryer was tested and the results modelled.

The thin layer dryer test results were employed to analyse the impact of the key factors that govern the process: temperature, drying velocity and relative humidity in the drying rates. In order to analyse the effect of the woodchip quality in the drying process, the initial results for the first sample of woodchip were compared with a second woodchip sample results.

The range of temperature and drying velocities were limited by the performance of the SATS, studied in next chapter 4. For the thin dryer configuration, for a maximum air flow of 220 m³/h, the experimental drying temperatures were expected lower than 50°C when SATS working in the most favourable conditions. Following the testing methodology commonly used by the researchers in the work presented in the literature review, section 2.1, each testing set was divided in groups of various tests at different temperatures: Thus, considering that the most common range of temperatures were between 20°C and 40°C, for the first woodchip sample, 4 tests were conducted at 20°C, 30°C and 40°C with different air flow rates: 55 m³/h, 110 m³/h, 165 m³/h and 220 m³/h. For the second woodchip sample testing set more drying tests were included and widened the range of temperatures from 10°C to 50°C.

The deep bed dryer introduced a high pressure drop in the solar dryer system and therefore SATS was expected to work with low flow rates at high temperatures. Thus the range of operating flow rates was drastically reduced to 110 m³/h while temperature range was increased to 65°C. The analysis of the thick layer configuration was focused on the study of the drying rates affected by the thickness of the layer. 3 set of tests with different woodchip layers: 10 cm, 20 cm and 30 cm were tested.

3.2.4.1 Parameters to control

Drying is a process in which air removes the moisture from a product. The dryer performance is defined by all the parameters that characterise the drying process:

- The dryer configuration: Shape and dimensions of the dryer.
- The product characteristics: MC₀, size and shape of the chip, wood type.
- The drying conditions: Drying velocity, temperature and relative humidity.

In order to facilitate the analysis and comparison of the test results, it was decided to dry approximately the same amount of water in all the tests. Thus as the MC_0 of the sample remained constant, the same weight was selected in all the tests. Because of the technical limitation introduced by the scale, the mass of the woodchip in the thin layer dryer tests was 3 kg, while in the thick layer dryer, the mass of woodchip was from 1 kg to 3 kg depending on the thickness of the layer.

Each drying test was described by the parameters of the air flow that were possible to adjust: temperature and velocity. Although the water content in the air or relative humidity also affected the drying process, it was not possible to control. However, water content in the air was measured and its values were found predominantly constant with not significant variations during the testing period, $\pm 1 \text{ g}_{\text{water}} / \text{kg}_{\text{air}}$.

The first characteristic variable, the drying velocity, was adjusted by selecting the adequate voltage of the DC power source that supplies electricity to the fan. The anemometer measured the velocity in the pipe and the average drying velocity on the tray was calculated by multiplying the velocity measured by a rate of areas as shown in equation 3.2.

$$V_{\text{drying}} = V_{\text{anemometer}} \frac{A_{\text{duct}}}{A_{\text{tray}}} \quad \text{Equation 3.2}$$

The air flow at ambient conditions was heated up until flow temperature reached the desired drying temperature. The heat was supplied into the system by the electric resistance and regulated by changing the voltage of the variac transformer. The heat was estimated to be proportional to the voltage and electric current measured.

3.2.4.2 Air flow in the dryer

Air properties were monitored during the drying test in order to control the operation of the dryer and to validate the results obtained. Air properties were measured at 3 points of the dryer: ambient air, before it reached the woodchip layer and the outlet air. Because the quality of the air was not uniform, in each of the points described in Figure 3.1.a and Figure 3.1.b, temperatures and RH were calculated as an average of a minimum of 2 or 3 measurements.

In the thin layer dryer, the drying velocity that characterized the drying test was calculated as an average of the velocity of the air that crosses the tray. However local velocities were observed to be non uniform. The differences in the local velocities were because of:

- The dryer box configuration: the air flow distribution in the dryer box implied that velocities at the back were observed to be 9% higher than in the front over the range of working air flows.
- The disposition of the woodchip on the tray: difference in the thickness of the layer and internal holes in the layer made the air move faster across the woodchip.

In an attempt to optimise the dryer prototype and decrease the local air velocity differences under the woodchip tray, 2 baffles were installed in the drying chamber aliened with the inlet air duct forming an angle of 45°. However the drying tests results derived from this modification did not show any remarkable benefit.

The optimisation of a woodchip dryer prototype should look at the local drying velocities around the woodchips considering the woodchip size. However for this research consideration was not given to the drying process at the boundary layer interface.

As the flow characteristics were not constant in the drying tray, the local values of the psychrometric properties after air flow crossed the tray were not homogeneous. Hence it was necessary to collect all the exhaust air in a chimney to help to obtain uniform average values of humidity and temperature measurements.

3.2.4.3 Mass /energy balance

The results obtained from each drying test were validated with a mass and an energy balance. The procedure was useful for ensuring the correct functioning of the system, making sure that there was not any air leakage, anomalies or measuring mistakes. The mass balance was especially helpful in the beginning when designing the dryer prototype.

Mass balance consisted in the comparison between measured and predicted amount of water dried in an interval of time. While energy balance helped to check the isentropic character of the drying process in which air flow temperature decreased when removing the moisture from the woodchip, with no enthalpy variation.

3.2.4.4 Tests

The thin layer dryer tests were divided into two sets for each woodchip type analysed. The testing period of the first sample was during the spring of 2007 while second sample tests were conducted in winter and spring of 2008. The second dryer tests were conducted in the summer of 2009 employing the third woodchip sample that consisted in rewetted woodchip from the second sample collection.

Drying tests were conducted in the university workshop, a large room with a large mass of air, where ambient conditions, temperature and RH, remained practically constant during the experimental testing.

During the period of each testing set, the moisture content in the air was a parameter which was not possible to control as it was affected by meteorological conditions and local weather changes. However, for the period that lasted doing a set of tests, values of humidity were observed in most of the cases in an interval of values ± 1 g water/ kg air. The average value of the humidity in the air measured during two testing weeks in February 2008 was 6.1 g water/ kg air. And during the month of June 2009 the average of humidity measurements was 9.3 g water/ kg air.

The drying test procedure was identical for each dryer configuration. Before starting the test, the dryer was well sealed and warmed up if it was required. Air flow temperature and velocity were adjusted to the drying characteristics of the corresponding experiment. The tests started once the woodchip was set on the tray and air flow was circulating at desired drying conditions. Woodchip was weighed periodically until the end of the test when the sample of woodchip reached the equilibrium. Once the sample was dried and the weight reading remained constant, the sample was removed from the tray and dried up in an oven at 105°C.

The scale was connected to the computer and this allowed the monitoring and collection of the weight data automatically into an EXCEL spreadsheet. The weight measurements were logged periodically in intervals of 1 minute in order to track precisely the gradual change of the woodchip weight. Thus, the number of data points for each drying tests was variable and depended on the time to reach the EMC. Temperature and relative humidity measurements were collected in a data logger at the same time interval and later uploaded in another EXCEL spreadsheet.

The data analysis of the drying tests for each set consisted of:

- Validation of the results obtained.
- Obtaining the drying parameters and drying curves.
- Studying the influence of the key parameters that govern the drying process.
- Modelling the drying curves.
- Finding a macro model equation that describes the dryer performance.

A set of modules were developed in order to process the data of the drying tests. Visual Basic for Applications, VBA, was the programming tool utilised to facilitate the calculation of the drying parameters and this could be combined with EXCEL spreadsheet. For the analysis of the drying data, 3 codes were developed:

- Drying curves and drying variables code which calculates and compares the drying parameters for all the tests in a drying set, **Appendix A1: Drying test data processing.**
- Mass and energy balance code which validates the testing operation and calculates the drying efficiencies using psychrometric relations, **Appendix A2: Modelling drying test data processing**
- Drying model code which predicts the drying process and validates the results obtained, **Appendix A3: Mass and energy balance.**

3.3 Results

3.3.1 Introduction

The present section summarises the results obtained from the experimental work on drying woodchip with low temperatures and low air flows. The section deals with the performances of the thin layer and the thick layer dryers are analysed separately. The results show the drying curves for various drying conditions and include the analysis of the drying rates, drying times and efficiencies as a function of the key factors that govern the dryer performance. The ultimate objective of the drying tests is to create a mathematical model to predict the performance of the woodchip dryer.

3.3.2 Thin layer dryer result

The first results analysed correspond to the set of tests for the thin layer dryer drying the first woodchip sample. The objective of this set of tests was to evaluate the dryer performance studying the drying rates as a function of the drying conditions. Once the testing procedure and methodology were established, 12 drying tests were conducted at 3 different drying temperatures for 4 flow rates. Table 3.2 shows the details of the drying test set corresponding to the first dryer prototype. Each test was characterised by the air flow velocity, V_{dry} , and the average drying temperature, T_{dry} , and average relative humidity, RH_{dry} , of the air before passing through the woodchip during the test.

Table 3.2: Characteristics of the drying tests set that corresponds to the first wood sample.

Test	Flow	V_{dry} (m/s)	T_{amb} (°C)	RH_{amb} (%)	T_{dry} (°C)	RH_{dry} (%)	W_0 (g)	W_{dried} (g)	MC_0 (%)
1	55	0.06	21.8	33.1	22	33.1	3,004	1,261	58.0
2	110	0.13	20.5	43.3	20.5	43.3	3,001	1,230	58.8
3	165	0.19	22	38.2	22	38.2	3,067	1,255	59.0
4	220	0.25	21.1	39.9	21	39.9	3,059	1,250	59.1
5	55	0.06	22.5	42.4	31.5	25.1	3,038	1,228	58.3
6	110	0.13	23.6	47.3	31	30.3	3,090	1,233	58.4
7	165	0.19	24.5	47.5	30.5	30.4	3,045	1,225	58.0
8	220	0.25	22.1	41.8	31.2	24.6	3,100	1,313	57.2
9	55	0.06	20.9	51.7	40.5	20.4	3,063	1,306	58.0
10	110	0.13	22	50.3	41	18.1	3,091	1,230	58.2
11	165	0.19	21.6	50.2	40.5	17.3	3,060	1,290	57.7
12	220	0.25	21.2	51.1	40	20.0	3,000	1,250	58.3

The mass of the woodchip sample selected was always $3,050g \pm 50g$ for all the tests, forming a thin layer of $3cm \pm 0.5cm$ thickness. During the testing period, no significant change in the quality of the woodchip stored and the initial moisture content was noticed and MC_0 remained in the same levels.

In order to compare the dryer performance when drying woodchip at different conditions, the woodchip must have the same initial drying quality and the amount of water to dry should be the same. Mass was not an adequate variable to compare as its value didn't reflect the quality of the sample. Therefore moisture content in wet basis is considered as a quality indicator. It was defined in equation 2.1 as the rate of water content in the sample, is an appropriate dimensionless variable commonly use for the analysis of the drying tests results.

A VBA tool was developed in order to compare the drying performance for various tests at once. Weight and time data of each test were adequately introduced in an EXCEL spreadsheet. For a reference MC_0 , the VBA program adjusted the data series for each test and calculated the drying parameters considered for the analysis and modelling of the dryer performance.

3.3.2.1 Moisture content

The quality of the woodchip was found to be uniform in all the drying tests conducted. All the MC_0 values of the samples tested were included within an interval between 60% and 57% MC. Therefore the reference MC_0 value for comparing the drying performance was 57%. Taking this value as a reference meant that the initial weight at 57% MC or the total amount of water to remove in each sample was not exactly the same. The difference between the maximum and the minimum initial weight was around 100g, 3.3% of the total weight.

Figures 3.5.a, 3.5.b and 3.5.c show the MC curves that correspond to 4 tests operating with various drying velocities at 3 temperatures: 22°C, 31°C and 40.5°C.

Drying curves have an exponential profile: In the first stages of the process, superficial water was easily removed by the air and MC rapidly decreased. It was then that the dryer worked more efficiently, as was discussed in section 2.1.2. Afterwards, MC values kept decreasing towards an asymptotic value, the equilibrium moisture content, EMC. The drying mechanism required more efforts to move the water from the inner to the surface of the woodchip. Therefore the slope of the curve decreases and the drying efficiency consequently also decreases. Finally when woodchip reached the EMC, the air crossed the woodchip removing no water and the weight of the sample remained constant.

The EMC depends on the woodchip characteristics and the quality of the air: temperature and humidity. Observing the MC graphs above, EMC values were found to be consistent in the tests conducted at similar drying temperature. The differences observed were due to the nature of the woodchip samples and variation in the humidity of the air. For each drying temperature, EMC value was estimated as the average of the EMC values obtained from the tests conducted at such a temperature: 12%, 8% and 6% were the EMC values associated to 22°C, 31°C and 40.5°C respectively.

Drying times in tests conducted at ambient temperature were appreciably much longer

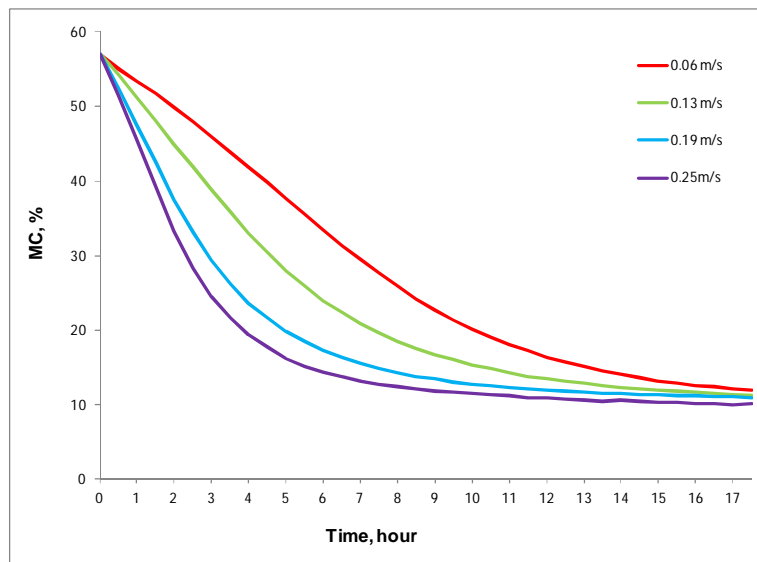


Figure 3.5.a: MC curves for 4 drying tests at 22°C.

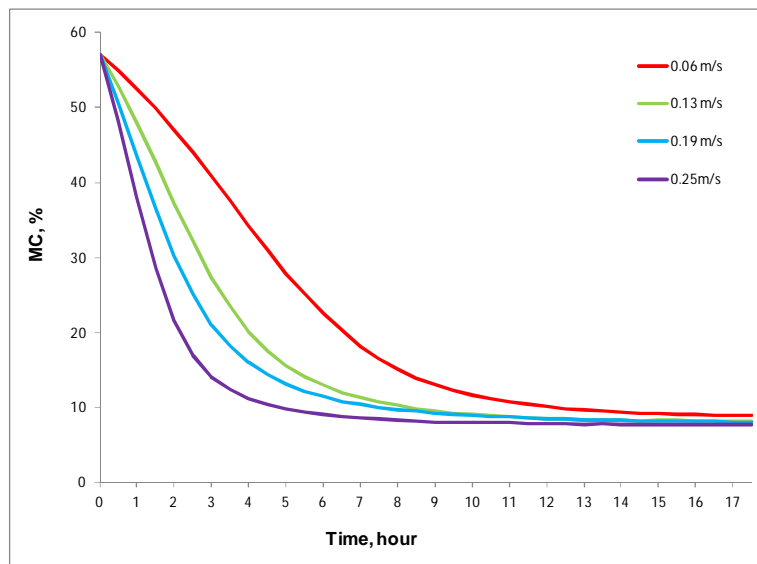


Figure 3.5.b: MC curves for 4 drying tests at 31°C.

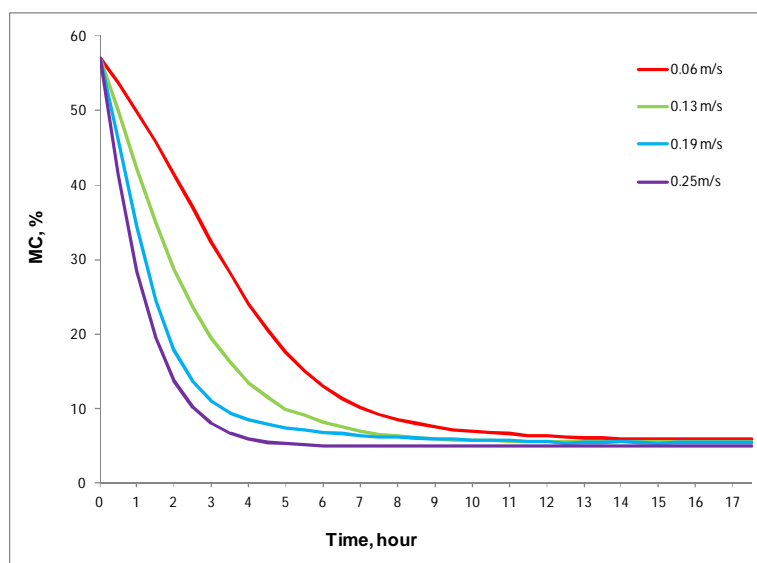


Figure 3.5.c: MC curves for 4 drying tests at 40.5°C.

than drying times for the same flows at higher temperatures. Increasing the drying temperatures enhanced notably the dryer performance reducing considerably the MC at the first stages of the process. As drying temperature increased, drying curves associated to the same flows were observed closer to each other.

Drying curves show how the water was removed from the woodchip during the test: At the beginning of the process, moisture was removed from the woodchip with more celerity than at the end when MC approached the equilibrium.

When drying woodchip for fuel purposes, the lower the MC is, the higher the heating value the woodchip has. However, the energy and the time employed for drying woodchip must be compensated by an increment in the quality. The times for reaching the final EMC were usually long and therefore a limit was established at 30% MC. As it was discussed in section 2.1.3, this value was considered adequate and sufficient for the dried woodchip quality. Thus having this MC as a reference, the drying times were calculated as the interval of time to dry the woodchip reducing MC_0 to the 30%. Table 3.3 shows the drying times required for drying the first woodchip sample.

Table 3.3: Drying times from 57% MC to 30% MC for first woodchip sample.

Test	T _{drying}	Flow	V _{drying}	Time _{drying}	Test	T _{drying}	Flow	V _{drying}	Time _{drying}
1	21°C	55 m ³ /h	0.06 m/s	6h 50min	7	31°C	165 m ³ /h	0.19 m/s	2h
2	21°C	110 m ³ /h	0.13 m/s	4h 30min	8	31°C	220 m ³ /h	0.25 m/s	1h 25min
3	21°C	165 m ³ /h	0.19 m/s	2h 55min	9	40.5°C	55 m ³ /h	0.06 m/s	3h 10min
4	21°C	220 m ³ /h	0.25 m/s	2h 20min	10	40.5°C	110 m ³ /h	0.13 m/s	1h 55min
5	31°C	55 m ³ /h	0.06 m/s	4h 40min	11	40.5°C	165 m ³ /h	0.19 m/s	1h15min
6	31°C	110 m ³ /h	0.13 m/s	2h 45min	12	40.5°C	220 m ³ /h	0.25 m/s	1h

3.3.2.2 Drying rates and efficiencies

The drying rate is a parameter that helps to compare the drying process for different products. It is defined as the amount of water evaporated in an interval of time and indicates the velocity of the drying process. Commonly the drying rate is represented with the drying time and with the MC of the product. Figure 3.6 and figure 3.7 show the graphics of the drying rate curves for various tests when drying at constant flow and constant temperature respectively.

The initial values of the drying rates were high as the gradient of vapour pressure between the woodchip surface and the air surrounding was maximum. Gradually, as the tests went on and woodchip got dried, the partial vapour pressure difference decreased

and the drying rate as well. Figure 3.6.b and figure 3.7.b represent the curves that show the relationship between the drying rate and the MC of the sample for each test. The higher the temperature or the velocity was, the higher the drying rate was at the beginning of the test. It was desirable to design a dryer which yielded high constant drying rates when drying woodchip in the beginning of the process, at least until reaching the MC limit, 30%. However the thin layer option did not provide good results in terms of drying efficiency.

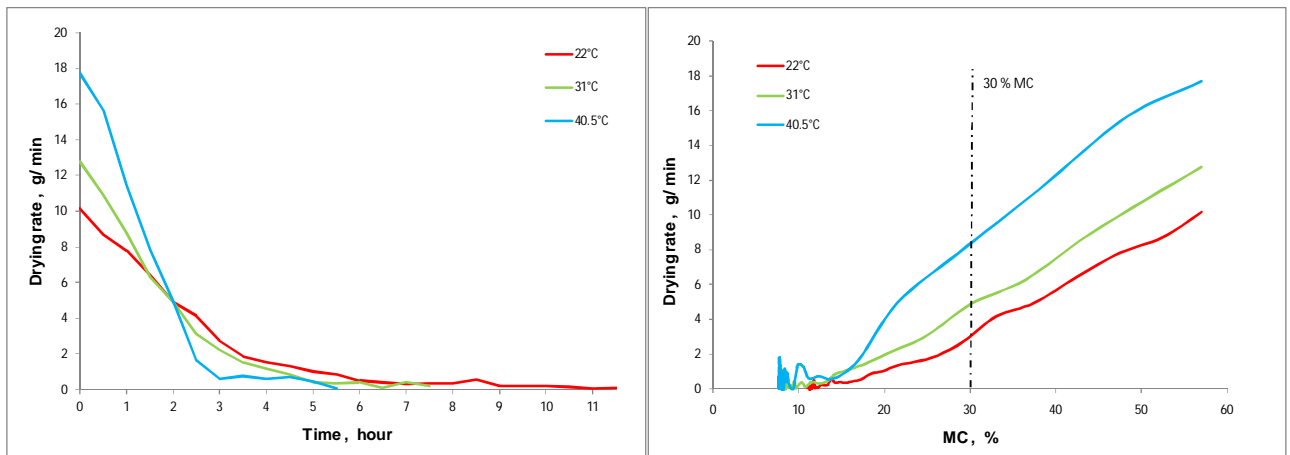


Figure 3.6.a and Figure 3.6.b: Drying rate vs time and Drying rate vs MC for 3 tests with a drying velocity of 0.19 m/s.

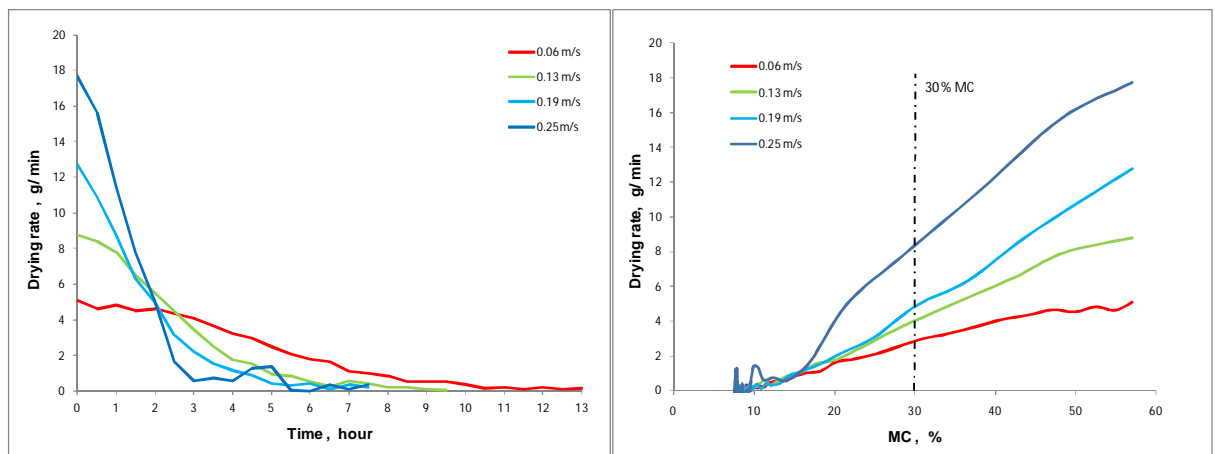


Figure 3.7.a and Figure 3.7.b: Drying rate vs time and Drying rate vs MC for 4 tests at 30°C.

The initial values of the drying rates were high as the gradient of vapour pressure between the woodchip surface and the air surrounding was maximum. Gradually, as the tests went on and woodchip got dried, the partial vapour pressure difference decreased and the drying rate as well. Figure 3.6.b and figure 3.7.b represent the curves that show the relationship between the drying rate and the MC of the sample for each test. The higher the temperature or the velocity was, the higher the drying rate was at the

beginning of the test. It was desirable to design a dryer which yielded high constant drying rates when drying woodchip in the beginning of the process, at least until reaching the MC limit, 30%. However the thin layer option did not provide good results in terms of drying efficiency.

The drying effectiveness or ‘pick-up’ efficiency evaluates the drying rate over the capacity of the air to absorb water from the woodchip. Thus drying effectiveness is defined by Brenndorfer (1985) as the ratio between the increment of humidity in the air after crossing the wet woodchip and the theoretical capacity of the air to absorb moisture content, equation 3.3.

$$\eta_{dryer} = \frac{w_o - w_i}{w_{sat} - w_i} \quad \text{Equation 3.3}$$

Where w_o is the absolute humidity of the air leaving the dryer, w_i is the absolute humidity of the air entering the dryer and w_{sat} is the absolute humidity that corresponds to the dew point temperature of the air entering the dryer.

The dryer efficiency was estimated as the amount of water evaporated from the woodchip divided in a period of time by the maximum water possible to evaporate by the air flow in the same period of time, equation 3.4.

$$\eta_{dryer} = \frac{W_0 - W_{time}}{\dot{m} \cdot \rho \cdot time \cdot (w_{sat} - w_i)} \quad \text{Equation 3.4}$$

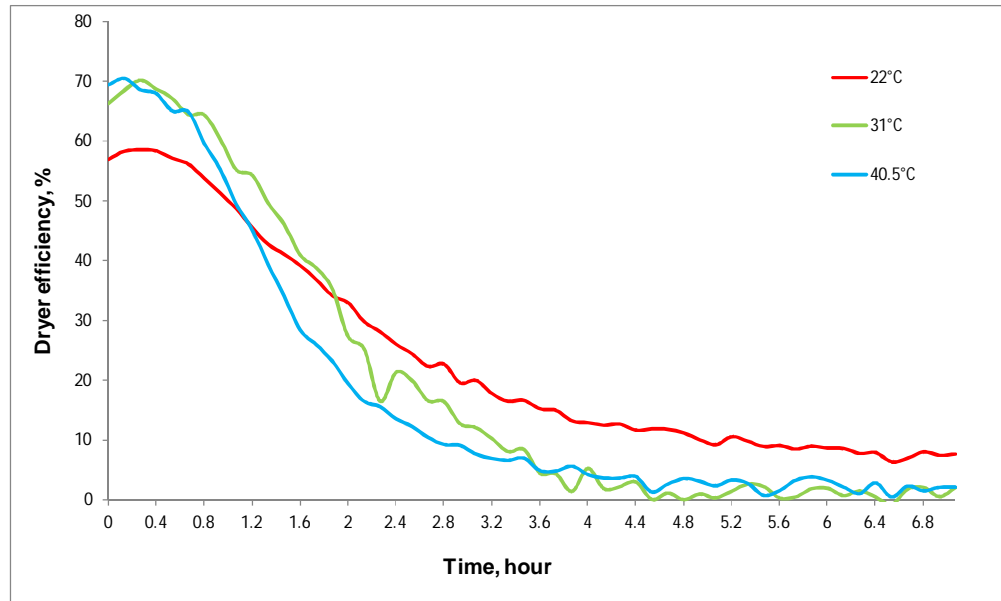
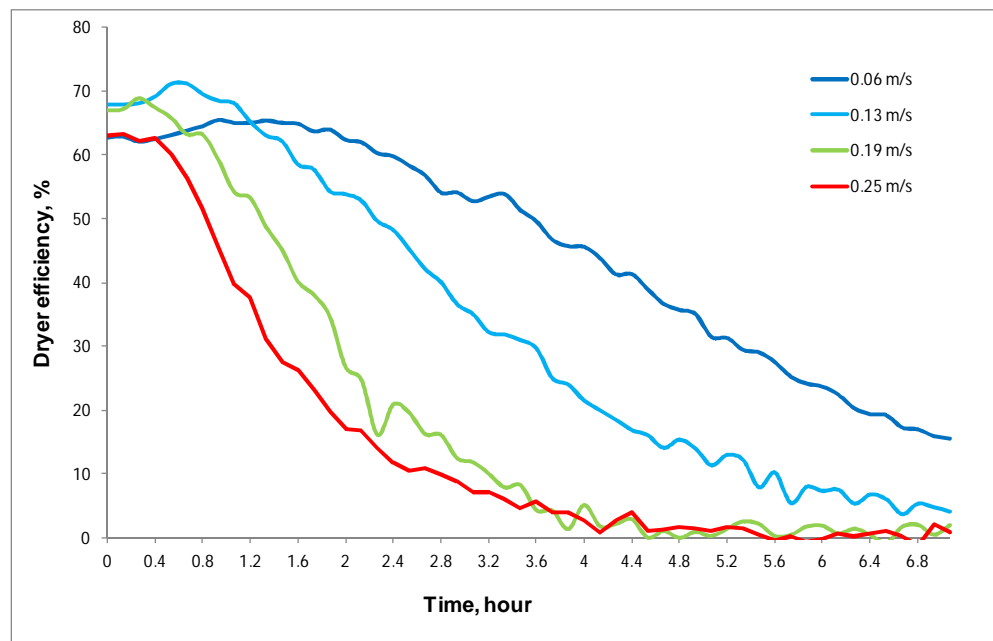
Where: W_0 is the initial mass of the woodchips and

W_{time} is the mass of the same sample after a period of time.

Figure 3.8.a and figure 3.8.b show the drying efficiencies curves for various tests corresponding to the thin layer dryer operating at various temperatures and various drying velocities respectively. In general, the drying efficiencies was low for all cases. As it was expected, at the beginning of the tests, drying efficiency was high. However as the woodchip MC decreases, drying efficiency decreases in a similar manner as the drying rates. Table 3.4 shows the average values of the pick-up efficiencies for the tests, drying the woodchip from 57% MC to 30% MC. It was observed that average drying efficiencies increased notably with temperature when dryer operated with the same flow rate. This can be justified as the internal migration of moisture in the woodchip was more effective at higher temperatures.

Table 3.4: Drying efficiencies when drying woodchip from 57% to 30% MC in the thin layer dryer.

Test	T _{drying}	Flow	V _{drying}	η _{drying}	Test	T _{drying}	Flow	V _{drying}	η _{drying}
1	21°C	55 m ³ /h	0.06 m/s	47.7%	7	31°C	55 m ³ /h	0.19 m/s	53.2%
2	21°C	110 m ³ /h	0.13 m/s	49.8%	8	31°C	110 m ³ /h	0.25 m/s	51.3%
3	21°C	165 m ³ /h	0.19 m/s	41.2%	9	40.5°C	165 m ³ /h	0.06 m/s	58.2%
4	21°C	220 m ³ /h	0.25 m/s	45.1%	10	40.5°C	220 m ³ /h	0.13 m/s	60.1%
5	31°C	55 m ³ /h	0.06 m/s	52.3%	11	40.5°C	55 m ³ /h	0.19 m/s	54.6%
6	31°C	110 m ³ /h	0.13 m/s	54.1%	12	40.5°C	110 m ³ /h	0.25 m/s	55.1%

**Figure 3.8.a: Dryer efficiency curves for 3 tests with a drying velocity of 0.19 m/s.****Figure 3.8.b: Dryer efficiency curves for 4 tests at 30°C.**

3.3.2.3 Test Comparison: 57% MC and 52% MC woodchips.

A second sample of woodchip was tested using the same thin layer dryer configuration. The initial objectives of the new tests were:

- Obtain results for a wider range of drying temperatures.
- Compare the dryer performance for two woodchip samples with different chip sizes.
- Find a correlation for drying process parameters as a function of the size.

The second woodchip sample tested was also Sitka spruce, so the internal structure of the wood was very similar to the first woodchip sample.

The characteristic dimension of the chip was 20 mm, two times the first woodchip sample size. As the characteristic size of the chip was larger, the ratio of surface area to volume of product decreased. Moreover, the size of the chip also affected the internal moisture migration mechanism as the distance the water had to travel to the surface was longer. The drying process characteristics were less favourable and drying times for the new woodchip tests would be expected to be lower than in the first woodchip sample, if the MC_0 was the same.

However, the MC_0 in the second woodchip sample was 52%. Therefore the amount of water to evaporate was lower than in the first sample. Table 3.5 shows the water content in the woodchip at the beginning and when dried at 30% MC for both woodchip samples. This difference of water also affected the drying process and therefore it was not possible to establish a rigorous correlation in order to compare the drying process for the woodchip samples selected.

Table 3.5: Weight, water content and water evaporated in two samples of woodchips.

Woodchip	Weight ₀	MC ₀	Water ₀	W _{dried}	Weight (30%MC)	Water (30%MC)	Water _{evaporated}
Sample 1	3,000 g	57%	1,710 g	1,290 g	1,842 g	552 g	1,158 g
Sample 2	3,000 g	52%	1,560 g	1,440 g	2,057 g	617 g	943 g

Following the same procedure and analysis described before for the first woodchip sample, a set of 16 tests were conducted for the same range of flow rates, covering a range of temperatures between 10°C and 51°C.

The results obtained from the drying tests were grouped in set of constant drying temperatures. Again the MC curves described a similar exponential profile as the MC

curves obtained for sample 1. As MC_0 was not the same in both samples, it was not possible to compare the drying curves in order to draw conclusions regarding the woodchip characteristics. Nonetheless, the dryer performance was analysed by observing the drying rates and calculating the drying times.

Figure 3.9.a and figure 3.9.b show the MC curves corresponding to the dryer performance when drying sample 1 and sample 2 at constant temperature and constant flow rate respectively. Graphics show similar curves profiles. Analysing a pair of tests at

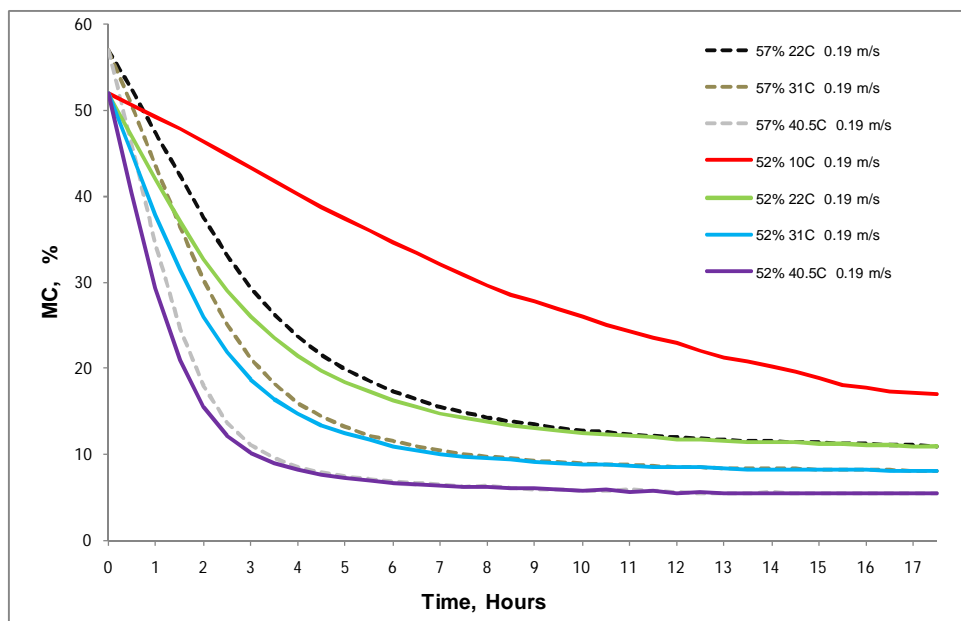


Figure 3.9.a: MC curves from drying tests at 0.19m/s, employing the first and the second woodchip sample.

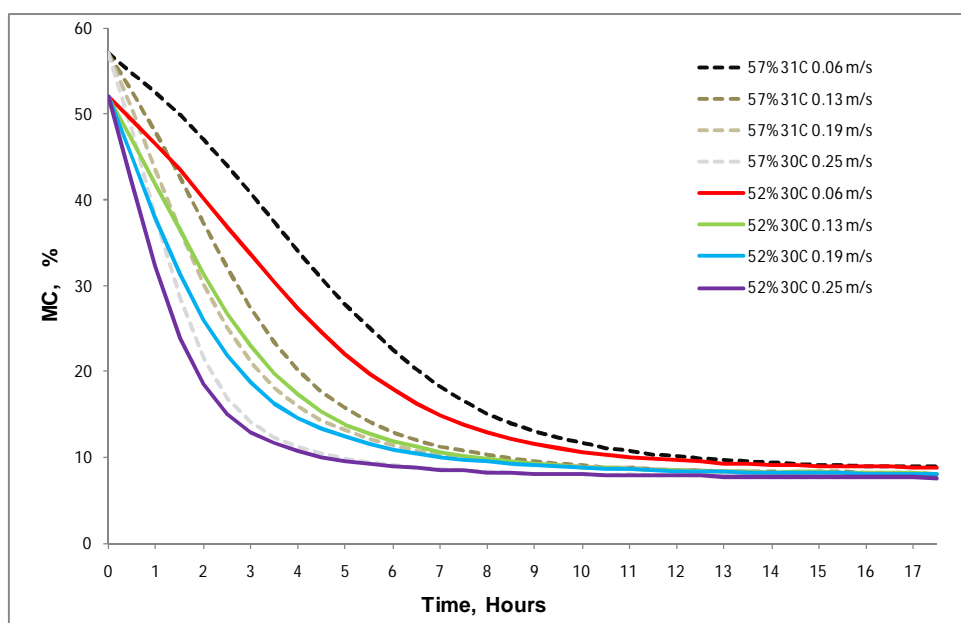


Figure 3.9.b: MC curves from drying tests at 30°C, employing the first and the second woodchip sample.

identical conditions, sample 1 MC curve started at 57% while the sample 2 MC curve started at 52%. Both curves converged to a similar EMC value at the end of the process. It was found that the slopes of the MC curves at the beginning were very similar for both woodchip samples and hence similar drying rates were expected. The above mentioned figures show that for all cases, the second woodchip sample MC curves were always ahead during the drying process, implying shorter drying times. Table 3.6 shows the drying times to reach 30% MC for the second woodchip sample that can be compared to drying times for the first woodchip sample in table 3.3.

Table 3.6: Drying times obtained from the second woodchip sample tests.

Test	T _{drying}	Flow	V _{drying}	time _{drying}	Test	T _{drying}	Flow	V _{drying}	time _{drying}
1	10°C	55 m ³ /h	0.06 m/s	22h	9	30°C	55 m ³ /h	0.06 m/s	3.5h
2	10°C	110 m ³ /h	0.13 m/s	12.3h	10	30°C	110 m ³ /h	0.13 m/s	2.1h
3	10°C	165 m ³ /h	0.19 m/s	7.7h	11	30°C	165 m ³ /h	0.19 m/s	1.6h
4	10°C	220 m ³ /h	0.25 m/s	5.8h	12	30°C	220 m ³ /h	0.25 m/s	1.1h
5	20°C	55 m ³ /h	0.06 m/s	5.4h	13	40°C	165 m ³ /h	0.19 m/s	1.2h
6	20°C	110 m ³ /h	0.13 m/s	3.7h	14	45°C	165 m ³ /h	0.19 m/s	1h
7	20°C	165 m ³ /h	0.19 m/s	2.4h	15	50°C	55 m ³ /h	0.06 m/s	2h
8	20°C	220 m ³ /h	0.25 m/s	1.8h	16	50°C	220 m ³ /h	0.25 m/s	40min

Although the effect of the woodchip size in the drying process was not possible to be quantified, the size of the woodchip was not a determining factor when drying woodchip in the thin layer dryer. It was the MC₀ in the woodchip or the amount of water to be evaporated that defined the drying rates and the progress of the drying process.

3.3.2.4 Comparison of drying 3kg and 4kg of 52% MC woodchip.

The drying performance depended on the thickness of the layer or the residence time of the drying air in the woodchip layer. Thus the amount of the woodchip to dry also affected the drying rates.

The mass of woodchip selected for the thin layer dryer tests was 3 kg. This amount was adequate for the dryer operation and it was always the same in order to compare the results of a set of tests. Increasing the thickness of the woodchip layer may have reported benefits when drying at the same drying conditions of air flow, temperature and RH. However, at the same time, increasing the mass of woodchip on the tray would also have caused an increment in the pressure drop which may involve negative consequences to the dryer performance.

This section illustrates a comparison between the dryer performances when drying two woodchip samples of 3 kg and 4 kg at identical conditions. The thickness of the layer was measured in different points of the tray, and the average was $3 \text{ cm} \pm 0.5 \text{ cm}$ and $4 \text{ cm} \pm 0.5 \text{ cm}$ for 3 kg and 4 kg test respectively. Table 3.7 show the characteristics of these tests.

Table 3.7: Characteristics of the 3 kg and the 4 kg drying tests.

Test	Flow	V_{dry}	T_{amb}	RH_{amb}	T_{dry}	RH_{dry}	W_0	W_{dry}	MC_0
3 kg	$165 \text{ m}^3/\text{h}$	0.19 m/s	$17.5 \text{ }^\circ\text{C}$	37%	$37 \text{ }^\circ\text{C}$	13%	3,080 g	1,468 g	52.3%
4 kg	$165 \text{ m}^3/\text{h}$	0.19 m/s	$18.5 \text{ }^\circ\text{C}$	40%	$37 \text{ }^\circ\text{C}$	12.50%	4,141 g	1,851 g	53.3%

Two factors were considered when comparing the results:

- 4 kg test had more volume of woodchip and the length of the air path across the chips is longer, therefore air flow can pick up more water from the woodchip.
- 4 kg of woodchip had more water to evaporate as table 3.7 shows. Therefore, at the beginning, for a prolonged period of time, air flow removed moisture from the woodchip more efficiently and left the dryer with higher humidity content.

Table 3.8 presents the theoretical values of the water contained in the woodchip and also the water evaporated in the process for each case.

Table 3.8: Weight, water content and water evaporated in 3 kg and 4 kg of woodchips.

W_0	MC_0	MC_{final}	Water_0	W_{dried}	Weight (30%MC)	Water (30%MC)	Water _{evaporated}
3,000 g	52%	30%	1,560 g	1,440 g	2,057 g	617 g	942 g
4,000 g	52%	30%	2,080 g	1,920 g	2,742 g	822 g	1,257 g

Figure 3.10.a and figure 3.10.b shows the comparison of the drying rates of both tests at identical operation conditions. It was observed that increasing the depth of the layer implied higher drying rates during the process. This meant that for the same drying conditions, the air removed more water from the woodchip and the dryer operated more efficiently. 1 hour and 20 minutes was required for drying 4 kg of woodchip from 52% MC to 30% MC, while for drying 3 kg woodchip, 1 hour was required.

In conclusion, the mass of the woodchip or the thickness of the dryer has to be selected carefully in order to optimise the production. Increasing the thickness of the

dryer implies higher drying rates and enhances the dryer efficiency. However a dryer with a deep layer configuration may imply low flow because of the pressure drop generated. Moreover, drying a deep layer of woodchip may imply a non homogenous quality of the dried product. A distribution of MC values may appear in the woodchip layer and in the same product over dried regions may exist while other parts remain wet.

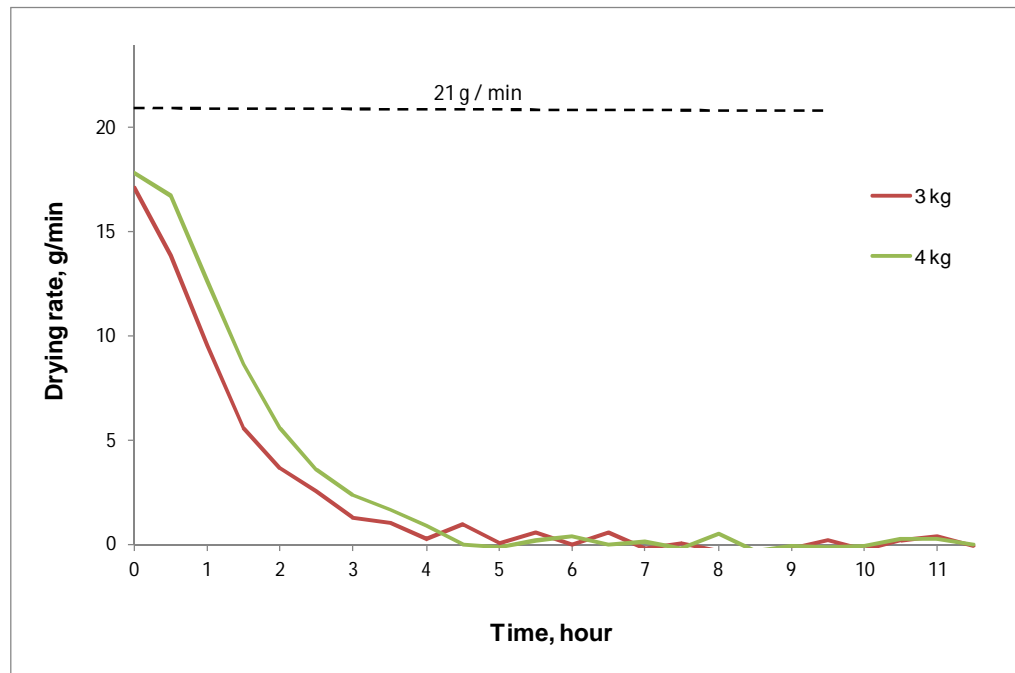


Figure 3.10.a: Drying rate curves obtained from the 3kg and 4 kg drying tests.

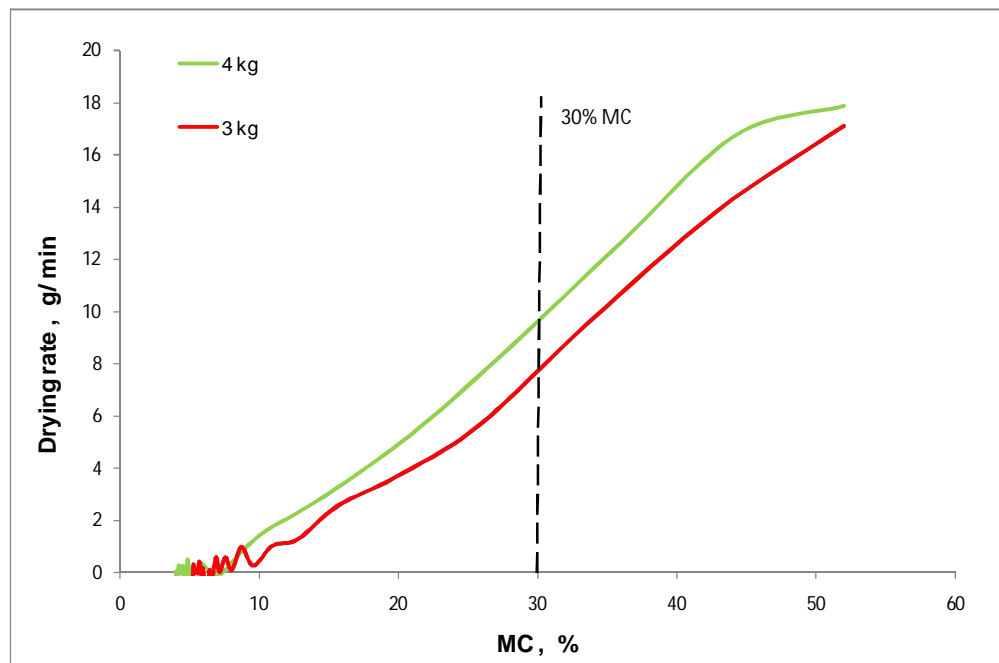


Figure 3.10.b: Drying rate vs MC curves obtained from the 3kg and 4 kg drying tests.

3.3.3 Thick layer dryer results

As it was observed in the previous section, the thin layer dryer results show that drying efficiencies were low which means that the drying potential of the pre-heated air was not efficiently used. A new dryer prototype based on a thick layer dryer was designed as an alternative to the thin layer dryer. Thus, the second dryer design was built and tested after the analysis of the results obtained from the thin layer dryer. The thick layer dryer configuration introduced major changes that brought new performance results:

- Tray area was reduced to a small square of 170 mm side.
- Three thicknesses of the woodchip layer were: 10 cm, 20 cm and 30 cm.

The new dryer configuration entailed an important pressure drop increment in the system. Therefore the maximum capacity of the fan was limited to 120 m³/h when operating with the SATS. This fact implied the necessity of increasing the range of temperatures of the dryer operation. Drying temperatures were expected to reach up to 70°C when working along with the solar air thermal system.

Three set of tests were taken for three layer thicknesses: 10 cm, 20 cm and 30 cm \pm 0.5 cm that corresponded to the loads of 1 kg, 2 kg and 3 kg of woodchip respectively. The woodchip employed was originally from the second sample of woodchip that it was left seasoning for half year. Before conducting the set of tests, woodchip was soaked into a bucket of water and later partially dried to 60 % MC. The quality of the woodchip to dry differs from the quality of the fresh woodchip sample as the inner structure of the chip may have change. However in the beginning of the process, drying rates are defined by the evaporation of the free water from the woodchip surface and the effect of the possible structural changes may be only appreciated in the last drying stage, in which water migration phenomena in the chips predominates.

The performance of the thick layer dryer was not analysed in as much detail as the thin layer dryer. The set of tests conducted for each woodchip layer configuration was comprised of 5 tests, the minimum of tests required to develop a model as a function of the drying conditions, as discussed in the next section 3.4.4.3. Table 3.9 shows the details of the drying tests for the thick layer dryer prototype.

Unlike the thin layer dryers, deep bed dryers are characterized by the creation of a drying front where the drying process takes place in a strip of the woodchip layer. The

drying front moves from the bottom to the top creating a gradient of moisture content in the woodchip sample. The size and velocity of the drying front depended on:

- Drying conditions: air velocity, temperature and RH.
- Quality of the woodchip: moisture content and woodchip shape.

In each test, the drying front was identified by monitoring the temperatures at several heights of the layer represented in Figure 3.1.b. Figure 3.11 shows the track of the variables that describe the test conducted for drying 20 cm layer of woodchip dried at 44°C with an air velocity of 0.64 m/s.

During the process, only the dried woodchips below the dryer front was at the selected drying temperature. Above the drying front, the drying air became saturated and the temperature decreased to the correspondent dew point temperature. Thus, in the drying front, the temperatures of the woodchips were between the drying and saturated temperatures. While the drying front did not reach the top of the layer, the outlet air left the dryer close to the saturation point or fully saturated at 100% RH.

Table 3.9: Characteristics of the drying tests conducted with the thick layer dryer.

10 cm thick woodchip layer									
Test	Flow ($\frac{m^3}{s}$)	V _{dry} (m/s)	T _{amb} (°C)	RH _{amb} (%)	T _{dry} (°C)	RH _{dry} (%)	W ₀ (gr)	W _{dry} (gr)	MC ₀ (%)
1	50	0.36	18.1	60.1	18.2	60.1	1,050	410	60.95
2	50	0.36	22.2	59.2	34.1	27.2	1,046	401	61.66
3	90	0.64	17.8	66.2	31.8	26.4	1,020	391	61.67
4	90	0.64	20.5	75.8	43.1	20.7	1,025	397	61.27
5	120	0.86	22.0	63.3	59.1	9.2	1,009	395	60.85
20 cm thick woodchip layer									
Test	Flow ($\frac{m^3}{s}$)	V _{dry} (m/s)	T _{amb} (°C)	RH _{amb} (%)	T _{dry} (°C)	RH _{dry} (%)	W ₀ (gr)	W _{dry} (gr)	MC ₀ (%)
1	50	0.36	23.9	54.5	24.0	54.5	2,012	779	61.28
2	90	0.64	25.2	60.3	31.9	45.7	2,005	783	60.95
3	90	0.64	21.2	74.9	44.1	30.1	2,040	787	61.42
4	120	0.84	24.8	74.7	38.2	30.0	2,011	785	60.96
5	120	0.84	25.2	71.1	60.9	9.4	2,031	804	60.41
30 cm thick woodchip layer									
Test	Flow ($\frac{m^3}{s}$)	V _{dry} (m/s)	T _{amb} (°C)	RH _{amb} (%)	T _{dry} (°C)	RH _{dry} (%)	W ₀ (gr)	W _{dry} (gr)	MC ₀ (%)
1	50	0.36	17.8	74.4	17.8	74.4	3,015	1,481	50.88
2	90	0.64	19.2	70.2	32.7	30.4	3,054	1,491	51.18
3	90	0.64	21.6	61.6	41.7	16.8	3,016	1,472	51.19
4	120	0.84	20.8	52.2	43.0	13.2	3,022	1,465	51.52
5	120	0.84	22.2	60.4	62.1	8.1	3,002	1,473	50.93

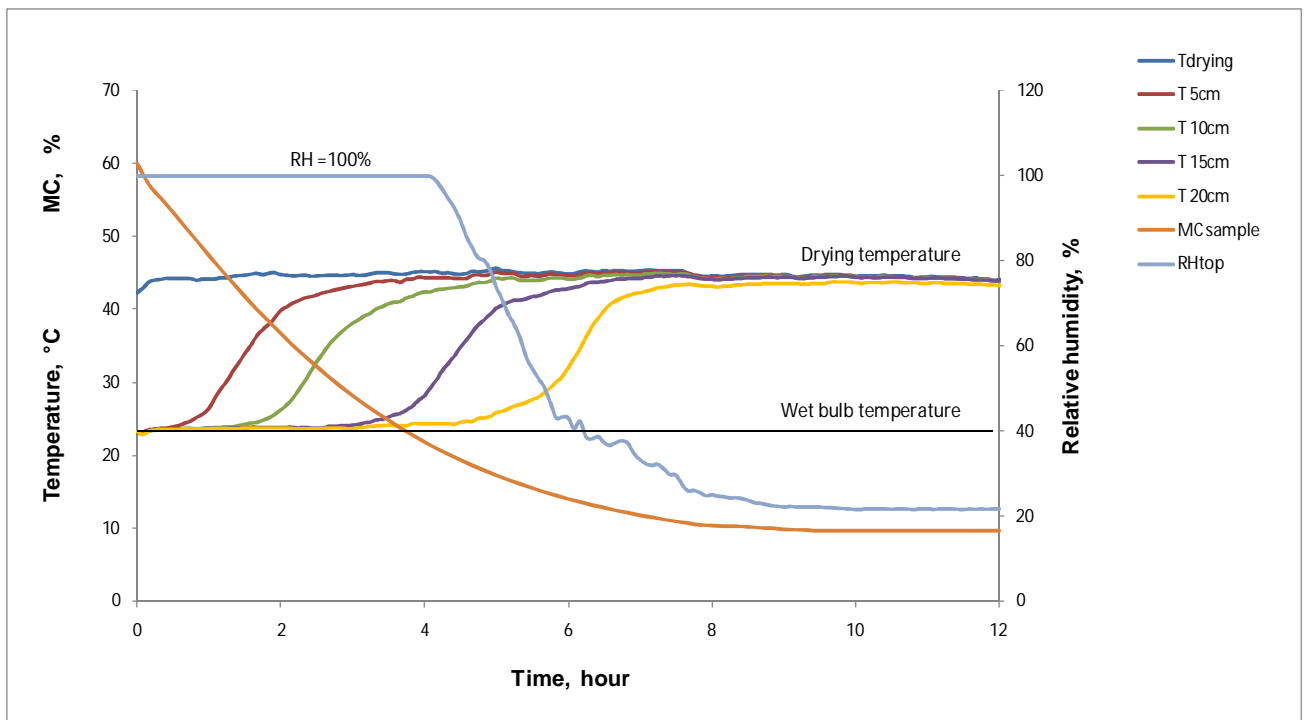


Figure 3.11: Data measurements obtained from a test with a 20cm woodchip layer.

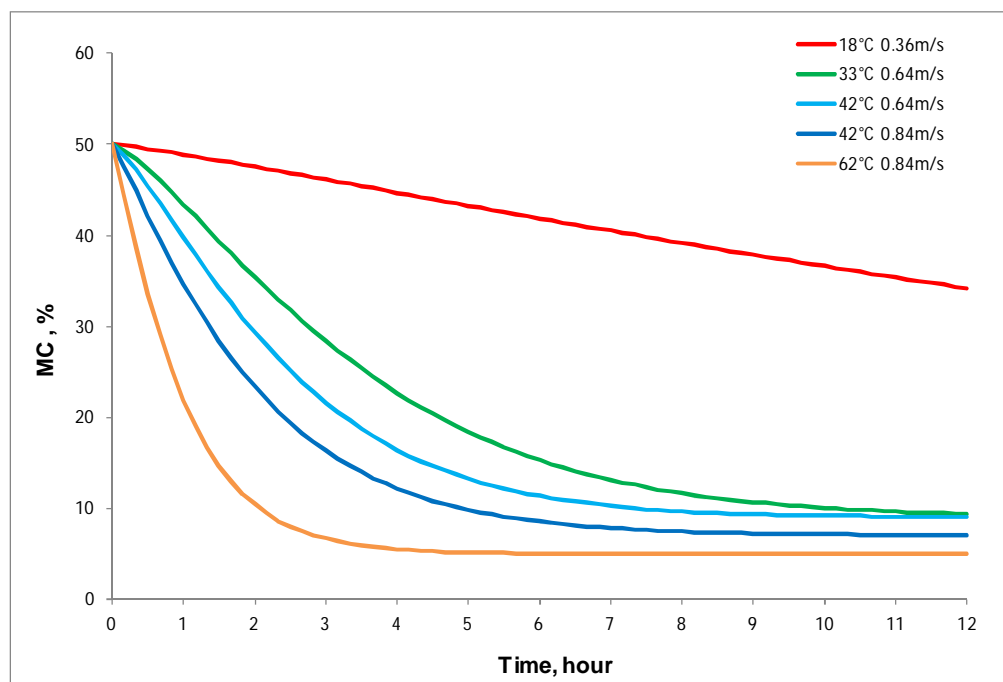


Figure 3.12: MC curves obtained from 5 drying tests with a 30cm deep bed dryer.

Figure 3.12 shows the MC curves corresponding to 5 tests taken for 30 cm layer drying tests covering a range of temperatures and air flow rates. As in the thin layer dryer tests, the shape of the drying curves obtained for the thick layer tests had also an exponential profile. Thus the procedure for modelling the dryer performance as a function of the key factors was the same for both dryer prototypes.

For any air flow rate, drying velocities in the thick layer dryer were 8 times higher than in the thin layer dryer as the new tray area was reduced to 1:8. High drying velocities increased the difference between the local vapour pressures in the air and the woodchip surface. However, increasing the drying velocities reduced the time the air is in contact with the woodchip. Thus each dryer configuration has an optimal drying velocity that maximizes the dryer efficiency.

In a thick layer dryer configuration, the air flow crossing the tray was in contact with a larger volume of woodchips. Thus the inlet air had a long path length to evaporate the moisture and therefore air flow easily left the dryer fully saturated at 100% RH or close to the saturation point at high relative humidity, especially in the beginning of the drying test.

Table 3.10: Results obtained from the drying tests conducted with the thick layer dryer

10 cm thick woodchip layer								
test	Flow(m ³ /h)	V _{dry} (m/s)	T _{dry} (°C)	RH _{dry} (%)	w.b.c (gr / kg air)	Drying time	Dry rate (gr/min)	Efficiency (%)
1	50	0.36	18.2	60.1	0.9	14h	0.7	82.2
2	50	0.36	34.1	27.2	3.4	3h	3.4	78.1
3	90	0.64	31.8	26.4	3.52	1h 40min	5.8	71.3
4	90	0.64	43.1	20.7	5.2	1h 15min	8.6	71.5
5	120	0.84	59.1	9.2	6.5	40min	13.2	68.9
20 cm thick woodchip layer								
test	Flow(m ³ /h)	V _{dry} (m/s)	T _{dry} (°C)	RH _{dry} (%)	w.b.c (gr / kg air)	Drying time	Dry rate(gr/min)	Efficiency (%)
1	50	0.36	24.0	54.5	1.6	16h	1.7	89
2	90	0.64	31.9	45.7	2.5	3h 10min	4.3	83.2
3	90	0.64	44.1	30.1	5.5	2h 10min	9.1	81.6
4	120	0.84	38.2	30.0	4.9	1h45min	10.2	76.6
5	120	0.84	60.9	9.4	10.5	45min	21	75.5
30 cm thick woodchip layer								
test	Flow(m ³ /h)	V _{dry} (m/s)	T _{dry} (°C)	RH _{dry} (%)	w.b.c (gr / kg air)	Drying time	Dry rate(gr/min)	Efficiency (%)
1	50	17.8	74.4	74	0.8	20h	0.6	93.3
2	90	32.7	30.4	30	3.21	2h 40min	5.8	88.7
3	90	41.7	16.8	17	5.8	1h 50min	9.4	84.1
4	120	43.0	13.2	13	5.6	1h 20min	11.8	77.5
5	120	62.1	8.1	8	9.6	40min	19.8	81

Table 3.10 shows the drying times and average values for efficiencies and drying rates observed in the beginning of the drying process until the woodchip sample reached the 30% MC. This table also includes the value of the water binding capacity of the air that corresponds to the drying conditions of each test.

Efficiencies registered in the deep bed dryer tests were observed to be much higher than in the thin layer dryer. Employing the same flow conditions, dryer 2 removed more water from the woodchip than dryer 1. It was observed that efficiencies were better with the depth of the woodchips bed.

Figure 3.13.a shows the drying rates from the 30 cm thick layer tests. In the beginning of each test, the drying air always left the dryer saturated and hence the drying rates were high and practically constant for an extended period of time. Once the drying front reached the top, the drying rate decreased gradually until the woodchip in the box reached the EMC for the test drying conditions. Figure 3.13.b represents the relationship between MC and drying rate values. It was observed that during the period of constant drying rate, MC in the woodchip was considerably reduced. When analysing the quality of the drying process, it is necessary to consider that the quality of the woodchip may not be uniform and the MC presented is an average value of the total woodchip sample: After a drying period, the product at the bottom may be over dried while top areas may remain with the MC_0 .

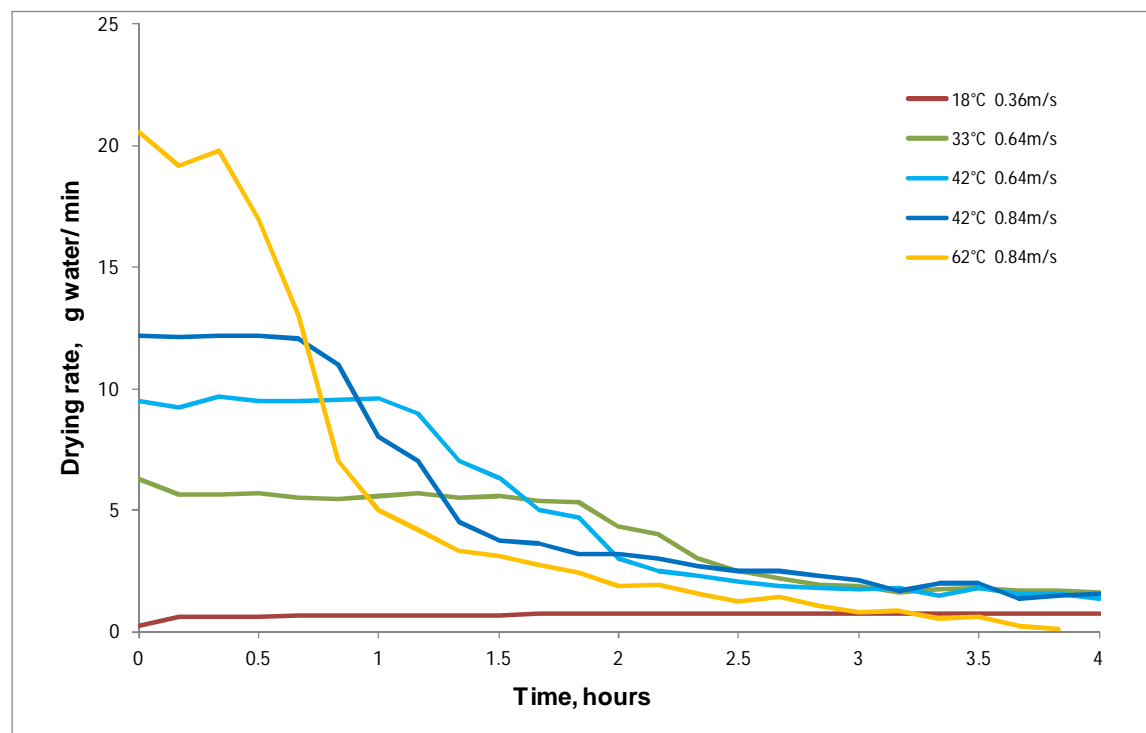


Figure 3.13.a: Drying rate vs time curves obtained from 5 drying tests with a 30cm deep bed dryer.

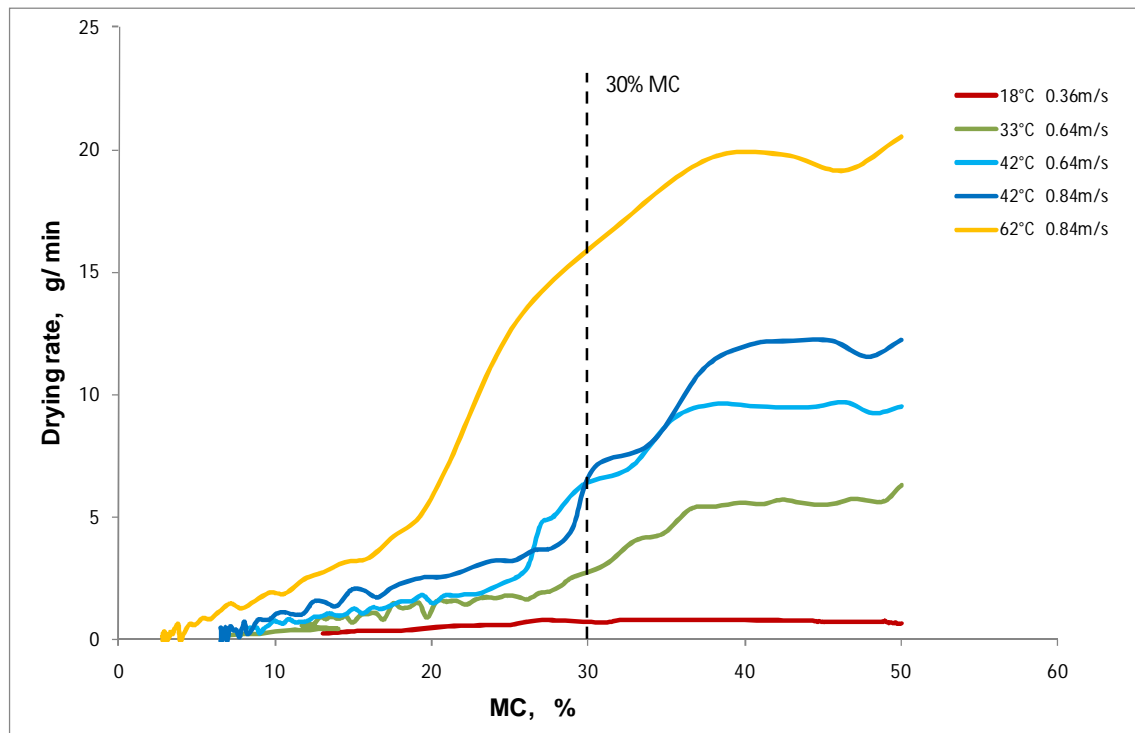


Figure 3.13.b: Drying rate vs MC curves obtained from 5 drying tests with a 30cm deep bed dryer.

3.3.4 Mass and energy balance

A VBA module was developed in order to process all the data obtained from each drying test in the same spreadsheet. The application helped to monitor the values of the drying variables and obtain the mass and the energy balance that validates the profile of the drying curves obtained.

The VBA code was based on the psychrometric equations that relate the humid air properties. These equations are developed in **Appendix A3: Mass and energy balance** in more detail. Based on the relative humidity and temperature measurements, the rest of the properties, used for the calculations, were obtained:

- Relative humidity
- Dry temperature
- Wet bulb temperature
- Moisture content in the air
- Enthalpy

The psychrometric properties were calculated for the ambient air, drying air and outlet air based on the temperature and relative humidity measurements. Thus the heating and the drying process of each drying test can be represented in the

psychrometric chart. Figure 3.14 shows schematically the process of 2 drying tests at constant air humidity but different drying temperatures.

Ekechukwu (1999) and Brenndorfer (1985) used the psychrometric chart to indicate quantitatively the water removing potential of the pre-heated drying air. This can be estimated as the difference between the moisture in the air at wet bulb temperatures: Figure 3.14 shows the notable difference between the drying potential of drying at ambient temperature, $w_2 - w_1$, and drying at a higher temperature, $w_4 - w_3$. In an adiabatic and irreversible process, the maximum amount of water that drying air flow can dry from the woodchips is proportional to this magnitude.

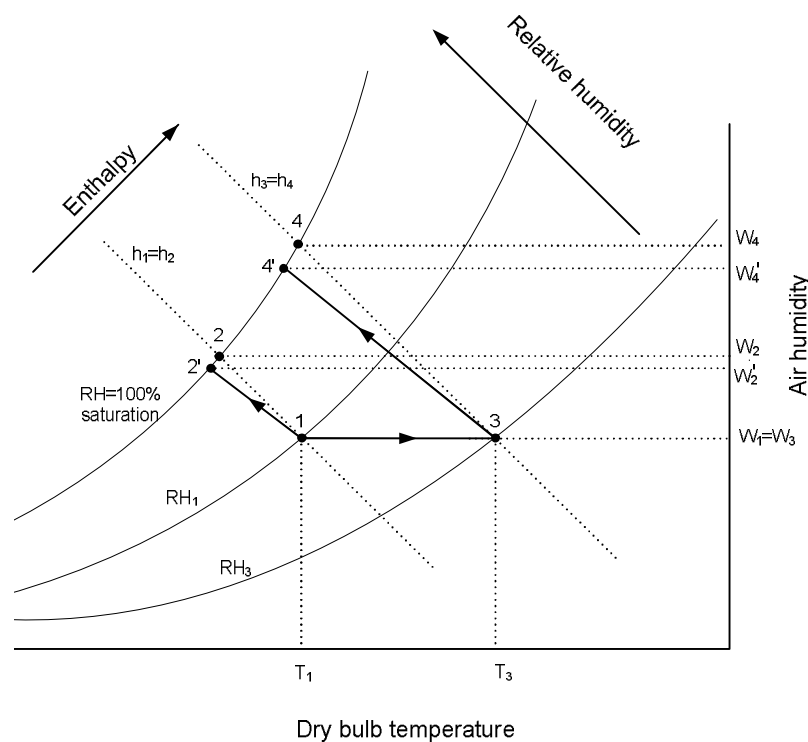


Figure 3.14: Psychrometric diagram of 2 drying tests.

However, any dryer performance is non-adiabatic and the irreversibility implies that outlet air will not reach the maximum difference of humidity as figure 3.14 shows, and instead will be slightly lower, points 2' and 4'. When the drying efficiency is 100% means that the drying air employs its capacity for picking up moisture from the woodchip and leaves the dryer fully saturated at 100% RH.

The mass balance was obtained by comparing the amount of water evaporated in a period of time calculated in two different ways: the first value was calculated as the difference of two weight measurements, and the second value was calculated using

psychrometric properties as the amount of water evaporated by the air flow during the given interval of time.

The mass of water removed by the air flow, $W_{\text{evaporated}}$, was calculated at 1 minute interval employing the psychrometric relations using the temperature and RH measurements of the dryer inlet and outlet. The water, ‘picked up’ by the air in a given period of time was the sum of the interval contributions calculated as the product of the air flow by the increment of moisture in the air during the interval of time, equation 3.5:

$$W_{\text{evaporated}} = \sum \dot{m} \cdot (w_{\text{outlet}} - w_{\text{inlet}}) \cdot \Delta t \quad \text{Equation 3.5}$$

Where: \dot{m} is the mass of air flow

w_{outlet} is the water content in the outlet air

w_{inlet} is the water content in the inlet air

Figure 3.15.a and figure 3.15.b show the mass balance of the tests described in the previous section. Each point of the curves represents the water evaporated during a period of time of 10 minutes. The majority of the tests provided an acceptable agreement between measured and predicted points in the mass balance curves.

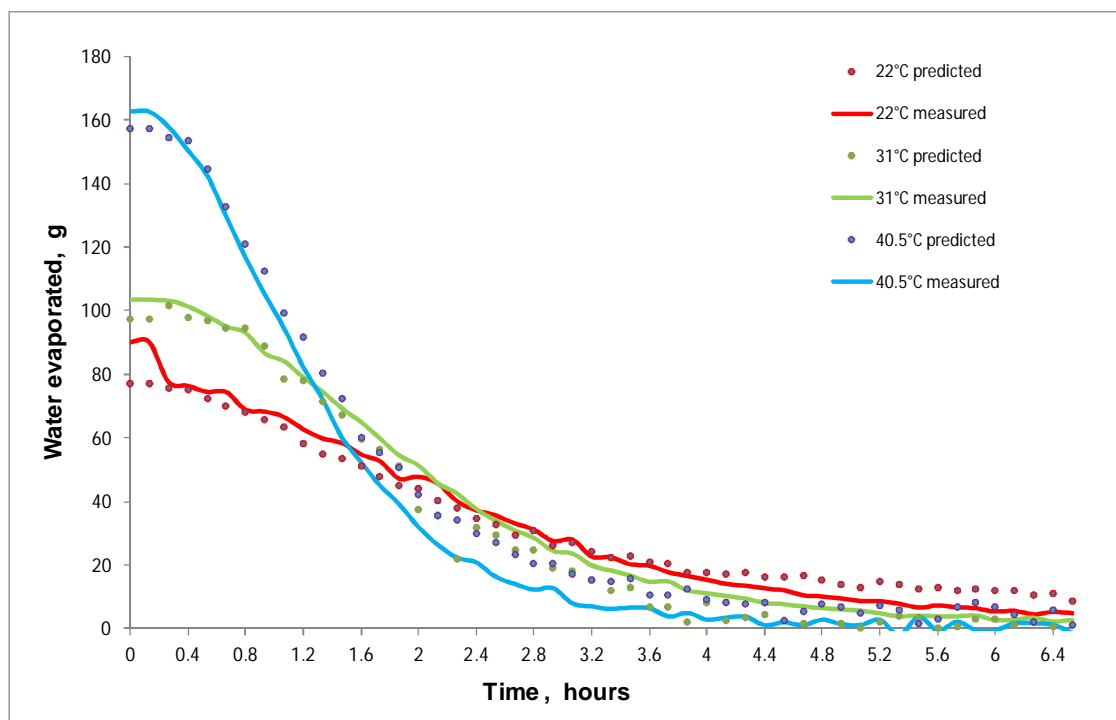


Figure 3.15.a: Mass balance obtained from 3 drying tests with a drying velocity of 0.1875 m/s.

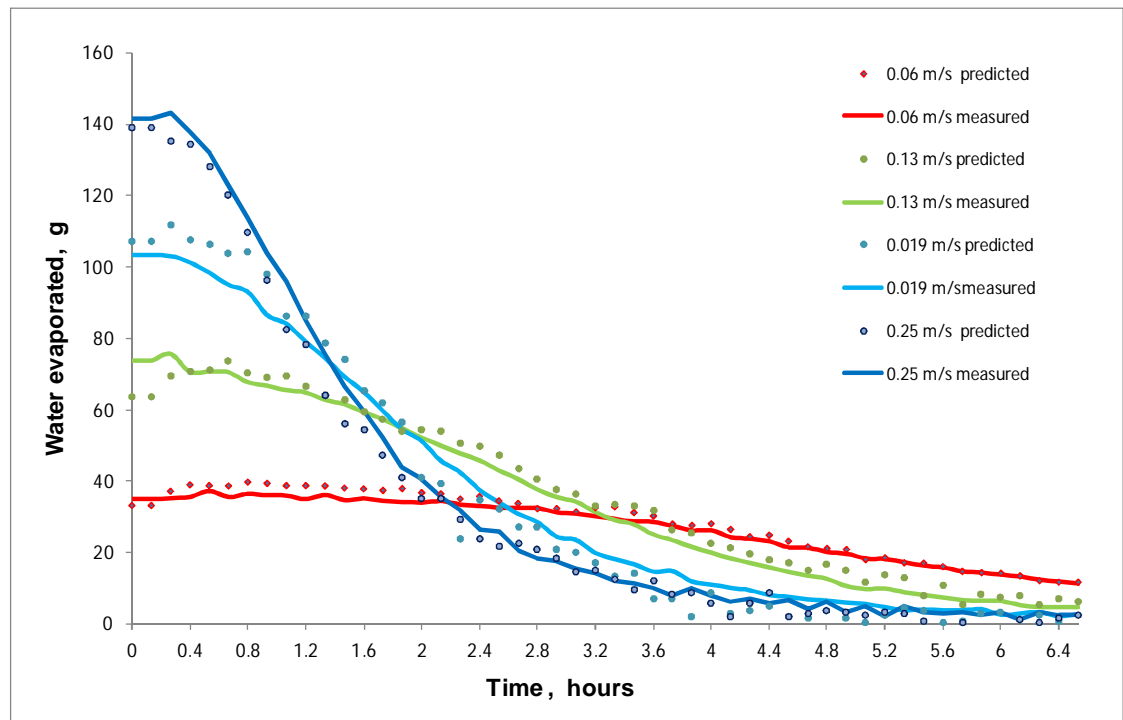


Figure 3.15.b: Mass balance obtained from 4 drying tests with a drying temperature of 30°C.

The predicted amount of water evaporated is based on the air psychrometric properties measurements. The errors associated with these readings are as given in table 3.1. As result, the predicted water evaporated can be associated with an error inherited from these measurements.

Running the model with the lower and the higher limits of the measurement, the water evaporated can be estimated accounting the error due to the uncertainty due to the instruments tolerance. Considering all sources of error in measurements such as temperature, relative humidity and flow rate, the error found in the mass balance was quantified between 6% and 12%. These high values are basically attributed to the significant error originated in the estimation of the water content in the air.

The relative error obtained in the different tests was always lower than 9.4% in the first stages of the drying process when MC was higher than 30%. This difference was associated to the propagation error caused due to the tolerance in the measurements of temperature and relative humidity.

The energy balance was estimated following a similar procedure used for the calculation of the mass balance. Two aspects were considered: Firstly, the heat input supplied by the power source, was compared to the increment of sensible heat gained by the air flow to reach the drying temperature, equation 3.6.

$$P_{input} \cdot \Delta t = \dot{m} \cdot \Delta t \cdot (h_{drying} - h_{ambient}) / 1000 \quad \text{Equation 3.6}$$

Where: P_{input} is the power input of the heater

$h_{ambient}$ is the ambient air enthalpy and

h_{drying} is the drying air enthalpy

The difference in power values described the heat losses registered in the duct and in the drying chamber. Heat losses in the dryer facility depended on the air flow and the difference between the ambient and drying temperatures. The optimisation of the dryer was out of the scope of the project and heat insulation was not used in the dryer prototype. In each drying test, in order to minimise the effect of the heat losses in the beginning of the process, the drying facility was pre heated with an air flow rate at the testing drying temperature. For example, figure 3.16 illustrates an energy balance example of the thin layer dryer working at 30°C with a flow rate of 165 m³/h. The power required to warm up the ambient air to the desired temperature was 367 W.

Secondly, the “adiabatic character” of the drying process was analysed. Theoretically drying is an adiabatic process in which there is no net heat contribution, thus it is expected no variation in the enthalpy of the drying fluid. Therefore, the difference of drying enthalpy between the inlet and outlet drying air is equal to 0, equation 3.7.

$$\dot{m} \cdot (h_{output} - h_{drying}) \cdot \Delta t = 0 \quad \text{Equation 3.7}$$

Where: h_{output} is the enthalpy of the air leaving the dryer

However in practice, drying is a non-adiabatic process and experimentally there was always registered a small difference between the inlet and outlet air enthalpy as figure 3.16 shows. Moreover, the outlet air is initially saturated of vapour at the corresponding dew point temperature. The sensible heat of the inlet air decreases as it is used to evaporate the moisture in the woodchip surface, cooling the woodchips down. Thus, with the drying process the woodchips increase their temperature until reaching the equilibrium, and then outlet air is at drying temperature. This implies the enthalpy difference shown in figure 3.16.

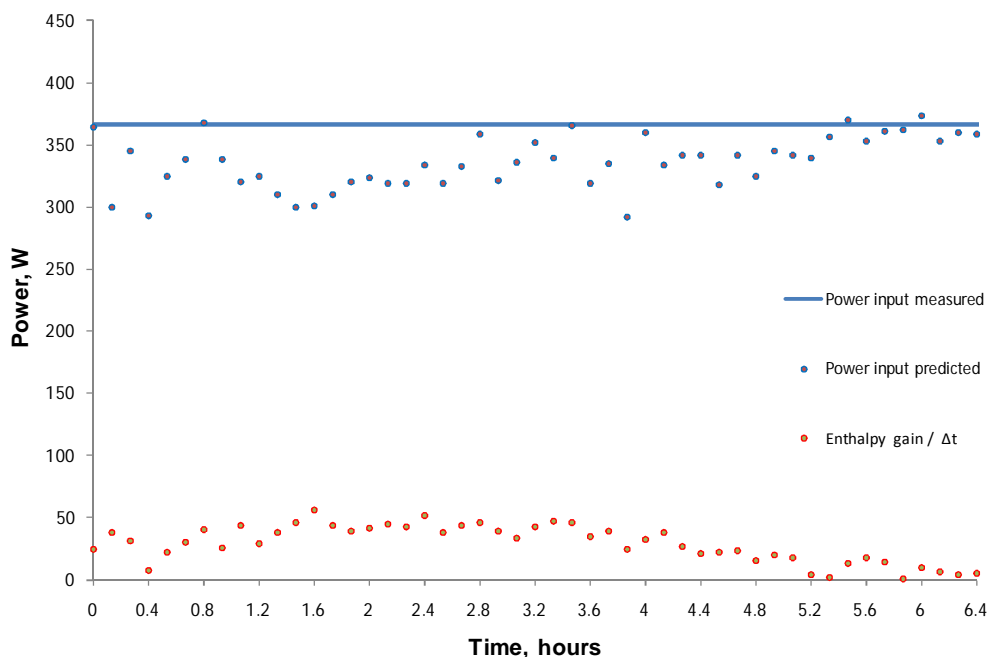


Figure 3.16: Energy balance for a drying test with a drying velocity of 0.1875 m/s and a temperature of 30°C.

3.4 Modelling

3.4.1 Introduction

The ultimate objective of the drying tests was to develop a model that describes the performance of the dryer for a range of drying conditions. The drying model simulated the woodchip dryer operation based on the results obtained from the drying tests. Thus using a statistical tool and following a methodology employed by other researchers, the tests conducted were analysed and useful correlations that described their results in a unique mathematical expression were obtained. Finally the predicted and measured values of the drying performance were compared in order to validate the model.

3.4.2 Modelling a drying test

The performance of the dryer was described using drying curves obtained from each test that represented the decrement of weight values with time, normally MC curves. In order to model the drying performance, an exponential mathematical approximation based on the theoretical analysis of the thin layer drying mechanism was developed, equation 3.8, already presented in section 2.1.4. A new dimensionless

variable named moisture ratio, MR, was defined as difference between the MC to reach the EMC divided by the total difference between MC_0 and the EMC. MR values were between 0 and 1.

$$MR = \frac{(MC - MC_{eq})}{(MC_0 - MC_{eq})} = e^{-kt} \quad \text{Equation 3.8}$$

The above equation, called the Newton model, was obtained from the solution of a differential equation and it has an exponential profile, Lewis (1921). The equation is defined by a unique parameter, k , which represents the 'kinematics' of the process. The value of this parameter depends on the dryer, product characteristics and drying conditions.

During the testing period of a drying set of test, the dryer setup was not modified and the woodchip characteristics remained constant. Thus for each test, the parameter of the model equation k was associated to the drying conditions: temperature and drying velocity.

MR curves obtained from experimental data were modelled using the best fit curve based on the exponential curve profile. The k values and the regression coefficients, R^2 , were obtained for each drying test in the set.

The software application employed for the statistical analysis of the drying model was the SPSS 16.0 statistical package tool, a versatile tool commonly used by researchers that facilitates the analysis of the model results.

Table 3.11 illustrates the results obtained from the regression analysis applied to the MR curves correspondent to the first sample of woodchip dried in the thin layer dryer.

Table 3.11: k values associated to each drying tests conducted with the first woodchip sample.

Test	T _{drying}	V _{drying}	k	R ²	Test	T _{drying}	V _{drying}	K	R ²
1	22°C	0.06 m/s	0.136 s ⁻¹	0.962	7	31°C	0.19 m/s	0.391 s ⁻¹	0.992
2	22°C	0.13 m/s	0.195 s ⁻¹	0.989	8	31°C	0.25 m/s	0.573 s ⁻¹	0.991
3	22°C	0.19 m/s	0.291 s ⁻¹	0.995	9	40.5°C	0.06 m/s	0.261 s ⁻¹	0.974
4	22°C	0.25 m/s	0.372 s ⁻¹	0.994	10	40.5°C	0.13 m/s	0.417 s ⁻¹	0.994
5	31°C	0.06 m/s	0.188 s ⁻¹	0.967	11	40.5°C	0.19 m/s	0.644 s ⁻¹	0.993
6	31°C	0.13 m/s	0.308 s ⁻¹	0.987	12	40.5°C	0.25 m/s	0.813 s ⁻¹	0.991

The Newton model is characterised by its simplicity, using only one parameter to characterise the exponential behaviour of the MR curve. However, the regression factor values shown in table 3.11 are relatively low and the modelled results are relatively low in comparison with other mathematical models. Thus, based on the same drying principles of the Newton model, other semi-theoretical mathematical models were developed and commonly used for describing the drying curves for other drying applications: Henderson-Pabis, Page, Logarithmic, Midilli and 2-terms exponential are models commonly compared in other research work, already presented in the literature review chapter in section 2.1.6.

As these mathematical models had more parameters in their equations and therefore contain more information for describing the MR curves, they can more closely describe the drying process. Thus, the MR curves were modelled employing the new mathematical expressions obtaining in general high regression coefficients and a good degree of fit between experimental and predicted curves. Table 3.12 shows the comparison of the statistical indicators, R^2 and the X^2 , obtained from different tests when using various mathematical model expressions to describe the MR curves.

Statistical indicators are associated to the goodness of the model that described the drying curves that corresponds to each of the tests: Thus the closer R^2 is to unity and the lower X^2 is, the better the model is. The Midilli model provided the best fit curves that described the experimental curves. However, Midilli's mathematical model equation employs 4 parameters, and the simplicity of the model equation is a key factor when building a drying macro model that integrates all the data collected: The more parameters in the mathematical model expression, the more drying data information is required to determine these parameters and hence more complex and difficult is to develop of a global drying model.

On the other hand, observing the statistical values of table 3.12, other mathematical expressions such as Page and 2-terms exponential models yielded almost as good statistical results as Midilli's model with high R^2 for all the drying tests. The selection of the most appropriate mathematical model to carry on with the study of the woodchip dryer performance was based on the simplicity of its expressions and the fitness of the experimental and predicted MR data. Considering the statistical results of Table 3.12 and observing the list of model equations in Table 2.1, the Page model was selected as the most adequate model to represent the drying process for woodchip. This mathematical model had a simple mathematical expression, based on the theoretical

Newton model equation, and only uses two parameters, k and n , to characterize the MR curves.

Table 3.12: Statistical results from the drying test models.

Nº test	T _{drying}	V _{drying}	Statistical indicator	Newton	Page	Henderson & Pabis	Midilli	2 terms exponential.	Logarithmic.
1	22	0.06	R ²	0.961	0.999	0.976	0.999	0.997	0.992
			X ²	0.003	7.87E-05	0.0022	4.05E-05	0.0002	0.0007
2	22	0.13	R ²	0.989	0.999	0.994	0.999	0.999	0.995
			X ²	0.0009	7.82E-05	0.0004	1.58E-05	0.00005	0.0003
3	22	0.19	R ²	0.995	0.996	0.996	0.999	0.995	0.997
			X ²	0.0003	0.000265	0.0002	6.46E-05	0.0003	0.0001
4	22	0.25	R ²	0.994	0.997	0.996	0.998	0.997	0.996
			X ²	0.0003	0.0001	0.0002	0.0001	0.0001	0.0002
5	31	0.06	R ²	0.967	0.996	0.980	0.999	0.997	0.983
			X ²	0.0030	0.0003	0.0018	3.49E-05	0.0002	0.0016
6	31	0.13	R ²	0.986	0.995	0.991	0.999	0.994	0.991
			X ²	0.0009	0.0003	0.0006	6.62E-05	0.0003	0.0006
7	31	0.19	R ²	0.991	0.992	0.992	0.998	0.991	0.996
			X ²	0.0004	0.0004	0.0004	0.0001	0.0005	0.0002
8	31	0.25	R ²	0.990	0.993	0.991	0.997	0.993	0.993
			X ²	0.0005	0.0003	0.0004	0.0001	0.0003	0.0003
9	40.5	0.06	R ²	0.974	0.998	0.983	0.999	0.998	0.985
			X ²	0.0022	0.0001	0.0014	3.36E-05	0.0001	0.0013
10	40.5	0.13	R ²	0.994	0.998	0.995	0.999	0.999	0.995
			X ²	0.0003	7.01E-05	0.0002	6.12E-06	0.00008	0.0002
11	40.5	0.19	R ²	0.992	0.995	0.993	0.997	0.995	0.995
			X ²	0.0003	0.0002	0.0003	0.0001	0.0002	0.0002
12	40.5	0.25	R ²	0.991	0.993	0.992	0.994	0.995	0.992
			X ²	0.0003	0.0002	0.0003	0.0001	0.0002	0.0002

As an illustration, Figure 3.17 shows the comparison between experimental and predicted curves obtained with Page model for a set of 4 tests at constant temperature, 31°C. The graphic shows the grade of fitness of the MR curves with a relatively high correlation coefficient. The modelled curves always showed an acceptable fitness, especially at the beginning of the process. Along the time, the difference between

predicted and experimental was more noticeable as woodchip approached the EMC. Having high correlation coefficients in the description of the drying curves for each test was essential in order to obtain a mathematical expression that describes all the tests together.

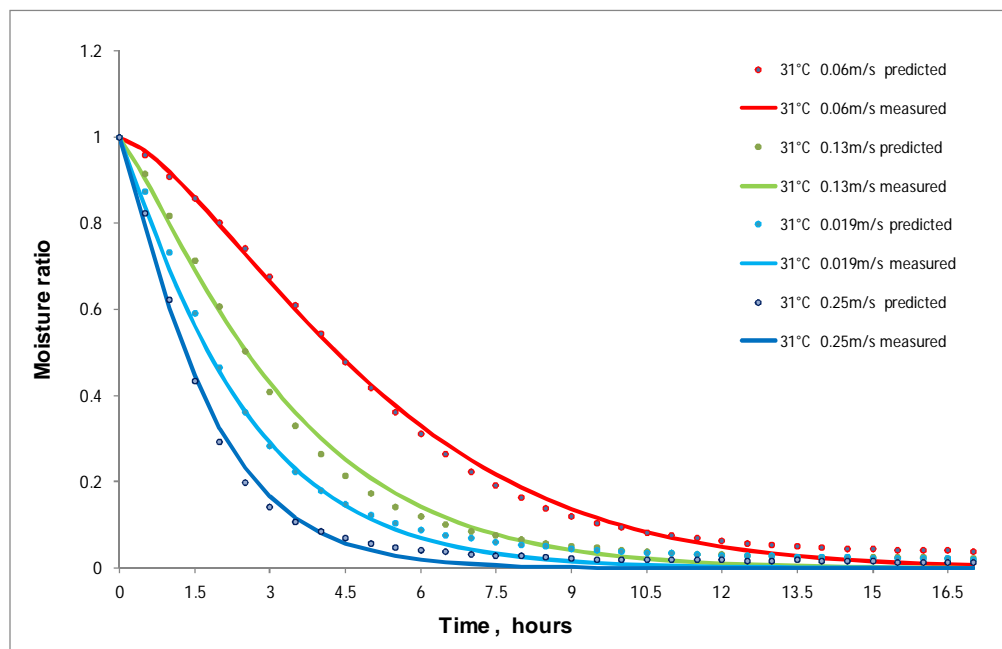


Figure 3.17: Measured and Page modelled MR curves obtained from 4 drying tests at 31°C.

3.4.3 Page model

The MR curves obtained from each drying test of the set were described using 2 parameters from the Page model equation: k and n . Table 3.13 shows the values obtained from the first woodchip sample tests. As each of the tests was conducted at a particular drying velocity and temperature, Page parameters were associated to the same drying conditions.

Table 3.13: Page model values for the constants.

Test	T_{drying}	V_{drying}	k	n	Test	T_{drying}	V_{drying}	k	n
1	21°C	0.0625 m/s	0.054 s^{-1}	1.44	7	31°C	0.1875 m/s	0.361 s^{-1}	1.076
2	21°C	0.125 m/s	0.134 s^{-1}	1.21	8	31°C	0.25 m/s	0.512 s^{-1}	1.16
3	21°C	0.1875 m/s	0.263 s^{-1}	1.07	9	40.5°C	0.0625 m/s	0.137 s^{-1}	1.43
4	21°C	0.25 m/s	0.317 s^{-1}	1.13	10	40.5°C	0.125 m/s	0.345 s^{-1}	1.18
5	31°C	0.0625 m/s	0.087 s^{-1}	1.43	11	40.5°C	0.1875 m/s	0.593 s^{-1}	1.14
6	31°C	0.125 m/s	0.224 s^{-1}	1.24	12	40.5°C	0.25 m/s	0.758 s^{-1}	1.16

The constant k represented the speed of the drying process and defined the slope of the curve at the beginning. The constant n was associated to the description of the exponential curve curvature and the shape of the MR curve when approaching to the equilibrium. Figure 3.18.a and figure 3.18.b show k and n values respectively, plotted as a function of temperature and drying velocities.

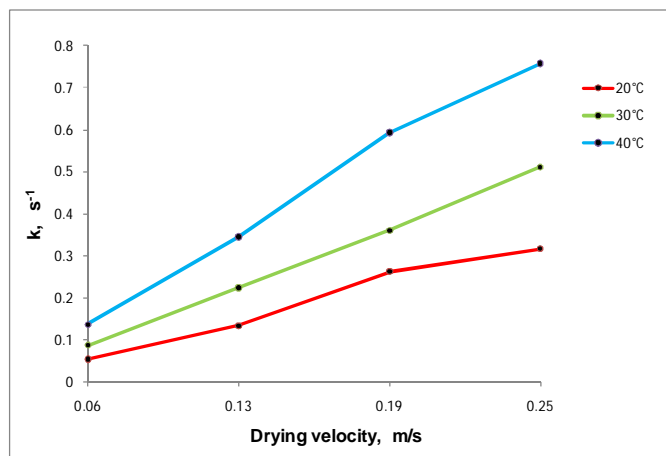


Figure 3.18.a: Representation of k values.

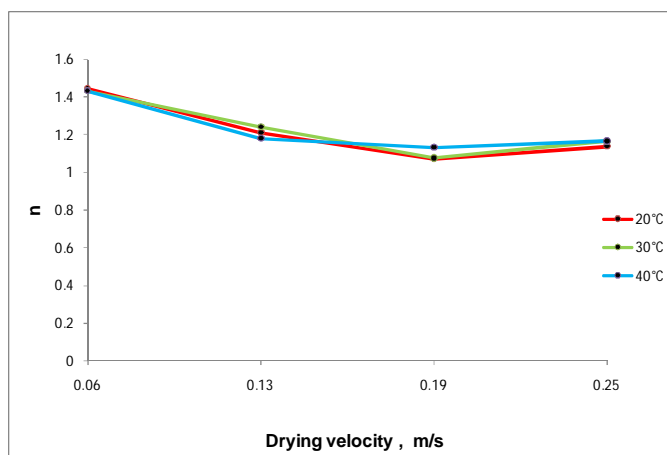


Figure 3.18.b: Representation of n values.

Figure 3.18.a shows a linear relationship between constant k and drying velocity or air flow rate: Supposing that moisture level in the air remain constant, 4 tests conducted at same drying temperature have the same psychrometric properties and hence same air capacity of removing water. Thus, an increment in air flow for this given air conditions imply a proportional increment in the drying rates and therefore k values has a strong correlation with drying velocities.

Regarding the parameter n , it was observed a strong relation between the n values and the drying velocities independently of the drying temperature. A similar conclusion

was concluded by Yaldiz *et al.* (2001) in their study based on the model developed by Page.

3.4.4 Drying macro model

3.4.4.1 Modelling a drying data set

In the previous section 3.4.3, the MR curves obtained from each drying test were modelled individually employing the Page model expression. In this section a macro drying model that integrates the information collected from the set of drying tests at once is developed. Having as a reference the Page model equation and the analysis of its parameters, a new expression was developed in order to calculate the MR curves as a function of the drying conditions. Thus the Page equation parameters, k and n , were calculated as a function of drying temperature and drying velocity.

The parameters k and n in the transformed Page mathematical equation were described as a linear combination of mathematical expressions such as linear, logarithmic, power and exponential equation type listed below: equation 3.9 to 3.12.

- Linear $Y=a+bX$ Equation 3.9
- Logarithmic $Y=a+\ln b$ Equation 3.10
- Power $Y=a \cdot X^b$ Equation 3.11
- Exponential $Y=a \cdot \exp(bX)$ Equation 3.12

When building a dryer model to describe the dryer performance, researchers find by “ trial and error ”, different equation combinations and finally select the expression that provides the best statistical results, Ertekin *et al.* (2004) and Midilli *et al.* (2003). In the previous section 3.4.3, the analysis of figure 3.18.a and figure 3.18.b gives an indication of how the relationship between the k and n parameters with temperature and velocity is. After trying various combinations of equations, the best MR model equation obtained followed the pattern shown in equation 3.13. Thus, the MR equation that describes a set of drying test was defined by time, temperature and velocity and 8 constants: a, b, c, d, e, f, g and h.

$$MR = \exp\left(-\left(a \cdot Velocity + b\right) \cdot \left(c \cdot Temp^2 + d \cdot Temp + e\right)\right) \cdot time^{\left(f \cdot Velocity^2 + g \cdot Velocity + h\right)} \quad \text{Equation 3.13}$$

The statistical package SPSS 16.0 program was the tool used to calculate the drying macro model constants of the MR equation. Because there were various independent variables: the drying time, velocity and temperature, the statistical problem had to be solved by means of regression analysis for non linear systems. The statistical analysis processed all the MR data from all the set of tests at once. The program found the best correlation and provided the values for the constants that yielded the best approximation between experimental and predicted MR data.

For each set of tests previously studied in both thin and thick layer dryer configurations, the values for all the constants were obtained using a statistical software.

For instance, equation 3.14 shows the MR equation of the drying macro model that describes the 12 drying tests conducted for the first sample of woodchip, 57% MC, in the thin layer dryer. The goodness of the model was quantified by the regression coefficient that was 0.996 in this particular case.

$$MR = \exp(-((0.15 \cdot V^2 - 0.036)(0.014 \cdot T^2 - 0.167 \cdot T + 5.92)) * t^{(18.06 \cdot V^2 - 7.07 \cdot V + 1.8)}) \quad \text{Equation 3.14}$$

The drying macro model was used to obtain the MR curves within the drying conditions range. Moreover MC curves were estimated as a function of the predicted MR and the equilibrium MC that depends on the temperature and air humidity. Therefore the results of the drying macro model compared the predicted and the experimental MC curves. Figure 3.19.a, figure 3.19.b and figure 3.19.c show the comparison of experimental and predicted MC curves for the first woodchip sample tests.

3.4.4.2 The error analysis of the drying macro model

The error of the model curves was studied based on the drying time differences. Experimental and predicted drying times were analysed especially in the first stages of the drying process, where the drying process of the woodchip is relevant for the study. In general, a good correlation between drying times was observed.

- For low drying velocity and low temperature tests, in which drying times were long, difference between the model and measured times was acceptable although high in comparison with other tests with more favourable drying conditions.
- The difference between the model and measured times was not accumulative and depended on the stage of the drying process: While the beginning and the final

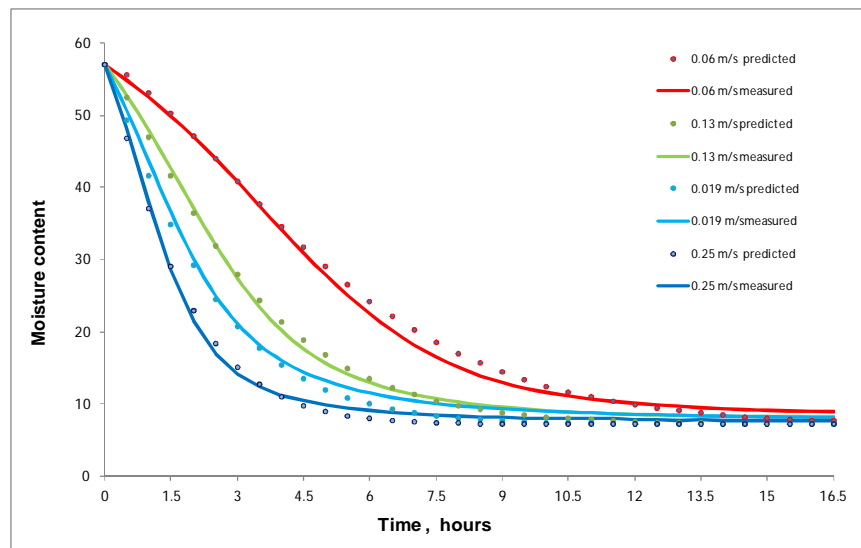


Figure 3.19.a: Predicted and experimental MC curves at 21°C for the first woodchip sample.

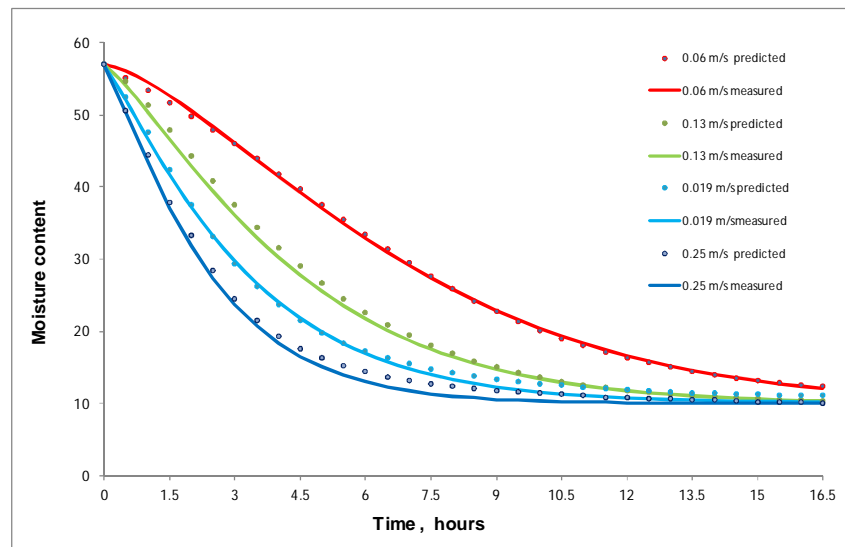


Figure 3.19.b: Predicted and experimental MC curves at 31°C for the first woodchip sample.

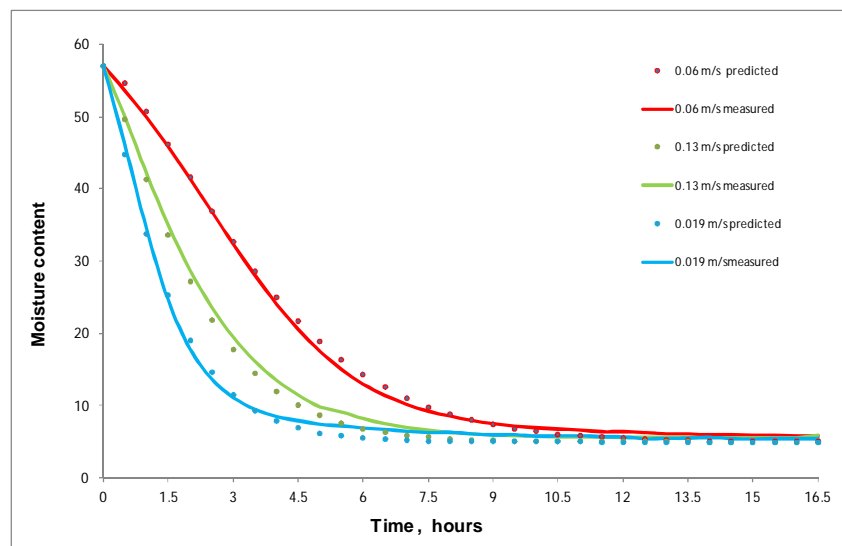


Figure 3.19.c: Predicted and experimental MC curves at 40.5°C for the first woodchip sample.

parts were usually well described, there was a zone between 25% and 15% MC where the difference between predicted and experimental values was notably higher.

It was also observed that the difference between the model and measured times depended on the drying conditions: for high temperature and high velocity conditions, a good agreement between predicted and experimental curves was always observed. Only in particular tests, this time difference in the zone between MC_0 and 30% MC was higher than 10 minutes. However for low flow and low temperature tests, where drying times were longer than 5 hours, this time difference in the beginning was higher and it could be up to 30 minutes.

Considering the uncertainty due to all sources of error in measurements such as temperature, relative humidity and drying air velocity, the woodchip dryer model predicts the MC with a maximum error on time basis of 10%, in the range of MC higher than 25%.

Figure 3.20 shows a comparison between predicted and experimental MC data for the 12 the tests the model was based on. Table 3.14 shows the statistical characteristics of the drying macro model for the woodchip sample 1 tests conducted in the thin layer dryer.

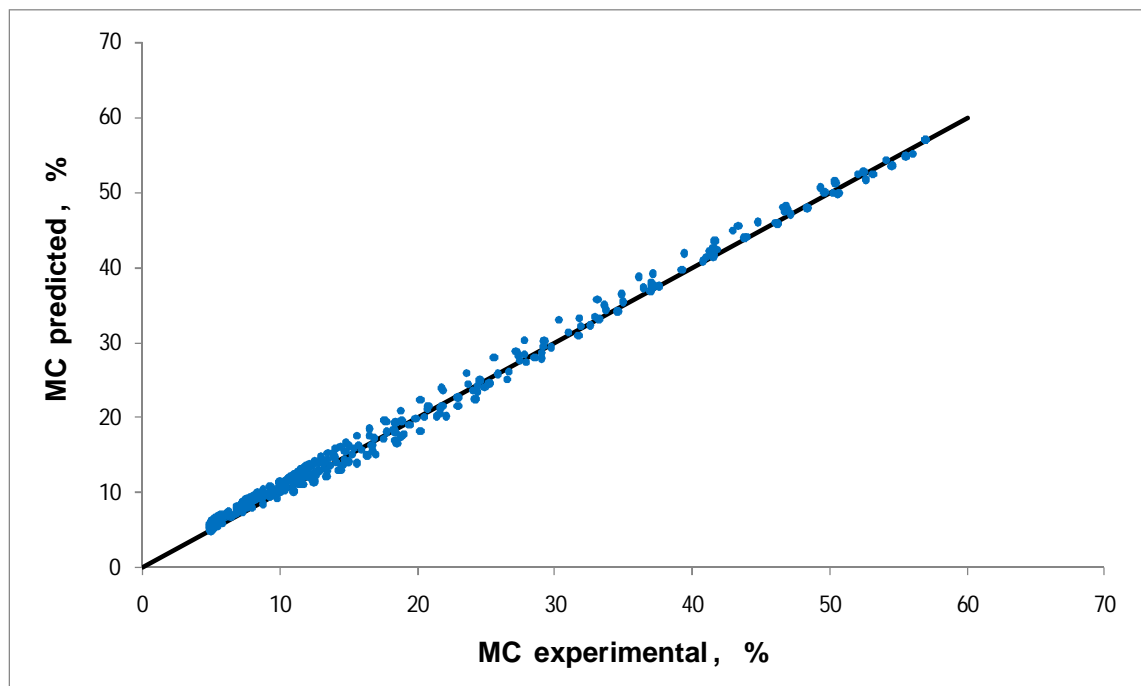


Figure 3.20: Predict vs experimental MC data for 12 drying tests with the first wood sample.

Table 3.14: Statistical indicator obtained when comparing measured and modelling MC in the first woodchip sample being dried with the thin layer dryer.

Statistical indicator	Values
a	1.012
b	0.825
R ²	0.996
MBE, %	0.583
RMSE, %	0.797
Skewness	0.722
Kurtosis	-0.695

The statistical results of comparing modelled and experimental results show that the regression line slope is slightly higher than the unit and this reveals that low range values are under predicted while high range values are over predicted. The correlation coefficient of 0.996 was high as most of points lay on the straight line. The RMSE and MBE provide an indication of the average error between experimental and modelled values. Their values are lower than 1% MC which indicates a reasonable good model precision. The low and positive value of skewness indicates that the distribution of points is skewed to the left. The negative low kurtosis value indicates that the point distribution is less peaked than the normal distribution and therefore the grade of dispersion is relatively high. Also, the low kurtosis value suggests that there are low outliers in the estimation.

3.4.4.3 Number of tests

When building a drying macro model, all the testing data was utilised for obtaining the constants of the Page model expression. However, the information or the minimum number of tests required to describe the woodchip dryer performance with an acceptable “degree of accuracy” can be reduced. As a consequence, the experimental work conducted in the lab for modelling the woodchip dryer performance can be decreased. This section analyses the results obtained from various drying models, developed with less input data, to describe the same woodchip dryer performance.

In order to find the minimum number of tests required to describe the dryer performance, a number of test combinations were employed for developing new drying macro models from the same set of tests. These new drying models results were compared to the original test data concluding that:

- The drying macro model that describes the dryer operation in a particular range of working conditions necessarily has to provide enough information of the process. The tests employed for modelling must be conducted at representative drying conditions, covering the minimum and the maximum of the drying conditions.
- Tests selected to develop the drying macro model necessarily have to have the same weighing in the final result. These tests should be representative of the dryer performance in the range of conditions. Otherwise a partial selection may induce errors: while model describes accurately the MC at high temperatures and high velocities, the same model may generate inaccurate MC values at the low drying conditions and vice verse.
- Tests conducted at predicted drying conditions should be preferably considered in order to have better description of the process in the common operation range.

For instance, when drying the second sample of woodchip in the thin layer dryer, 16 tests at different drying conditions were conducted. The performance of the dryer was modelled using 7 different test combinations obtaining 7 model equations, equation 15 to equation 21, shown below in table 3.15.

Table 3.15: Model equations obtained from the thin layer dryer performance with the second woodchip sample.

16 tests	$MR = \exp(-((0.155 \cdot V^2 - 0.006)(0.007 \cdot T^2 - 0.47 \cdot T - 2.29)) * t^{(1.34 \cdot V^2 - 0.37 \cdot V + 1.2)})$	Equation 15
12 tests	$MR = \exp(-((0.132 \cdot V^2 - 0.009)(0.007 \cdot T^2 - 0.32 \cdot T - 1.04)) * t^{(1.61 \cdot V^2 - 0.5 \cdot V + 1.3)})$	Equation 16
8 tests	$MR = \exp(-((0.138 \cdot V^2 - 0.007)(0.008 \cdot T^2 - 0.5 \cdot T - 2.11)) * t^{(4.86 \cdot V^2 - 1.75 \cdot V + 1.4)})$	Equation 17
5* tests	$MR = \exp(-((0.128 \cdot V^2 - 0.008)(0.009 \cdot T^2 - 0.55 \cdot T - 2)) * t^{(9.5 \cdot V^2 - 3.3 \cdot V + 1.6)})$	Equation 18
5** tests	$MR = \exp(-((0.132 \cdot V^2 - 0.006)(0.009 \cdot T^2 - 0.57 \cdot T - 2.1)) * t^{(10.1 \cdot V^2 - 4.0 \cdot V + 1.6)})$	Equation 19
5*** tests	$MR = \exp(-((0.129 \cdot V^2 - 0.007)(0.009 \cdot T^2 - 0.55 \cdot T - 2)) * t^{(9.7 \cdot V^2 - 3.5 \cdot V + 1.6)})$	Equation 20
4 tests	$MR = \exp(-((0.26 \cdot V^2 - 0.011)(0.004 \cdot T^2 - 0.69 \cdot T - 10)) * t^{(32 \cdot V^2 - 11.1 \cdot V + 1.9)})$	Equation 21

The previous drying model equations were based on the data obtained from 16 tests, 12 tests, 8 tests, 5 tests and 4 tests. Attending to the conditions presented before, figure 3.21.a and figure 3.21.b shows graphically the selection of the tests for each drying model:

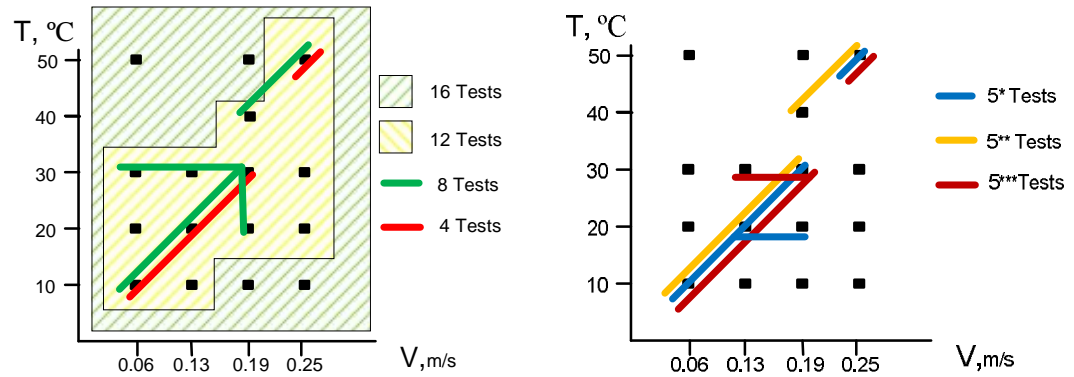


Figure 3.21.a and 3.21.b: Drying model tests selection graphics.

From each woodchip dryer model equation presented above new drying curves were obtained to describe the 16 tests conducted for this set of tests. Table 3.16 shows the statistical results obtained from comparing the predicted MR values and the experimental MR values obtained from 16 drying tests.

Table 3.16: Statistical indicator values obtained from modelling the thin layer dryer performance when drying the second woodchip sample.

Statistical indicator	16 tests	12 tests	8 tests	5* tests	5** tests	5*** tests	4 tests
a	1.001	0.995	0.990	1.012	1.003	1.022	1.120
b	-0.071	-0.040	0.255	0.131	-0.184	-0.356	0.874
R ²	0.998	0.998	0.994	0.990	0.990	0.991	0.941
MBE, %	0.050	0.133	-0.075	-0.316	0.130	-0.056	1.175
RMSE, %	0.256	0.591	0.760	1.118	0.383	0.883	2.541
Skewness	0.977	0.972	0.987	1.768	1.297	1.003	2.755
Kurtosis	-0.356	-0.390	-0.365	-0.616	-0.362	-0.547	-1.628

Reducing the number of tests, the macro model was based on, from 16 to 5 caused a progressive decrement in the accuracy of the model. The changes observed between experimental and predicted curves were negligible and the time basis error remained the same. Furthermore, the statistical indicators presented in table 3.16 show similar regression characteristics for all these considered models. The indicators show good correlation between experimental and modelled data, as discussed in section 3.4.4.2.

However when the macro model drying equation was based only on 4 tests data, the correlation between predicted and experimental data was not satisfactory. The statistical indicators: R^2 , MBE and RMSE show a decrement in the goodness of the model results comparing to the previous model results. For this case, the kurtosis value is -1.628 and it indicates a high level of dispersion as in a uniform distribution. Thus, 4 tests were not sufficient to develop the drying macro model and it was concluded that a minimum of 5 tests were the minimum required to develop the Page model with an acceptable degree of accuracy in the description of the drying process. In order to validate this conclusion, the study presented the results of 3 different model equations based on the data of 5 tests combinations, 5*, 5** and 5***, selected following the criteria presented before. The statistical indicators for these 3 models yielded similar results with no substantial variations.

3.4.4.4 Modelling the thick layer dryer

Unlike the thin layer dryer set of tests, the drying macro model for each thick layer dryer configuration was based on 5 drying tests. Experimental drying curves obtained from the thick layer dryer tests were modelled using a Page model expression following the same procedure as in the thin layer dryer modelling. The model equations obtained to describe the performance of the thick layer woodchip dryer within the range of drying velocities and temperatures of the tests presented in table 3.9, equation 22 to equation 24. Table 3.17 shows the equations that describes the experimental MR curves of the thick layer dryer performance.

Table 3.17: Model equations obtained from the thick layer dryer performance for different woodchip layers.

10cm	$MR = \exp(-((0.53 \cdot V^2 - 0.011)(0.005 \cdot T^2 - 0.056 \cdot T - 0.75) * t^{(0.63V^2 - 0.11V + 0.71)}))$	Equation 22
20cm	$MR = \exp(-((0.92 \cdot V^2 - 0.057)(0.011 \cdot T^2 - 0.02 \cdot T - 0.28) * t^{(0.38V^2 - 1.3V + 0.17)}))$	Equation 23
30cm	$MR = \exp(-((0.26 \cdot V^2 - 0.087)(0.014 \cdot T^2 - 0.037 \cdot T - 0.81) * t^{(0.01V^2 - 0.18V + 0.55)}))$	Equation 24

Figure 3.22 shows the correlation between modelled and experimental MC values for 15 tests conducted with the thick layer dryer. Bias points are observed in the plot correspond to the 20cm woodchip layer tests whose model equation did not yield as good results as the 10cm and 30cm thick layer model equations. Table 3.18 summarizes the statistical results corresponding to the comparison between predicted and

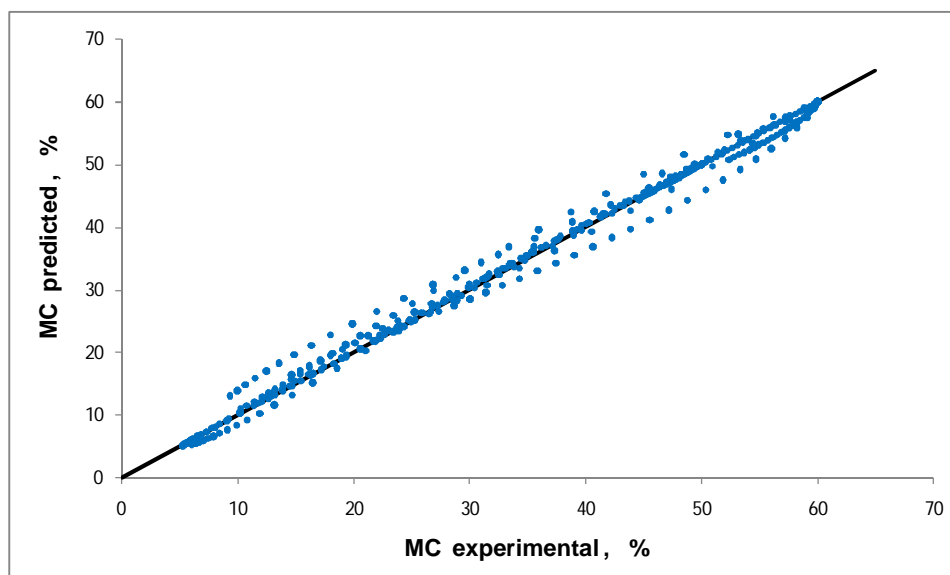


Figure 3.22: Predict vs experimental MC data for 15 drying tests data obtained from the thick layer dryer.

experimental MC data for each set of tests. The correlation coefficients, that indicate the goodness of the model, were: for the 10cm layer model 0.996, for the 20cm layer model 0.946 and for the 30cm layer model 0.990. The RMSE values confirm that the 20 cm thickness dryer model has higher difference error than the other two models. The negative skewness indicated that point distribution is skewed to the right and the negative kurtosis shows that the point distribution is not peaked. The high kurtosis values are associated to the dispersion of few points and the low amount of points employed in the regression analysis.

Table 3.18: Statistical indicator values obtained from modelling the thick layer dryer performance with different woodchip layers.

Statistical indicator	10cm	20cm	30cm
a	0.307	0.903	0.580
b	0.996	0.946	0.990
R ²	0.999	0.983	0.999
MBE, %	-0.154	-0.058	-0.275
RMSE, %	0.435	1.328	0.457
Skewness	-0.399	-0.172	-0.232
Kurtosis	-1.182	-1.472	-1.298

3.4.4.5 Validation of the results

The results of the drying macro models developed were validated by comparing the experimental and predicted results at new drying conditions within the range of drying velocities and temperatures tested. For instance, Figure 3.23 shows the validation of the results corresponding to a test conducted with the thick layer dryer for 30cm of woodchip dried with a drying velocity of 0.5 m/s at 50°C. Despite the difference in the MC when reaching the equilibrium, the predicted MC curve was satisfactory in the beginning of the process.

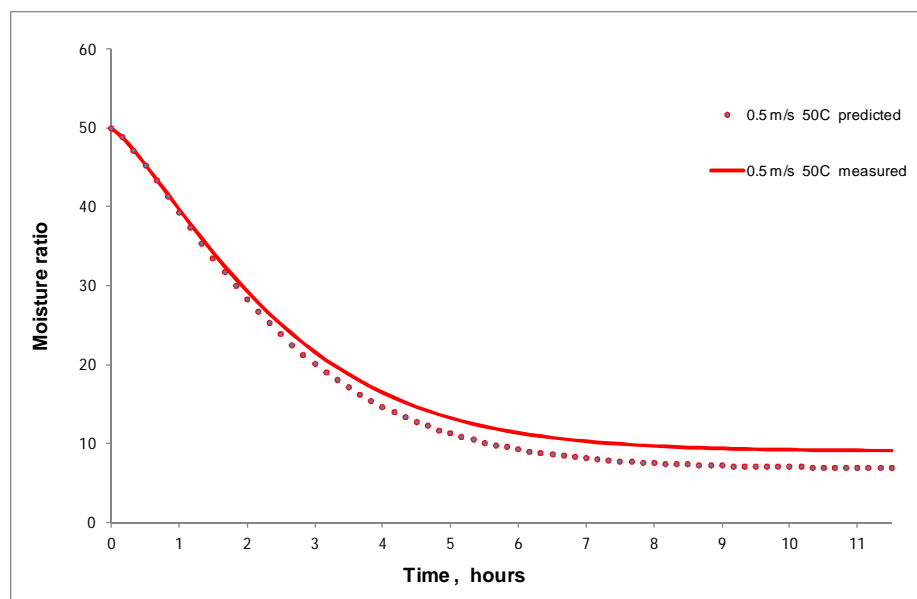


Figure 3.23: Validation of the drying model with a drying test set at 50°C with a drying velocity of 0.5m/s.

Moreover in the previous section 3.4.4, the goodness and the reliability of the drying macro model results in the thin layer dryer were already noted when only 5 tests were employed to predict correctly the MC curves of a set of 16 tests.

The woodchip dryer model results were not validated for an extended range of drying conditions. The present work was limited to the study of the woodchip dryer performance when operating in a range of drying conditions, in temperatures and drying velocities, expected to find when the woodchip dryer operates along the solar air heater.

3.5 Summary

In this chapter, two different dryer prototypes were built and tested in order to analyse the process of drying woodchip. The designs of the dryer configurations: a thin

layer and a thick layer dryer were based on the thermal output and flow capacity of the SATS introduced in Chapter 1.

The thin layer dryer consisted of a drying box with a square box with 510 mm side and it was the first configuration to be tested. Two set of drying tests were conducted at various drying conditions for two samples of woodchips with different qualities. The analysis of the process consisted in the study of the MC curves, drying rates and drying times as a function of control parameters: drying temperatures and drying velocities. It was observed that drying rates were directly proportional to the capacity of air to evaporate water, which depended on the temperature and air humidity. Likewise, it was noted that drying rates were directly proportional to the air flow rates although the thin layer dryer efficiency may decrease with the drying velocity.

When drying two different woodchip samples with the same thin dryer prototype, it was observed that the size of the chips was not a determining factor: In the beginning of the process, the mechanism of drying consisted in evaporating the free water contained in the chips, and therefore drying rates were similar. Then the sample with a lower MC_0 dried faster as there was less water to evaporate.

The thin layer dryer performance was compared for two tests with different thicknesses, 3 kg of woodchip forming a layer of 3 cm and 4 kg of woodchip forming a layer of 4 cm, at identical drying conditions of temperature, humidity and drying velocity. The results showed that increasing the layer of the woodchip implied enhanced drying rates and therefore enhanced dryer efficiencies as the air crossing the woodchip has a longer contact path with the woodchips and hence more chances to remove more moisture.

The second dryer prototype had a reduced tray area, 170 x 170, and the layer of product was deeper, 30 cm layer for 3 kg of woodchip. Thus the thick layer dryer was expected to operate with higher drying velocities and lower flow rates due to the notable increment in pressure drop. Because the drying conditions were subjected to the SATS thermal performance, it was expected that the thick layer dryer would work with high range of temperatures. In the thick layer dryer, the air-woodchip contact path length was longer, therefore drying rates and efficiencies were found notably higher than in the thin layer dryer. Dryer efficiencies were higher with deeper woodchip layers.

In order to find an adequate model that describes the performance of the dryer, a series of mathematical expressions were derived to describe the MR curves obtained from each drying test. Based on the statistical results and the simplicity of the equation,

Page model, characterised by only two parameters, was finally selected as the most suitable mathematical expression.

A drying macro model based on the Page model equation was developed for each set of tests conducted with either the thick or thick layer dryers. In each case, the drying macro model predicted the MC values at any drying condition within the range of temperatures and drying velocities studied. A statistical analysis assessed the goodness of the model comparing the predicted and experimental MC values obtaining acceptable regression values always higher than 0.99. The time basis error study revealed the good agreement between the predicted and experimental MC values especially in the beginning of the drying process. Finally, the statistical analysis revealed that a minimum of 5 tests MR data were necessarily required for developing the macro model.

The analysis of the thin layer dryer and the thick layer dryer performances has not revealed which one is more suitable for the woodchip solar dryer. The drying rates are strongly dependant on temperature and flow rates in both cases. However when woodchip dryer works along the SATS, it is expected that the thin layer dryer operates with relatively high flow rates and low drying temperatures, whereas the thick layer would work with high temperatures and low flow rates.

The SATS for pre-heating air increases the temperature of the air flow and therefore the air capacity to remove water from the product. Depending on the dryer configuration, it will operate with high air flow rates and low drying temperatures and vice versa. Thence, it is necessary to analyse the performance of the woodchip dryer and the SATS working together in order to decide which one is the best woodchip dryer.

4. SOLAR AIR THERMAL SYSTEM

4.1 Introduction

The present chapter describes the characteristics and performance of the solar air thermal system, SATS, employed in the woodchip solar dryer. The SATS was a novel prototype designed to operate exclusively with solar energy. It was comprised of two parts: a solar collector used for heating up the air and a PV driven fan that delivers the warm air flow through the collector to the drying system.

The SATS design was based on previous work in solar thermal applications conducted by Grassie (2006) for storing heat using a bed of pebbles and the study of a PV driven roof slate ventilation system for preheating conducted air by Odeh et al. (2006).

This chapter is divided in three main sections:

- The first part deals with the methodology adopted during the experimental work. The technical aspects of the design of the solar air collector and the PV driven fan are discussed. The testing procedure and testing conditions in the study of the SATS performance are also described.
- The second part presents the results obtained from the testing work including an analysis of the pneumatic characteristics of the solar dryer and the thermal performance of the SATS.
- The third part includes the results of modelling the performance of the SATS based on the results obtained previously. The goodness of the model is studied employing a regression analysis. The model results are validated comparing predicted and experimental values in various tests.

4.2 Methodology

The operation principles of the studied SATS were already introduced in chapter 1.

4.2.1 Solar air collector design

4.2.1.1 Introduction

The proposed SATS studied in this project was based on the design of a transpired plate collector, TPC. The solar air collector studied was a simple design that comprised three parts: a wooden frame, a metal absorber plate and an optional glazing cover.

In order to study a cheaper alternative to the original design, the transpired plate was replaced by a fabric absorber plate forming a flat plate configuration in which the air flow passed in contact with the back of the absorber. Figures 4.1 and 4.2 show sketches of each of the SATS configurations studied.

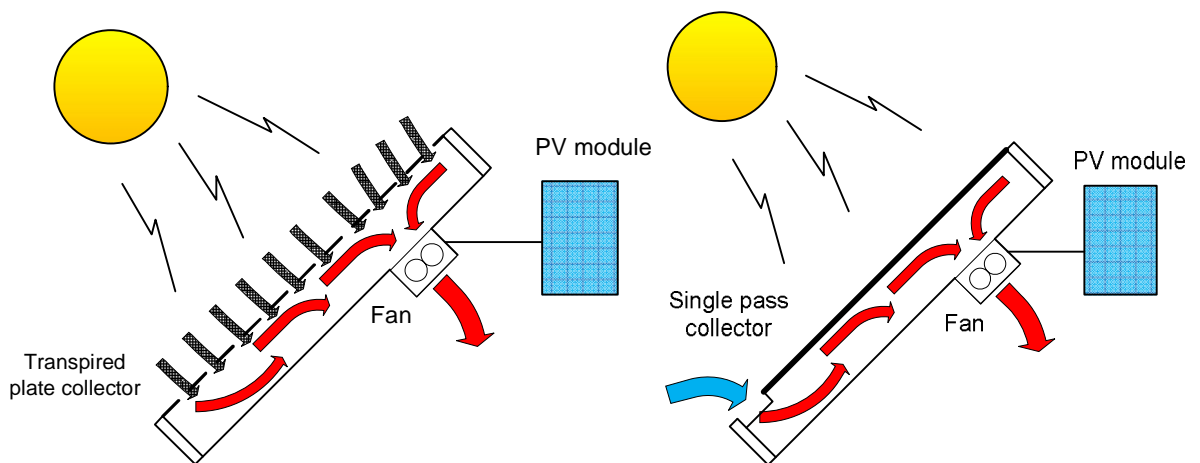


Figure 4.1.a and figure 4.1.b: Drawing of a transpired plate collector (left). Drawing of a flat plate solar air collector (right).

4.2.1.2 Absorber plate

The two functions of the absorber plate are to capture the solar radiation and to transfer the heat to the air. The design of the absorber plate is critical for the performance of the SATS: Technical aspects such as collector dimensions and materials employed necessarily affect the SATS thermal behaviour.

The absorber transpired plate was made of 1.5 mm thick aluminium sheet with an estimated thermal conductivity of 237 W/m K, Incropera (1996). For any solar air collector, using aluminium implies a high degree of temperature uniformity across the absorber plate. Aluminium is a light material with good mechanical resistance and high durability in different weather conditions. However it is an expensive material and the manufacturing process is also costly. The sheets were perforated using a CNC machine; this appliance drilled the holes automatically from a control numeric program that described the operations required. However the machine only accepted sheets of metal of 500 x 600 mm maximum. Therefore the area selected for the solar collector was

bound to have dimensions based on these absorber unit sizes. Thus 1.8 m^2 , $1000 \times 1800 \text{ mm}$, was the collector area selected.

According to Duffie et al. (1985), there is a range of values for the parameters in each collector configuration where the heat transfer is optimal. Grassie (2007), based on a numerical analysis, stated that for a perforated plate made of 1.5 mm thick aluminium plate, the optimal values for the parameters of the absorber collector corresponded to 2 mm diameter holes and 20 mm pitch distance. Two transpired plates were built and tested in order to compare the results. The first configuration was characterised by the hole distribution previously suggested and as an alternative a second configuration with lower number of holes characterised by a 3 mm diameter hole distribution with a 30 mm pitch distance. The absorber plate characteristics are shown in Table 4.1. Both hole distributions can be compared in Figure 4.2.

Table 4.1: Absorber plate characteristics

	material	N° holes	Diameter	pitch	area	porosity	thickness	conductivity
Absorber plate 1	Aluminium	4176	2mm	20mm	$1,8\text{m}^2$	0.73%	1,5mm	237 W/m·K
Absorber plate 2	Aluminium	1680	3mm	30mm	$1,8\text{m}^2$	0.66%	1,5mm	237 W/m·K

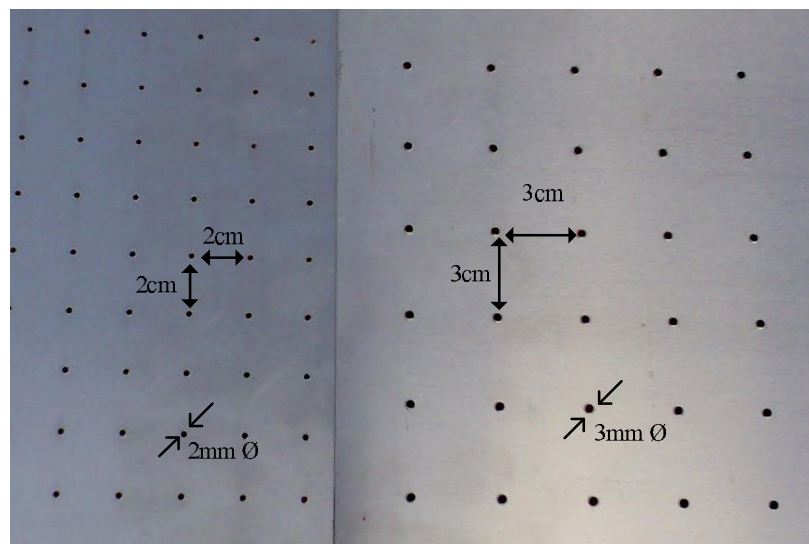


Figure 4.2: Details of the aluminium transpired plates.

The optical properties of the aluminium plate were not good as it had a high reflectivity index. Therefore the aluminium plates were painted in matt black to increase the absorptivity and to achieve better efficiencies. The selective coating was considered for reducing surface emissivity and hence radiant heat loss. However the suppressed

radiant heat losses are more pronounced at higher temperatures than are generally experienced in the proposed air heater. Thus black matt coating was the economical option selected.

4.2.1.3 Glazing cover

The glazing plate is the component of the collector used for reducing the heat losses on the top of the collector. An optional channelled polycarbonate glazing sheet was mounted on the wooden frame and covered the solar collector. Based on expected temperatures and hence convection heat losses, the glazing cover was held 60 mm from the absorber plate. The polycarbonate material has acceptable values of optical transmissivity, temperature resistance and also it has a reasonable period of life without changing optical properties. The channelled shape of the cover provides good insulation and mechanical resistance to protect the collector from environmental factors such as rain or dirt. However the glazing plate affects the amount of solar radiation that reaches the absorber plate as it introduces a degree of reflectivity. Levels of transmissivity for the polycarbonate are high for a wide range of wavelengths. However, this parameter is affected by the inclination angle made by the sun beams and the collector plane. Thus for inclination angles higher than 30°, the reflection of the direct sunlight affects the thermal performance of the solar collector, Duffie et al. (1985).

The sheet of polycarbonate was assembled into the cover frame using silicon paste in order to seal the gaps avoiding air leakages and also to prevent the water condensation in the channels.

4.2.1.4 Wooden case

Two identical wooden cases for each solar dryer configuration were built with identical geometric characteristics. They were mounted side by side onto a roof structure. They had a rectangular shape defined by the area of the collector described before: 1m x 1.8m. Figure 4.3 and figure 4.4 show the details of the wooden frame design. The volume of the box was defined by the area of the collector and the depth of the plenum: 160 mm height. Aluminium plates were held by lateral supports, one longitudinal and two transversal bridges which were nailed onto the frame and provided rigidity to the wooden frame.

The construction material recommended by the technicians was 18 mm plywood board. This material has appropriate physical properties as it is light, resistant and easy

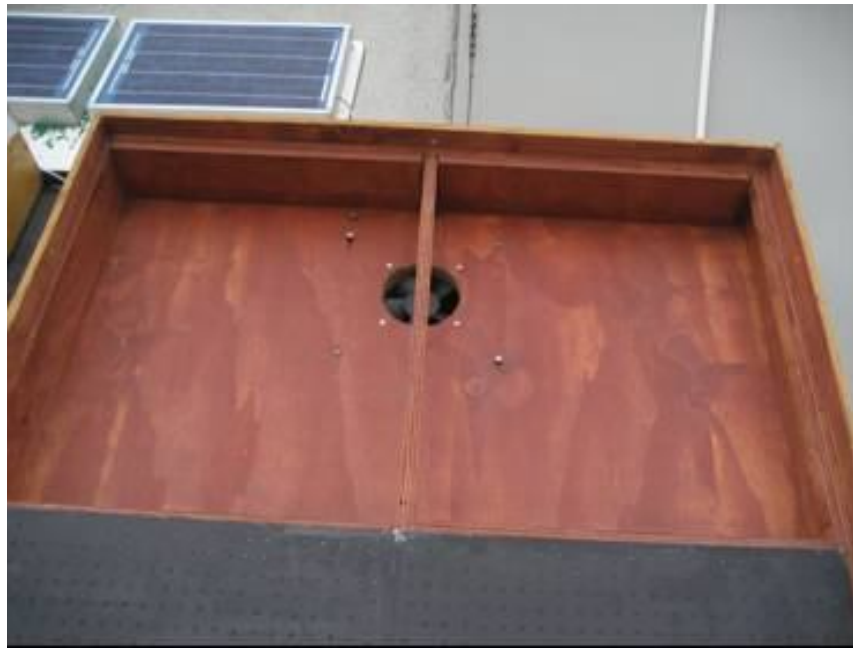


Figure 4.3: Wooden frame details, holding the absorber plates and fan location at the back.



Figure 4.4: Solar collector testing rig on the roof.

to manipulate, facilitating the manufacturing process. In order to protect the wooden case from weather conditions, the wood was painted with varnishing protector.

A 150mm diameter hole for the fan was located at the centre of the rear backing plate on the top of the collector. In the lower section of the collector, 40 holes of 25 mm diameter were drilled for air inflow as an inlet for the collector when the glazing cover was used. Regards the restriction on airflow in the system, the opening area of the transpired plates were $1.188 \times 10^{-2} \text{ m}^2$ and $1.314 \times 10^{-2} \text{ m}^2$ for the 3mm \varnothing TPC and 2mm \varnothing TPC configuration respectively. While the total opening area of the 40 holes in the glazing cover was $1.96 \times 10^{-2} \text{ m}^2$. Thus the major restriction to flow was produced by the holes in the transpired plate.

The back of the plate was made also using the same material as the frame, 18mm plywood. Although it is always desirable to minimise the heat losses of a solar collector, the aim of this project was to develop a cheap prototype reducing the costs including. Thus, no insulation material was employed to minimise the heat losses on the back and the side areas of the solar air collector. However, a large area the 80% of the back of the collector plate area was protected from the direct contact to the ambient air by the wooden structure that held the SATS.

4.2.1.5 Flat plate collector configuration

A simple and economical solar flat plate collector was built and studied. The alternative collector comprised the same SATS frame. The transpired aluminium plate was replaced by a fabric sheet made of black polythene. When attaching the plate to the collector frame, a small gap was left at the bottom of the collector to let the air in, estimated in the 3% of the collector area.

The change in the absorber configuration meant different flow distribution and different thermal performance: The heat collected by the black fabric was transferred to the inlet air flow through the back of the absorber plate in the plenum. As the heat was not transferred at the top of the absorber to the air, important heat convection losses to the ambient were generated. Thus using a glazing cover for reducing heat losses was expected to enhance the thermal performance in this configuration.

The Polythene sheet, despite not having good optical properties and low conductivity, was selected as a cheap absorber material alternative to be tested. This material is widely used in gardening to protect goods, such as wood fuel, from the rain.

4.2.2 PV driven fan design

Air circulation in the SATS was provided by a small capacity fan driven by a photovoltaic panel. The flow delivered by the fan into the drying system naturally depends on electrical characteristics of both the PV module and fan, and also on the pneumatic characteristics of the system. The PV module and the fan were selected to provide a range of flow that could, by design, give useful ΔT . The fan consumed all the electrical power yielded by the PV module.

4.2.2.1 Fan

The fan selected for the solar dryer prototype was an axial fan model 5W 12VDC PASPT. The characteristic curve provided by the maker, PAPST (2003), described the head losses with the flow rate when working at the nominal voltage, 12V. The maximum air flow was of 49l/s or 180m³/h when working with no pneumatic resistance. The electrical fan characteristics were measured experimentally. The start-up point was obtained with the rotor locked and it was defined by a voltage of 2.66 V and a current of 140 mA. After the start-up, the fan presented a resistive behaviour. The value of its electrical resistance was 28.6 Ω at 12 V, drawing a current of 0.419 A.

4.2.2.2 PV module

In the market, there was a wide range of PV modules with different power and electrical characteristics. The main criterion in the selection of the PV module capacity was maximising the usage of the energy collected from the solar radiation.

For the selected fan, two BP photovoltaic modules were considered with two different nominal powers namely 5 W_P and 10 W_P. Figure 4.5.a and figure 4.5.b show two graphs of the schematic interaction of electrical characteristics between the fan and the PV modules considered.

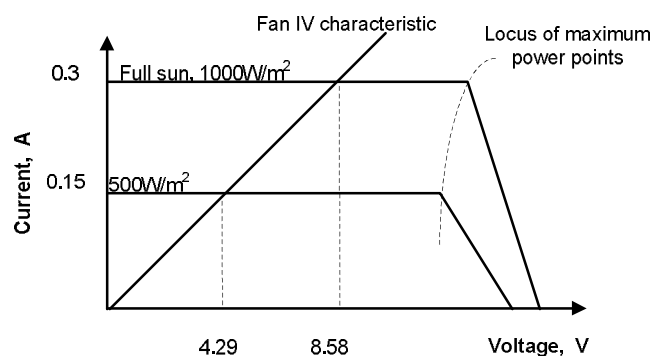


Figure 4.5.a: 5W PV module fan electrical characteristics.

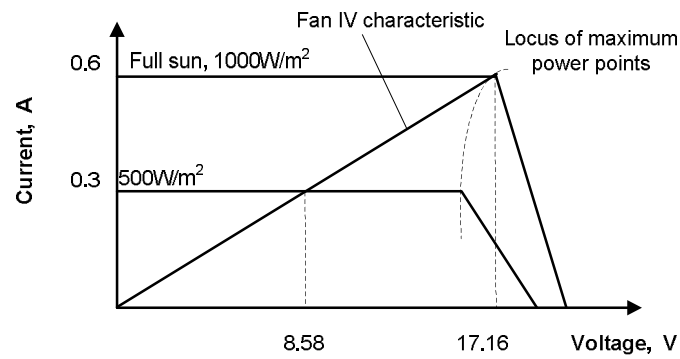


Figure 4.5.b: 10W PV module fan electrical characteristics.

The PV driven I-V characteristic is represented by Figure 4.5.a and figure 4.5.b showing the operational voltages of the fan motor and the PV modules for two solar radiation levels. Observing the graphics, it is concluded that the $5 W_p$ fan will work more efficiently when coupled with a PV module of $10 W_p$ as IV points of the fan are closer to the locus of maximum power of this particular PV module. The PV driven fan voltage reaches its nominal voltage, 12V, at irradiance value of $710W/m^2$, considered a “good sunshine” in Scotland. This means that fan might operate above its capacity in high irradiance periods and this may limit its lifespan. The fan may receive twice its power capacity from the PV module when operating at “full sun” conditions, however, Grassie (2006) did not report any signal of fatigue or damage in a similar PV driven fan installation after long term laboratory testing at high voltages. Moreover, considering the typical irradiance profiles for the testing location, the high voltage performance at these “full sun” conditions are limited.

Coupling the $5 W_p$ fan motor to a higher capacity PV module also reports an important advantage to the system performance. The threshold irradiance, associated to the minimum voltage of the fan to start working, is low and therefore the SATS operational periods can be expected longer.

4.2.2.3 The ducting characteristics

The SATS also comprised of a ducting section that linked the end of the solar collector with the woodchip dryer. This ducting section was 1.2m long for the first dryer while for the second dryer configuration it was 1.5m long. The material employed was an aluminium semi rigid corrugated ducting with a level of extension of 80% over the maximum length. This component was cheap and easy to assemble with the other parts of the woodchip solar dryer. Two metal square-round adaptors were used to connect the ducting with the dryer and the collector. The ducting element was relatively short and it

had no thermal insulation was applied on it. However it introduced notable heat losses that were considered in the woodchip solar dryer performance when calculating drying temperatures. Moreover, the ducting also introduced a pressure drop which affected the total air flow circulating in the system.

4.2.3 Instrumentation

4.2.3.1 Pyranometer

The main indicator of the quality of the sunlight is the irradiance. An adequate reading of its magnitude was essential for analysing the results obtained. The global irradiance indicates the levels of solar radiation per square meter. A pyranometer was used for measuring total solar radiation, the sum of beam and diffuse radiation. The instrument used a thermal detector, a thermopile with black coating that absorbed solar radiation to measure the thermal radiation for certain range of the electromagnetic spectrum. This type of pyranometer had a double crystal to protect it from the ambient and also to avoid the convection heat losses. Thus the heat absorbed by the thermopile was converted into a voltage signal that was proportional to the solar radiation.

The pyranometer sensor employed was a model Kipp and Zonen CM 11 and it was located in the same plane as the solar collectors and the PV module, figure 4.6. The sensitivity of the pyranometer employed was $5.6 \mu\text{V}/\text{W}\cdot\text{m}^2$. The instrument was calibrated by the manufacturer before the testing period and had an accuracy of 3% in all the range of measurements.



Figure 4.6: Pyranometer instrument employed to measure the solar radiation.

Measurements were obtained in mV and logged in a data logger. After in a spreadsheet, they were converted into W/m^2 just multiplying the measurement values by the sensitivity constant. The reading error was proportional to the tolerance in the voltage measurement of the data logger, ± 0.05 mV, which caused a total ± 9 W/m^2 error in irradiance measurement.

4.2.3.2 Thermocouple

Measuring the air temperatures at several points of the SATS was fundamental for the analysis of the collector performance. The thermocouple sensors employed for the solar testing were the same as utilised in the drying tests, k-type thermocouples described in the section 3.2.2.3.5. The thermocouples were calibrated in the university lab. The sensor accuracy was $\pm 0.5^\circ\text{C}$ and the reading error derived from the data logger was $\pm 0.1^\circ\text{C}$.

4.2.3.3 Relative humidity sensors

The relative humidity was measured periodically although it was not a key parameter in the thermal collector performance. However it was of interest in keeping the solar collector dry as the water in the system reduces the latent heat of the air when evaporating, affecting the collector outlet temperatures. The relative humidity sensors employed were the same as employed in the drying tests described in the section 3.2.2.3.4.

4.2.3.4 Flow meter

The air flow meter TM AV6 employed for the drying tests was also used for measuring the air velocity in the duct of the solar dryer configurations. The 100mm diameter vane anemometer was located at the end of the flexible duct and just at the entry of the dryer. The characteristics of the anemometer were described in the previous section 3.2.2.3.3

4.2.3.5 Anemometer

The effects of the wind were noticeable in the SATS performance. Although it was desirable, the wind speed was not measured directly in the same location as the solar dryer. However, a meteorological station was located 10 meters from the experimental equipment. The wind speed values were not appropriate for the numerical analysis as the anemometer was not close enough to the experimental apparatus. However, wind speed measurements were taken to evaluate the windy days.

4.2.3.6 Pitot tube installation

In order to measure the characteristic curves of the fan and the ΔP -Q curves of the system, measurements of static pressure and dynamic pressure were required. A Pitot tube installation, comprised of a Pitot instrument and an inclined manometer, was built for measuring the pressure in the system. The operation of the system is simple. A volume of fluid in the inclined manometer is displaced as a function of the air pressure differences in the Pitot tube. There are several configurations to measure the total, static and dynamic pressure. Figure 4.7 shows a schematic illustration of how the Pitot tube works.

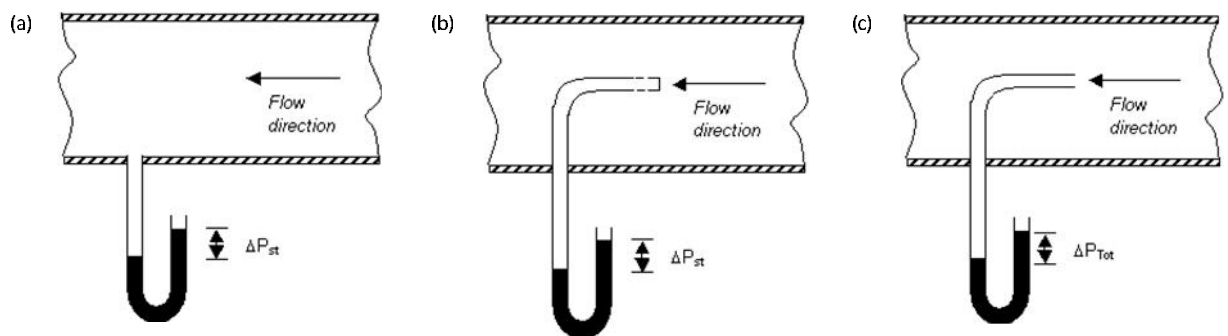


Figure 4.7: Pitot tube configurations for measuring pressure in fluid systems. Perry et al. (1984).

The total pressure is the sum of the static and dynamic pressure. The static pressure describes the difference between the inside and outside disregarding any motion in the system. The static pressure is constant on a surface which moves with the fluid. So the pressure on a surface parallel to the direction of the flow must be measured and thus the opening of the Pitot static tube is on the side of the tube as shows Figure 4.7.b. It was easy and preferable to measure the static pressure as shown in Figure 4.7.a. The total pressure, the sum of the static and dynamic pressures, was measured with the opening facing the flow as in Figure 4.7.c.

The measurement of the dynamic pressure at any point is associated to the local velocity at the exact location where the pressure was measured. The Pitot tube is commonly used to measure the dynamic pressure and the average velocity in the duct section. So for each flow rate measurement, a set of at least 12 measurements at different distances from the centreline is required. An average of the dynamic pressure can be determined by finding the weighted average of these measurements. Odeh (2006), applied a correcting method to calculate the average of the dynamic pressure

from a single measurement of maximum velocity at the centreline, (McCabe et al. 1985)

The dynamic pressure is converted in average dynamic pressure using the equation 4.1. In which f is the friction factor calculated as a function of the roughness of the pipe and Reynolds. The value of f was 0.75 for all the range of air flow rates considered, Odeh, (2006).

$$\frac{\bar{P}_{dynamic}}{P_{dyn_max}} = \frac{1}{1 + 3.75\sqrt{\frac{f}{2}}} \quad \text{Equation 4.1}$$

Figure 4.8 shows the inclined manometer that was employed for measuring the pressure differences. The instrument was a simple inclined tube that contained liquid of 880 kg/m^3 density. Liquid displacements from a reference point were proportional to the pressure difference and depended on the position of the tube. The manometer was levelled off and set to zero using the knobs available. Each angle position had a calibration constant to convert displacement into pressure measure. Using always an appropriate angle position, the uncertainty in taking a pressure reading was 1mm, which corresponded to 0.86 Pa.

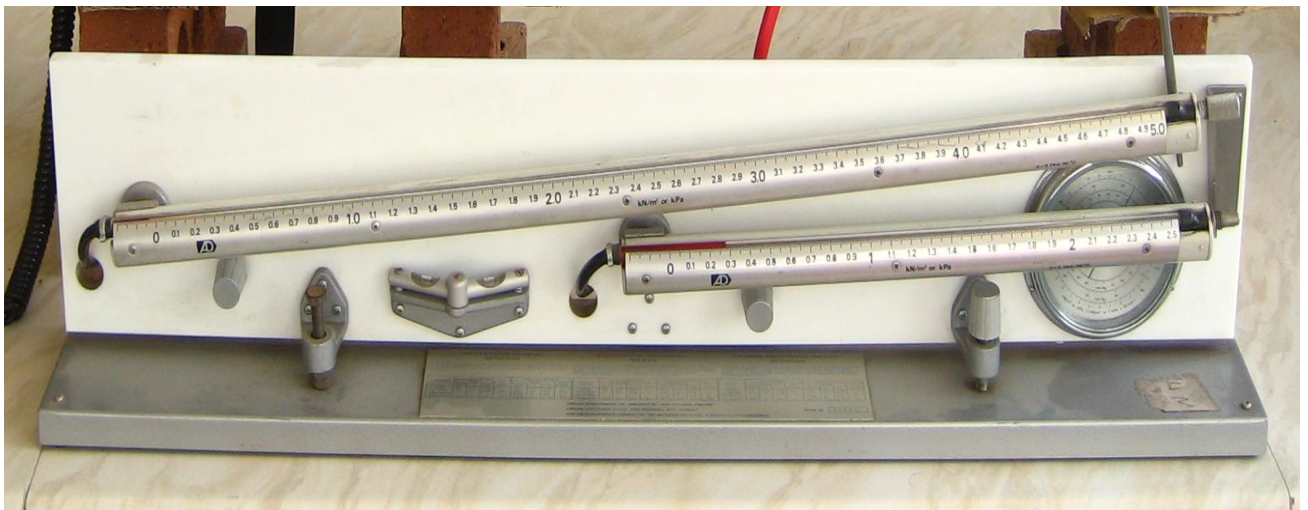


Figure 4.8: Inclined manometer tube to measure pressure.

4.2.3.7 Error analysis methodology

In Table 4.2 the errors caused in each of the readings due to instrument tolerance are given. These values are used to calculate errors in the predicted values through

propagation of error. The approach taken here is to run the model developed, not only for the measured values but also for their lower and upper limits.

Throughout this chapter whenever predicted values are compared to measurements, the calculated errors are simply a representation of how far the calculated value is from measurements. So errors are calculated as the difference divided by the measured value.

Table 4.2: Quantities to be measured, instrumentation and measurement errors

Measurement	Unit	Instrument	Instrument precision	Reading error
Voltage	V	Multimeter	± 0.01 V	± 0.1 V
Temperature	$^{\circ}\text{C}$	k-type thermocouples	± 0.5 C	± 0.1 C
Relative humidity	%	Humidity sensor	$\pm 4\%$ points	-
Irradiance	W/m^2	Pyranometer	$\pm 3\%$	$\pm 9.7\text{W}/\text{m}^2$
Air flow velocity	m/s	Velocimeter	$\pm 1\%$	± 0.01 m/s
Pressure drop	Pa	Inclined manometer	± 1 Pa	± 0.86 Pa

4.2.4 Testing procedure

4.2.4.1 Pneumatic characteristics

The thermal performance of any solar air collector depends on the air flow that circulates through the system. In the SATS considered, the air flow rates depended on:

- Electrical connection between PV module and fan.
- Pneumatic characteristics of the SATS, including the fan characteristics and pressure drop across the system.

Therefore, the thermal performance of the SATS could not be disassociated from the dryer system and solar collector tests were conducted with the dryer coupled.

The pneumatic characteristics of the solar dryer were experimentally analysed in the laboratory using the Pitot tube installation. ΔP - flow curves were obtained for all the components of the solar dryer separately: solar collector configurations and both thin and thick layer dryers. Once the pneumatic characteristics of the system and the electrical relationship between fan and PV module were known, the ultimate purpose was to model the relationship between the environmental factors and the air flow that later will be used for drying.

The procedure for obtaining the air flow curves as a function of the environmental factors was the following:

1. Irradiance-voltage relation for the fan and PV panel when are coupled.
2. Fan characteristic curves at different voltages.
3. Pressure drop characteristics at same voltages.
4. Modelling air flow.

1. In previous studies, Odeh et al. (2006) modelled the electrical characteristics of the fan and the PV module in order to obtain the I-V curve for each element used for predicting operational voltages. However, in the current study, the analysis of the experimental electrical operation points between fan and PV module was considered sufficient.

The performance of the PV module depends on ambient factors such as irradiance and temperature, Eckstein et al. (1990). This dependence was simplified when modelling the operational voltages as a function of irradiance. A relation between the operational voltage and irradiance was established and later used to model the flow.

2. The pneumatic characteristics of the system were studied in order to assess the effect of the pressure drop in the solar collector and in the dryer. The main purpose of this study was to find a relationship that describes the flow rate as a function of the irradiance for each solar dryer configuration.

A simple installation was built for measuring the pressure drop and flow as shown in Figure 4.9. The instrument consisted of a rigid pipe of 141 mm diameter and 2.5 m long with a restriction valve installed at the outlet of the pipe. The fan was fixed at the inlet of the duct and the static pressure across the fan was measured using the manometer and a Pitot tube. The inclined manometer was used for measuring the static pressure and it was located 50 cm from the fan. The Pitot tube was employed for measuring the total pressure and it was inserted in the pipe at the centre about 1m from the fan. Although air velocity could have been estimated using a relationship between average velocity and dynamic pressure, White (1986), air flow was measured using the pipe flow meter. Tests were conducted in the lab installations during a short period of time at $21 \pm 1^\circ\text{C}$.

Firstly, the characteristic curves of the solar woodchip dryer fan, 5W fan, were obtained experimentally. They were useful for the analysis and validation of further

results. Thus, ΔP -Q curves were obtained at various input voltages, keeping the angular velocity of the fan constant.

For each voltage selected, starting from a fully open valve, the opening of the valve was modified increasing the pressure until the valve was completely closed. A series of air flow, static and total pressure readings were logged. The same procedure was followed in reverse way, from a shut valve to wide open valve.

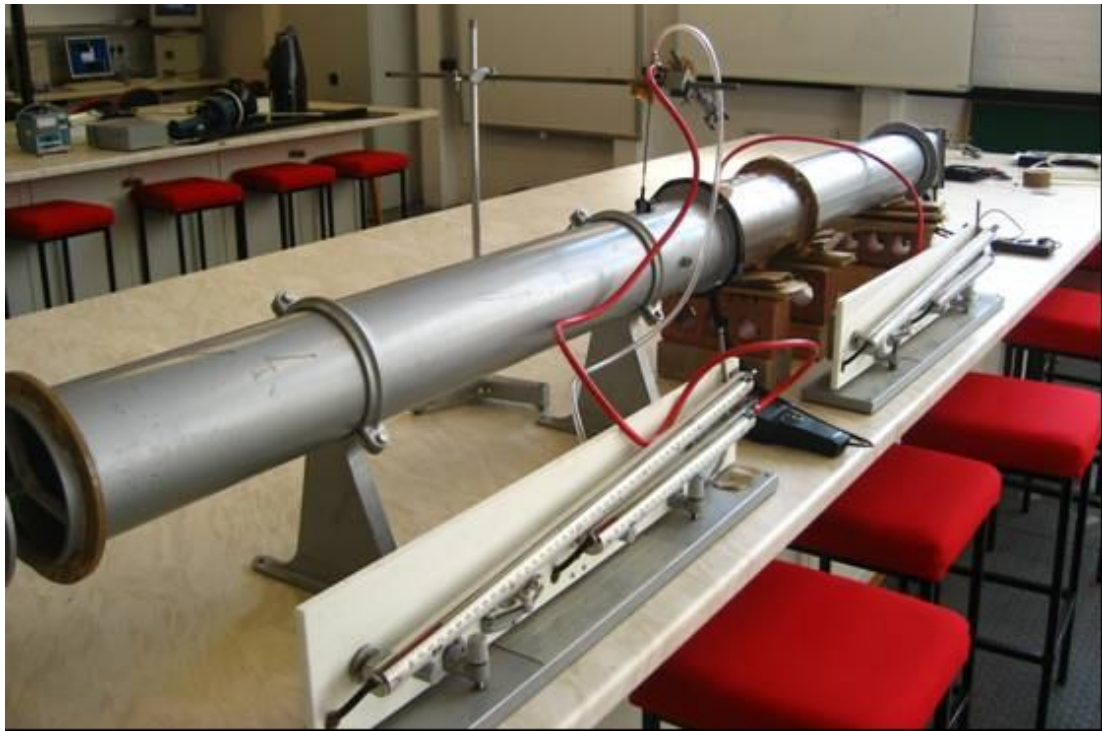


Figure 4.9: Pitot tube installation for measuring the pressure drop in the system.

3. Using the same installation for measuring the ΔP -Q curves, the head losses of the solar dryer system were measured. The total head losses can be expressed as the linear sum of the pressure drop contribution of each element of the system.

In the solar dryer, there were three parts that introduced the total pressure drop of the system: the dryer, the solar collector and the ducting pipe.

$$\Delta P_{\text{total}} = \Delta P_{\text{dryer}} + \Delta P_{\text{ducting}} + \Delta P_{\text{collector}} \quad \text{Equation 4.2}$$

The pressure drop corresponding to each element was studied separately. Two sets of tests were conducted: the first set analysed the pressure drop in the woodchip dryer and the second set of tests analysed the pressure drop contribution of the solar collector.

The first set of tests assessed the following dryer configurations:

- Thin layer dryer with no load.
- Thin layer dryer with 3 cm woodchip layer.
- Thick layer dryer with no load.
- Thick layer dryer with 10cm, 20cm and 30cm woodchip layer.

And second set of tests assessed the following solar collector configurations:

- 2 mm \emptyset unglazed TPC.
- 2 mm \emptyset covered TPC.
- 3 mm \emptyset unglazed TPC.
- 3 mm \emptyset covered TPC.
- Flat plate collector with a fabric absorber plate.
- Glazed flat plate collector with a fabric absorber plate.

ΔP -Q curves were obtained for each element following the same procedure: Each element to be tested was attached to the installation. The Pitot tube apparatus was connected into the pneumatic circuit always measuring the pressure drop in the fan. Air velocities were always measured with the air flow meter inserted in the centre of the duct.

Pressure drop and air flow values were obtained for the same voltages selected previously to build the characteristic curves of the fan. These pairs of values corresponded to the operational points that formed the pneumatic curves which can be represented in the characteristic curve of the fan.

4. The main purpose of the pneumatic study was to obtain a model that described the air flow as a function of the environmental conditions for each solar dryer configuration. Thus operational points of the pneumatic curves were associated to voltage values and modelled using a second order polynomial curve.

In the study of the pneumatic performance of the fan, ΔP -Q curves are commonly evaluated at constant angular speed and air density. However, the pneumatic characteristics obtained in the lab should be corrected when the system operates outdoors. Using dimensional analysis, it is possible to establish a relationship between pneumatic parameters and also create new ΔP -Q curves at different operational conditions of angular speed, ω , and air density, ρ , as shows equations 4.3 and 4.4, White (1986).

$$Q_1 = Q_2 \left(\frac{\omega_2}{\omega_1} \right) \quad \text{Equation 4.3}$$

$$\Delta P_1 = \Delta P_2 \left(\frac{\omega_2}{\omega_1} \right)^2 \left(\frac{\rho_2}{\rho_1} \right) \quad \text{Equation 4.4}$$

For a constant level of irradiance, voltage or angular speed, the pneumatic operational points calculated previously are affected by air density values. Density is a property which depends on the atmospheric pressure and air temperature.

Atmospheric pressure is a parameter that depends on weather conditions and especially on the location altitude. In practise, this parameter was neglected considering that the solar dryer worked at same altitude above the sea level.

The effect of the temperature on the ΔP is difficult to evaluate as operating temperatures are not the same for the fan and the rest of the solar dryer: In case that the whole system worked at the same temperature, the ΔP values in the fan characteristic curve and ΔP -Q curve of the system would be both proportional to the density rate as shown in equation 4.4 while air flow would remain the same as shown in equation 4.3. Figure 4.10 illustrates this case. Temperatures in solar collector and dryer were not uniform and considering the density effects increases the complexity of the analysis and computational calculations dramatically. Considering uniform temperatures in the system are theoretically valid when the solar air collector operates in stationary conditions and also for the thin layer dryer performance. However the effect of the air density in a thick layer, in which average temperature across the woodchip layer is lower than drying temperature, may not be negligible.

In this project, when modelling the air flow, it was considered that the system operates with uniform temperatures: collector temperatures and drying temperatures were the same, simplifying notably the computational cost. In further work, a detailed fluid dynamical study of the solar collector and dryer separately can be developed in order to consider the distribution of temperatures in the calculation of the modelled air flow.

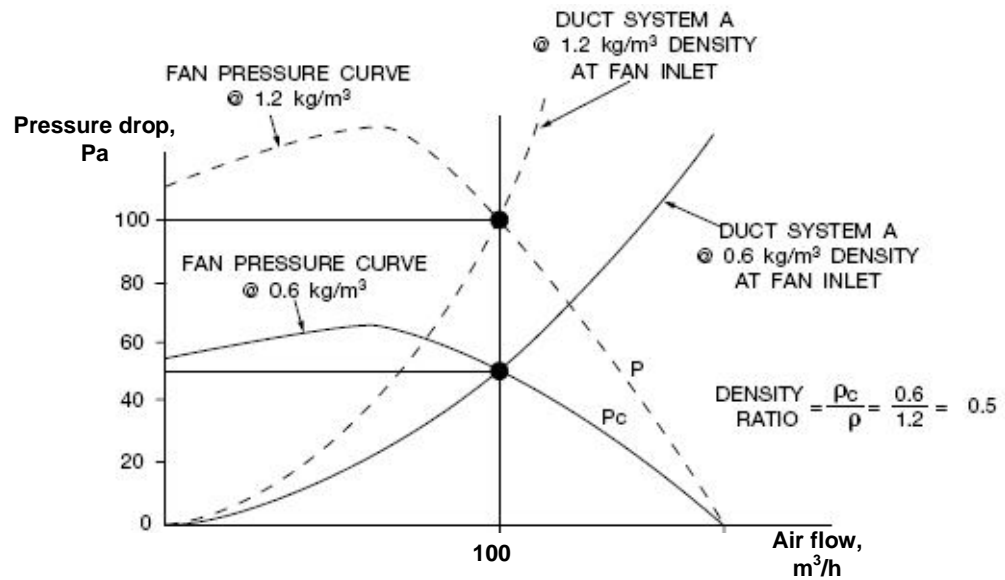


Figure 4.10: Effect of the density on the pneumatic curves, Clarage (2008).

The $\Delta P - Q$ points of the pneumatic curves were associated to voltage values. Hence, for each solar dryer configuration, the flow values were described as a function of voltages and modelled with a quadratic best fit curve. Each flow - voltage curve was combined with the voltage - irradiance curve from modelling the PV driven fan connection as a function of irradiance. A new relation was formed between air flow and irradiance for each solar dryer configuration.

Finally predicted air flow based on the laboratory tests results was compared with experimental air flow data.

4.2.4.2 SATS thermal testing

4.2.4.2.1 SATS tests

The main objectives of the SATS tests are to study and to model the thermal performance of the presented SATS. In the previous section, it was shown that, under certain assumptions, the air flow can be modelled as a function of the solar radiation. As a consequence, in each solar dryer configuration, the description of the thermal performance of the STAS can also be simplified assuming that there is a unique operating flow regime that depends on the irradiance.

SATS tests analysis were classified in two set of tests associated to each dryer configuration: For the thin layer dryer, the solar thermal system performance was studied using the six solar collector configurations:

- 2 mm TPC unglazed.
- 2 mm TPC covered
- 3 mm TPC unglazed.
- 3 mm TPC covered.
- Flat plate collector with a fabric absorber plate.
- Glazed flat plate collector with a fabric absorber plate.

For the thick layer dryer, only two SATS configurations were tested for 3 woodchip layers.

- 3 mm TPC unglazed.
- 3 mm TPC covered.

The analysis of the SATS tests through the year provided enough information to describe quantitatively and qualitatively the thermal performance of the SATS under Scottish weather conditions.

Each SATS test was conducted outdoors and consisted in collecting the data necessary to describe the SATS thermal performance. The data to be analysed included temperatures at different locations of the solar collector, irradiance and PV voltages logged continuously during the testing duration.

The thermal performance of the SATS was represented as the increment of temperature of the inlet air as a function of irradiance.

In general, the study of the thermal performance of any SATS depends on key operational factors: air flow, ambient temperature, solar radiation and wind. The effects of these factors plus the transient effects due to variability of the testing conditions were reflected in the ΔT curves.

Frequently researchers analyse the performances of solar air collectors doing experimental tests at constant flow rates for obtaining the characteristic curve of the solar collector which relates efficiencies with $(T_1 - T_a)/G_T$. However in this research, the thermal behaviour of the solar air collector was analysed when it operated with the PV driven fan. The analysis of the TPC performance was not necessary for the SATS thermal analysis. Therefore, the thermal performance analysis of each TPC was not rigorously comparable as the SATS operated with variable air flows which depended on irradiance.

The aim of this part of the project was to describe the thermal behaviour of the SATS under Scottish weather conditions and to compare its performance under different collector configurations. The majority of the SATS tests were conducted under unstable weather conditions as most of the testing days were cloudy and windy. SATS tests were conducted throughout the year, from the beginning of the summer from 2008 until the end of the summer 2009, in order to have a representative and valuable data of the thermal performance of the SATS considering the key factors involved. Nonetheless, solar collector tests were preferably conducted on clear sky and windless days.

4.2.4.2.2 SATS testing rig

The testing rig characteristics are summarised as follows:

- The solar dryer facility was set up on the roof of a Napier Edinburgh University building, facing the South. The azimuth angle was 190° South. The solar collector structures were mounted over a portable wooden shelter whose roof had an inclination angle of 45° .
- The PV modules and the pyranometer were installed next to the solar collectors in the same plane. During the testing period, both dryers were fixed to the wooden structure.
- Ducting pipes, apparatus and other instrumentation like data loggers were kept in the shelter protected from climate adversities.
- The solar collector was instrumented with RH sensors and thermocouples for measuring the air psychrometric characteristics at 3 points: ambient, outlet of the collector and just below the drying tray. 3 thermocouples and 2 RH sensors were set up at each point. Moreover, ambient air sensors were kept in a shaded location in order to protect the sensors from direct sunlight.
- The data acquisition system logged the thermocouples and RH sensors measurements and voltages from the pyranometer and the PV driven fan every minute.
- The air flow meter was set at the end of the ducting pipe when SATS was connected to the thin layer dryer configuration and in the middle of the ducting when SATS was connected to the thick layer dryer. Air flow measurements were not logged but periodically measurements were taken

in order to control the right operation of the PV module and fan connection.

- Wind speeds were registered in a meteorological station located 10 meters from the solar dryer facility. Wind speed average values were associated to the tests in which wind was appreciably strong.
- During the experimental time, a sample of woodchip was placed on the dryer tray to introduce a pressure drop corresponding to each dryer setup.

4.2.4.2.3 Collector time constant

It was necessary to determine the time constant of the solar collector in order to evaluate the transient behaviour of the collector thermal performance. The value of the collector time constant was considered in the selection of an appropriate time interval for the quasi steady state or steady state.

Duffie et al. (1985) defines the time constant, τ , as the time required for the fluid leaving the solar collector to attain 63.2% of its steady state value following a steep change in incident radiation or inlet fluid temperature. Thus the time $\tau_{\text{collector}}$ at which the equality for equation 4.5 is reached is the time constant of the collector.

$$\frac{T_{\text{outlet},t=\tau} - T_{\text{inlet}}}{T_{\text{outlet},t=0} - T_{\text{inlet}}} = \frac{1}{e} = 0.368 \quad \text{Equation 4.5}$$

Where $T_{\text{outlet},t=\tau}$ is the collector outlet temperature at $\tau_{\text{collector}}$, $T_{\text{out},t=0}$ is the collector outlet temperature when step change was and T_{inlet} is the temperature of the inlet air.

The ASHRAE (1977) outlines two standard procedures for estimating the collector time constant. The first one consists in operating at nearly steady state conditions with controlled inlet temperature and air flow. The solar radiation is abruptly shut off by shading the collector and decreasing the inlet temperature while air flow remains constant. The second way for estimating the collector time constant consists in changing abruptly the temperature of the inlet fluid from a value well above ambient temperature to a value near the ambient.

Because of the simplicity of the solar collector installation, for technical reasons, the calculation of the time constants was done following the first testing procedure described above.

4.2.4.2.4 Solar data processing

The ideal weather condition for conducting solar collector test was when there was a clear sky and irradiance values were stable for long periods of time. Unfortunately this desirable condition was not frequent in the testing location and irradiance values usually oscillated.

In the performance analysis of the SATS, using instantaneous data values during periods in which irradiance values were not constant could lead to erroneous interpretation of the results. Therefore not all the solar data were valid and a criterion for defining the validity of data points was necessary. When processing the SATS test data, an algorithm was designed to separate the valuable data from raw data.

The valuable data to be considered in further analysis were subject to a condition of stability associated with the time constant of the solar collector, previously calculated. Grassie et al. (2002) suggested that the valuable data selected should satisfy the following condition:

$0.95 < \left| G_{T_i} / G_{T_{i-1\text{min}}} \right| < 1.05$ during at least the interval of time set by the time constant.

Where G_{T_i} is the solar radiation value at any time and $G_{T_{i-1\text{min}}}$ is the previous solar radiation value measured before one minute interval.

During the solar tests, instrument readings were collected into the data logger and later converted into measurements using a data processing spreadsheet programmed in Visual Basic, in detail described in **Appendix A4: SATS**. This program code developed several functions for the SATS data processing and analysis:

1. Transform the raw data from the data logger into temperature, irradiance and RH data.
2. Select the valuable data that met the steady state condition.
3. Generate the $\Delta T - G_T$ curves for the steady state data.
4. Calculate the air flow values using the flow model as a function of irradiance values.
5. Calculate the heat gain and efficiency for the points selected.
6. Model the collector outlet temperature and validate the results with experimental data
7. Calculate the heat losses in the ducting section and calculate the drying temperatures.

Since the air flow was modelled solely as a function of the irradiance and ΔT depends on the air flow and the irradiance. The SATS entails a particular thermal performance in which ΔT was exclusively represented as a function of the solar radiation values.

The analysis of the SATS results consisted in observing the thermal performance ΔT curves, of the SATS when operated with different solar collector configurations. The analysis included the study of the relationship between ΔT and the key factors that govern the thermal performance:

- Wind speed
- Ambient temperature
- Solar collector temperature
- Solar radiation

The ΔT - irradiance curves obtained from each SATS configuration with solar dryer 1 and solar dryer 2 were modelled using a simple mathematical expression. The SATS thermal performance model results were compared with the results obtained from the SATS operation at various weather conditions. A statistical study was conducted to evaluate the accuracy of the thermal model using the statistic parameters presented in section 2.1.6.

4.3 Results

4.3.1 Introduction

In this section the results obtained from the experimental tests conducted to the study of the SATS performance are presented. The results are presented in two sections: the study of the pneumatic characteristics and the study of the thermal characteristics of the SATS.

4.3.2 Pneumatic performance

4.3.2.1 PV driven fan electrical connection

The study of the pneumatic system of the SATS implies the knowledge of the nature of the PV drive fan electrical connection and the factors that govern it. PV

module performance depends on environmental factors such as irradiance, temperature and wind speed, Buresch (1983).

The voltage of the PV module connected to the fan was logged for all the SATS tests conducted. Experimentally a clear dependence of the voltage values on the irradiance was observed. PV module temperature and wind speed affected the operational voltages, however their effect was observed rather low and for a constant irradiance level, the operational voltage yielded was very similar in summer and in winter conditions. Figure 4.11 shows the similarity of two curves that represent the voltage as a function of the irradiance for two different situations: in winter with 8°C ambient temperature and in summer with 20°C ambient temperature.

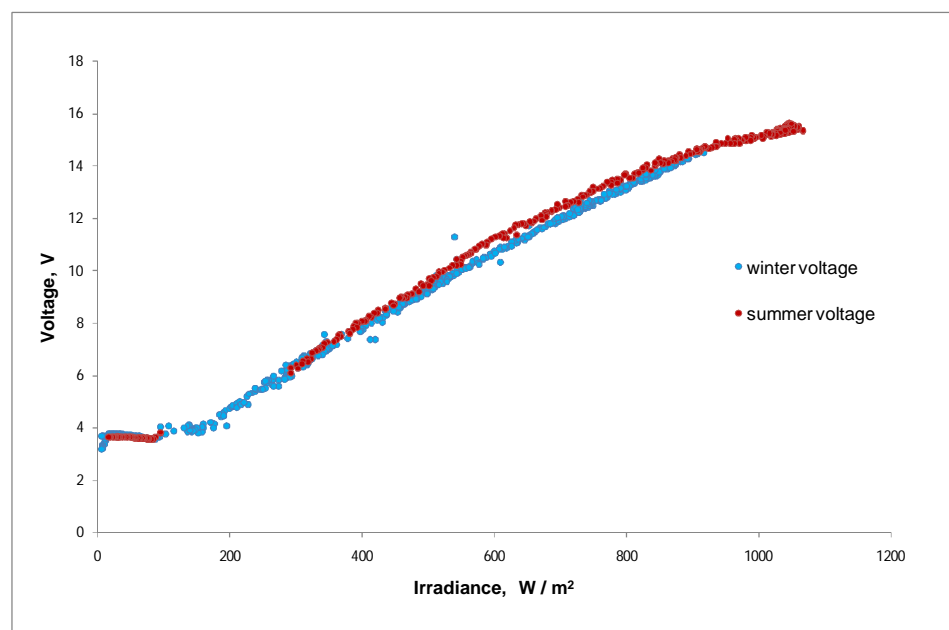


Figure 4.11: PV driven fan voltages as a function of irradiance measured in winter and in summer.

Furthermore, although it can be expected that the maximum PV module power decreases when increasing PV module temperatures, the experimental tests results showed opposite behaviour, in warmer days the fan voltage was slightly higher than in cold days. This fact can be explained by the nature of the electrical PV driven fan connection in which operating points in the I- V curve lay on the top of the curve where I_{CC} is constant in each irradiance value.

Grassie (2006) showed that the relationship between the experimental PV driven fan voltage and irradiance in the operative range can be modelled using the best fit

quadratic equation. Equation 4.6 is the equation that describes the fan voltage data obtained from 10 SATS tests and the corresponding regression coefficient, R^2 , was 0.95.

$$V = -9.5 \cdot 10^{-6} \cdot G_T^2 + 0.0251 \cdot G_T - 0.4694 \quad \text{Equation 4.6}$$

4.3.2.2 Fan Characteristics

The characteristic curves of the fan employed in the SATS were calculated experimentally using the Pitot tube installation for a series of voltages. The characteristic curves of the fan were not strictly required for modelling the air flow. However, they were obtained in order to verify the right functioning of the testing apparatus and to visualize the level of the system pressure drop. Figure 4.12 shows the curves corresponding to 7 voltages considered for the study. Pressure drop values and air flow rates measured experimentally at nominal voltage had a good agreement with the curve provided by the maker. Thus the accuracy of the testing apparatus was guaranteed.

For each voltage, following the procedure of other researchers Grassie (2006) and Stein *et al.* (2008), ΔP - Q curves were described using a fourth order polynomial best fit curve.

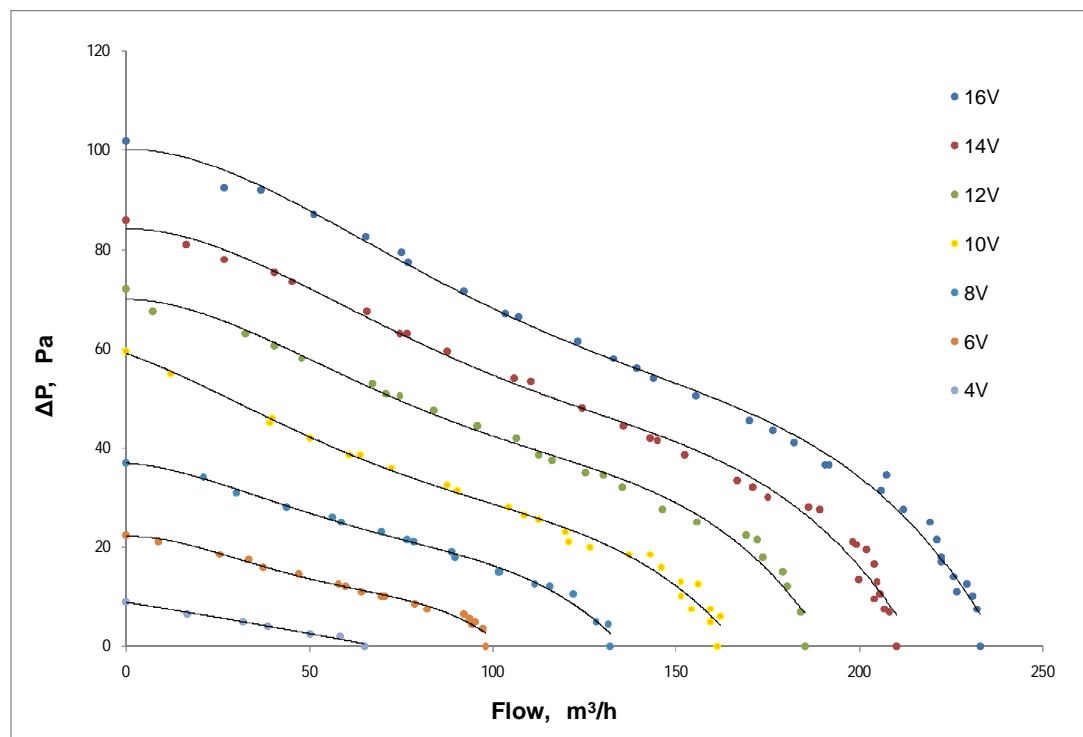


Figure 4.12: Characteristic curves of the fan at 7 voltages.

4.3.2.3 Pneumatic characteristics in the woodchip dryer

The graphics in figure 4.13 and figure 4.14 show the pressure drop introduced by the thin layer and thick layer dryer, dryer 1 and dryer 2 configuration respectively. Pairs of ΔP and air flow rates, ΔP -Q, are plotted forming a quadratic curve associated to each fan voltage. The curves show the pneumatic characteristics in the woodchip dryer with and without a load of woodchip. The graphics show a notable difference between the pneumatic characteristics of the thin and thick dryer systems. When testing the solar

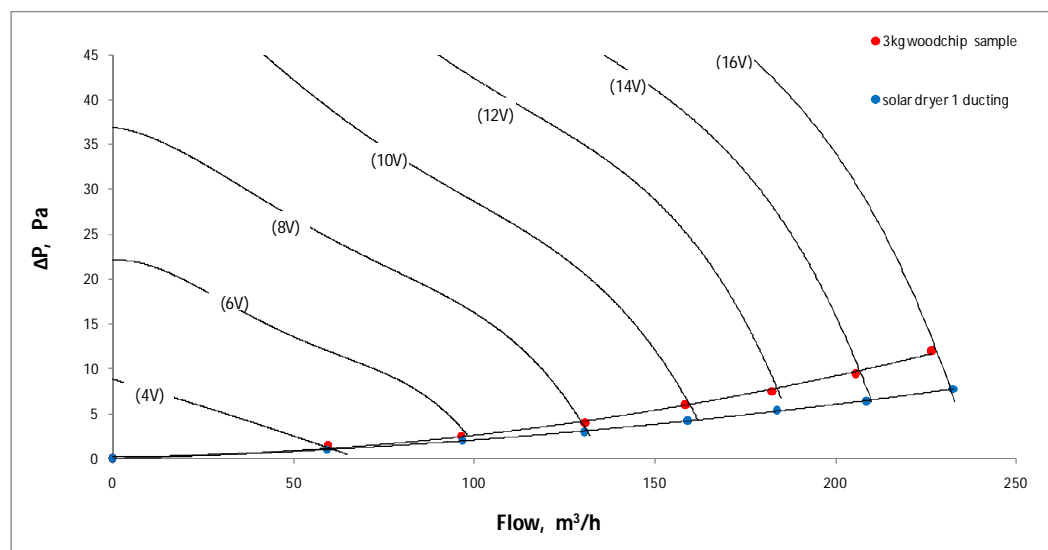


Figure 4.13: ΔP -Q curves obtained from the thin layer dryer, dryer 1.

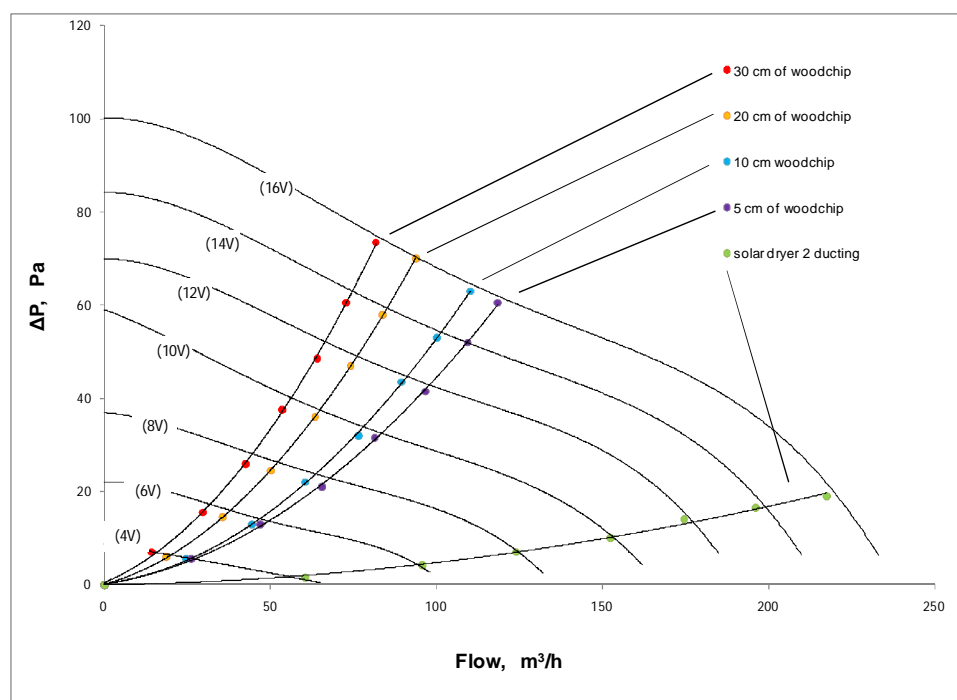


Figure 4.14: ΔP -Q curves obtained from the thick layer dryer, dryer 2.

woodchip dryer operate with free woodchip load, it was considered all the aspects that may affect the pressure drop in the system as the chimney, the ducting tube, optional baffles in the drying box and the effect of the anemometer instrument in the duct. ΔP values measured in both dryer configurations were low: at an air flow of 200m³/h, dryer 1 had 5 Pa and solar dryer 2 had 15 Pa. Loading 3 cm of woodchip layer in the thin layer dryer implied only a little increment of ΔP and hence flow rates were rather high. However, the thick woodchip layers in dryer 2 introduced an important ΔP to the system and as a consequence the air flow was low.

The factors that produce the increment of ΔP in the woodchip dryer can be analysed using the ΔP equation for friction losses in viscous pipes, White (1986), equation 4.7:

$$\Delta P = K_f \cdot \frac{L}{D} \cdot \frac{\rho V^2}{2} \quad \text{Equation 4.7}$$

Where: K_f : is a constant that depends on the woodchip characteristics

D: is a characteristic pneumatic dimension of the tray area.

L: is the height of the woodchip layer

ρ : is the density of the air that changes with air temperature in drying process.

V: is the drying velocity.

The equation confirms that the thick layer dryer configuration, with a small tray area and a deep layer and also operates with high velocities, introduces higher ΔP than in the thin layer dryer configuration.

Moreover, the ΔP curves obtained experimentally when testing 2 different samples of woodchip in dryer 1 or in dryer 2 didn't reflect any appreciable difference. The experiments in dryer 2 were conducted for various layer thicknesses and the woodchip was tested with different MC levels.

4.3.2.4 Pressure drop in the solar air collector

The ΔP -Q curves obtained from all the solar air collector configurations considered in the study are shown in Figure 4.15. The solar air collector was attached to the Pitot testing apparatus. Each collector configuration was tested following the same procedure as before. The graphic shows that:

- The flat plate collector with a fabric absorber introduced less ΔP than any other configuration.
- There was a noticeable difference between the pneumatic characteristics of the 2mm TPC and 3mm TPC.
- The glazing cover introduced pressure drop in the solar air collector and it meant a flow reduction in the system.

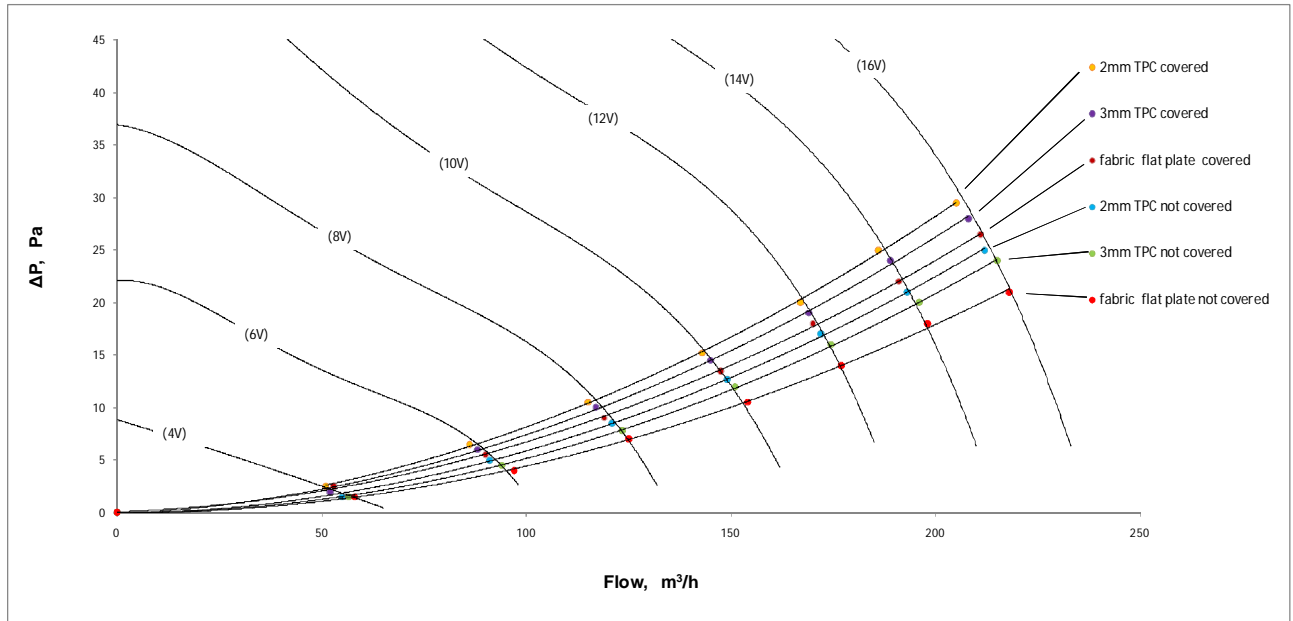


Figure 4.15: ΔP -Q curves obtained from 6 solar air collector configurations in solar dryer 1.

The ΔP -Q curves of the two TPC studied had noticeable differences since the size and the number of holes was different. Table 4.1 showed that theoretically, the TPC with 3 mm hole distribution had lower porosity than in the 2 mm TPC. However when manufacturing the plates, the pneumatic characteristics of the 2 mm hole plate was modified. Probably because of the wrong combination of drilling velocity and the size of the drill when perforating the aluminium plate, a piece of burr was found in many of the holes. This aluminium burr meant a reduction of the holes section, decreasing the porosity of the plate and obstructing the air circulation, increasing the local velocities.

The pressure drop in the TPC configurations was estimated employing the equations given by Kutcher (1995) and Summers (1995) for unglazed TPC, presented in section 2.2.2.3.2. The ΔP -Q curves obtained theoretically are shown in Figure 4.16 along with the experimental ΔP -Q curves measured in the lab. The graphic shows an adequate correlation between predicted and experimental curves for the 3mm TPC. However in the case of the 2mm TPC, the predicted and experiential curves don't fit

because of the obstruction found in many of the TPC holes that modified the TPC porosity.

The calculations revealed that the 90% of the total pressure drop is due to the singular losses caused by the inlet air crossing the holes. Thus the pressure drop in the TPC was found to be heavily dependant on the plate porosity and the hole size. The second relevant contribution, estimated at the 10% of the total pressure drop, was due to the fluid acceleration in the collector plenum. The pressure drop because of the bouyancy effect and the friction between air and plate were practicably negligible.

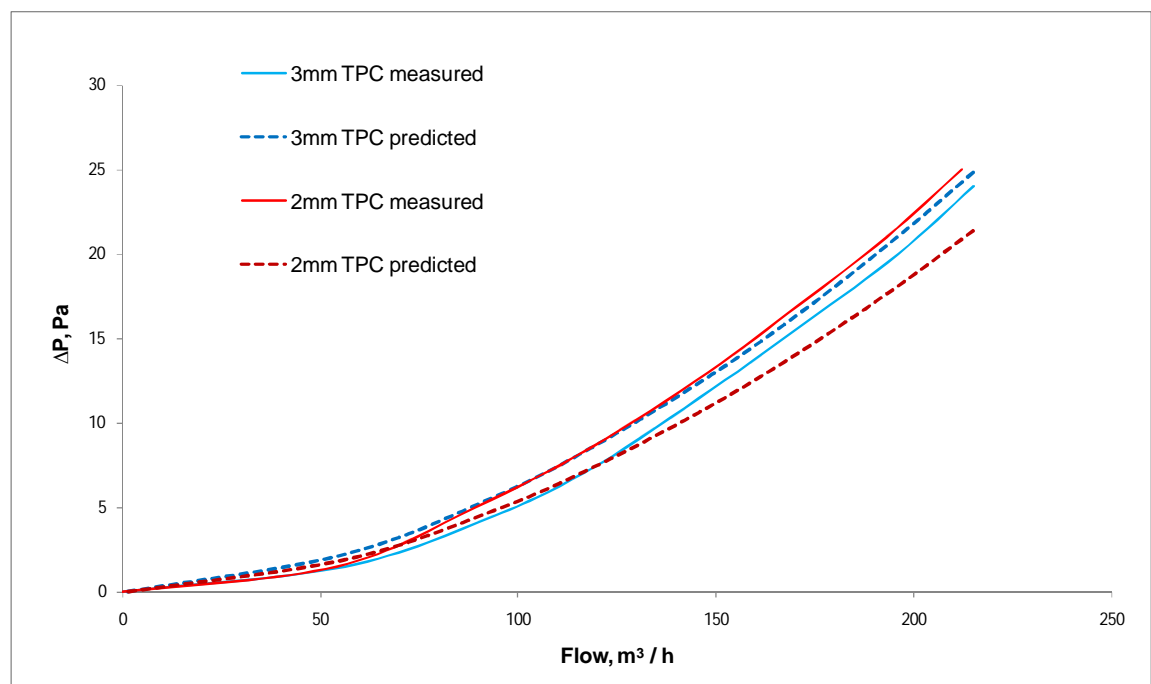


Figure 4.16: Predicted and experimental ΔP -Q curves from 2 unglazed TPCs.

4.3.2.5 Total pressure drop in the system

The original woodchip solar dryer configurations were mounted in the lab in order to study their pneumatic characteristics. Figure 4.17 and figure 4.18 shows the ΔP -Q curves obtained from the solar dryer 1 and solar dryer 2 respectively. ΔP -Q curves always described quadratic profiles. There were notable differences between the pneumatic behaviour of the dryers studied: For the same PV driven voltage, solar dryer 1 yielded air flow rates considerably higher than in solar dryer 2. At 16V fan voltage, the solar dryer 1 operates with air flows of 200 m³/h, whereas the fan in solar dryer 2 delivers less than 100 m³/h, half of its air flow capacity at free load.

The pressure drop obtained in the thick dryer was considerably high and this critically affected the performance of the solar dryer 2. Air flow rates were low and therefore high outlet temperatures were expected from its SATS thermal performance.

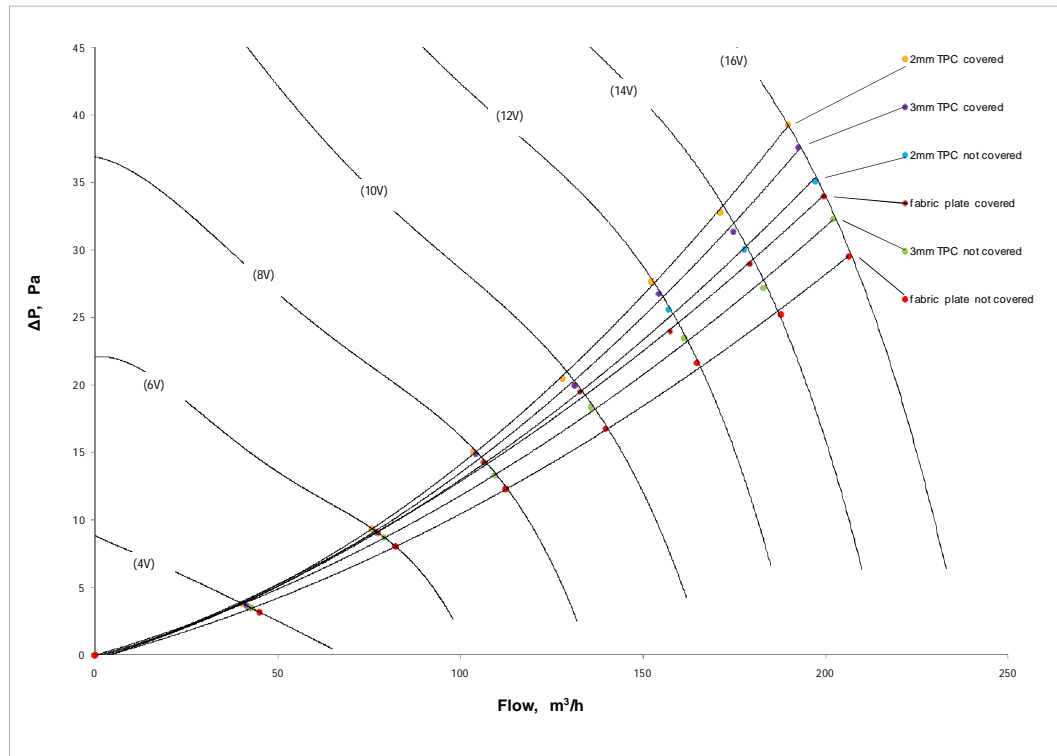


Figure 4.17: ΔP -Q curves obtained from 6 solar air collector configurations with dryer 1.

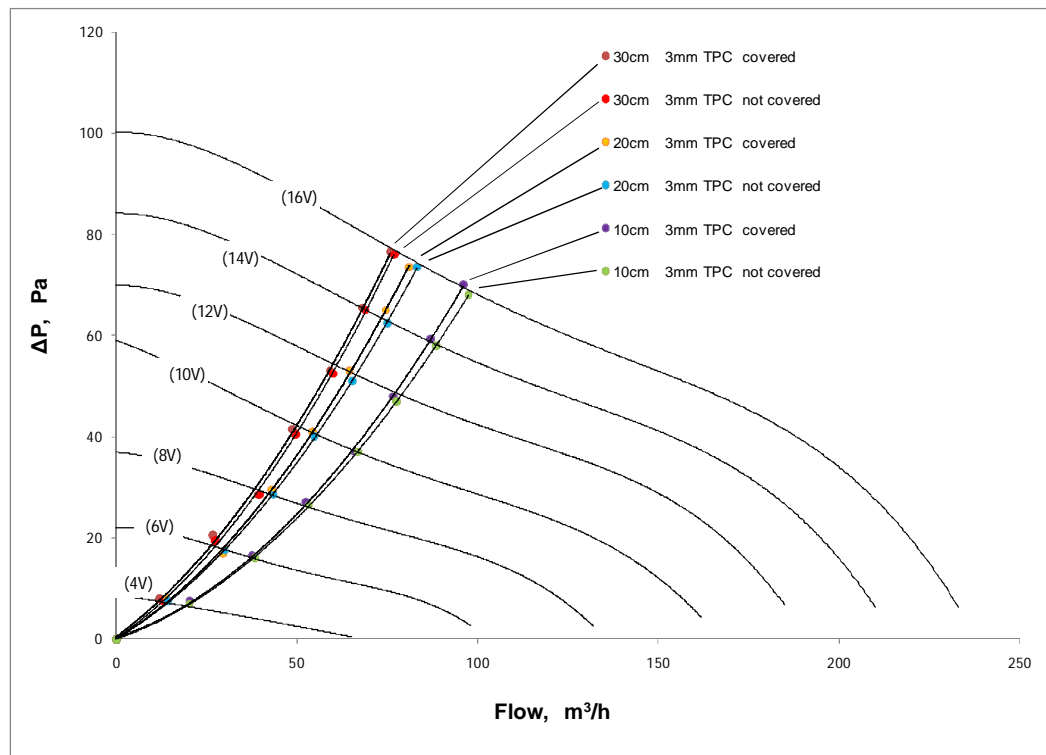


Figure 4.18: ΔP -Q curves obtained from 2 solar air collector configurations with dryer 2.

4.3.2.6 Modelling the air flow

In the previous section, the pressure drop was analysed through each part of the solar woodchip dryer. Thus, for each possible woodchip dryer – collector configuration, it is possible to estimate the air flow rates as a function of voltage. Considering that operational voltages from the 10W PV panel driven and the 5W fan connection were described as a function of irradiance values, air flow rates in the SATS were calculated and modelled exclusively as a function of irradiance. The air flow in each solar dryer configuration was modelled with a quadratic function. Table 4.3 and table 4.4 show the air flow model equation and the threshold irradiance values for solar dryer 1 and solar dryer 2.

Table 4.3: Air flow in solar dryer 1 with 6 collector configurations

n	Collector configuration	Air flow equation (m ³ /h)	G _T threshold (W/m ²)
1	2mm TPC - not covered	$Q = -1.7539 \cdot 10^{-4} \cdot G_T^2 + 0.397 \cdot G_T - 20.4$	170
2	2mm TPC - covered	$Q = -1.6810 \cdot 10^{-4} \cdot G_T^2 + 0.382 \cdot G_T - 19.7$	195
3	3mm TPC - not covered	$Q = -1.7969 \cdot 10^{-4} \cdot G_T^2 + 0.408 \cdot G_T - 20.2$	170
4	3mm TPC - covered	$Q = -1.7148 \cdot 10^{-4} \cdot G_T^2 + 0.388 \cdot G_T - 20.0$	190
5	Flat plate - Fabric- not covered	$Q = -1.9095 \cdot 10^{-4} \cdot G_T^2 + 0.430 \cdot G_T - 26.4$	165
6	Flat plate - Fabric - covered	$Q = -1.6550 \cdot 10^{-4} \cdot G_T^2 + 0.382 \cdot G_T - 18.5$	180

Table 4.4: Air flow in solar dryer 2 with 2 collector configurations

n	layer thickness	Collector configuration	Air flow equation (m ³ /h)	G _T threshold (W/m ²)
1	10 cm	3mm TPC - not covered	$Q = -0.8797 \cdot 10^{-4} \cdot G_T^2 + 0.2011 \cdot G_T - 17.1$	290
2	10 cm	3mm TPC - covered	$Q = -0.9056 \cdot 10^{-4} \cdot G_T^2 + 0.2028 \cdot G_T - 17.5$	290
3	20 cm	3mm TPC - not covered	$Q = -0.7650 \cdot 10^{-4} \cdot G_T^2 + 0.1771 \cdot G_T - 18.6$	310
4	20 cm	3mm TPC - covered	$Q = -0.7502 \cdot 10^{-4} \cdot G_T^2 + 0.1753 \cdot G_T - 18.8$	310
5	30 cm	3mm TPC - not covered	$Q = -0.6846 \cdot 10^{-4} \cdot G_T^2 + 0.1611 \cdot G_T - 17.2$	330
6	30 cm	3mm TPC - covered	$Q = -0.7008 \cdot 10^{-4} \cdot G_T^2 + 0.1629 \cdot G_T - 18.4$	330

The irradiance threshold associated to the fan-motor stall characteristics was measured experimentally for each solar dryer configuration. As it was discussed in the literature review, two voltages defined the stall conditions of the fan-motor: the starting and the stalling voltages. However, when pneumatic characteristic of the fan was tested, the difference between these voltages was negligible and therefore only one irradiance threshold value was taken. Because of the high pressure drop in solar dryer 2, the irradiance threshold values were notably higher than in solar dryer 1, as table 4.3 and table 4.4 shows.

This limiting factor was a key factor in the woodchip solar dryer performance. Therefore solar dryer 1 with lower threshold irradiance values was expected to work longer periods than the solar dryer 2, especially considering the poor weather conditions of the location.

Figure 4.19.a shows the air flow values as a function of the solar radiation obtained from the performance of the solar dryer 1 comprising a 3 mm unglazed TPC. The graphic shows a good correlation between various air flow measurements and predicted data. Figure 4.19.b shows the profile of irradiance values and air flow predicted values during a SATS test. The fan performance is characterised by continuous fluctuations proportional to the solar radiation as voltage levels were sensitive to irradiance changes. The transient regime of the fan operation was not included in the study although a quick response to changes was always observed.

The fan operation shifted from stalled to starting conditions and vice versa when solar radiation values oscillated around the irradiance threshold. This behaviour was

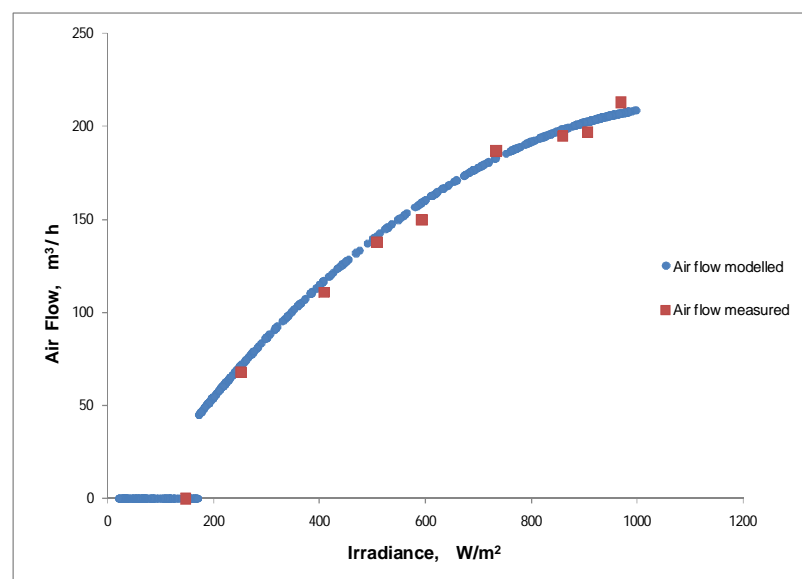


Figure 4.19.a: Flow vs irradiance curve for 3mm TPC in solar dryer 1

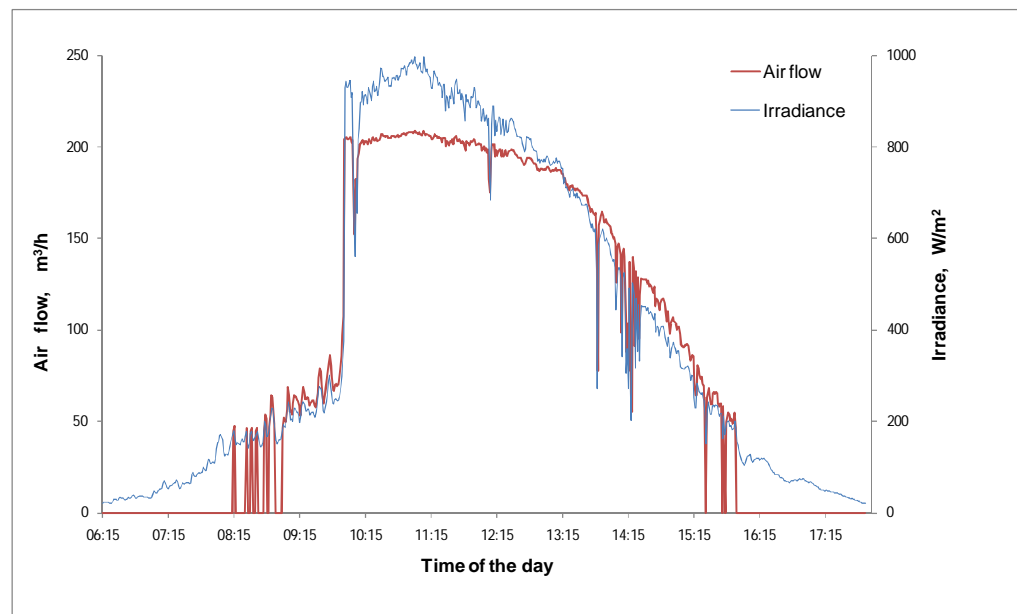


Figure 4.19.b: Irradiance data and air flow predicted values in solar dryer 1 during a test.

observed particularly early in the morning or late in the afternoon. Fatigue effects derived from continuous voltage fluctuations and starting/stalling oscillations may affect to the lifespan of the fan.

Figure 4.20.a and figure 4.20.b shows the results of modelling the air flow in solar dryer 2 comprising a 3mm unglazed TPC and a 20 cm thick layer. The modelled curves show good agreement with the experimental air flow measurements. Despite the air flow rates being low: $81 \text{ m}^3/\text{h}$ at $1,021 \text{ W}/\text{m}^2$ and the irradiance threshold, $302 \text{ W}/\text{m}^2$, was rather high, the pneumatic model described with satisfactory accuracy the air flow during the SATS test.

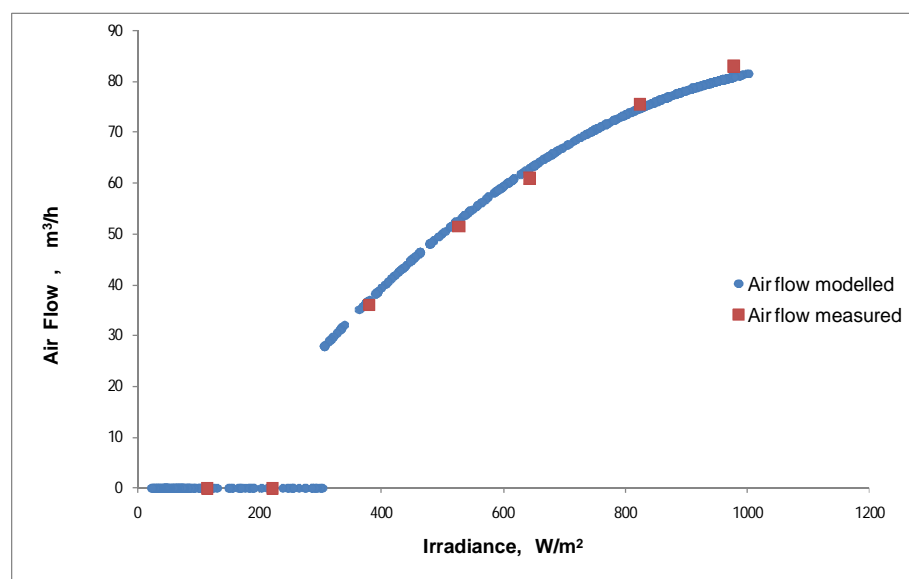


Figure 4.20.a: Flow vs irradiance curve for 3mm TPC in solar dryer 2

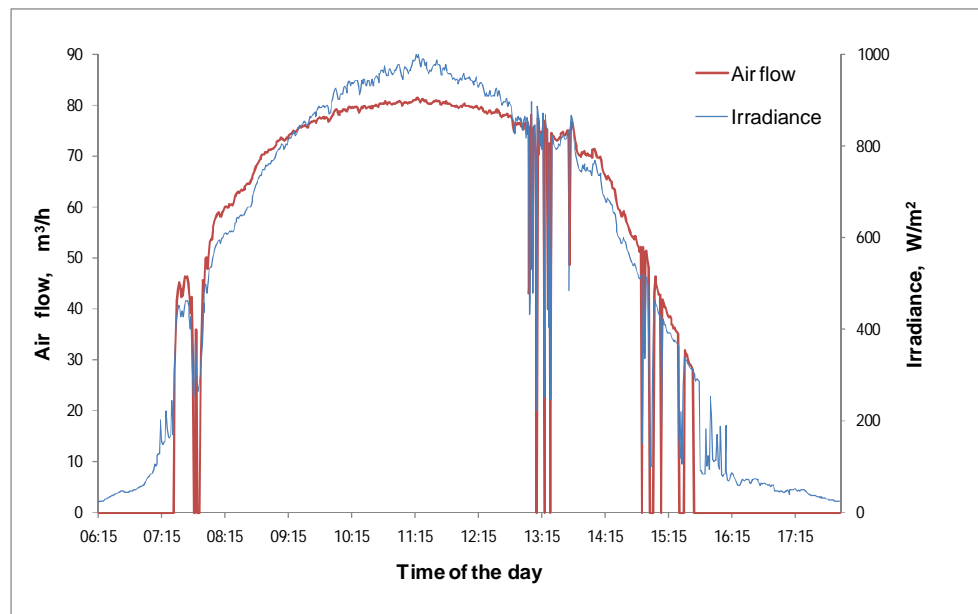


Figure 4.20.b: Irradiance data and air flow predicted values in solar dryer 2 during a test.

The air flow in the SATS was modelled using a simple expression. Although the experimental and the predicted air flow values have a satisfactory correlation, there is an error derived from various assumptions taken in the analysis. They are summarised below:

- The PV driven fan operation voltage was modelled as a function of irradiance without considering the effect of the PV plate temperature or the wind speed.
- The air density effect in the fan and system ΔP -Q curves was not taken into account when calculating the air flow at field conditions.
- The air flow in the SATS may be altered by the wind conditions that create local pressure differences that affect the average air flow circulating the system.
- Since the model is based on experimental results, the predicted flow rate is expected to have some error. Considering all sources of error in measurements such as voltage, irradiance, air flow velocity and pressure drop, the model predicts the voltage of the PV driven fan with an error of 3% and a flow rate with a maximum error of 7% for any of the solar woodchip dryer configurations.

4.3.3 SATS thermal performance results

The thermal performance of the SATS was studied for various collector configurations. All the results shown in this section are based on outdoor experimental work. The SATS tests were conducted under different weather conditions during a period of a year in order to obtain representative data of the SATS performance.

However there were not many days with stable irradiance and stable weather conditions and this influenced the testing schedule and even the quality of the results.

The results presented in this section can be summarised as follows:

- Estimation of the collector time constant for the glazed and unglazed TPC
- Study of the thermal performance of the SATS connected to the thin layer dryer when operating with 6 different collector configurations.
- Study of the thermal performance of the SATS connected to the thick layer dryer configurations operating with 2 different TPC configurations.
- Analysis of the key parameters that intervenes in the SATS performance.
- Modelling the SATS performance for all the cases previously studied.

4.3.3.1 Time constant

The time constant of the TPC was obtained from solar tests conducted in a clear sky day at noon. Irradiance was high at “full sun” conditions and there was no appreciable wind. Temperature and solar radiation readings were logged in 10 second intervals. At the beginning of each test, the SATS operated on steady state regime for a prolonged period of time under constant conditions. The incident solar radiation was abruptly reduced to zero by shielding the collector from the sun. The PV module remained uncovered, thus the fan kept functioning supplying the same level of air flow rate. Collector inlet and outlet air temperatures were continuously monitored until they reached a new steady state. Air flow rate was measured before and during the process.

The same procedure was followed in the reverse way: starting with the collector shielded and PV driven fan functioning with a high flow rate, the cover was removed from the collector and outlet temperature increased until reaching the steady state.

Figure 4.21.a and figure 4.21.b show the results of the collector time constant tests that correspond to the 3 mm unglazed TPC. The graphics show a difference between the transient of the heat transfer process when the solar collector is cooled down and warmed up: In a step decrease in irradiance, initially the air in the collector and the components were at the maximum temperature achievable, for the corresponding test conditions. When the collector was shielded, inlet air at ambient temperature circulated through the collector mixing with the existing warm air in the plenum. It also removed the heat stored by the parts of the collector including the heat collected by the absorber plate. The heat transfer transient was quick in the beginning and $\tau_{\text{collector}}$ was 1 minute

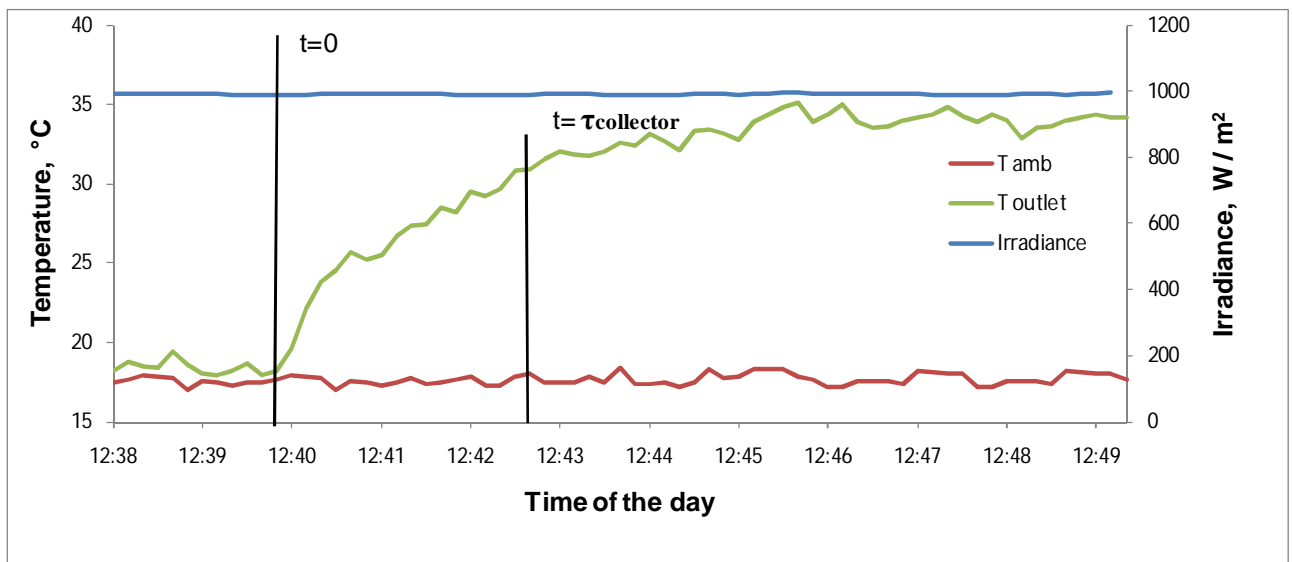


Figure 4.21.a: Heat transfer transient due to a step increase in irradiance for a SATS with 3mm TPC.

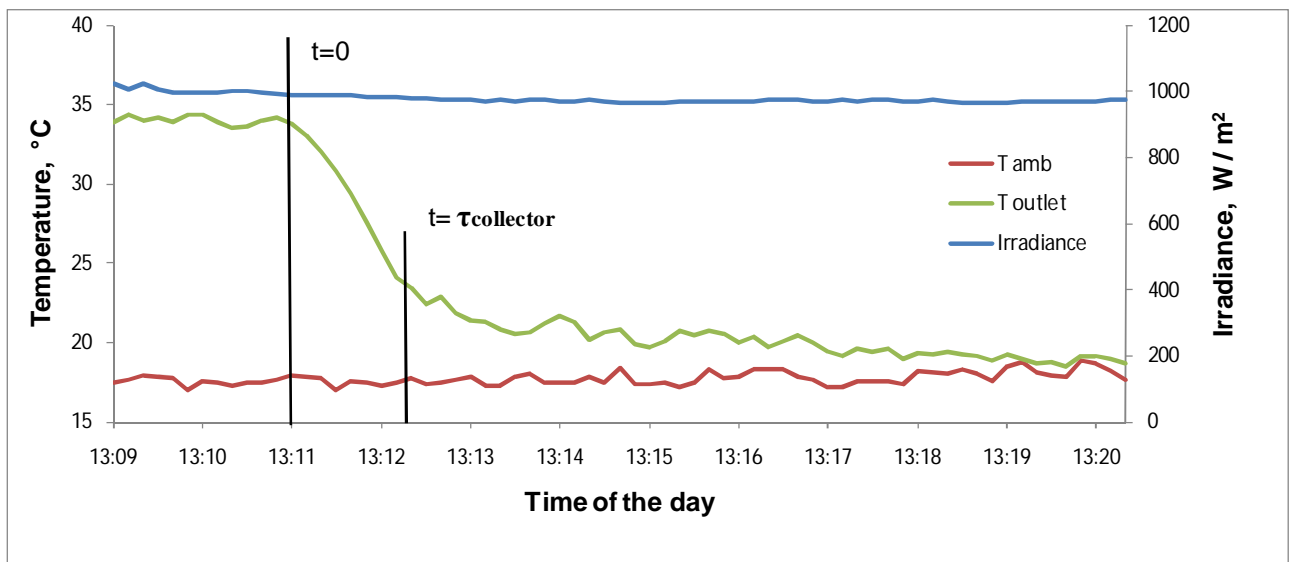


Figure 4.21.b: Heat transfer transient due to a step decrease in irradiance for a SATS with 3mm TPC.

and 20 seconds. However, the time to reach the steady state was much longer, around 9 minutes. A similar transient time was observed in a step increase in irradiance test for the same collector. However, in this case $\tau_{\text{collector}}$ was found to be higher than before, 2 minutes and 50 seconds. Despite the air flow and the energy increment theoretically being the same in both tests, heat transfer transient was different. The gradient of temperatures experimented in the beginning of the second test were not as high as in the first test. Solar collector parts and plenum air were initially at ambient temperature and gradually increased their temperature using the heat from the inlet heated air. Outlet air flow gradually increased its temperature as the collector warmed up. Moreover, in a step

increment in irradiance, heat losses in the system made longer the transient, while in the reverse way heat losses contributed to decrease the transient time.

The time constants obtained from two collector configurations are shown in Table 4.5. The $\tau_{\text{collector}}$ values were longer when adding a glazing cover to the TPC since the thermal mass or air volume in the collector was larger and therefore more time was required to reach the steady state.

Table 4.5: $\tau_{\text{collector}}$ test results for a 3mm TPC covered and uncovered.

n	Collector plate	test	Irradiance	Q_{initial}	Q_{final}	$\tau_{\text{collector}}$	Transient time
1	3mm TPC, not covered	step decrease in G_T	1000 W/m ²	200 m ³ /h	200 m ³ /h	1' 20sec	8 min
2	3mm TPC, not covered	step increase in G_T	1000 W/m ²	200 m ³ /h	200 m ³ /h	2' 50sec	11 min
3	3mm TPC, not covered	step decrease in G_T	1000 W/m ²	200 m ³ /h	100 m ³ /h	3' 10sec	15 min
4	3mm TPC, not covered	step decrease in G_T	1000 W/m ²	200 m ³ /h	70 m ³ /h	4' 10sec	20 min
5	3mm TPC, covered	step decrease in G_T	1000 W/m ²	190 m ³ /h	190 m ³ /h	2' 10sec	10 min
6	3mm TPC, covered	step increase in G_T	1000 W/m ²	190 m ³ /h	190 m ³ /h	3' 50sec	14 min
7	3mm TPC, covered	step decrease in G_T	1000 W/m ²	190 m ³ /h	100 m ³ /h	4' 20sec	20 min

The collector time constant values were used as a reference for defining the minimum interval of time required in the analysis of the steady state data. However, in the SATS performance, in the SATS transient, a step in irradiance also implied a step in air flow and in air temperature, increasing the complexity of the thermal analysis. The transient of the step increase in irradiance was well described by the experimental test as the step increase in air flow was also included. However, the step decrease in irradiance tests did not show the expected SATS response: the collector, initially uncovered was shaded and the fan was forced to operate at certain air flow rate, forcing air to circulate through the collector. Thus for the tests 3, 4 and 7 in table 4.5, the step decreasing in irradiance implied a step decreasing in air flow, increasing the time constant.

Thus, the interval of stability taken for the selection of the solar collector test data for the collector analysis was the rounded major time constant registered. Then 5 minutes was estimated as the minimum period of time required for processing solar test data under stable steady conditions with nearly constant irradiance values.

4.4.3.2 SATS thermal performance

In the previous section, it was discussed that the SATS has a unique operation regime since the description of the PV driven fan performance was simplified and air flow rates depended on irradiance. Thus the heat gain by the collector and the temperature increments, ΔT , were also estimated as a function of the solar radiations.

4.4.3.2.1 SATS with a TPC thermal performance

Figure 4.22 and figure 4.23 present the SATS performance during two consecutive days when working with an unglazed and glazed 2mm TPC respectively. Tests were conducted on 13/03/09 and 14/03/09, days in which the weather was predominantly sunny and cold.

In each solar test, ΔT values were plotted as a function of irradiance forming a scattered cloud of points with a high degree of dispersion. The majority of these points reflected the transient regime and they were not valid for the analysis of the SATS thermal performance. Therefore using a data selection algorithm, few ΔT - G_T points were selected based on the steady state criterion. The points selected showed a proportional relation between ΔT values and irradiance.

When the SATS performance experienced a step in irradiance, the outlet temperatures were affected by the change in the amount of heat input and by the change in air flow rate. Thus a step in irradiance increment meant also an increment in air flow, implying quicker transient response and vice-versa. As a consequence, the SATS performance had a slow and a quick transient behaviour that were reflected in the profile of collector outlet temperatures. For instance, having initial clear sky conditions, when a cloud suddenly shielded the SATS both heat input and air flow dropped. Then collector outlet air temperature decreased slowly as the result of mixing a small inlet air flow at ambient temperature and the warm air in the collector. Inversely, when the shaded collector cleared out, the SATS experienced an increment in heat and flow, so outlet temperatures were dominated by the heated inlet flow and not by the air remaining in the plenum.

Figure 4.23.a and figure 4.23.b show the thermal performance of the SATS having a glazed 2mm TPC. The glazing cover in the solar collector reduced the heat losses of the SATS and therefore increased the efficiency of the solar air collector. The maximum outlet temperature registered was 35.5°C and the maximum ΔT was 21°C for 930 W/m².

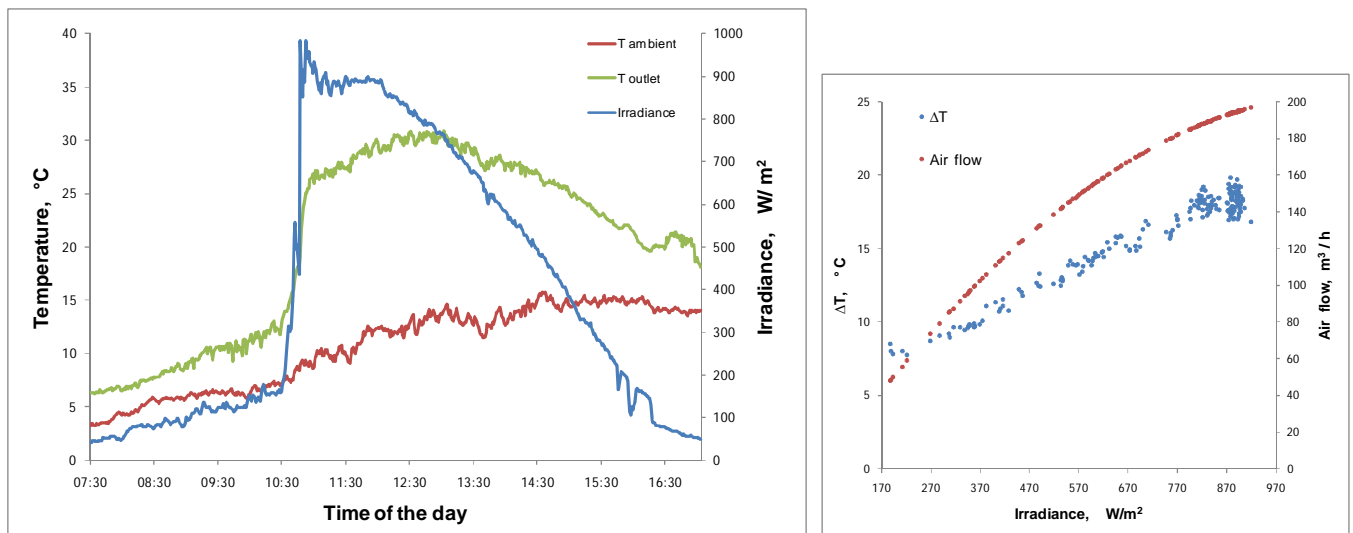


Figure 4.22.a and figure 4.22.b: Thermal performance of SATS with 2mm unglazed TPC.

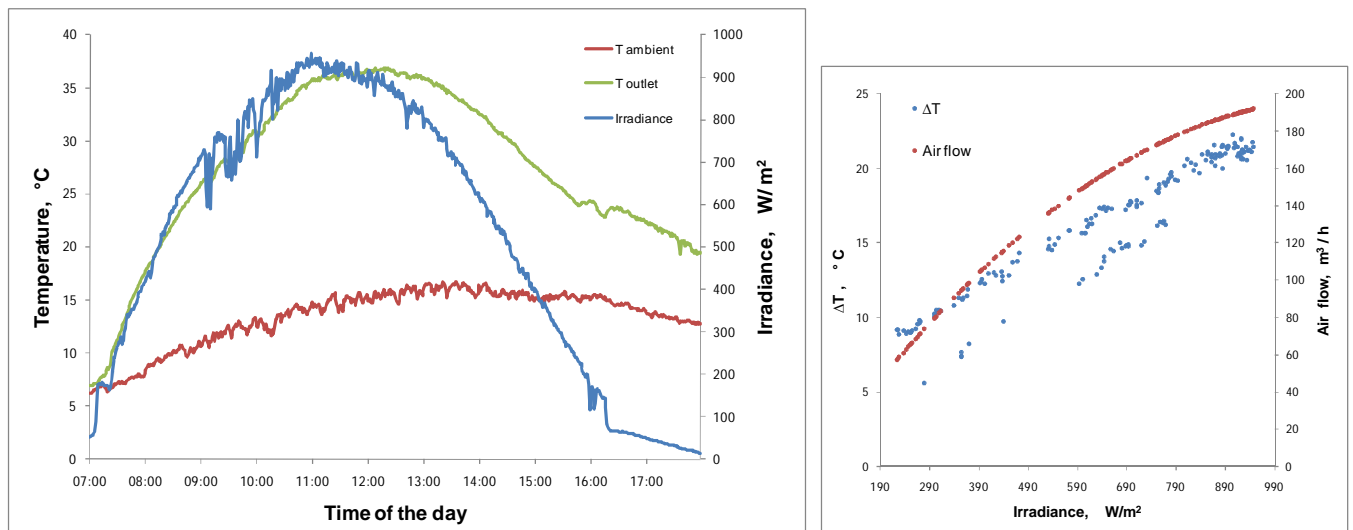


Figure 4.23.a and figure 4.23.b: Thermal performance of SATS with 2mm TPC using glazing cover.

In general, the SATS comprising a glazed TPC yielded higher outlet temperatures for all the range of irradiance due to the reduction in heat losses.

Another relevant consideration, observed from the majority of experimental SATS tests results, is a dual thermal behaviour due to morning and afternoon testing conditions: Observing figure 4.23, the irradiance data curve presented a symmetrical shape in a day with almost clear sky conditions. However, in the ΔT - G_T graphic, 2 lines of points were obtained from a SATS test since morning ΔT data were lower than afternoon ΔT . In the morning, the useful heat transferred to the inlet air was employed to warm up the air in the plenum and collector parts that were initially at ambient temperature. However, in the afternoon, the solar air collector parts were already warmed up and inlet air received the heat collected by the absorber was mixed with the plenum air already warmed air.

Therefore, morning $\Delta T - G_T$ curve started near 0°C for 0 W/m^2 as collector was at ambient temperature when there is no solar radiation. Morning and afternoon $\Delta T - G$ data converged to the point of maximum irradiance.

$\Delta T - G$ curves also show the ΔT points in which irradiance values were lower than the threshold in which the fan starts operating. These points, near the origin of coordinates, correspond to the early morning or late evening data and were not valid for the analysis of the thermal behaviour of the SATS.

Figure 4.24 and figure 4.25 present the SATS performance during two consecutive days when working with an unglazed/ glazed 3mm TPC respectively. Tests were conducted on 02/04/09 and 03/04/09, weather in those days was predominantly sunny and there was a gentle breeze of air with appreciable wind speeds that reached 3 m/s.

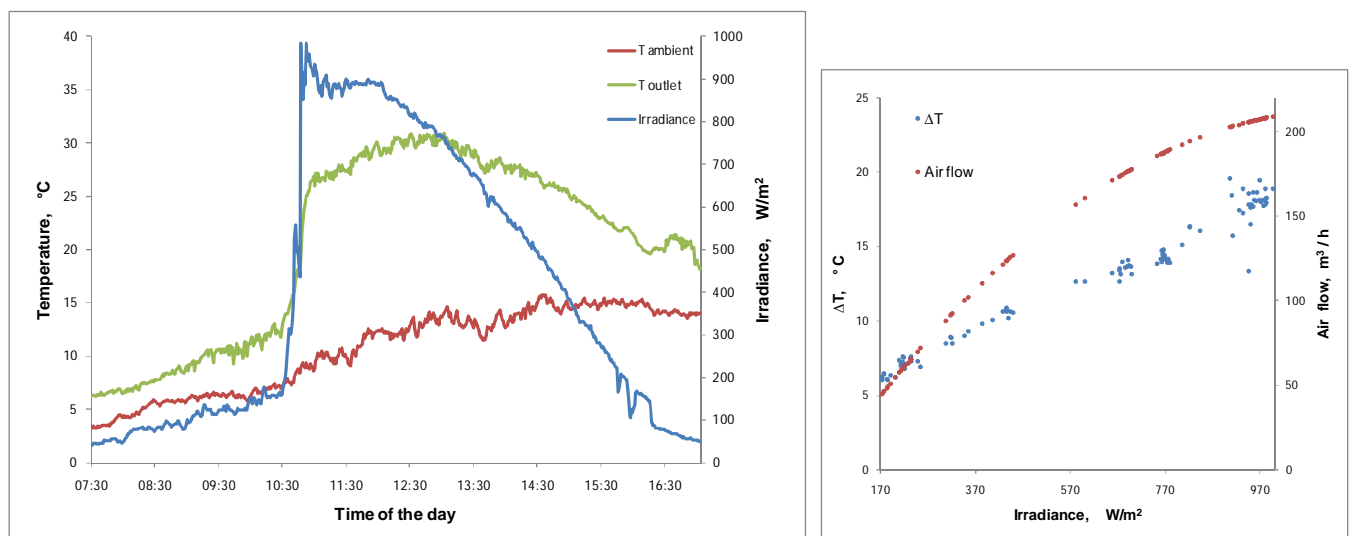


Figure 4.24.a and figure 4.24.b: Thermal performance of SATS with 3mm unglazed TPC.

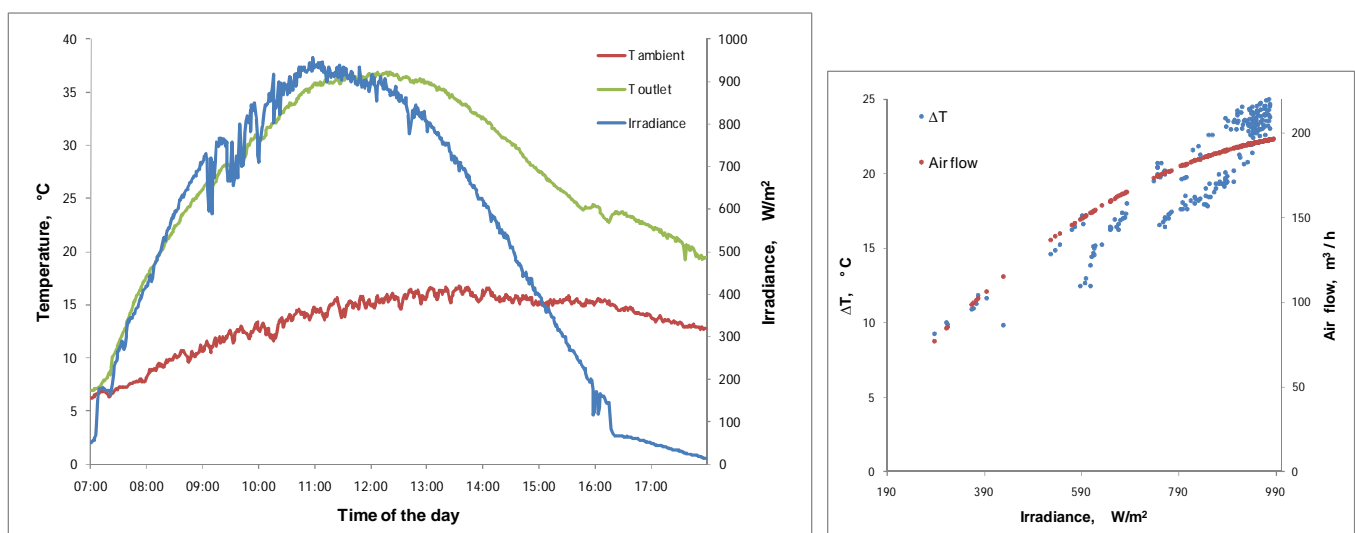


Figure 4.25.a and figure 4.25.b: Thermal performance of SATS with 3mm TPC using glazing cover.

Outlet temperature profiles and $\Delta T-G_T$ curves were similar to the ones obtained from the SATS with the 2mm TPC tests. Maximum collector outlet temperatures were 31°C and 39°C corresponding to the 3mm TPC with and without glazing cover respectively.

The graphics show oscillations in the irradiance values which described periods of time in which cloud spells shaded the SATS. The clouds movement was reflected in the curves as irradiance peak values.

4.4.3.2.2 Difference between 2mm and 3mm TPC

The performance of the SATS was compared when operated with a different TPC configuration. Thus the SATS operating with an unglazed 3mm TPC yielded collector ΔT similar or slightly lower than the SATS when operating with an unglazed 2mm TPC in the same conditions.

The difference in the SATS thermal performance was attributed to the difference in

- hole distribution in the transpired plate collector.
- flow rate or collector air sucking velocity.

The geometry of the absorber plate affects the heat exchange effectiveness between the TPC and the inlet air. The size of the hole and the pitch distance combination defines the collector porosity that directly affects the TPC performance and therefore the SATS performance too. In a particular TPC configuration, any change in perforation diameter affects the heat exchange only moderately. For a constant air flow, reducing the pitch distance has a notable benefit on the heat exchange effectiveness as there is less tendency to develop hot spots between perforations, Leon et al. (2007).

On other hand, the TPC heat transfer is strongly affected by the stream of air that approaches the hole, sucking the thermal boundary layer over the plate into the plenum. The higher air flow and higher approaching velocity are, the more efficient the heat transfer is and better efficiencies are.

The comparison of the SATS thermal performance results didn't show any outstanding difference in the TPCs thermal performance since the TPCs employed had a similar geometry. However the interpretation of the results helped to understand the thermal behaviour.

Experimentally, for the same irradiance levels, the SATS with the unglazed 3mm TPC yielded higher flow rates than with the unglazed 2mm TPC. Despite the air flow

difference being small, the amount of warmed air in the thermal boundary layer sucked in was higher.

In general, ΔT values for both collector configurations were slightly higher in the 3mm TPC because at the same irradiance level, a higher heat gain difference was compensated with a higher flow.

When the SATS operated with a glazed TPC, figure 4.23 and figure 4.25.b, there was no noticeable difference between the ΔT curves. The small difference observed in the performance of the collectors was again associated to the air flow - irradiance relationship. Environmental factors such as wind and ambient temperature had smaller effects than in unglazed plate configurations.

4.4.3.2.3 Flat plate - fabric collector performance

Figure 4.26 and figure 4.27 show the thermal performance of the SATS operating with a flat plate collector with an absorber plate made of polythene fabric. The tests were conducted with the collector uncovered and covered on 31/05/09 and 01/06/09 respectively.

The optical characteristics of the polythene were not good since the plate had a glossy texture. Thermal characteristics were not favourable either as polythene has low conductivity. This may imply a temperature distribution in the collector surface with possible hot spots and consequent radiation losses. Moreover, bare flat plate collectors are not as effective as TPC as heat losses by convection on the top surface are very high.

Because of the favourable testing conditions, the maximum collector outlet temperatures reached were relatively high: 45°C and 35°C when collector was covered and uncovered respectively. ΔT values obtained were reasonably high considering that the fabric absorber collector yielded higher flow rates than other collector configurations.

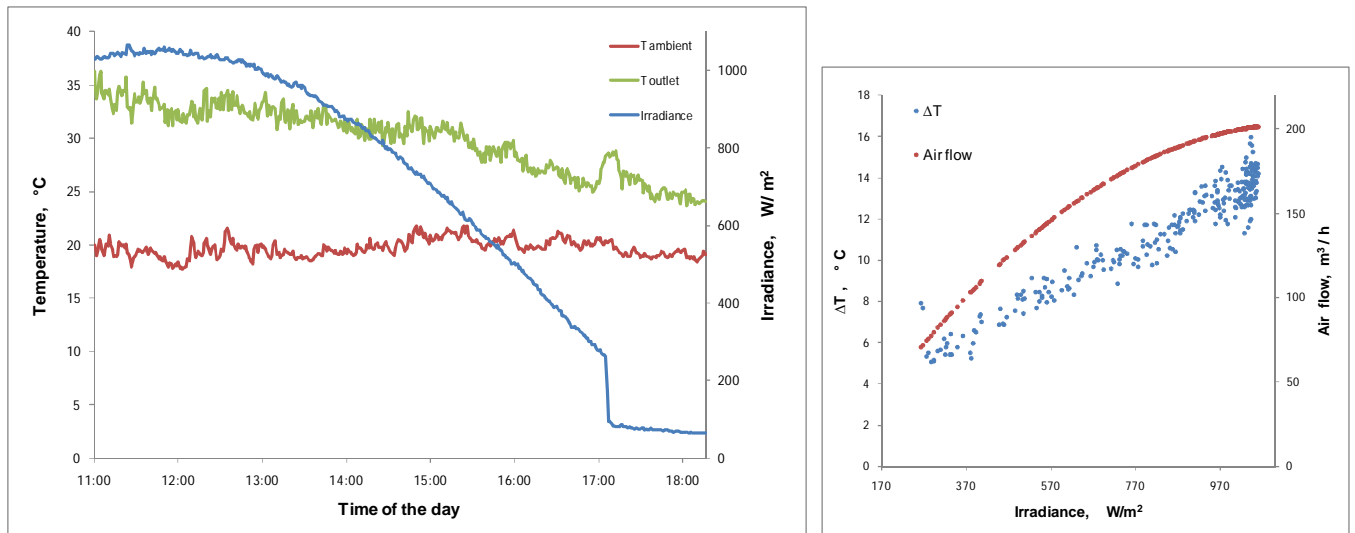


Figure 4.26.a and figure 4.26.b: Thermal performance of the SATS with a flat plate made of fabric.

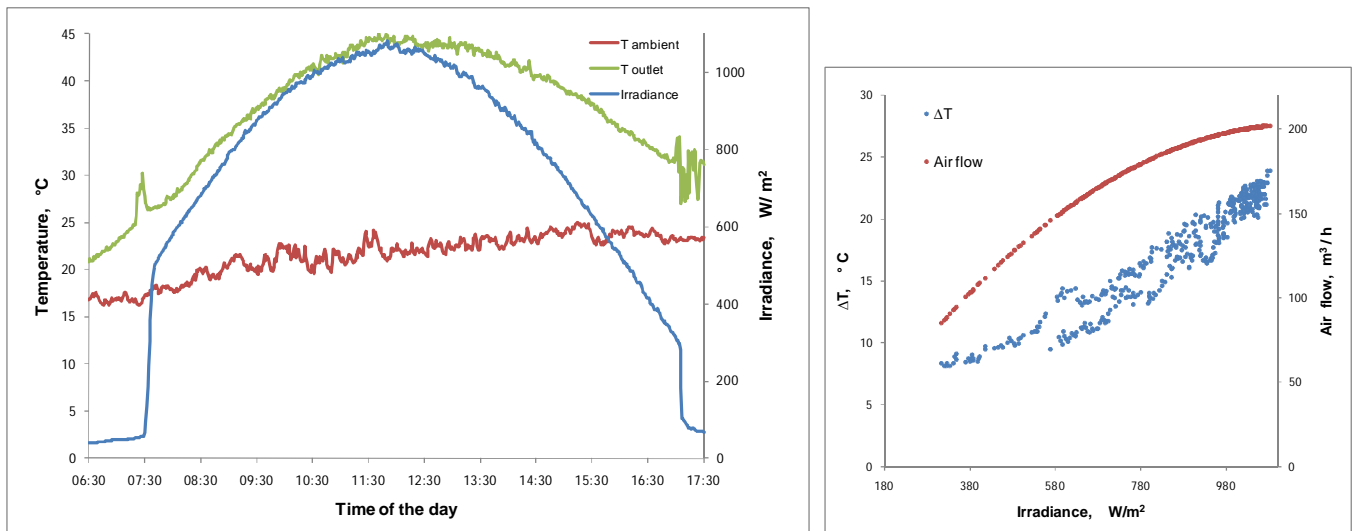


Figure 4.27.a and figure 4.27.b: Thermal performance of the SATS with a flat plate collector made of fabric and with glazing cover.

4.4.3.2.4 SATS thermal performance when working along with dryer 2.

The following set of graphics, from figure 28 to figure 33, shows the thermal performance of the SATS operating with the 3mm TPC. The SATS was connected to the thick layer dryer and the performance of the SATS was tested for three different layer thicknesses of woodchip: 10cm, 20cm and 30cm creating various air flow conditions. The SATS tests were conducted in the month of June 2009.

The SATS inlet air flow experienced an important reduction due to the high pressure drop introduced by the thick dryer. As the SATS operated with much lower flow rates, it was expected that the TPC operated with high temperatures, increasing

both convective and radiant heat losses to the ambient, and therefore decreasing solar collector efficiency.

Because of the high pressure drop introduced by the dryer, the collector air flow was low. This meant a reduction in the negative pressure to suck the air surrounding the transpired plate holes. Air flow approaching the holes was in a laminar regime and Reynolds numbers across the holes were estimated low, lower than 700. As a consequence, the heat transfer was not adequate: fluid and thermal boundary layers thicknesses were thicker, causing notable negative effects in the thermal performance of the transpired plate.

TPC thermal performance depended on the inlet air sucking the thermal boundary layer through the holes into the plenum. Kutscher (1994) stated that for an approaching velocity higher than $110\text{m}^3/\text{h m}^2$, 25 Pa of negative pressure across the absorber plate is required to ensure the absorption of the thermal boundary layer is sucked through the holes. Thus, a lower negative pressure through the collector due to the high pressure in the dryer system meant less amount of warm air surrounding the absorber being sucked in. The convective heat losses to ambient were appreciably higher in the thick layer configuration. Moreover, as there was less amount of heat evacuated by the inlet air, the collector plate reached high temperatures, increasing the radiant heat losses from the absorber.

Wind effects were more noticeable when the TPC operated with low air flow as the thermal boundary was thicker and therefore the action of the wind removing heated air was more effective. Furthermore, the solar air collector parts presented high temperatures which meant high heat losses through the collector frame to ambient.

The glazing cover helped to reduce the convection heat losses from the top of the absorber plate to ambient and the wind effects. Thus, the glazing enhanced the SATS thermal performance obtaining better efficiencies when TPC is working with low flow rates. The heat collected between the glazing cover and the absorber plate may raise the air temperatures implying high absorber temperatures with its consequent radiant losses.

For instance, the SATS with a covered 3mm TPC, operating with the 30 cm thick woodchip layer dryer at full sun conditions yielded an air flow of $75\text{ m}^3/\text{h}$. At this condition, the maximum outlet temperature registered was 82°C and ΔT was 65°C .

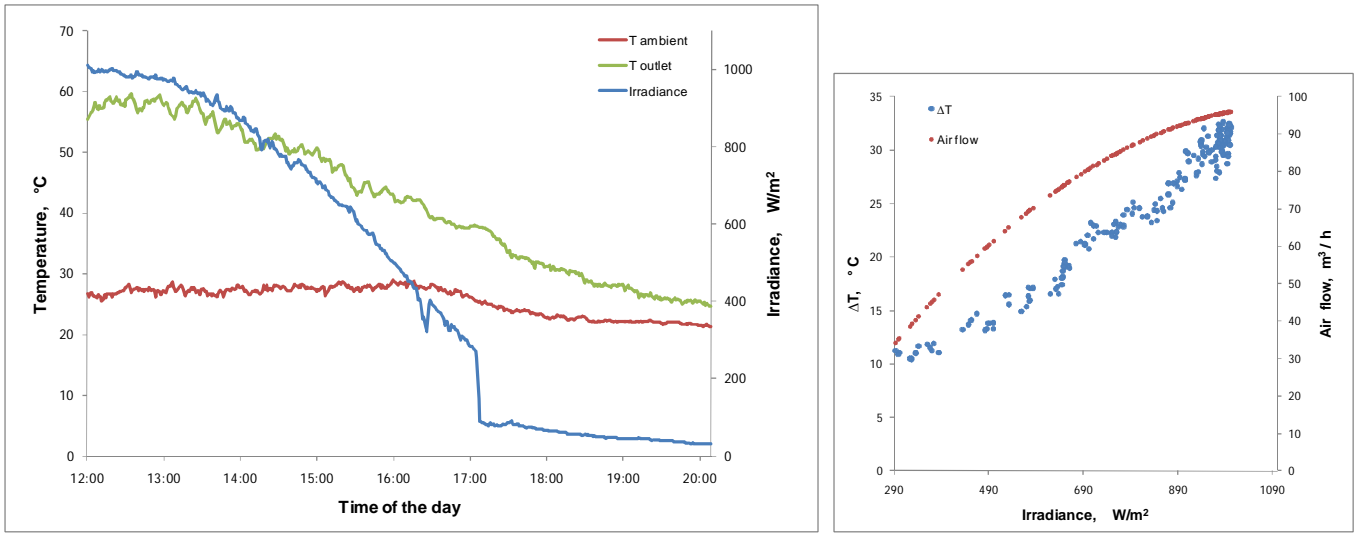


Figure 4.28.a and figure 4.28.b: Thermal performance of the SATS with 3mm TPC operating with 10cm woodchip layer in solar dryer 2.

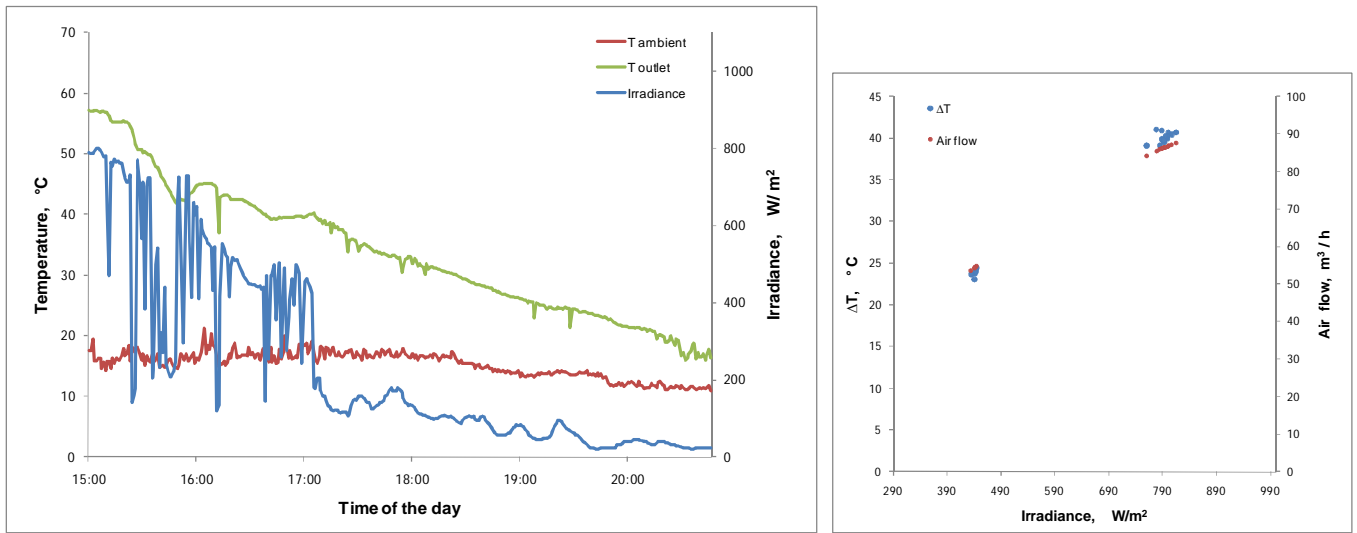


Figure 4.29.a and figure 4.29.b: Thermal performance of the SATS with glazed 3mm TPC operating with 10cm woodchip layer in solar dryer 2.

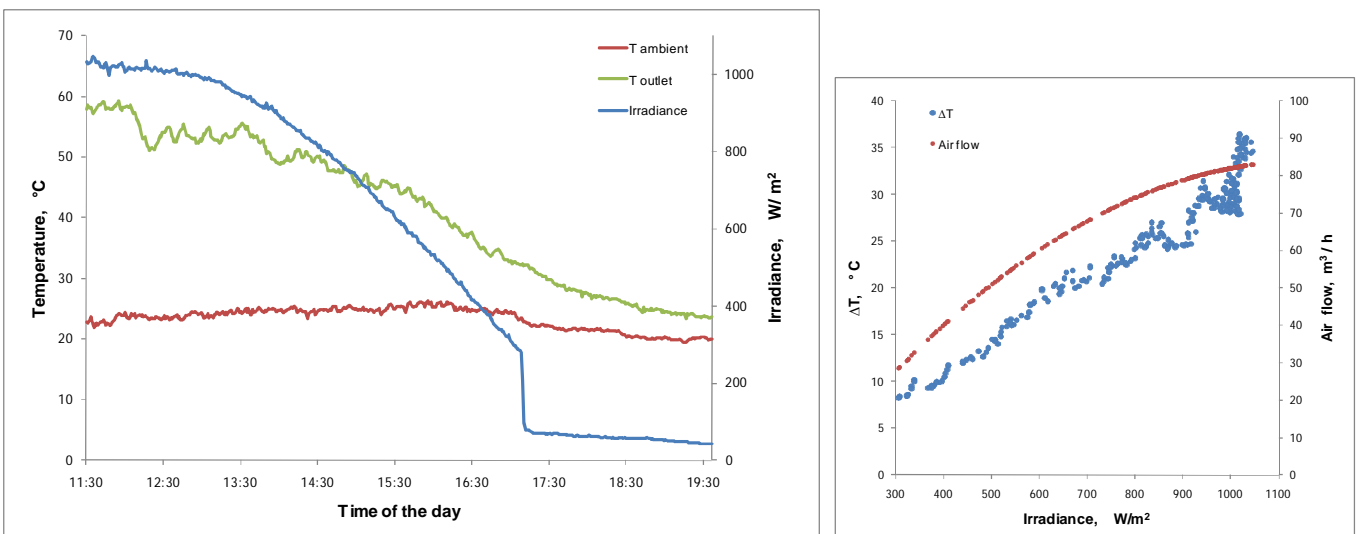


Figure 4.30.a and figure 4.30.b: Thermal performance of the SATS with 3mm TPC operating with 20cm woodchip layer in solar dryer 2.

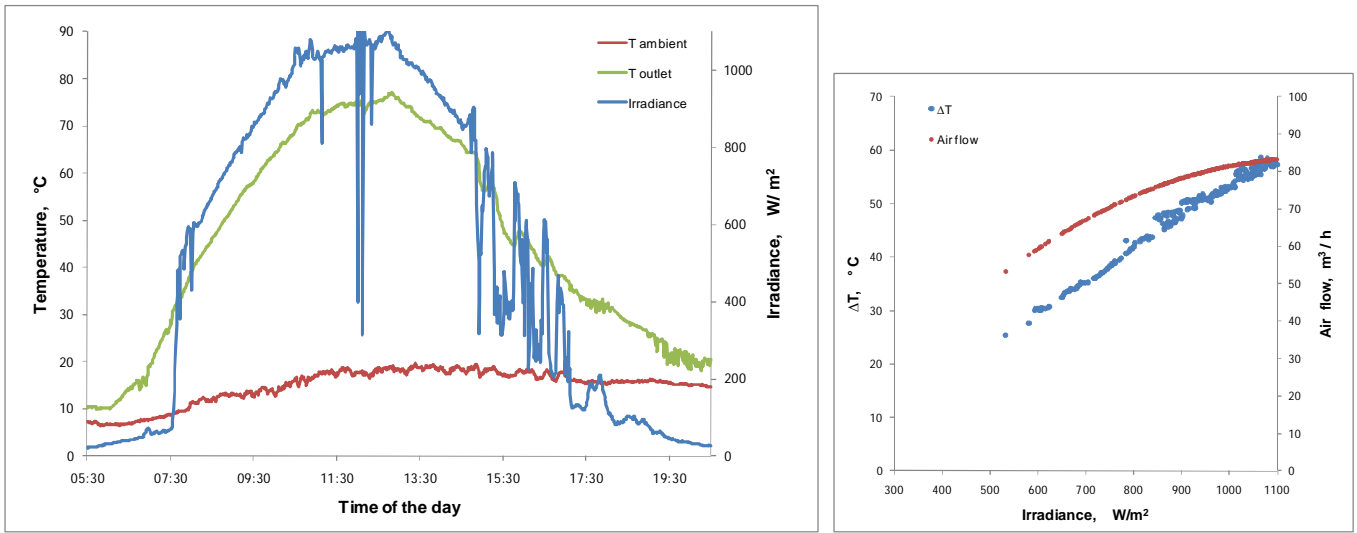


Figure 4.31.a and figure 4.31.b: Thermal performance of the SATS with glazed 3mm TPC operating with 20cm woodchip layer in solar dryer 2.

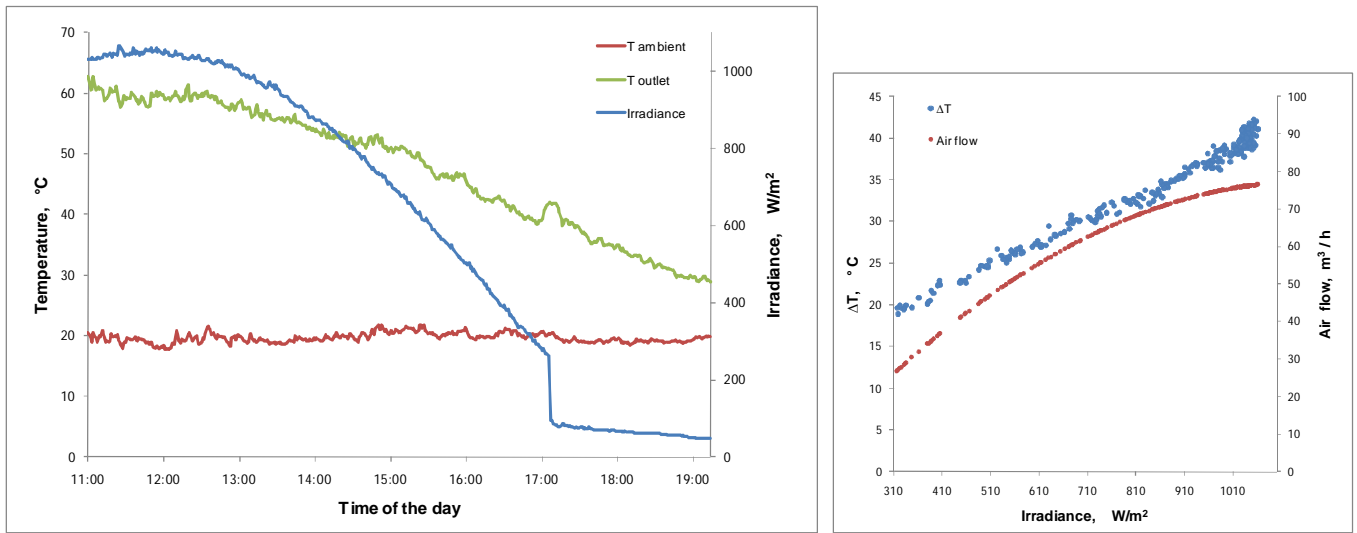


Figure 4.32.a and figure 4.32.b: Thermal performance of the SATS with 3mm TPC operating with 30cm woodchip layer in solar dryer 2.

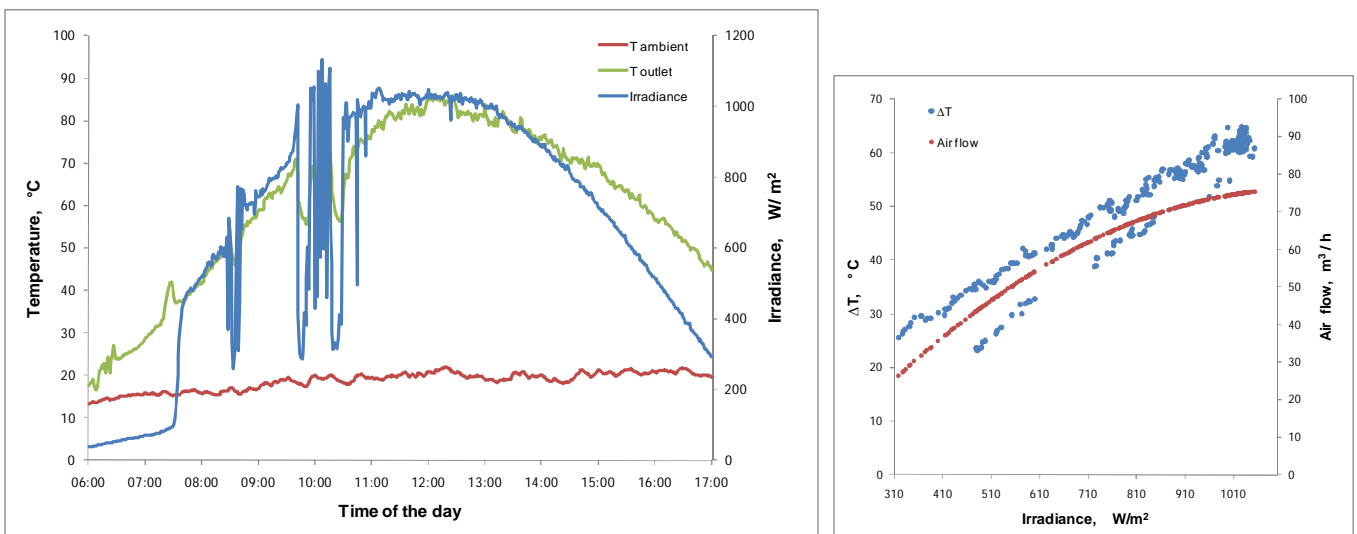


Figure 4.33.a and figure 4.33.b: Thermal performance of the SATS with glazed 3mm TPC operating with 30cm woodchip layer in solar dryer 2.

4.4.3.3 SATS thermal efficiencies

The thermal efficiencies of the SATS were estimated for all the cases studied processing the steady state data points. SATS efficiencies were calculated as the ratio of dividing the useful heat by the total heat received by the collector, equation 4.8.

$$\eta_{collector} = \frac{\dot{m}_{air} C_p (T_o - T_i)}{G_T \cdot A} \quad \text{Equation 4.8}$$

For each data point, the useful heat was calculated proportional to the increment of enthalpy of the inlet air that raised its temperature going through the collector. The air flow values employed in the calculations were obtained from the air flow - irradiance model.

Figure 4.34.a and figure 4.34.b show the efficiency values obtained from the SATS operating with a glazed and unglazed 2mm TPC respectively. The corresponding SATS performances associated with these tests are described in Figures 4.22 and 4.23. The graphics show that the highest efficiencies were obtained with maximum flow rates at high solar radiation. Using a glazing cover resulted in a small increment in the SATS efficiencies despite the air flow reduction.

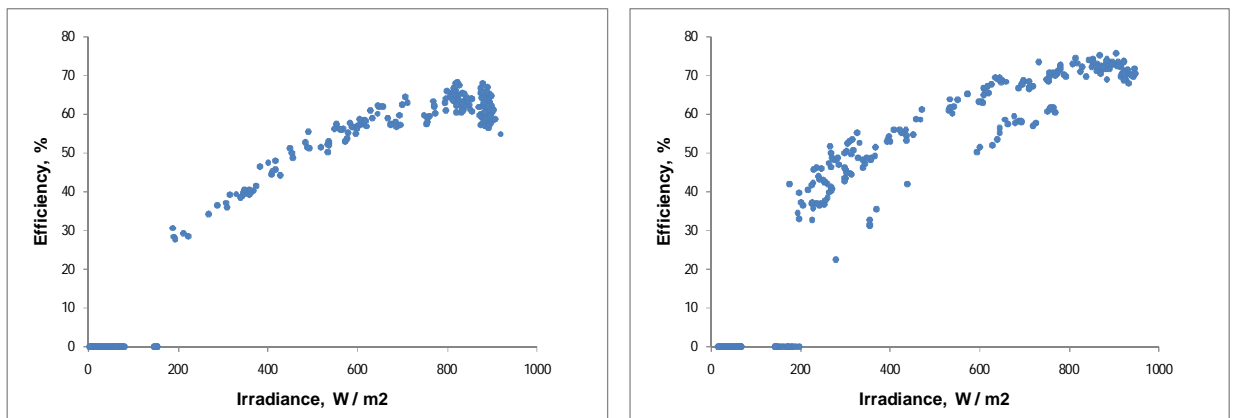


Figure 4.34.a and figure 4.34.b: Thermal efficiencies for the SATS with 2mm TPC unglazed (left) and glazed (right).

Table 4.6 shows the efficiency values obtained when SATS operated at 1000 W/m² in solar dryer 1 and solar dryer 2. In general, SATS thermal efficiencies were high when the collector was connected to the thin layer dryer. If the collector was connected to the thick layer dryer, thermal efficiencies dropped dramatically because of the low flow rates. Glazing cover saved a high degree of heat losses enhancing the thermal

efficiencies. The glazing cover was especially beneficial for the SATS when operating with the thick layer dryer.

Table 4.6: Maximum collector efficiencies registered in the tests.

Solar dryer 1		Solar dryer 2	
Collector	Efficiency	Collector	Efficiency
2mm TPC not covered	71.3 %	10cm 3mm TPC not covered	52.1 %
2 mm TPC covered	75.5 %	10cm 3mm TPC covered	64.1 %
3mm TPC not covered	70.7 %	20cm 3mm TPC not covered	47.5 %
3 mm TPC covered	78.1 %	20cm 3mm TPC covered	63 %
Single pass, fabric plate	55 %	30cm 3mm TPC not covered	45.2 %
Single pass, fabric plate covered	67.9 %	30cm 3mm TPC cover	59.7 %

4.4.3.4 Effect of the wind

The effect of the wind on the solar air collector performance of the SATS is negative. Wind increases the heat losses of the solar air collector and therefore reduces its efficiency. The heat losses derived from wind effects depend on:

- Air flow rate or approaching air velocity to the collector
- Wind speed
- Temperature of the collector
- Ambient temperature

The wind altered the profile of local velocities and temperatures on the absorber plate and increased the heat losses, especially in the direction the wind blows. Depending on the inlet air velocity/wind speed rate, more or less hot air located in the thermal boundary layer would be pulled into the collector or removed by the wind generating heat losses.

The lack of appropriate instrumentation and controlled testing conditions limited the analysis of the effect of the wind on the solar air collector. However, analysing the results obtained from the solar air heater provided a qualitative assessment of the wind effects. Windy days were very common during the testing period because of the nature of the Scottish climate. Windy days were associated with the weather instability and therefore SATS tests conducted in these days didn't provide results reliable enough to

formulate valid correlations on the SATS performance. Nonetheless, conclusions were drawn from observing the SATS tests results.

- Wind effect was noticeable in any TPC configuration in the SATS, especially when SATS operated with the thick layer dryer.
- Small and medium wind gusts produced a light effect in the TPC thermal performance in solar dryer 1, when operating with medium or high flow rates.
- Wind effects were especially strong when TPC operated at medium or low air flow, especially at cold ambient temperatures, causing fluctuations in the outlet temperature values.
- The use of the glazing cover reduced efficiently the effect of the wind and the convection heat losses. The benefit of using cover was more noticeable in the solar dryer 2 configurations than in the solar dryer 1.

Besides the direct effect of the wind in the solar collector thermal performance, the wind had a particular effect in the local irradiance values and local ambient temperatures. Wind causes the movement of the clouds in the sky and consequently a continuous oscillation in the solar radiation received. This implied long transient period of unstable values of the weather conditions that affect the efficiency of the SATS.

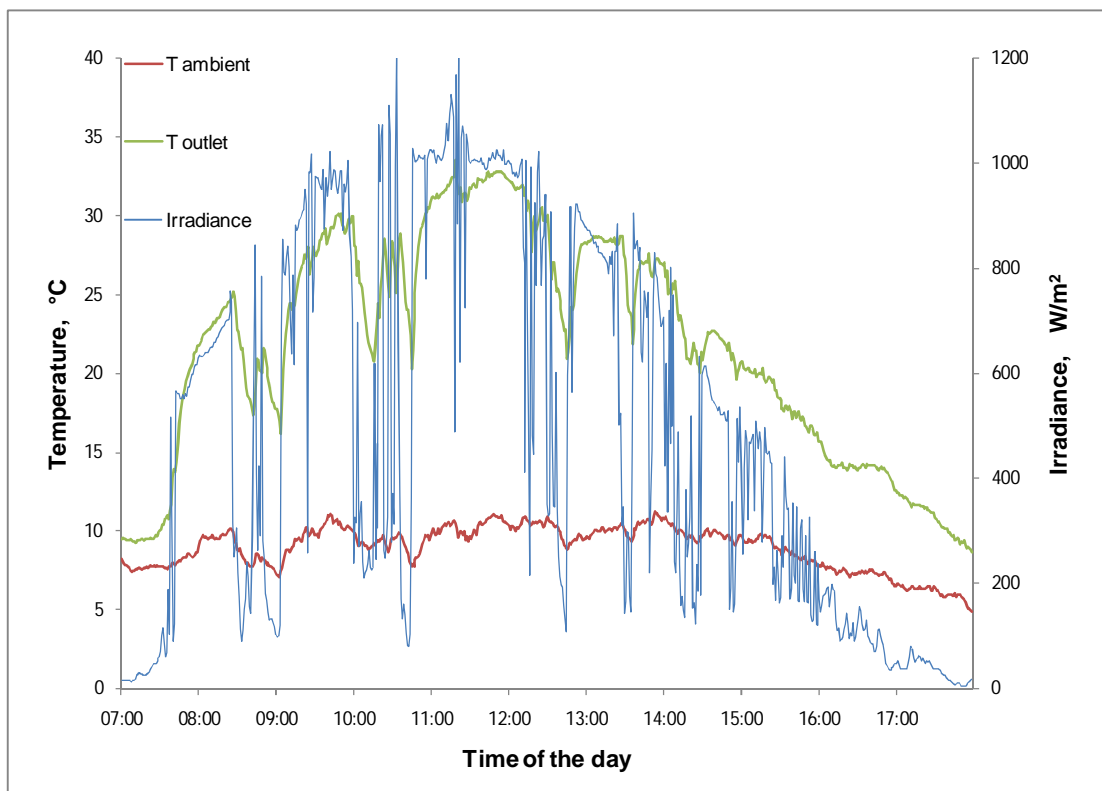


Figure 4.35: SATS with 3mm TPC performance in a windy day.

Figure 4.35 shows the thermal performance of the 3mm TPC operating with solar dryer 1 in a windy summer day. The day was partially sunny with scattered clouds, air velocities measurements fluctuated between 1m/s and 6m/s. The graphic shows a continuous oscillation of irradiation values which is interpreted as the movement of the clouds caused by the wind during the testing time. Outlet temperatures followed the trend of the irradiance values up and down without reaching the steady state.

4.4 SATS thermal model

4.4.1 Modelling the collector outlet temperatures

The SATS performance has been analysed in the previous section showing the experimental $\Delta T - G$ curves for different solar air collector configurations. The thermal performance of each solar collector configuration was modelled in order to obtain a simple correlation that described the collector outlet temperature as a function of the environmental parameters.

Thus, the collector outlet temperature was estimated as the result of summing the ambient temperature plus the temperature rise calculated as a function exclusively of the irradiance, equation 4.9.

$$T_{outlet} = T_{ambient} + \Delta T \quad \text{where} \quad \Delta T = f(\text{Irradiance}) \quad \text{Equation 4.9}$$

The SATS model for various collector configurations was based on experimental results such as shown in the set of graphics shown from figure 4.22 to figure 4.33 and the SATS air flow model presented before.

In the graphic obtained from each SATS thermal performance, the $\Delta T - G_T$ steady state data were modelled employing a simple linear correlation. The description of the daily thermal performance was divided into two periods: morning and afternoon. Thus for each collector configuration, two correlations were obtained for the calculation of ΔT as a function of irradiance using the best fit linear curve.

For instance, figure 4.36 shows the ΔT modelled for the unglazed 3mm TPC working in the solar dryer 1 which thermal performance is plotted in figure 4.23.b.

The morning ΔT model curve was defined by a line that connects the point with highest $\Delta T - G_T$ and the origin of coordinates. The afternoon ΔT model curve was the line had the highest $\Delta T - G_T$ points in common with the morning line. However the slope of

this line was lower which meant that temperature rise for low irradiance were higher than in the morning ΔT data.

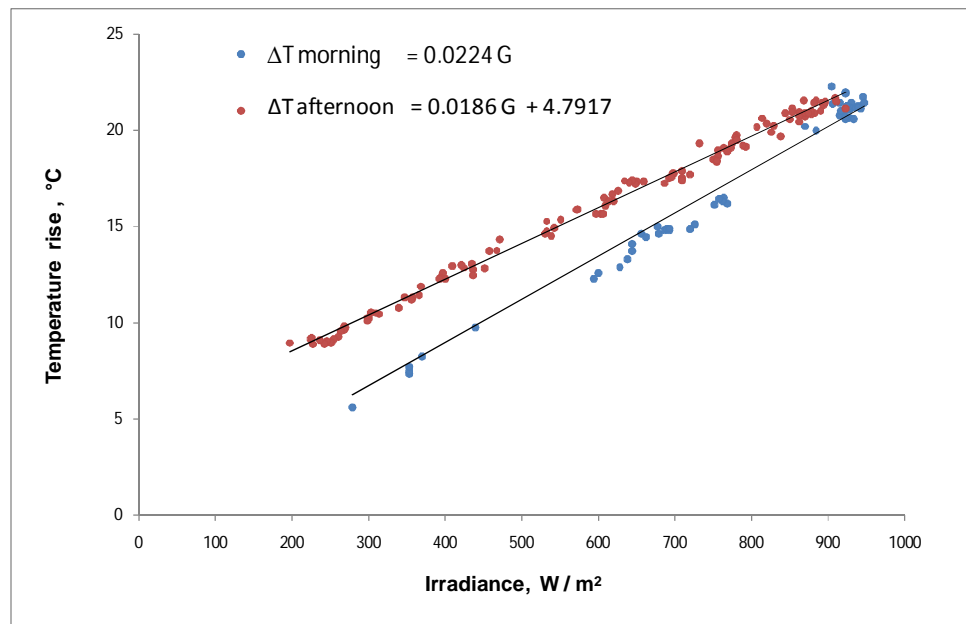


Figure 4.36: ΔT model obtained from the performance of SATS with 3mm glazed TPC.

Two linear regression curves were obtained for all the collector configurations considered for the solar dryer 1 and the solar dryer 2. Table 4.7 and table 4.8 shows the best fit curve equation and regression parameter, R^2 , obtained from modelling the stable ΔT points from each SATS test.

Table 4.7: ΔT modelling curves for SATS with various collector configurations operating with solar dryer 1.

Collector configuration	ΔT afternoon, °C	ΔT morning, °C	R^2 (afternoon data)	R^2 (morning data)
2mm TPC	$\Delta T = 0.0164 \cdot G_T + 3.8$	$\Delta T = 0.0213 \cdot G_T$	0.946	0.982
2mm TPC covered	$\Delta T = 0.0186 \cdot G_T + 4.7$	$\Delta T = 0.0224 \cdot G_T$	0.994	0.975
3mm TPC	$\Delta T = 0.0142 \cdot G_T + 4.0$	$\Delta T = 0.0192 \cdot G_T$	0.927	0.957
3mm TPC covered	$\Delta T = 0.0222 \cdot G_T + 3.1$	$\Delta T = 0.0251 \cdot G_T$	0.978	0.965
Fabric, flat plate	$\Delta T = 0.0108 \cdot G_T + 2.4$	$\Delta T = 0.0131 \cdot G_T$	0.929	0.958
Fabric, flat plate covered	$\Delta T = 0.02 \cdot G_T + 0.9$	$\Delta T = 0.0210 \cdot G_T$	0.973	0.979

The ΔT modelling curves were based on the steady state ΔT data of only one test conducted for each configuration. The level of dispersion of the ΔT - G_T points in the graphic was reflected in the regression parameters which were reasonably high for the different ΔT modelling curves. This approach is very simple and describes the steady

state thermal performance in all the operational regime of the SATS configuration. However, the transient effects in the SATS performance, caused by the fluctuation of irradiance values and air flow, were not included.

Table 4.8: ΔT modelling curves for SATS with 3mm TPC configurations operating with solar dryer 2.

Woodchip layer	Collector configuration	ΔT afternoon, °C	ΔT morning, °C	R^2 (afternoon data)	R^2 (morning data)
10cm	3mm TPC	$\Delta T = 0.0317 \cdot G_T$	$\Delta T = 0.0317 \cdot G_T$	0.982	0.982
10cm	3mm TPC covered	$\Delta T = 0.0407 \cdot G_T + 7.6$	$\Delta T = 0.0514 \cdot G_T$	0.923	0.989
20cm	3mm TPC	$\Delta T = 0.0340 \cdot G_T$	$\Delta T = 0.0340 \cdot G_T$	0.993	0.993
20cm	3mm TPC covered	$\Delta T = 0.0528 \cdot G_T + 7.3$	$\Delta T = 0.0533 \cdot G_T$	0.978	0.977
30cm	3mm TPC	$\Delta T = 0.0285 \cdot G_T + 10.1$	$\Delta T = 0.0397 \cdot G_T$	0.992	0.985
30cm	3mm TPC covered	$\Delta T = 0.0512 \cdot G_T + 10.4$	$\Delta T = 0.0636 \cdot G_T$	0.983	0.985

4.4.2 Error and Validation of the model

The validation of the model results consisted in the comparison between predicted and experimental collector outlet temperatures obtained from the thermal performance of the SATS when working at various weather conditions.

Figure 4.37 shows the results of the performance of the SATS with a glazed 2mm TPC connected to the thin layer dryer. The test was conducted on the 02/03/09, a cloudy day with no appreciable wind. The graphic shows a good correlation between predicted and measured collector outlet temperatures along the test. In SATS tests where the collector was glazed it was generally observed that: the step increment in irradiance was well represented whereas the step decrement in irradiance was not satisfactorily represented. Moreover early morning and late afternoon data were also well predicted.

Figure 4.38 shows the results of the performance of the SATS with an unglazed 3mm TPC connected to the thin layer dryer. The test was conducted on 28/04/09, cloudy and windy day with appreciable wind during the day. Wind speed reached a maximum of 4 m/s. In SATS tests in where the collector was unglazed, the predicted outlet temperatures were more sensitive to step changes in irradiance and notable differences were observed between predicted and experimental data early in the morning and late in the afternoon. Nonetheless figure 4.38 shows an acceptable correlation between experimental and predicted data during windy conditions that involved a prolonged periods of irradiance fluctuations.

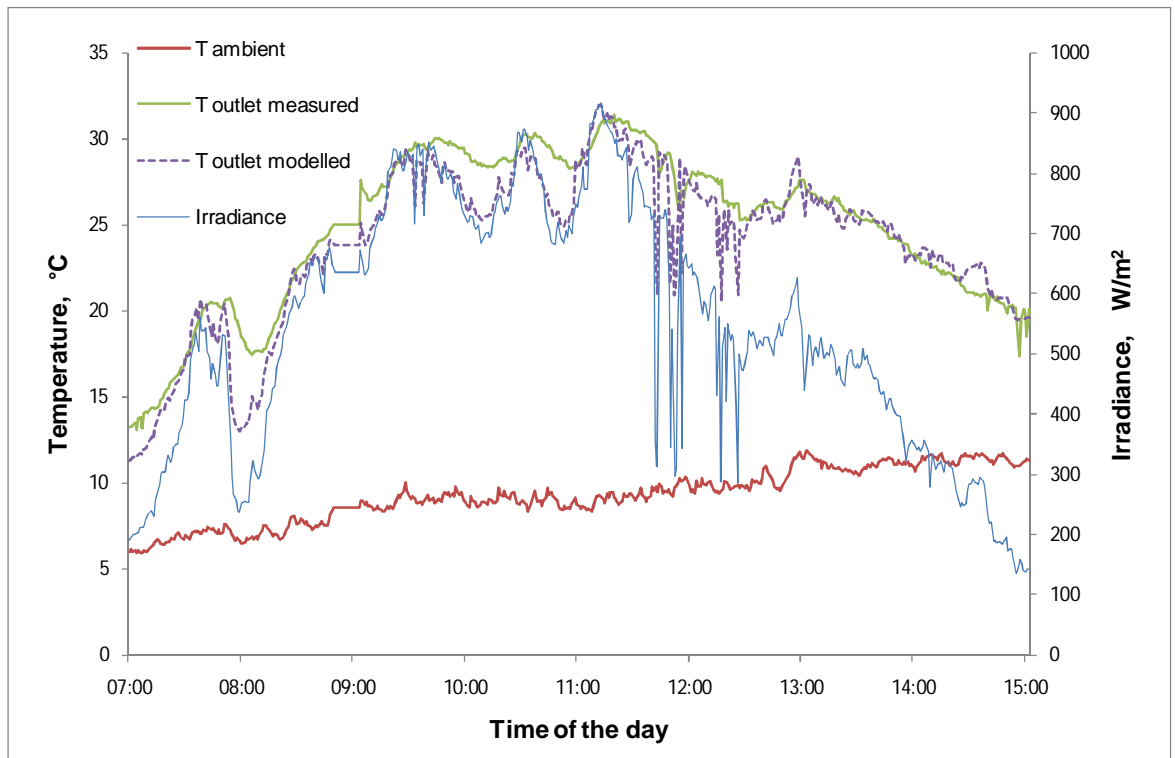


Figure 4.37: Predicted and experimental collector outlet temperatures obtained from the SATS with 2mm glazed TPC operating in solar dryer 1.

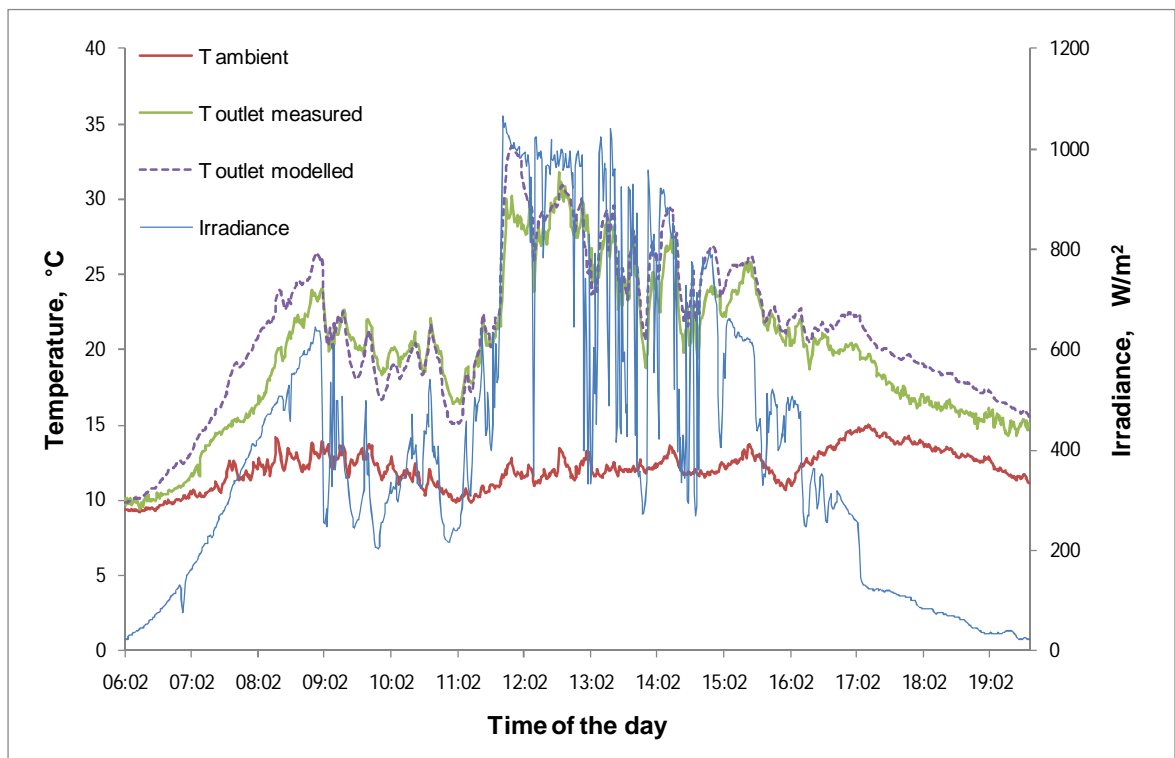


Figure 4.38: Predicted and experimental collector outlet temperatures obtained from the SATS with 3mm TPC operating in solar dryer 1.

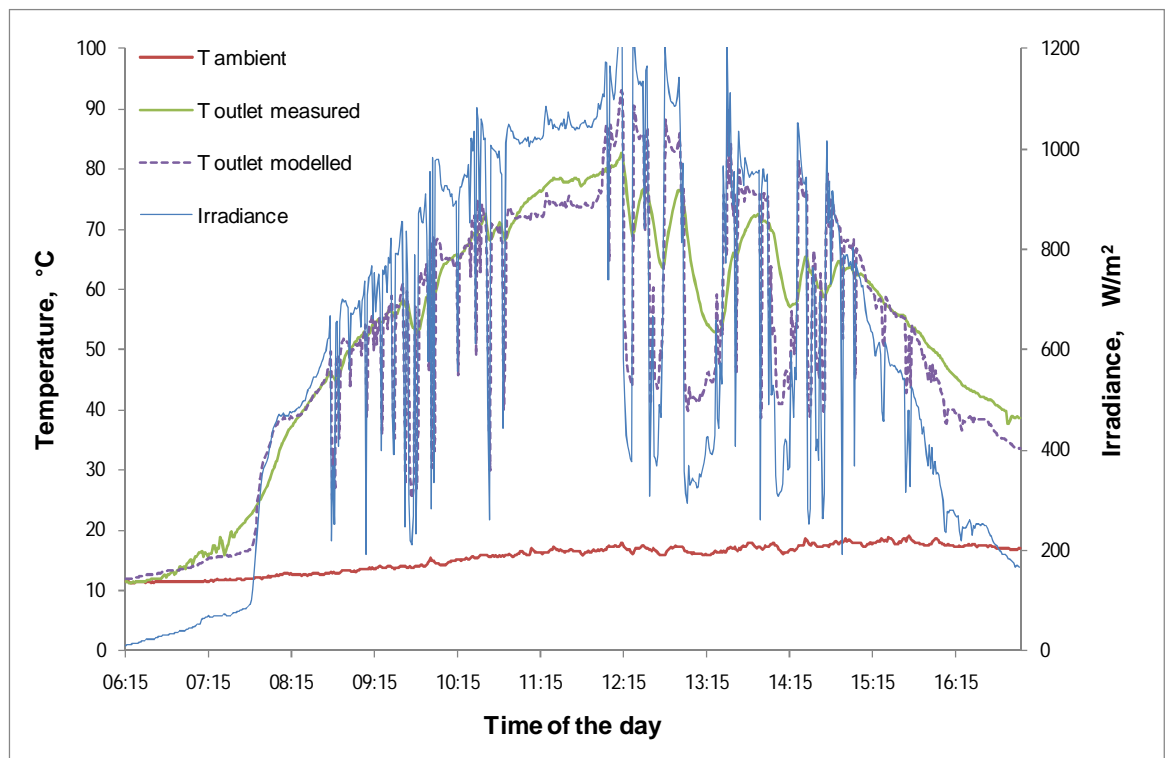


Figure 4.39: Predicted and experimental collector outlet temperatures obtained from the SATS with 3mm TPC operating in solar dryer 2 with 30cm woodchip layer.

The error model was evaluated as the difference between the predicted and measured collector outlet temperature at any time during the test. The maximum difference between predicted and measured values observed was 5°C in the most unfavourable case or 16%.

Figure 4.39 shows the results of the performance SATS with a glazed 3mm TPC connected to the 30 cm thick layer dryer. The test was conducted on the 22/08/09, a day predominantly sunny with continuous gusts of wind that moved the clouds. Wind speed reached a maximum of 6 m/s. In SATS tests where the collector was connected to the thick layer dryer, the range of collector outlet temperatures was high and therefore the difference between predicted and measured temperatures was bigger. The SATS performance model satisfactorily predicted the collector outlet temperatures in steady conditions. However the transient regime, generated by the continuous oscillation in irradiance, implied an important error in the prediction of the temperatures. The major temperature difference was observed especially after a step decrement in irradiance.

The error of the SATS predicted performance when working with the thick layer dryer was bigger because the range of operating temperatures was larger. The maximum difference between modelled and experimental temperatures observed in the validation tests was 25°C in the transient just after a step decrement in irradiance.

The error of the ΔT model due to the step in irradiance could have been minimised using a correction factor. In the estimation of the collector outlet temperature during the transient state, previous irradiance and temperature data shall be considered. Thus the correction factor is related to the thermal inertia effects in the collector and calculated based on the time constant of the collector. This parameter can correct the effects of sudden changes in irradiance. In this study the effects of the transient was not included because of lack of adequate experimental conditions to examine in detail the transient regime for both step in irradiance and step in air flow in the operation range. Thus, the SATS model presented does not include this factor and estimated ΔT values are always proportional to solar radiation.

The performance of the SATS was modelled with a simple mathematical expression. The error in the calculation of the predicted collector outlet temperatures are due to a series of simplifications taken when modelling the SATS performance and the uncertainties due to the tolerance of the instrumentation:

- The thermal model was based on the data obtained from one day with favourable weather conditions.
- The effect of the continuous variations on irradiance values in the transient regime was partially described. While the model reasonably provides a good correlation between predicted and experimental outlet temperatures in case of a step increase in irradiance, the step decrease in irradiance brought a high error component in the model.
- The wind effects in the SATS performance were not included in the model. Wind affected the performance of the SATS because it causes an increment in heat losses in the system, especially in the unglazed collector configurations. Moreover, it usually involves the movement of the clouds causing solar radiation oscillations and consequent transient regime in the SATS performance.
- Since the model is based on the experimental results, the predicted collector outlet air temperature is expected to have some error due to the measure tolerance of the instruments. Considering all sources of error in measurements such as temperature and irradiance, the propagation error was quantified between 7% and 14% for any of the solar woodchip dryer configurations. These high values are basically attributed to the significant error in measuring the temperatures in the system.

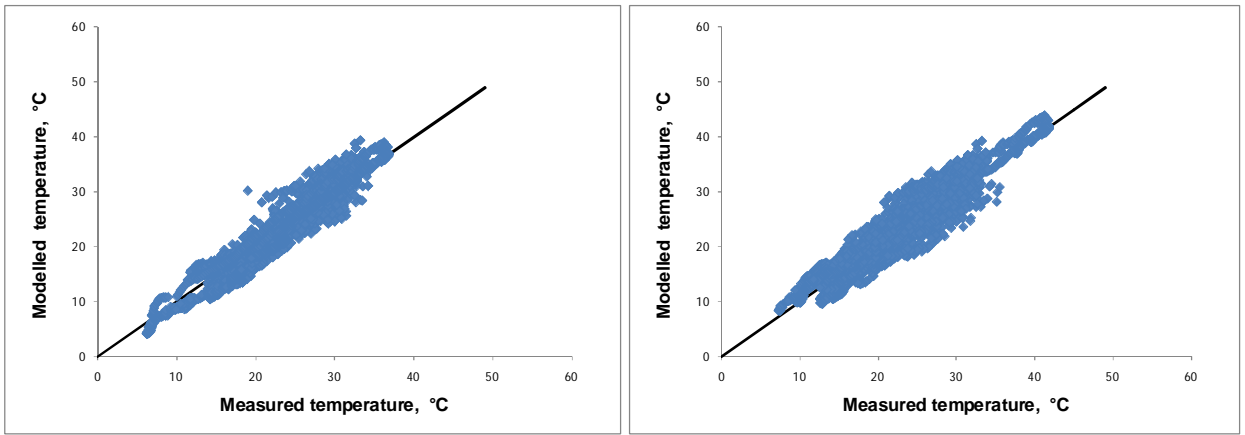


Figure 4.40: (left) Modelled vs predicted temperatures in SATS with 2mm TPC no covered and dryer 1.

Figure 4.41: (right) Modelled vs predicted temperatures in SATS with 2mm TPC covered and dryer 1.

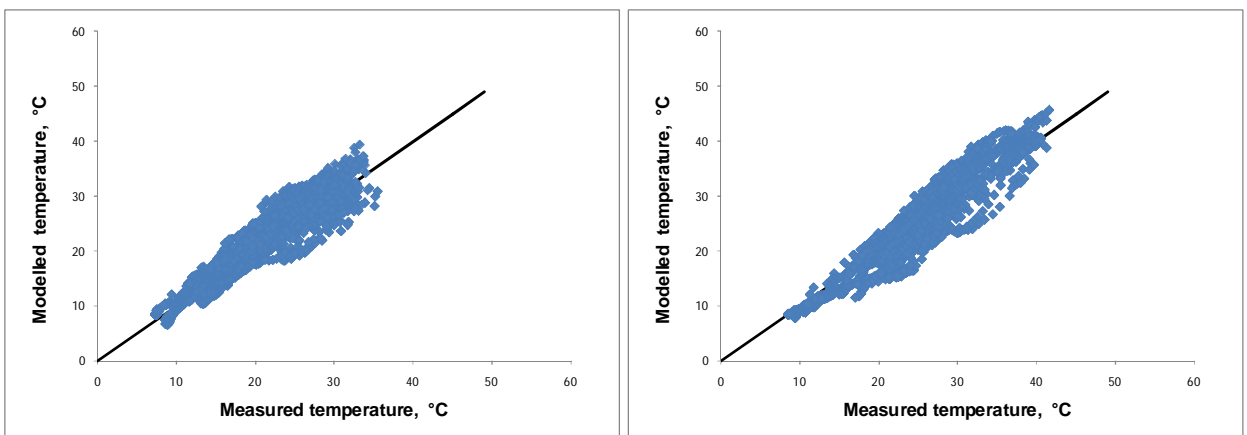


Figure 4.42: (left) Modelled vs predicted temperatures in SATS with 3mm TPC no covered and dryer 1.

Figure 4.43: (right) Modelled vs predicted temperatures in SATS with 3mm TPC covered and dryer 1.

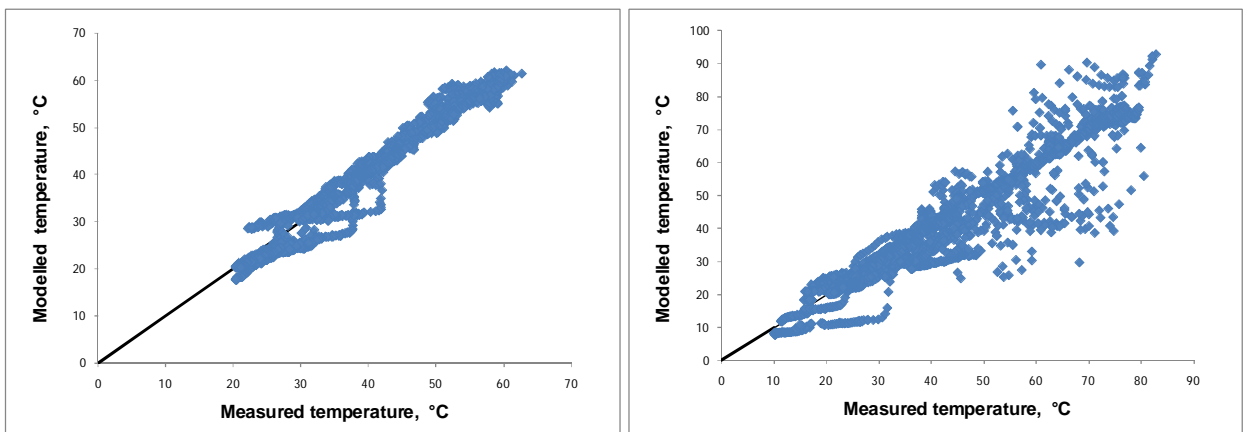


Figure 4.44: (left) Modelled vs predicted temperatures in SATS with 3mm TPC no covered and dryer 2.

Figure 4.45: (right) Modelled vs predicted temperatures in SATS with 3mm TPC covered and dryer 2.

The goodness of the model was analysed comparing predicted and measured outlet temperatures of the solar air collector for various tests at different weather conditions. Figure 4.40 to figure 4.45 show the comparison of experimental and

modelled data obtained from various tests conducted in the study of the SATS system during a year.

Using VBA programming tools, an EXCEL spreadsheet was developed to compare predicted and measured outlet temperature. A statistical analysis, shown in table 4.9, completed the study of the thermal performance model estimating the typical regression parameters: R^2 , MBE, RMSE, Skewness and Kurtosis.

Table 4.9: Statistical values of the linear correlation between predicted and measured data

Dryer	Solar collector	N ^o tests modelled	a	b	R ²	MBE (°C)	RMSE (°C)	Skewness	Kurtosis
Solar dryer 1	2mm unglazed TPC	7	-0.66	1.03	0.916	-0.18	1.87	-0.15	-0.14
Solar dryer 1	2mm glazed TPC	8	-0.03	1.02	0.903	-0.47	2.14	0.04	-0.55
Solar dryer 1	3mm unglazed TPC	7	0.25	1.02	0.897	-0.78	2.11	-0.02	-0.85
Solar dryer 1	3mm glazed TPC	8	-2.98	1.10	0.933	0.26	2.46	0.03	-0.68
Solar dryer 1	Fabric flat plate	4	-1.55	1.04	0.973	0.19	1.29	1.06	-1.10
Solar dryer 2	3mm unglazed TPC	4	-4.26	1.09	0.956	0.23	4.98	1.13	-1.64
Solar dryer 2	3mm glazed TPC	4	-3.21	1.01	0.900	3.45	5.86	-0.19	-1.73

The statistical values shown in table 4.8 indicate similar characteristics in the results obtained from modelling the performance of the SATS for various collector configurations. In each SATS model, the slope of the best fit line, b , was above the unity and the negative value of the y-intercept, a , suggest an underestimation of the predicted temperatures at low irradiances and an overestimation of predicted collector outlet temperatures at high solar radiation levels. R^2 values are relatively high and indicate a satisfactory accuracy for the regression model despite of the simplifications assumed. The MBE values are observed low in all the cases studied. The negative value means that the average model data are overestimated. The RMSE values, which indicate the average distance of the predicted data from the best fit curve, were relatively low and similar in the thermal models when using TPC covered and uncovered for solar dryer 1. Higher RMSE values are observed in the thermal model correspondent to solar dryer 2 with thick layer dryer as outlet temperatures were higher and therefore the difference error between predicted and modelled temperatures too. The skewness was relatively low for most of the models and did not show remarkable skew tendency in the point distribution. Negative kurtosis values indicate a notable grade of dispersion of the distribution. Respect the normal distribution, the distribution of the points obtained from the different thermal model has a lower and wider peak similar to the uniform distribution. Figures 4.40 to 4.46 shows an important degree of dispersion reflected in the kurtosis values, particularly the thermal models for solar dryer 2 have higher

kurtosis as the range of temperatures was higher and the number of points in the statistical analysis was lower.

4.5 Heat loss modelling

The outlet temperature of the solar collector was modelled in the previous section. However in the study of the solar dryer performance, drying temperatures were calculated considering the heat losses in the ducting. The solar collector outlet was connected to the dryer using a pipe made of aluminium semi-rigid corrugated ducting. The solar dryer 1 had 120 cm of this pipe in a vertical position while the solar dryer 2 had 150 cm pipe in a vertical position.

The heat losses from the pipe to the ambient were estimated considering radiant heat losses from surface to ambient and the natural convection contribution.

The convective heat losses in the vertical corrugated pipe were calculated using the correlations of natural convection for a vertical cylinder, equation 4.10 to equation 4.13, Incropera et al. (1996).

$$Ra = \frac{g \cdot \beta \cdot (T_s - T_{amb}) \cdot L_{duct}^3}{(\alpha \cdot \nu)_{air}} \quad \text{Equation 4.10}$$

$$Nu = \left[0.825 + \frac{0.387 \cdot Ra^{1/6}}{\left[1 + (0.492 / Pr)^{9/16} \right]^{8/27}} \right]^2 \quad \text{Equation 4.11}$$

$$h = \frac{Nu \cdot k_{duct}}{L} \quad \text{Equation 4.12}$$

$$q_{losses,convection} = h \cdot A_{duct} \cdot (T_s - T_{amb}) \quad \text{Equation 4.13}$$

In order to simplify the heat transfer problem and the computing calculations, the mean temperature of the surface was assumed as the collector outlet temperature. Air properties were calculated for the average temperature between ambient and collector outlet temperatures.

The radiant heat losses from the aluminium duct to the surrounding air were estimated using the Stefan- Boltzmann law, involving the total radiating area, absolute

temperature of the radiating body and surrounding ground and sky, as equation 4.14 shows below, Incropera et al. (1996).

$$q_{losses,radiation} = \frac{1}{2} \varepsilon_{duct} \cdot \sigma \cdot A_{duct} \cdot (T_{duct}^4 - T_{ground}^4) + \frac{1}{2} \varepsilon_{duct} \cdot \sigma \cdot A_{duct} \cdot (T_{duct}^4 - T_{sky}^4) \quad \text{Equation 4.14}$$

Where $\varepsilon_{duct}=0.11$ was the aluminium duct emissivity (Calex Ltd, 2008) and σ is Stephan-Boltzmann constant.

Drying temperatures were finally calculated as a function of the air flow, collector outlet temperature and the heat losses, equation 4.15.

$$T_{drying} = T_{outlet} - \frac{(q_{losses,convection} + q_{losses,radiation})}{\dot{m} \cdot C_p} \quad \text{Equation 4.15}$$

Experimentally, the heat losses percentage over the total heat gain varied with the performance of the collector. In solar dryer 1 heat losses oscillated from 10% to 20% while in solar dryer 2 heat losses were up to 30% over the heat gained by the collector.

The heat losses in the ducting were estimated with the heat transfer equations presented above. The results showed a good agreement between the experimental and predicted heat losses from the ducting to the ambient. The rate between radiant and convection heat losses depended on the collector outlet temperature. It was observed that in the solar dryer 2, whose ducting was 30% larger and the collector outlet temperatures normally higher, the radiant heat losses were significantly much higher than in the solar dryer 1.

4.6 Summary

In this chapter, the analysis of the performance of a SATS prototype which has been designed and built to pre-heat air in the solar woodchip dryer was presented. The SATS comprised a PV driven fan and a solar air collector. Various collector configurations were utilised in order to learn about the behaviour of the SATS when working at different weather conditions. The initial solar air collector employed was based on the transpired plate collector. A flat plate collector with a fabric absorber plate was also tested.

The SATS performance was determined by the operation of the PV driven fan. It was observed that the PV driven fan operational voltages were mostly dependant on the incident solar radiation. PV module temperature and wind were factors that were neglected when modelling the PV driven fan performance. The PV driven fan operation voltages were successfully described as a function of irradiance employing a quadratic curve. As a consequence of this simplification, for any SATS configuration, there was a unique operational regime in which air flow depends exclusively on the incident solar radiation.

The pneumatic characteristics of both the solar collector and the woodchip dryer affected the thermal performance of the SATS. While the pressure drop introduced by the thin layer dryer was small, the pressure drop in the thick layer dryer was notably high implying low air flows. The solar collector introduced some pressure drop. Experimentally, it was observed that the flat plate collector had less pressure drop than the TPC and the glazing cover increased the pressure drop of each collector configuration by equal amounts. The pressure drop in the TPC was also estimated with a theoretical approach in which the friction between inlet air and the transpired plate holes was the most important factor. The total pressure drop of the solar woodchip dryer affected to the minimum level of solar radiation to overtake the fan stall conditions to start operating. Finally the air flow for each solar dryer configuration was modelled employing a second order polynomial curve as a function of irradiance.

The analysis of the thermal performance of the SATS was presented for various collector configurations in the solar dryer 1. In the case of TPC, the porosity was a key factor in the thermal performance. Comparing the performance of the SATS when working with a 2mm TPC or a 3mm TPC in identical ambient conditions, the collector with higher porosity had lower pressure drop and operated with higher air flow. As increments of temperature were found very similar, the collector with higher porosity implied higher SATS efficiencies. The SATS efficiencies were close to 70% at 1000W/m^2 for both TPC. Using the glazing cover reduced the heat losses and improved the SATS thermal efficiencies up to 6%. The collector with fabric absorber plate provided relatively good results for the SATS performance despite the high heat losses from plate to ambient.

The SATS performance was also studied when operating with the solar dryer 2. Increasing the thickness of the woodchip layer affected directly the SATS performance as it meant a reduction in the air flow and therefore the collector temperatures were

high. The radiant and convective heat losses from collector to ambient were notably high and the use of the glazing cover was significant. SATS thermal efficiencies when it operated in the solar dryer 2 were lower than 52.1%. When employing a glazing to cover the TPC, SATS efficiencies increased by up to 64.1%.

For all the cases considered in the study, the ΔT of the SATS performance was modelled linearly as a function of the solar radiation. The collector outlet temperature was modelled with a simple expression considering exclusively the steady state data of the tests. The error of the model was evaluated comparing the predicted and experimental data for various tests conducted at different weather conditions. The model yielded acceptable results although the wind effect in the collector performance or the effect of sudden irradiance changes in the transient were not included in the SATS model.

The analysis of the SATS in the solar dryer 1 and the solar dryer 2 has not revealed which option is more suitable for drying woodchip: Although the SATS in solar dryer 1 works with high flow rate and low ΔT , the same SATS in solar dryer 2 works with low flow rate and high ΔT . Although thermal efficiencies were notably higher in the SATS when working in solar dryer 1, the results obtained in this chapter it is not possible to claim which solar dryer is the optimal for drying woodchip. It is necessary to combine the results obtained from the woodchip dryer and the SATS performance in the integral study of the woodchip solar dryer in order to obtain major conclusions

5 SOLAR WOODCHIP DRYER

5.1 Introduction

This chapter presents the study of the novel solar woodchip dryer prototype by integrating the woodchip dryer and the SATS studied and modelled in chapter 3 and chapter 4 respectively. The performance of the solar woodchip dryer was modelled employing the empirical results obtained from the woodchip dryer and the SATS. Thus a macro model has been developed to estimate the production of dried woodchip.

The solar dryer macro model, SDMM, is a tool that simulates the solar woodchip dryer performance and predicts the amount of woodchip that can be dried in a given period of time. The results obtained from the SDMM will be used to evaluate the feasibility of the solar woodchip dryer prototype as an option for drying woodchips under Scottish weather conditions.

The present chapter is divided in three sections:

- The first part presents the analysis of the solar woodchip dryer operation. In order to validate the SDMM, the experimental results obtained from the solar dryer tests are compared with predicted results. A set of results from the SDMM, including daily and annual simulations under Scottish weather conditions, are presented. These results will be used to draw conclusions about the performance of a woodchip solar dryer when working in Scotland.
- The second part deals with the feasibility and employability of the solar woodchip dryer prototype based on its energy savings, productivity and economical aspects.
- The third part discusses the potential advantages of using a solar energy application based on a TPC application to dry woodchip at large scale in a similar location.

5.2 Solar dryer macro model

5.2.1. Introduction

The solar dryer macro model, SDMM, is a data processing tool that simulates the performance of the solar woodchip dryer for a given period of time. It is supposed that the woodchip dryer works with a batch feeding system and each time the woodchip is dried to the required MC, the tray is replaced by a new one with wet woodchip.



Figure 5.1: Solar dryer 1 installed on the roof of the university.

The SDMM has been developed using VBA programming tools in an Excel spreadsheet environment. The code of the program was written in separated modules that simulate the performances of the SATS and woodchip dryer separately. The SDMM code processes input weather data to calculate the drying conditions for obtaining the drying rates. The SDMM accepts various types of weather data input. Moreover, drying woodchip and SATS performance characteristics can be easily modified in the code, although necessarily the SATS characteristics should be compatible with the dryer configuration. The code of the solar woodchip dryer model is commented and in detail described in **Appendix A5: SDMM**.

5.2.2 SDMM structure

The macro model SDMM comprises three modules:

- 1st module deals with the input weather data set. It reads the weather data for a period of time and saves them in an appropriate format to facilitate the calculations.
- 2nd module simulates the SATS performance and calculates the air flow and the collector outlet temperature for the period of time considered.
- 3rd module simulates the dryer operation employing the drying conditions previously calculated. It estimates the amount of woodchip that dries from MC_0 to MC_{final} during the given period of time.

The first part of the SDMM arranged the input weather data in an adequate format in order to deal with large amount of data. The SDMM allows processing both daily and annual weather data sets using the same programming structure.

The daily set of data corresponds to the measured data collected during a SATS test. In order to evaluate the solar woodchip dryer performance for various weather conditions, 6 different days were selected to represent the Scottish weather conditions through the year. Each day is characterized by their profile of temperature and irradiance values measured experimentally in the SATS testing site. Table 5.1 includes a brief description of such days, showing daily average temperature, the total solar energy received during the day and a qualitative description of the weather.

Table 5.1: Climate conditions observed for the 6 days considered for the daily analysis.

n° day	date	Average Temperature	Daily solar radiation	Description of the day
day 1	18/03/2009	11,2 °C	20.93 MJ/m ²	Sunny winter day, sky predominantly clear with eventual clouds and wind was not appreciable.
day 2	10/04/2009	8,3 °C	16.35 MJ/m ²	Spring cold day. It was cloudy and the wind was strong. The wind speed average was 6 m/s.
day 3	14/03/2009	8,5 °C	7.42 MJ/m ²	Winter cold day with low temperatures. Sky was patched by clouds with eventual sunny spells. Noticeable wind was registered.
day 4	31/05/2009	14,0 °C	27.93 MJ/m ²	Spring sunny day with warm temperatures. Cloudless sky during most of the day.
day 5	08/08/2009	15,2 °C	21.77 MJ/m ²	Summer windy day with warm temperatures. Predominantly cloudy with occasional sunny spells. Wind speed average was 5.2 m/s.
day 6	26/07/2009	13,6 °C	10.36 MJ/m ²	Overcast and windy summer day with mild temperatures. Wind speed average was 3.2 m/s.

The annual data set consists of a collection of weather data measured hourly during the year 1991 in Edinburgh. The data includes the solar radiation, psychrometric properties of the air and wind speed. The solar radiation was adjusted to the required inclination angle of 45° using an algorithm based on the model developed by Muneer (2004).

In order to work with a common structure of data, both daily and annual data are adapted to a common data interval of 1 minute. Thus each day comprises 1440 weather data.

The second part of the SDMM program simulates the SATS operation processing the weather data. For a selected solar collector configuration, air flow and collector outlet temperatures were estimated employing the SATS flow and thermal models for the given period of time. Heat losses in the ducting, between the collector outlet and the dryer inlet, were also calculated in order to estimate drying temperatures.

In the third module, the SDMM implements the operation of either the thin layer or the thick layer woodchip dryer, processing the SATS output data or drying air flow data obtained in the previous module. In this module, it is supposed that the dryer is fed automatically once the woodchip are dried from its initial MC_0 to the MC required.

Initially the tray contains woodchip with MC_0 which means that $MR = 1$. Successively, in each interval of time, the Page drying model constants, k and n , are calculated as a function of the drying conditions: temperature and drying velocity. Then new MR are obtained and later converted into MC and weight values. The process goes on until woodchip output reaches the minimum MC level required, usually 30% MC. At this condition, the drying module of the SDMM automatically replaced the dried woodchip for a tray with new woodchip with the same weight and MC_0 . The final output of the SDMM is the weight of total woodchip dried during the selected period of time.

The versatility of the SDMM is limited and it is not possible to change freely any part of the solar dryer without considering the rest of the solar dryer components. Changing the configuration of either the dryer or the SATS implies major changes in the solar dryer operation. As the solar dryer elements performances are interconnected and performance depends on the characteristics of other components, it is not possible to introduce or to change new elements without re-calculating the SATS or dryer models parameters.

Figure 5.2 shows a diagram of the four main elements that comprise the solar woodchip dryer system interconnected through the variables that govern their behaviour. This chart shows only the variables taken into account for modelling the solar dryer performance.

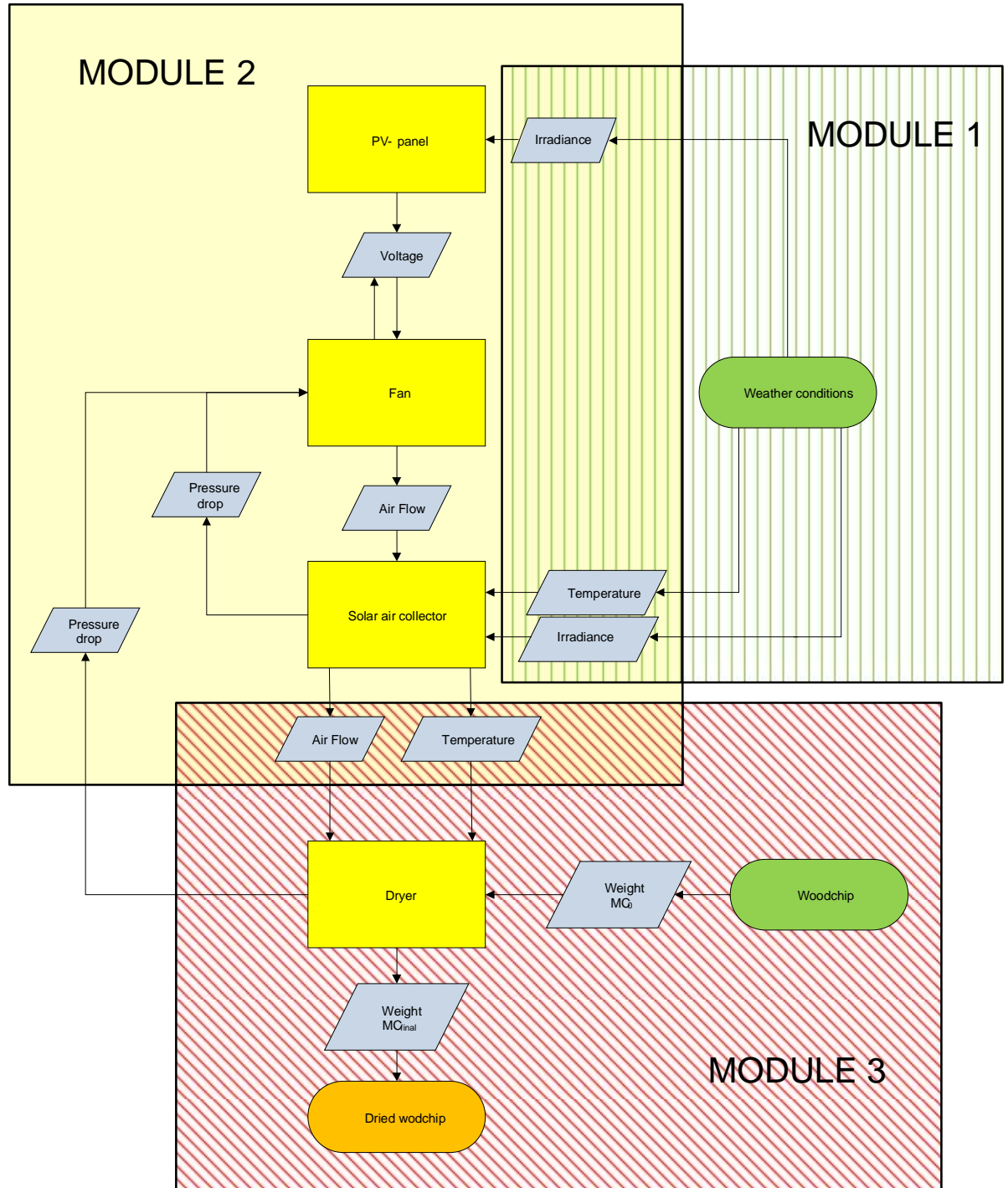


Figure 5.2: SDMM modules diagram.

For instance, selecting a new PV module or fan type means a new electrical connection and consequently, new air flow and different SATS thermal behaviour. Likewise a dryer modification also implies new pneumatic characteristics and therefore a different SATS thermal behaviour.

The SDMM requires three basic sets of data to predict the performance of a solar dryer application.

- In chapter 3, it was concluded that a minimum of 5 drying tests were required to develop the drying macro model based on Page model equation. This model determinates the MC of the product being dried by a specific dryer operating within a range of temperatures and drying velocities.
- In chapter 4, it was shown that the air flow blown by the PV driven fan, working within the solar dryer, can just be described just measuring experimentally the correlation between air flow and irradiance.
- The collector outlet temperatures from the SATS can be modelled as a function of solar radiation and ambient temperature. The correlation can be obtained from a unique test with the SATS operating in steady state conditions with clear sky.

Figure 5.3 shows a diagram of all the solar woodchip dryer cases simulated with the SDMM. The performance of the solar woodchip dryer 1 was simulated for 6 different solar collector configurations and for 2 different samples of woodchips. On other hand, the performance of the solar woodchip dryer 2 was simulated for 2 collector configurations and 3 woodchip layer configurations.

5.3 SDMM results

5.3.1 Solar dryer tests validation

The goodness of the SDMM simulation results has been assessed by means of a series of validation tests in which predicted and experimental results were compared. In such tests, like in the SATS experimental tests, the drying flow and temperatures were predicted. In addition, in the solar dryer validation tests, the weight of the woodchip was measured and ultimately predicted and compared with experimental values.

The procedure and analysis of the solar dryer validation tests was the same as in the SATS tests, including the control of the woodchip sample weight. Thus the weight variation of the woodchip sample on the tray was considered in the analysis of results.

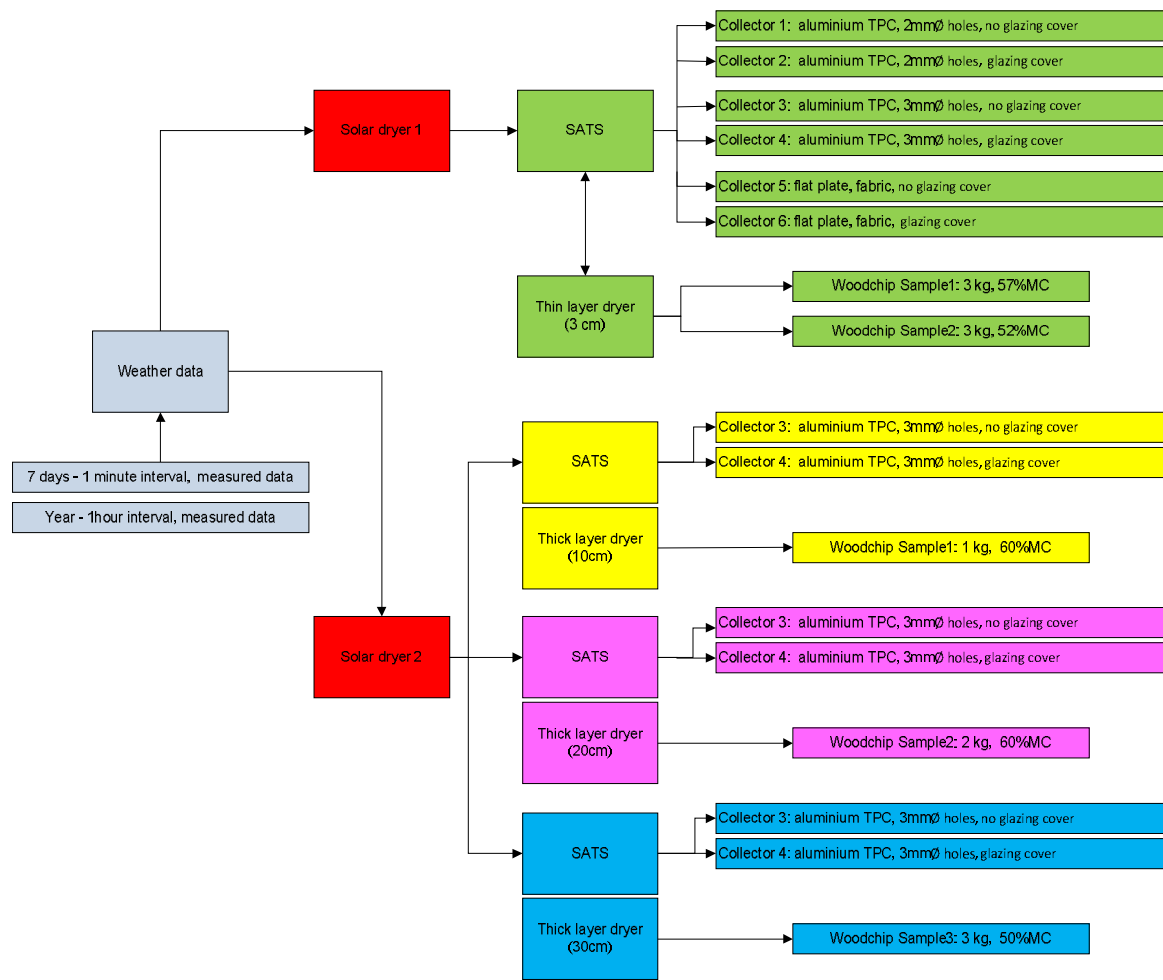


Figure 5.3: Diagram of SDMM simulations conducted

The reproducibility of the SATS and dryer testing conditions was guaranteed as there was no change in the configuration of the system. However the woodchip employed in the validation tests had not the same quality as the one used in the drying tests despite coming from the same wood sample: while the drying model was based on the results obtained from drying fresh wood, in the solar dryer validation tests, the same sample of woodchip, dried naturally to low MC levels, was re-wetted to 55 % MC, similar to the same woodchip sample when it was fresh. Possible changes in the internal structure may imply different drying performance.

5.3.1.1 Solar dryer validation results

In this section, 3 solar dryer validation tests are presented. All the tests were conducted employing the solar dryer 1 comprising the thin layer dryer and the glazed 2 mm TPC. The amount of woodchip to dry in each test was 3 kg and its MC_0 was 55%.

Figure 5.4 represents the solar dryer validation test results obtained in a warm and

sunny day. In the beginning of the test, the PV driven fan operated at full capacity and delivered steady constant high flow at high temperature into the dryer. The water easily evaporated and the weight of the sample rapidly fell down to levels of equilibrium moisture content around 7% MC. The weight and the MC remained practically constant despite the favourable testing conditions. The SDMM simulation results were reasonably satisfactory despite a noticeable difference between predicted and measured weight observed through the test. The maximum difference was 130 gr.

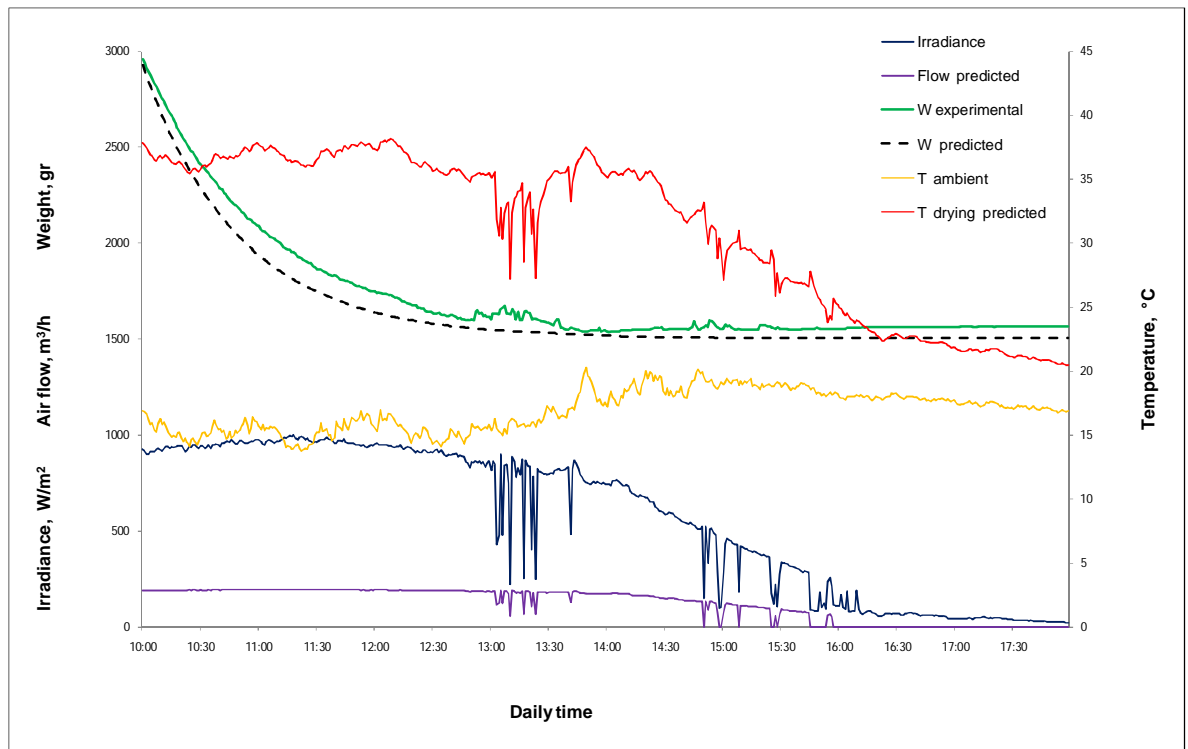


Figure 5.4: Solar dryer validation test in a sunny day.

Figure 5.5 shows the results obtained from a solar dryer validation test conducted in a warm and overcast day. The SATS performance was poor as received solar radiation was low and the PV driven fan only operated for short periods of time. In the beginning of the test, predicted and experimental weight values had a good correlation. However there were intervals in which the predicted air flow was zero and the experimental weight of the woodchip slowly decreased.

Figure 5.6 shows the results obtained from a solar dryer validation test conducted in a warm and windy day with cloudy spells. SDMM results followed the trend of the experimental values although there was a notable difference between predicted and experimental values since the beginning. The graphic shows an accumulative error that fades away as the woodchip sample reaches the EMC.

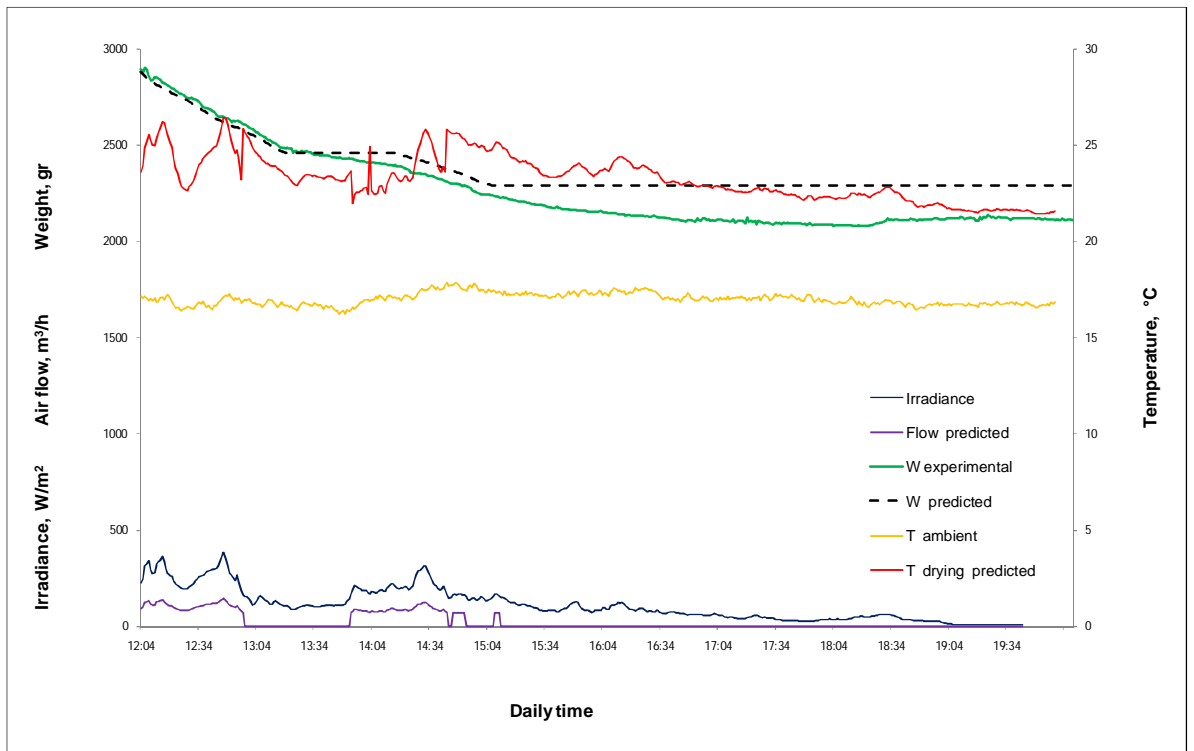


Figure 5.5: Solar dryer validation test in a warm overcast day.

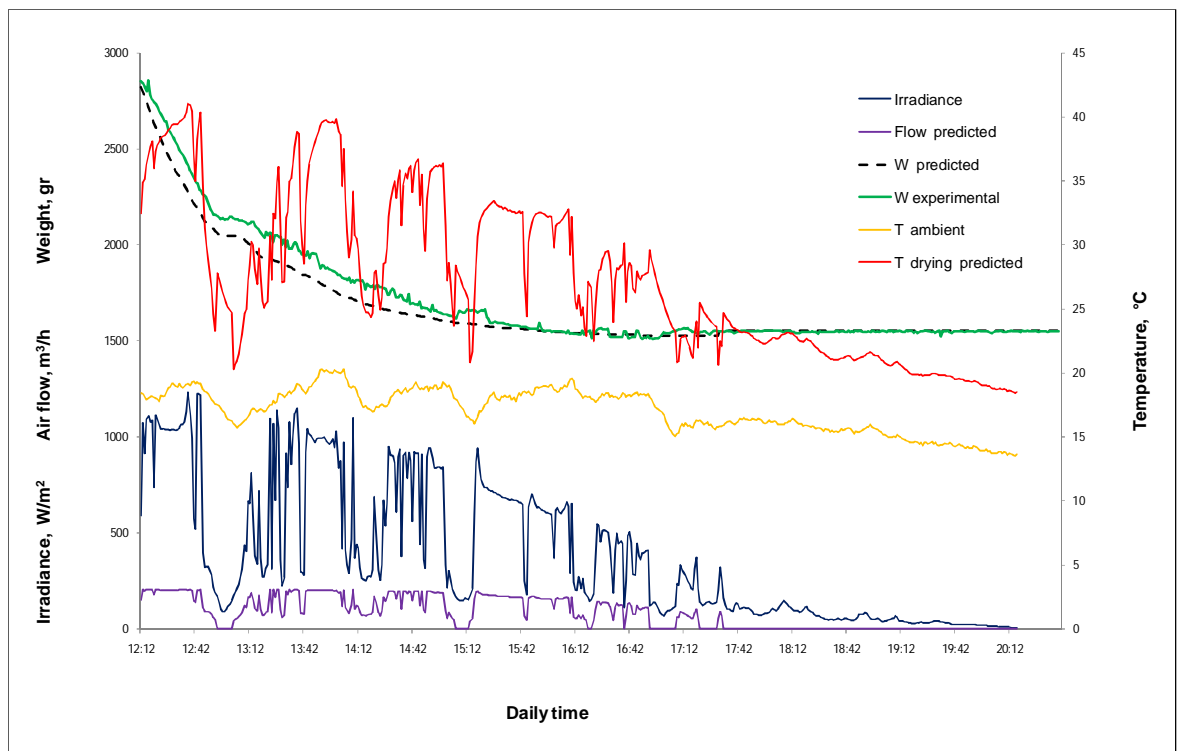


Figure 5.6: Solar dryer validation test in a cloudy/ sunny warm day.

5.3.1.2 The error analysis

The error of the modelling curves was evaluated in two ways:

The error on weight basis, equation 5.1, was proportional to the difference between predicted and experimental weight at a given time. The maximum error registered in the validation tests was 11.1%.

$$Error_{weight} = 100 \cdot \left| \frac{W_{exp} - W_{pred}}{W_{exp}} \right|_{time} \quad \text{Equation 5.1}$$

$$Error_{time} = \left| \frac{Time_{exp} - Time_{pred}}{Time_{exp}} \right|_{MC} \quad \text{Equation 5.2}$$

Time error basis was defined as the coefficient between the difference of the experimental and predicted time at a given MC level and the experimental value, equation 5.2. In the validation solar dryer tests, when MC was higher than 30%, the maximum error on time basis registered was 15%.

SDMM error in the validation tests were associated to a sum of factors related to the SATS model and also the woodchip drying model:

- Woodchip sample: quality of the wood and MC_0
- Drying model error.
- SATS thermal model error.
- SATS air flow model error.

The predicted amount of dried woodchip is based on the characteristics of the woodchips and the measurements of irradiance and ambient temperature. The errors associated with these readings are as given in table 3.1 und table 4.2. Moreover the drying process characteristics, the air flow rate and the thermal output were also determinate experimentally and they are too associated with error. As result, the predicted dried woodchip of the model can be associated with an error inherited from these measurements.

Running the model with the lower and the higher limits of the measurement, the dried woodchip can be estimated accounting the error due to the uncertainty due to the instruments tolerance. Considering all sources of error in measurements such as temperature, irradiance and flow rate, the error of the SDMM was quantified between 10% and 16% for any of the solar woodchip dryer configurations. These high values are basically attributed to the significant error originated in the SATS thermal error.

5.4.2 SDMM simulation

The SDMM simulations predict the amount of product that can be dried by the solar woodchip dryer during a given period of time. Firstly, the drying conditions, air flow and SATS output temperature, were estimated from the weather data employing the selected collector configuration model. Later the batch-drying process was simulated during the given period of time. The woodchip tray is replaced once the MC has reached a minimum of MC of 30%.

Figure 5.7 shows the results of the SDMM simulation that corresponds to the solar dryer employing 3 different collector configurations. The input weather data corresponds to a windy day depicted in figure 5.6. The best results were obtained with the glazed 3mm TPC configuration since for 3 times the woodchip sample was dried down to 30% MC. The other collector configurations implied lower solar collector performance and for only 2 times the woodchip sample was dried to 30% MC.

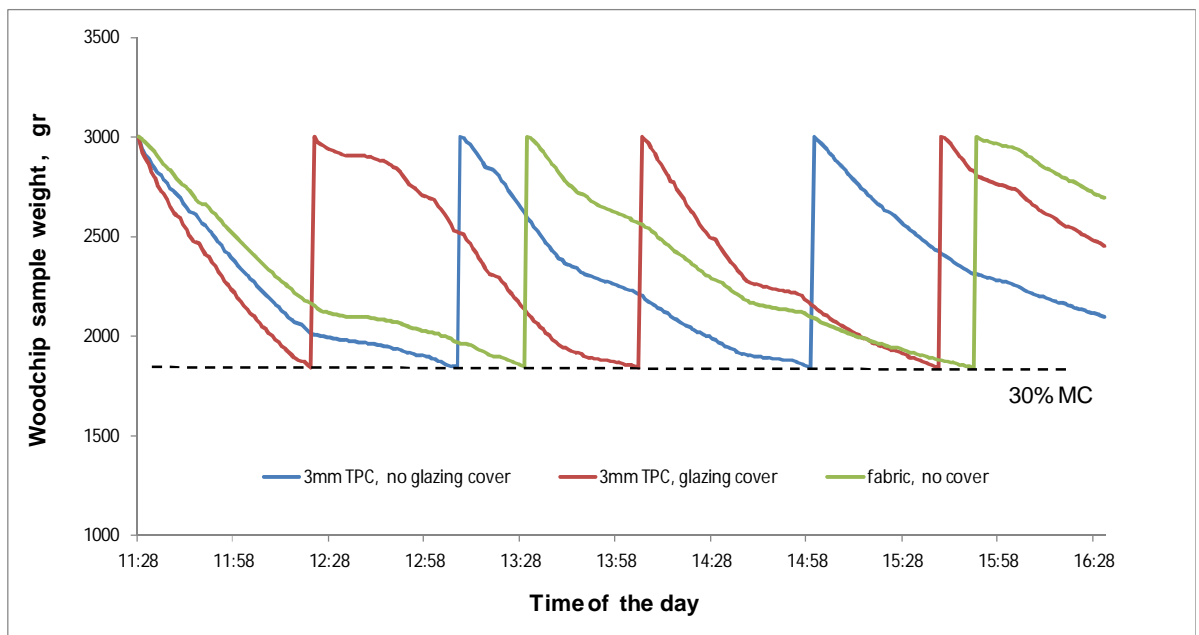


Figure 5.7: Drying simulation results for 3 solar dryer configurations working at identical weather conditions.

5.4.3 SDMM results for daily weather data

The present section presents the SDMM daily simulations results. The analysis of these results provides an indication of the drying capacity of the solar dryer when working under different weather conditions.

Figure 5.8 presents the results obtained from the SDMM simulations on 6

different days described in section 5.2.2. The graphic shows the amount of woodchip, originally from sample 2 that can be dried using the solar dryer 1 operating with 6 different solar collector configurations. The simulation results of the SDMM for each solar woodchip dryer configuration depended on the performance of the woodchip dryer and SATS system operating together and the profiles of irradiance and temperature for each day selected.

The performance of the solar woodchip dryer is strongly dependant on ambient temperature and on the season of the year. On cold days, despite of the solar radiation received by the SATS, the resulted drying temperatures are low and therefore the dryer production is low. However, on warm days, the resulted drying temperatures are high enough to produce adequate drying rates and therefore dry more wood. Moreover, in winter days, usually cold days, the total solar energy received by the SATS is lower than in summer.

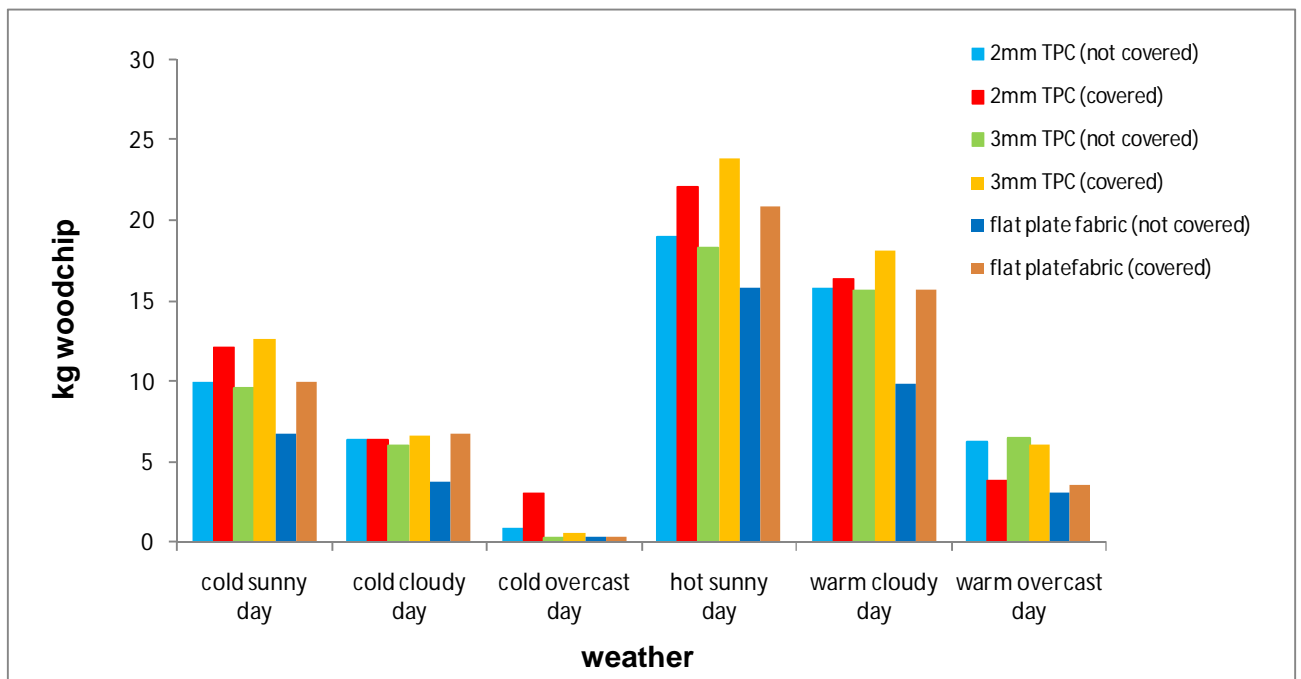
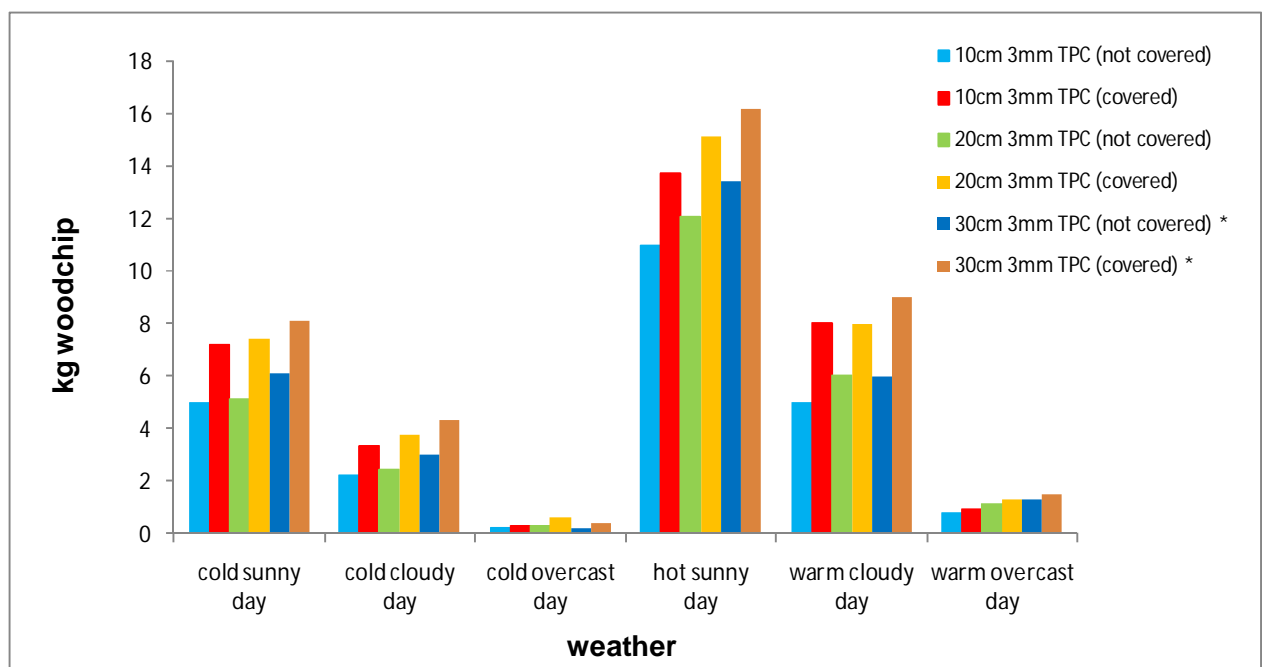


Figure 5.8: SDMM simulation of solar dryer 1 operating on 6 days at different weather conditions.

In general, it is observed that the solar woodchip dryer is more efficient when the solar collector is protected with a glazing cover. Unglazed collectors yield similar results for the different days selected. Using a glazing cover implies a reduction in heat losses and a consequent increment in drying temperature. This has resulted beneficial for the solar dryer as the simulation results show that increasing the temperature compensates the air flow reduction in the SATS. The results in figure 5.8 shows that the

SATS configuration with a 3mm TPC produces better drying conditions in comparison to other SATS with different collector configuration. The production of the solar dryer comprising a collector with a fabric absorber plate is comparable to the production of the same dryer with other TPC configurations.

Likewise, figure 5.9 shows the results obtained from the SDMM that simulates the performance of solar dryer 2 on 6 different days. The woodchip production in solar dryer 2 was much smaller when comparing it to the solar dryer 1 production at same conditions. The graphic also reflects a notable difference between the solar dryer production in cold and warm days. Although the thick layer dryer operate with higher drying efficiencies, the thermal performance of the SATS operating with a thick layer dryer was low. Its pneumatic characteristics were unfavourable and it introduced high pressure drop into the system, yielding low flow rates and high temperatures and consequent heat losses. Moreover, high pressure drop implies also high irradiance



(*) 30cm woodchip layer dryer tests were conducted with a woodchip sample of 50% MC.

Figure 5.9: SDMM simulation of solar dryer 2 operating on 6 days at different weather conditions.

threshold for the PV driven fan to start working. Covering the TPC reduces the flow but implied higher drying temperatures and overall better conditions for drying more woodchip. The increment in the thickness of the woodchip layer has a positive effect in the solar dryer performance, especially in days with high solar radiation. Figure 5.9 shows how increasing the woodchip layer, implies higher productivity. However the results shows that 30 cm layer woodchip dryer has notably better productivity at

identical weather conditions as the woodchip MC is 50% and in the other cases 60%. An optimal thickness can be found for this solar woodchip dryer configuration, considering simultaneously the drying performance and the pneumatic characteristics of the system. However, in this project, the optimisation of the woodchip dryer is not addressed and it is proposed as a further work.

5.4.4 SDMM results for annual weather data

5.4.4.1 Solar dryer 1 annual production

The results of the SDMM simulations processing annual weather data are shown in this section. The analysis of these results indicates the annual capacity of the solar woodchip dryer.

Figure 5.10 shows the production of dried woodchip predicted for each month of the year. The annual operation can be divided in two seasons: cold and warm season. During the cold season, winter and autumn months, the solar dryer production was very small due to the low solar radiation received and the low ambient temperatures. Three months were not productive at all, while there were three months in which woodchip dried production was lower than 150 kg. During the warm season, spring and summer months, SDMM estimated better results and the most productive month was July.

The SDMM simulation results revealed that the best collector configuration was the 3mm TPC with a glazing cover. In chapter 4, it was found that the SATS operating

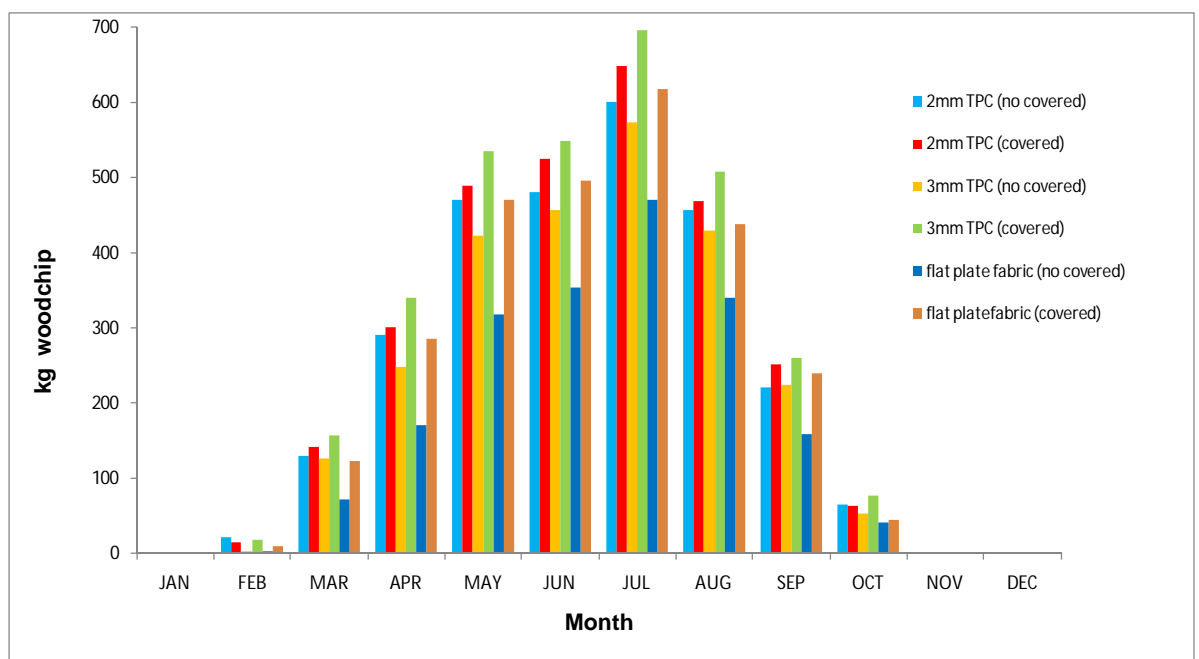


Figure 5.10: SDMM annual simulation for solar dryer 1.

with the 3mm TPC had better outcome than with the 2mm TPC. Adding a glazing cover to the collector was a clear benefit in all the cases, as the heat losses in the collector were reduced and the outlet temperatures were elevated.

Table 5.2: Annual dried woodchip production in solar dryer 1.

Weather data set	2mm TPC (not covered)	2mm TPC (covered)	3mm TPC (not covered)	3mm TPC (covered)	fabric flat plate (not covered)	fabric flat plate (covered)
1990 hourly measured data	2,538 kg	2,901 kg	2,778 kg	3,138 kg	1,929 kg	2,724 kg

Table 5.2 shows the total amount of dried woodchip produced by the solar thin layer dryer operating with 6 different collectors. The maximum amount of dried woodchip estimated in a year was 3,138 kg for the glazed 3mm Ø TPC configuration. It has to be noted that the annual input weather data did not introduce any fluctuation or oscillation in the SATS performance. The hourly weather data did not reflect either the irradiance peaks or the continuous fluctuations due to the clouds. A better approach could have been achieved by employing measured data with a small interval. Average weather data set was not convenient as the solar dryer woodchip performance was sensitive to small weather variations.

5.4.4.2 Solar dryer with a SATS comprising a 3mm TPC

Figure 5.11 shows the results of the SDMM simulations that predict the woodchip

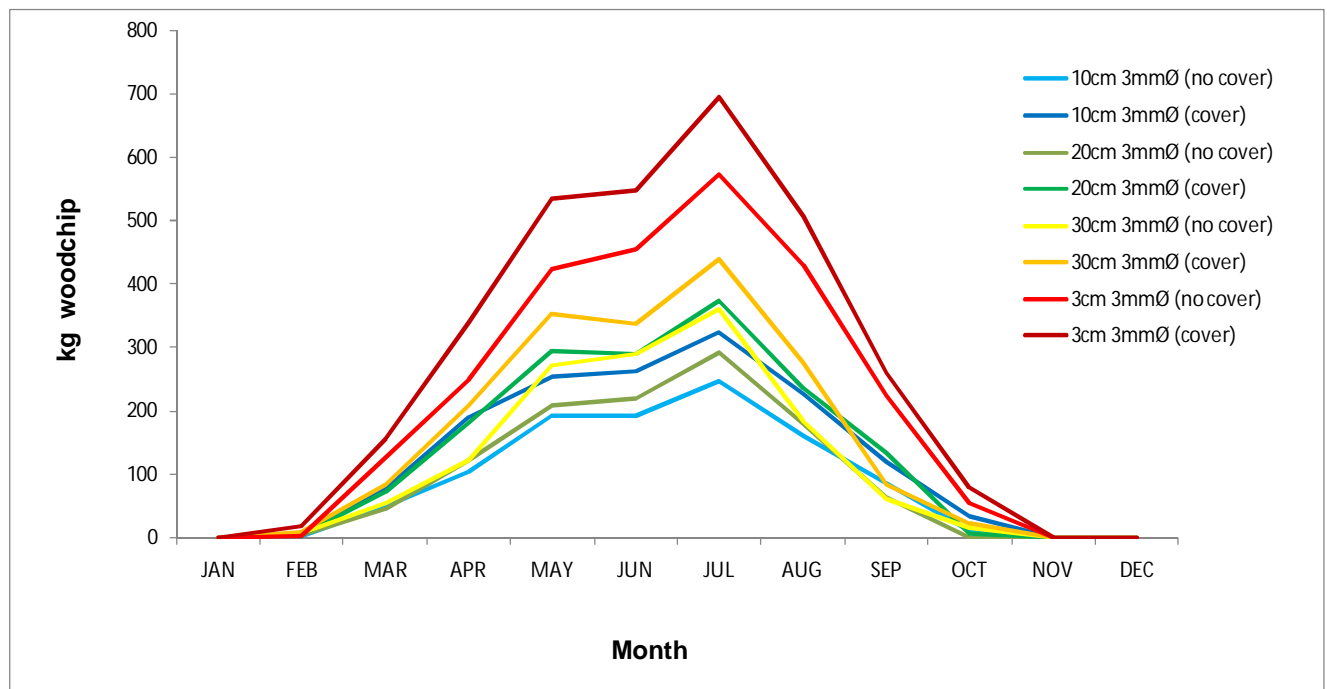


Figure 5.11: Comparison of the annual operation for solar dryer 1 and dryer 2 employing the SATS with a 3mm TPC covered and uncovered.

production for the solar dryer 1 and solar dryer 2 using the same SATS configuration with a 3mm TPC. The thin layer solar dryer was more efficient than the thick layer dryer when using the same SATS. The dryer design is crucial as it affects to the total air flow and to the drying rates. An optimal design of the woodchip dryer should firstly address the pressure drop of the system and later try to improve the drying process.

5.4.4.3 SDMM annual simulations for two woodchip types.

In chapter 3, two different woodchip samples were dried in order to study the dryer performance. The analysis revealed that the product characteristics such as MC_0 , size of the chips and wood properties were determining factors that affected to the drying rates, especially in thin layer dryers. Experimentally, it was observed that MC_0 was the factor that governed the drying process.

The annual dried production of these two different types of woodchip were estimated and compared by means of SDMM simulations conducted with identical SATS characteristics.

Figure 5.12 shows the annual dried production obtained for sample 1 with 57% MC_0 and sample 2 with 52% MC_0 . Since there is a difference in the total amount of water to be evaporated, it is expected that the sample with higher MC_0 would require longer drying times. The difference in the production is reflected in the graph. The maximum production for both cases was when SATS operated with a glazed 3mm TPC. The annual production for sample 1 was 2,680 kg of woodchip, 17% lower than production for sample 2 which was 3,138 kg.

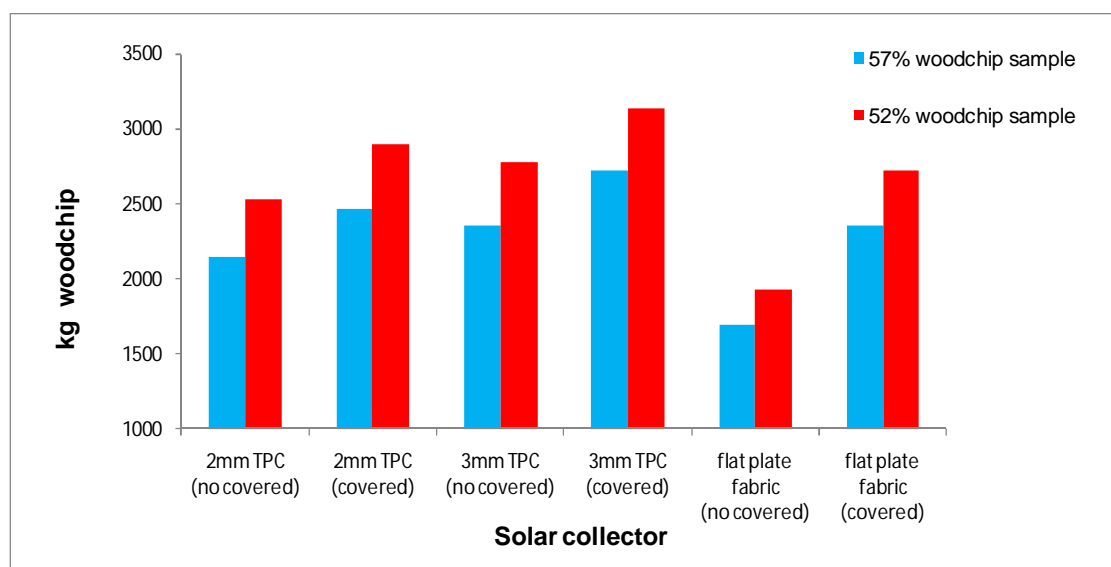


Figure 5.12: SDMM annual simulation for the solar dryer 1 drying two woodchip samples.

5.5 Evaluation of the solar woodchip dryer.

5.5.1 Solar dryer effectiveness

In previous section 5.4.3 the annual production of dried woodchip was estimated for 2 dryers operating with various SATS configurations. It was found that at identical weather conditions, the solar thin layer dryer dried more woodchip and therefore it was more efficient than the solar thick layer. Therefore, for the rest of the section, the analysis continues with the best solar dryer configuration which is formed by the thin layer dryer and 3mm TPC.

The effectiveness of the system was calculated as the product of the dryer efficiency and the thermal efficiency of the SATS. The solar dryer effectiveness can be also estimated as the coefficient between the total woodchip dried and the maximum amount of woodchip that the solar dryer could dry during a period of time, equation 5.3. In the calculation of the solar dryer effectiveness, the PV driven fan electrical operation efficiency was not taken into account. Both terms in equation 5.3 were calculated considering the modelled air flow as the maximum for each level of irradiance.

$$\eta_{solar_dryer} = \frac{Woodchip_{dried}}{Woodchip_{dried} (\eta_{collector} = 100\%, \eta_{drying} = 100\%)} \quad \text{Equation 5.3}$$

In section 3.3.3 the analysis of the thin layer dryer performance revealed that drying efficiencies were generally not high. In the range of drying temperatures and velocities, the dryer reduced the MC_0 of the woodchip to 30% with efficiencies values between the 50% and 60%.

The SATS with a TPC worked efficiently, especially when weather conditions were favourable. In full sun operation, air flow rates were high and unglazed TPC efficiencies values were around 70%. Efficiencies can reach up to 80% when using a glazing cover.

Table 5.3 illustrates the calculation of the solar dryer effectiveness based on the annual SDMM simulation results. It compares the estimated production of the solar dryer with the drying capacity when solar dryer operates with maximum drying and collector efficiencies.

Table 5.3: Monthly woodchip drying production and solar dryer effectiveness.

	JAN	FEB	MAR	APR	MAY	JUN	JUL	AUG	SEP	OCT	NOV	DEC	YEAR
Woodchip dried, kg ($\eta_{\text{collector}}=100\%$, $\eta_{\text{drying}}=100\%$)	80	224	655	1074	1478	1469	1746	1314	830	332	125	35	9,448
Woodchip dried, kg ($\eta_{\text{drying}}=100\%$)	60	104	366	649	924	913	1077	773	472	154	47	11	5,570
SDMM outcome, kg	0	18	156	339	534	549	696	507	261	78	0	0	3,138
Solar Dryer effectiveness, %	0	8	24	32	36	37	40	39	31	24	0	0	33

The table shows the estimated values of the monthly and annual drying capacity of the solar dryer when working under Scottish weather conditions. Thus, the solar collector studied has an annual drying capacity of 9,448 kg of woodchip. This value was much larger than the SDMM annual production estimated for the thin layer dryer, 3,138 kg of woodchip. Thus, an optimisation in the dryer configuration or modification in the SATS may easily enhance the performance in order to increase the efficiency of the system.

The annual solar dryer effectiveness was 33% which meant that the solar dryer system dried only one third of the maximum amount of woodchip possible to dry. The table shows that only for 6 months the average effectiveness of the collector was higher than 30%. For the rest of the months, the solar dryer is not suitable as efficiencies and production are too low.

5.5.2 Energy saving

The novel woodchip solar dryer had the advantage of working exclusively with solar energy for pre-heating ambient air. The monthly and annual energy savings produced by the SATS were quantified when it worked with a 3mm TPC. Table 5.4 shows the total solar energy received by the collector and the estimation of the total amount of energy utilised to rise the collector air temperature. The solar collector average efficiencies were estimated as the rate of the utile heat collected by the maximum energy available from the sun during a period of time, equation 5.4. The PV module energy contribution and efficiency was not evaluated. The air flow rates employed in the estimations were modelled as a function of the irradiance.

$$\eta_{solar_collector} = \frac{\sum \dot{m} \cdot C_p \cdot \Delta T \cdot \Delta t}{\sum G \cdot A \cdot \Delta t} \quad \text{Equation 5.4}$$

Table 5.4 shows the estimation of the monthly and annual amount of solar energy received and collected by the SATS for pre-heating the drying air. There was a notable difference in the solar collector operation between cold and warm seasons as was reflected earlier in the results obtained from the SDMM simulations.

Table 5.4: Energy collected by the SATS and average solar collector efficiencies in a year.

	JAN	FEB	MAR	APR	MAY	JUN	JUL	AUG	SEP	OCT	NOV	DEC	YEAR
Energy received, kWh ($\eta_{collector}=100\%$)	29	72	194	320	392	370	427	311	214	92	39	12	2,472
Energy collected, kWh (3mm TPC, glazing)	10	32	110	208	258	236	274	182	121	41	13	3	1,488
Solar collector efficiency, % (3mm TPC, glazing)	33	45	57	65	66	64	64	59	56	45	33	26	60
Energy collected, kWh (3mm TPC, no glazing)	9	29	97	183	225	206	238	159	106	37	12	3	1,305
Solar collector efficiency, % (3mm TPC, no glazing)	29	40	50	57	57	56	56	51	50	40	31	24	53

The annual thermal efficiency obtained from the SATS with a TPC was 53%. This is a reasonable value considering that the solar air collector usually operated at low-medium flow rates where collector efficiencies were rather low. When using a glazing cover, the TPC efficiency was higher, and the SATS annual thermal efficiency was 60%.

5.5.3 Study of feasibility

In the introduction chapter, the importance of the drying process in the woodchip chain supply in order to improve the quality of the product by reducing its moisture content was discussed. The ultimate objective of the solar dryer application is to reduce the drying and storing times and save production costs.

So far, the analysis of the presented solar dryer prototype covers all the technical aspects that affect the production of dried woodchip. However, the viability of this solar dryer for being an alternative requires the study of its employability and feasibility under operative conditions. Augustus Leon et al. (2002) suggest a list of factors to be taken into account for the practical assessment of the solar dryer:

- Volume of product
- Quality of the initial product and final product
- Drying season
- Drying times
- Costs of drying

5.5.3.1 Volume of woodchip.

The woodchip to dry is for energy purposes and therefore the objective of the solar dryer is to maximise the production of dried woodchip in order to cover a demand of fuel. The annual SDMM simulation results, obtained in previous sections, served as a reference for the amount of dried woodchip that may be produced by the solar woodchip dryer. These quantities can be compared with the annual demand of woodchip for various heating installations in order to define the range of application. Table 5.5 shows an estimation of the annual demand of woodchip for various cases with different heat loads in a high latitude location.

Woodchip installations usually require large amounts of wood fuel during the year. The final amount of demanded product depends on the heat load, the number of full load equivalent hours the installation works yearly and the quality of the product to burn.

Table 5.5: Heat demand in 4 cases, Cotton (2005).

	heat load, kW	full load hours equivalent	Energy/year, kWh	Tonnes of woodchip (0%MC, 5.2 MWh/tonne)	Tonnes of woodchip (30%MC, 3.5 MWh/tonne)
3 bedroom house	15 "peak load"	1,000	15,000	2.8	4.2
Offices	50– 150	1,400	210,000	40	60
Secondary School	500 – 2,000	1,000	2,000,000	380	570
Hospital	800 – 5,000	3,000	15,000,000	2,800	4,200

The best output of the solar woodchip dryer obtained from the SDMM simulation is 3.13 tonnes of woodchip at 52% MC which is equivalent to 2.1 tonnes of woodchip at 30% MC. This value is only comparable with the demand of woodchip estimated for a small house during a year. Thus the unique group of potential users that may be interested in the solar woodchip dryer prototype are small users that produce their own woodchip for their own consumption. The solar woodchip dryer prototype may be an alternative drying method for land owners that deal with their own fuel production and

search for economical solutions. Moreover, because of the low production, the design of the solar dryer application has to be simple and adaptable to the storing facilities.

5.5.3.2 Quality of the initial and final product.

The solar woodchip dryer prototype has reasonable performance efficiencies when drying fresh woodchip from high to medium MC levels. However when drying woodchip to low MC values, drying efficiencies may noticeably decrease since removing water at low MC requires more energy to evaporate the internal moisture in the woodchip.

Furthermore, the initial quality of the woodchip was an important factor as it was observed in section 5.3. Any reduction in the MC_0 before drying woodchip with the solar dryer implies shorter drying times and more dried woodchip production. Combining solar and natural drying may report important benefits when drying woodchip in a small scale.

5.5.3.3 Drying season.

In the previous section 5.5.1, the SDMM simulations showed that solar dryer efficiencies were very low during the cold season of the year. Thus the solar dryer operation time is reduced to the spring and summer months in which average ambient temperatures are warm and daylight periods are long. The season for drying woodchips using the solar dryer coincides with the period in which natural drying is more effective.

Necessarily, the viability study of the solar dryer prototype has to consider the performance of other drying alternatives such as natural drying. In high altitude countries, it is a common practice to leave the wood logs seasoning outdoors for a minimum of a year after harvesting the trees. This may reduce the wood MC down to acceptable levels for burning. However, the final quality of the wood is variable and it depends on the weather conditions: rain fall, ambient temperature and relative humidity.

Besides the solar drying tests, natural drying tests were also conducted during the spring and summer time. Table 5.6 shows the change in MC observed in various woodchip samples left drying outdoors for one day. The final MC values varied with the weather conditions although drying times were found very short for a thin layer of woodchip. The moisture in the superficial layers was removed quickly by the air surrounding however thick woodchip layers required longer drying times.

Overall, high drying rates were observed when the woodchip was naturally dried since the frequent wind makes the air circulate effectively over the woodchip layer. It was observed that natural drying for thin layers was quite effective and large amount of woodchip could be dried by spreading the product on a large area. Experimentally increasing the thickness of the layer created a distribution of MC in the product and the average final MC was higher.

Table 5.6: Natural drying sample results after 1 day drying

Day	Weather like	Sample weight	Thickness	MC ₀	MC _{final}
29/05/2009	Sunny and warm	4 kg	10 cm	60 %	29 %
30/05/2009	Sunny and warm	4 kg	10 cm	65 %	32 %
08/07/2009	Overcast	3 kg	10 cm	55 %	41 %
09/07/2009	Raining	3 kg	10 cm	41 %	50 %
10/07/2009	Cloudy and windy	3 kg	10 cm	50 %	35 %

5.5.3.4 Drying times

The solar woodchip dryer performance depends on the weather conditions and therefore its production is not constant. Drying times are not constant and vary with drying conditions. This implies an important disadvantage to the dryer design as a continuous feeding system is not feasible to be installed for controlling the woodchip input. Thus, an additional automatic feeding system is necessary. This feeding system may be controlled by using electronic logic circuits or by developing a PV driven application whose performance is also governed by the solar radiation. Anyhow, this system may reduce the effectiveness of the solar dryer installation and it will increase the production costs.

5.5.3.5 Economical analysis

An economical study of the solar dryer has been included in order to assess the viability of the prototype installation. The solar woodchip dryer prototype has two main advantages: Firstly, it is an independent system that operates with no connection to the electrical grid. And secondly, operation and maintenance costs are low as the unique moving part of the system is the fan. However the dryer application needs a peripheral system to control the production. This may increase the complexity of the system and the drying costs.

Table 5.7 shows the costs derived from each of the components that comprise the solar woodchip dryer. The total cost, obtained as the sum of all the contributions, can be used as an approximation of the price of the solar woodchip dryer prototype. The total price should also consider the labour costs.

Table 5.7: Solar dryer component costs

	Description	Quantity	Price/unit	Price	Supplier Reference
PV module	10W _p PV/SX 310 BP	1 unit	£100	£100	BP solar (2007)
Fan	PAPST, 5W, 12 VDC	1 unit	£25	£25	PAPST (2003)
Absorber plate	aluminium 1.5mm sheet	1.8m ²	14£/m ²	£28	Forward metals (2009)
Glazing plate	twin wall polycarbonate sheet	1.8m ²	12£/m ²	£24	Wickes (2010)
Collector frame	18mm plywood	3.5m ²	10£/m ²	£35	A1 building supplies Ltd (2010)
Collector structure	L- rod steel	-	10£/m	-	Metals4u (2010)
Dryer frame	10mm plywood	1.6m ²	8£/m ²	£15	A1 building supplies Ltd (2010)
Tray	Metallic mesh 6mm x 6mm	0.3m ²	3.5£/m ²	£1	4wire Ltd (2010)
Ducting	1.5 m aluminium flexible ducting	1.5 m	3.5£/m	£5.25	Ductingshop (2010)
			TOTAL	£233.5	

The direct cost also includes all the manufacturing and operations required to assemble the solar dryer parts and for installing the system at the location. The main actions to build the solar dryer are:

- Manufacturing operation with CN machine for drilling the holes in absorber plate.
- Painting the absorber plate with black mate or selective surface painting.
- Assembling the collector wooden frame components.
- Painting all the wooden surfaces with varnish protector.
- Assembling the dryer components.
- Installing the solar collector into the metallic structure and connecting it to the dryer.

The estimated total cost of the solar woodchip dryer includes manufacturing and material costs although the above operations and actions necessarily need to be considered in the total costs.

The solar dryer requires a minimum of maintenance and manpower to supervise the production. Moreover, the material utilised as the wooden structures of the dryer and

the collector limit the lifespan of the system. Thus the benefits of installing a solar woodchip dryer are not clear if considering other economical alternatives as natural drying and seasoning wood logs.

5.5.3.6 Conclusions from the study of feasibility.

In conclusion the solar dryer prototype studied didn't satisfy the minimum requirements for being an alternative solution for drying woodchips. Although the idea of using a SATS for pre-heating air is attractive, drying woodchip in a cabinet box is not feasible and present serious problems. These are three main drawbacks that make the system not viable.

- Low production.
- Non continuous production.
- Storing problems.

Despite of the woodchip dryer and the SATS performance, the solar air dryer prototype is not suitable for drying woodchips for fuel because of its small capacity. Even if the production of dried woodchip was still considerable, the system has serious drawbacks as the system necessitates long period of time to dry and also requires a space to store the wet and the dried woodchip.

Storing and drying woodchips have to be addressed at the same time in order to save costs, especially in applications with low scale productivity. The woodchip dryer necessarily has to be adapted to the storing facilities. Employing this particular solar dryer with a PV driven fan is not the most convenient as its operation and its production heavily depend on the weather conditions and this may be counterproductive.

However, the same SATS may be more effective for ventilation when drying wood logs or stored wood piles indoors. Particularly, the studied SATS prototype can be an interesting device for drying wood logs in places where the electrical connection to the grid is not available. The SATS probably can be employed effectively in a solar kiln dryer or also in a wood fuel store where a pile of logs dries in a closed cabinet.

Scaling up the SATS system using a larger solar collector and employing a higher PV driven fan capacity may increase the woodchip production. However the main drawbacks as storing and automatic control problems will still remain.

Despite of the solar dryer performance, it was found that a TPC installation may save a notable amount of energy when preheating air during the warm season. In projects in which there is a high volume of product, the solar air heater may be used to backup the main energy system of the dryer and its purpose is to save energy, Hollick (1999). Thus, in a woodchip drying installation with a forced ventilation system, the benefit of using a transpired plate collector installation should be taken into account as the heat collected increases the air capacity of drying.

In order to obtain an approach towards woodchip production that would be feasible with a large solar dryer, next section assesses a large solar transpired plate application for drying woodchip under Scottish conditions.

5.6 Solar wall for drying woodchip

Transpired plate collectors have been employed widely in pre-heating air applications. In this section, the potential of utilising a large TPC for drying woodchip has been assessed. Based on experimental results about the performance of the Solar Wall application, a simulation tool has been developed in order to estimate the capacity of drying woodchips under certain conditions. Thus the results obtained are taken as a reference to estimate the production of dried woodchips and energy savings when TPC operate under Scottish weather conditions.

5.6.1 Solar wall drying model

The solar wall drying model, SWDM, has been developed to study the viability of using a solar air heater for drying woodchip in large scale production. The code was developed using VBA programming tools to process weather input data from an EXCEL spreadsheet. The results obtained from the SWDM simulations are not based on experimental work. However they represent a reasonable approximation of what a real solar woodchip dryer application may produce.

Firstly the program simulated the operation of a large TPC installation based on the Solar wall performance calculating the collector outlet temperature for a given air flow rate. Secondly the drying capacity is estimated as the maximum amount of water that circulating air can remove from the product. And finally based in the drying capacity of the dryer, the total amount of woodchip that can be dried is obtained. The

code of the Solar wall drying model is commented and in detail described in **Appendix A6: SWDM**.

The sequence of actions is described below:

1. Process the weather data available in an adequate format and calculate the psychrometric characteristics of the ambient air data.
2. Calculate the psychrometric characteristics of the air at ambient wet bulb temperature.
3. Calculate the drying temperature and psychrometric characteristics of the drying air for a given heat and flow input.
4. Calculate the psychrometric characteristics of the air at drying wet bulb temperature.
5. Calculate the amount of water evaporated when a given air flow circulates at ambient temperature and also at drying temperature.
6. Calculate the energy proportional to the difference between ambient and drying air enthalpies.
7. Based on the maximum water evaporated during a period of time, calculate the amount of dried woodchip when drying a product with a given MC_0 down to MC_{final} .
8. Calculate the energy of the woodchips at MC_{final} and the increment of energy because of drying. Finally the energy contained in the woodchips is compared with the solar energy collected by the solar wall.

The weather input data employed for the SWDM simulations was a set of hourly data collected during the year 1991 in an Edinburgh location, used previously for the SDMM simulations.

The thermal performance of the Solar Wall is based on the experimental results obtained by Hollick (1999), Figure 5.13. The thermal performance was obtained for various flow rates where ΔT presented a linear relationship with solar radiation. In addition, the ΔT values obtained from the TPC performance in chapter 4 were comparable to the values for the solar wall performance. The collector outlet temperatures were calculated exclusively as a function of irradiance and ambient temperatures. The negative effect of the wind in the solar wall performance was not taken into account because of the increment in the complexity of the calculations. Thus

the total energy collected may be overestimated in periods of time with windy conditions.

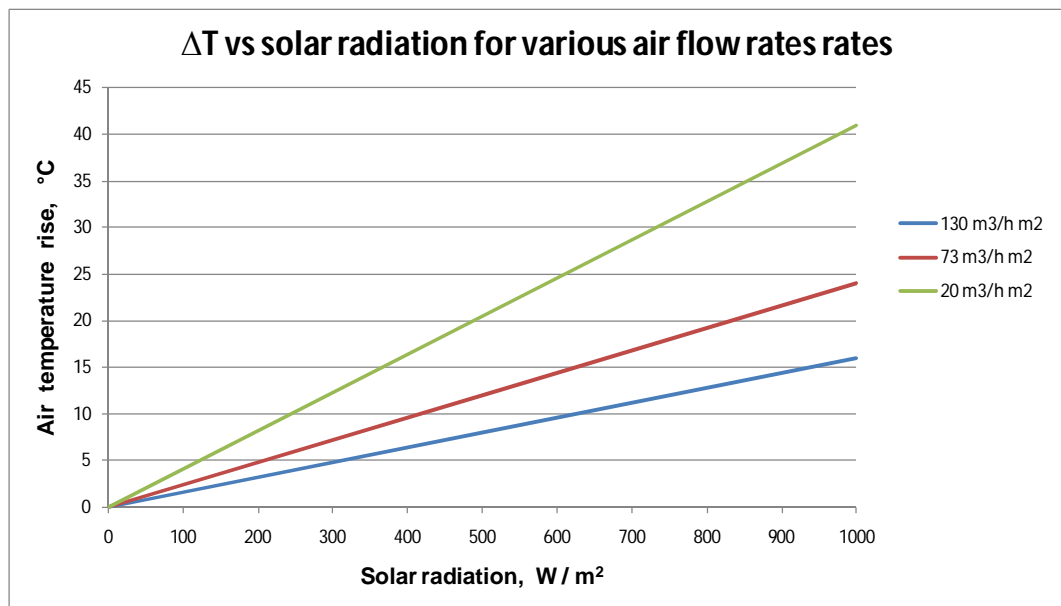


Figure 5.13: Solar wall collector performance.

On other hand, it is considered that the most suitable dryer configuration to work with a large solar wall installation is a deep bed dryer. In the literature review chapter, there were presented various cases in which forced air ventilation systems were used to dry woodchips. The applications consisted of high load capacity dryer systems that operate with large amounts of woodchip, forming a deep layer of several tonnes of woodchips. Mc Govern (2007) and Gigler et al. (2000) monitored the characteristic variables of the drying process. They observed that almost during the whole process, moist air left the dryer completely saturated or with a relative humidity between 90% and 100%, independently of the initial quality of the product. Only at the end of the drying process, air was not saturated and drying efficiencies decreased. Thus for the SWDM simulations, the dryer efficiency was taken as a constant during the process, 90% over the maximum drying capacity of the air. The dryer efficiency includes all the irreversibilities involved in the drying process.

5.6.2 Solar wall dryer results

The SWDM simulation results presented provided a valuable reference for the estimation of the solar woodchip dryer performance in a large scale. Two cases are studied for two different solar wall sizes when working with various air flow rates.

At the same time, the results bring out the importance of the woodchip quality in the drying process. The water to be evaporated depends on the initial and final quality of the woodchip and therefore the total dried woodchip production depends on the MC_0 and the MC_{final} .

5.6.2.1 Case 1: Small solar wall dryer: 20m²

In the first case studied, the SWDM simulates the performance of a solar dryer that consists of a 20 m² solar wall and a deep dryer. The solar dryer is set to work 12 hours per day, from 8:00 am to 8:00 pm every day.

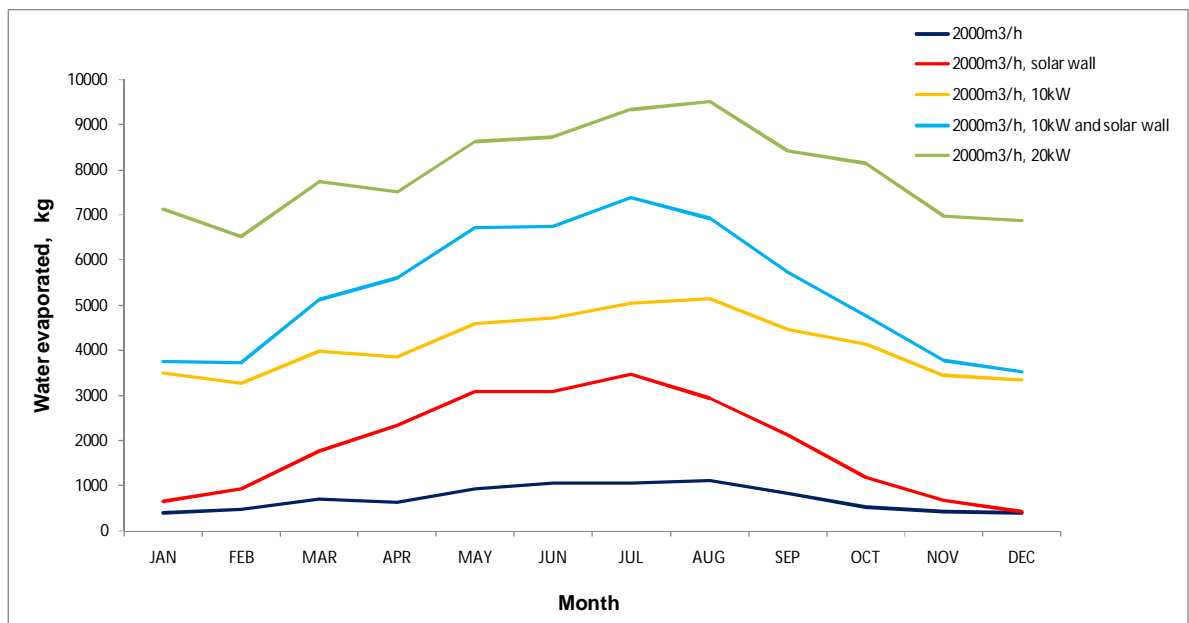


Figure 5.14: Drying capacity of the solar wall dryer using different heating inputs.

SWDM simulation results in figure 5.14 shows the values of the maximum amount of water that can be evaporated in each month of the year when using different preheating systems. The air flow that circulates in the solar wall dryer system does not dependant on irradiance and a constant flow is delivered during the operation. The air flow selected in this case was 2000 m³/h. Thus, this air flow implies that in the solar wall installation there is an approaching air velocity of 100 m³/h m². The different curves correspond to the SWDM simulations when air circulates without preheating and also when air was preheated by different heating resources: a 20 m² solar wall, a 10 kW and 20 kW heaters. Complementarily the results also shows the simulation results of the 20 m² solar wall operating with a heat source of 10 kW systems simultaneously.

The graphic shows that using a pre-heating system increases the potential of evaporating water and therefore increases the production of woodchip. The solar wall

results are effective for 8 months of the year, however between November to February the solar wall is not appropriate for being used. The solar wall installation either implies an increment in the total product to dry or a reduction of costs by saving energy. It was observed that the contribution of the solar wall in the total production was very similar when another heat source worked along with it.

Table 5.8 analyses the annual production of the solar dryer comprised of 20m² TPC operating with 4 different air flow rates or air collector velocities. The table includes the amount of woodchip that would be dried reducing the moisture in the product from 50% MC₀ to a MC_{final} of 20%.

In order to evaluate the action of drying, the energy gain of the woodchip has been estimated as the difference of the woodchip energy before and after drying. Woodchip energy values were calculated by multiplying the weight of the wood and the low heating value at its corresponding MC.

The annual energy rate was defined by the division of the increment of the woodchip energy gain and the total solar energy collected. The values showed that the increment of energy in the woodchip dried during a year was very similar to the energy savings produced by the solar collector. The table values show that energy rate increases with air flow. This is reasonable since the TPC thermal efficiencies also increase with the air flow.

In this study, only the thermal energy savings are considered despite the electrical energy consumption may be considerably high. The total fan energy consumption depends on the power required to overcome the pressure drop because of the woodchip bed. The dryer installations usually requires of large capacity fans.

Table 5.8: Performance of 20m² solar dryer at different flow rates.

Air velocity m ³ /h m ²	Flow m ³ /h	MC ₀ %	MC _{final} %	Weight ₀ kg	Weight _{final} kg	LHV@50%, kWh/Kg	LHV@20%, kWh/Kg	Woodchip energy gain, kWh	Collector energy saving, kWh	Energy rate
50	1000	50	20	37,531	23,457	2.2	4	11,259	11,655	0.96
75	1500	50	20	47,241	29,525	2.2	4	14,172	13,751	1.03
100	2000	50	20	54,575	34,109	2.2	4	16,372	14,814	1.10
125	2500	50	20	62,326	38,953	2.2	4	18,697	16,027	1.16

Table 5.9 shows the SWDM simulations results of the 20m² solar wall for drying a deep bed of woodchips with different MC₀ and MC_{final} values. The production results

are based on the maximum amount of water that the 20 m² solar wall operating with an air flow of 2,000 m³/h can dry during a year: 22,739 kg. Assuming a drying efficiency of 90% constant for all the cases, the total water evaporated in a year is 20,465 kg.

Table 5.9: Performance of 20m² solar dryer operating with an approaching air velocity of 100m³/ h m².

Air velocity m ³ /h m ²	Flow m ³ /h	MC ₀ %	MC _{final} %	Weight ₀ kg	Weight _{final} kg	LHV@ MC ₀ kWh/Kg	LHV@ MC _{final} kWh/Kg	Woodchip energy gain, kWh	Woodchip energy _{final} , kWh	Energy increment %
100	2000	60	20	40,932	20,466	1.6	4	16,372	81,863	20.00
100	2000	50	20	54,576	34,110	2.2	4	16,372	136,439	12.00
100	2000	40	20	81,864	61,398	2.8	4	16,372	245,590	6.67
100	2000	60	30	47,754	27,288	1.6	3.4	16,372	92,778	17.65
100	2000	50	30	71,631	51,165	2.2	3.4	16,372	173,960	9.41
100	2000	40	30	143,261	122,795	2.8	3.4	16,372	417,504	3.92

The table shows how the initial and final quality of the woodchip determines the total amount of woodchip that can be dried. The higher the MC₀ or the lower MC_{final} is, the lower the amount of woodchip is dried. The results obtained confirm that reducing the MC₀ can be valuable in order to yield large productivity. Therefore natural drying in the first stages combined with solar drying may report important benefits.

The energy gained by the woodchips is proportional to the amount of water evaporated. In each case, it is estimated exactly the same amount, 16,372 kWh, because of the linear relation between the low heating value and MC.

The energy increment is defined as the rate between the energy gained and the energy in the woodchip. For the same solar dryer, was higher in the cases where MC₀ was high or MC_{final} low.

The energy increment represents the percentage of energy gained because of drying by the total energy of the woodchip. In the same drying conditions, the energy increment rate is higher for the sample of woodchip with high MC₀ and low MC_{final}.

5.6.2.2 Case 2: Large solar wall dryer: 100m²

In the second case studied, the SWDM simulates the performance of a solar dryer that consists of a 100 m² TPC and a deep bed dryer. This case may represent a closer approach to a real situation where a woodchip producer stores woodchip and installs a transpired plate collector in the most favourable façade. The solar dryer is set to work 12 hours per day, from 8:00 am to 8:00 pm every day.

Table 5.10 analyses the annual production of the solar dryer comprised of 100 m² TPC operating with 4 different air flow rates. Because of the linearity of the equations employed in the calculations, the woodchip production and the energy savings are proportional to the results obtained in case 1. The energy savings because of the TPC installation are quite considerable. Moreover, using the TPC as a backup system for pre heating the air can be used in a larger dryer installation to dry more woodchips per day.

Table 5.10: Performance of 100m² solar dryer at different flow rates.

Air velocity m ³ /h m ²	Flow m ³ /h	MC ₀ %	MC _{final} %	Weight ₀ kg	Weight _{final} kg	LHV@60%, kWh/Kg	LHV@20%, kWh/Kg	Woodchip energy _{final} , kWh	Woodchip energy gain, kWh	Energy saving, kWh	Energy rate
50	5000	50	20	187,658	117,286	2.2	4	469,146	56,297	58,275	0.96
75	7500	50	20	236,206	147,629	2.2	4	590,516	70,861	68,756	1.03
100	10000	50	20	272,878	170,549	2.2	4	682,196	81,863	74,073	1.10
125	12500	50	20	311,630	194,768	2.2	4	779,075	93,489	80,137	1.16

Table 5.11 shows the SWDM simulation results obtained from the performance of 3 TPC dryers with different areas working with a constant air flow rate.

Table 5.11: Performance of 3 solar dryers operating at the same air flow rate.

Area m ²	Air velocity m ³ /h m ²	Flow m ³ /h	MC ₀ %	MC _{final} %	Weight ₀ kg	Weight _{final} kg	Woodchip energy _{final} , kWh	Woodchip energy gain, kWh	Energy saving, kWh	Energy rate
80	125	1000	50	20	249,304	155,815	548,468	74,791	64,110	1.166
100	100	1000	50	20	272,878	170,549	600,333	81,863	74,073	1.105
125	80	1000	50	20	304,972	190,607	670,939	91,491	87,559	1.044

The larger the area of the solar collector is, the more energy is collected and the higher are the drying temperatures. Thus, the installation with smaller area operates with higher collector velocities and produces lower collector outlet temperatures. The TPC with larger area receives more solar radiation and works with lower collector velocities; therefore it produces higher collector outlet temperatures and the dried woodchip production is larger.

5.6. Summary

In this chapter the performance of the solar woodchip dryer prototype has been modelled in order to estimate the production of dried woodchip for a given period of

time. Thus the SDMM tool has been developed to simulate the operation of the solar woodchip dryer prototype under Scottish weather conditions. The SDMM is based on the experimental results obtained from the woodchip dryer and the SATS. This tool obtained the drying conditions from the weather input data and later simulated the drying process to estimate the woodchip dried production.

The SDMM simulation results served to compare the performance of various solar woodchip dryer configurations studied. The results harvested from the daily weather data revealed that the thin layer dryer configuration was more efficient than the thick layer dryer configuration. Moreover, the best solar dryer performance was obtained when the SATS comprised the glazed 3mm TPC. The results obtained from the annual weather data showed that for this configuration, the production was 3,138 kg of dried woodchip. The average annual dryer effectiveness was 33%. However during the cold season including the months of autumn and winter, the solar dryer performance was very low as the weather was not good and the SATS thermal performance was also low.

The feasibility study of the solar woodchip dryer didn't show an optimistic prospect for using the prototype as an alternative for drying woodchips. Although the analysis showed that the system had a relatively low cost and low maintenance, there were important drawbacks to consider. The low annual production and the difficult integration of the dryer in the storing facilities made the system no suitable for drying woodchip for fuel in small scale. Moreover, the woodchip production was not continuous as it depends on the weather and therefore an automatic feeding system may be needed to be designed, increasing the total costs.

The SATS based on a PV driven fan has not resulted as an adequate system for pre-heating air for drying woodchips in particular. However a large installation of transpired plate collector, such as solar wall, can save important amount of energy to the woodchip producers. This system, as it can be installed integrated in the storing façade or roof, can be easily adapted in a force ventilation dryer installation as a backup for pre heating the drying air.

A solar woodchip dryer tool based on the solar wall performance was developed in order to provide a realistic approach of the annual woodchip production with a medium/ large scale solar woodchip dryer. The production of dried woodchip and the energy savings were estimated for 2 different situations. The results showed the benefits of combining natural drying and solar energy for producing larger amount of dried woodchips.

6. CONCLUSION AND FURTHER WORK

6.1 Introduction

Energy plays an important role in the socio-economical and political situation of the countries. Modern societies use more energy resources every year resulting in increased environmental concerns associated with the global warming and climate change. Ensuring a secure, clean and affordable supply of energy, using local resources, is essential for the sustainable development of a modern society.

Scotland has a large potential in renewable energies, especially in off-shore wind and tidal resources for power generation. Moreover, the country has an important production of forestry resources that can contribute to cover partially the heating demand, particularly in remote places off the gas grid. Thus during last decade many projects have been carried out to create a wood fuel market and benefit the local economies.

Technology and new techniques have been developed in order to enhance the efficiencies of wood processing. Within the wood fuel chain supply, drying is essential as the moisture content in the wood sets the quality of the product. Removing water from wood is necessary in order to reduce storing and handling costs and to increase the heating value of the wood.

The thesis presented a novel system for drying woodchips using solar energy. This system comprised a solar air thermal system, SATS, and a small capacity woodchip dryer. The SATS consists of a solar collector based on a transpired plate collector and also a PV driven fan whose performance depends mostly on the incident solar radiation. The pre heated air from the collector is employed to dry a small amount of woodchip set on the tray of the woodchip layer.

The aims of the current thesis were to analyse the characteristics of both woodchip dryer and SATS performances and to develop a model for predicting the production of dried woodchip from the solar woodchip dryer prototype described above. The approach involved laboratory tests to study the dryer performance and the pneumatic characteristics of the solar dryer, field tests to analyse the thermal performance of the SATS within the solar dryer and a feasibility study of the novel

woodchip dryer prototype. This chapter of the thesis presents the conclusions regarding the modelling and testing of the system. Areas of further work in order to improve the understanding of this system are then suggested.

6.2 Summary of conclusions

Results gathered from the experiments are as follows:

6.2.1 Drying woodchips

The methodology adopted for the study of the woodchip dryer prototypes was appropriate to analyse the woodchip drying process.

The drying curves obtained from the drying tests, employing either the thin or the thick layer dryer prototype, had always an exponential behaviour. Drying rates were proportional to the water binding capacity of the drying air. For constant drying conditions in relative humidity and temperature, the drying rates were proportional to the drying velocity.

When employing the thin layer dryer to dry woodchips from MC_0 to 30% MC, average drying efficiencies were between 50% and 60%. The lower the MC in the woodchip was, the lower the drying rate and drying efficiency were. When drying two types of woodchips with different qualities at similar drying conditions, in the beginning of the process the drying rates were very similar. Therefore independently of the size of the woodchip, the sample with lower MC_0 dried quicker down to the limit desired.

When employing the thick layer dryer to dry woodchips from MC_0 to 30% MC, average efficiencies were found between 70% and 90%. As the layer of woodchips was thicker, the air-woodchip contact path length was longer. Therefore drying air removed water more effectively yielding higher drying rates and higher dryer efficiencies.

Page model was selected as the most suitable mathematical model equation to describe the exponential drying curves obtained from each drying tests conducted with either thin or thick layer dryers.

Based on the Page model expression, for each set of tests, a macro model was successfully developed to estimate the MC as a function of drying parameters: temperature, velocity and relative humidity. A minimum of 5 test results were required for modelling the drying performance with a reasonable accuracy.

6.2.2 PV driven fan flow modelling

The operational I-V points from the PV module and fan electrical interaction were successfully described as a function of solar radiation. The effect of the PV plate temperature on the PV driven fan voltage was found negligible.

Pressure drop in the dryer system was determined by the tray area, the thickness of the woodchip and the drying velocities. It was found that the pneumatic characteristics of the thick layer dryer design were not favourable for a solar dryer design because of the high pressure drop introduced by the woodchip layer and the high drying velocities. The solar dryer configurations, comprising the thick layer dryer, operated with very low air flow rates.

The pressure drop in the solar dryer conditioned the PV driven fan operation. Thus the threshold solar radiation values, associated to the PV driven fan starting performance, were considerably higher in the solar dryer with a thick layer of woodchip than in the thin layer.

The pressure drop measured in various solar collector configurations was low. The TPC introduced slightly higher ΔP than the flat plate collector made of fabric. The ΔP -Q curves of the unglazed TPCs were successfully described using the equations suggested by Kutcher (1995). The results revealed that pressure drop was mostly caused by the friction between air and the holes in the plate. Thus the pressure drop mainly depended on the porosity of the collector and the suction velocity. The glazing cover increased slightly the pressure drop in all the solar collector configurations.

Based on the ΔP -Q curves and the electrical connection of the PV driven fan, the air flow was modelled exclusively as a function of irradiance. Thus, for each solar dryer configuration, a 2nd order polynomial best fit curve was obtained. The flow model results showed good agreement with the experimental values measured in the field.

6.2.3 SATS thermal performance

The thermal performance of the SATS was obtained experimentally for each solar dryer configuration. The SATS performance was simplified to a unique operational mode, assuming that the air flow circulating the system depended exclusively on the solar radiation. Thus, in each solar dryer case, the collector ΔT depended on irradiance values. Parameters such as the thermal mass of the system temperature, the wind and cloudiness affected significantly the SATS performance.

The thermal performance of the SATS slightly changed when modifying the hole size or hole distribution of the unglazed TPC. The collector outlet temperatures depended on the air flow circulating the system and therefore on the pneumatic characteristics of the solar dryer configuration. The heat gain and thermal efficiencies increased with flow and therefore with solar radiation. For the same level of irradiance, the different unglazed TPC produced similar ΔT . Therefore the TPC that operated with higher air flow transferred more collected heat to the inlet air.

The SATS thermal performance was not efficient when working with the thick layer dryer. Air flow rates were too low and were not enough to ensure the right functioning of the solar collector and elevated heat losses were registered. However, the SATS performance obtained notable efficiencies when operating with the thin layer dryer. At $1,000\text{W/m}^2$, the thermal efficiency of the SATS comprising the 3mm TPC was 71.3%. The glazing cover in the TPC meant a moderate reduction in the air flow that was compensated saving heat losses. The 3mm TPC covered with a glazing cover produced a maximum efficiency of 78.1% at 1000W/m^2 .

The SATS thermal performance was modelled employing the steady state data obtained at stable solar radiation conditions. The steady state points selected from each solar collector tests showed a linear relationship between ΔT and solar radiation. Two ΔT curves that corresponded to morning and afternoon data described the SATS performance during one day. A statistical regression analysis showed a reasonable correlation between predicted and experimental data obtained from the SATS at various weather conditions. The error of the model was mainly associated to the lack of parameters to describe the transient. A correction factor based on the collector time constant may reduce the model error.

Wind implied heat losses in the collector and modified the steady state regime of the SATS performance. The wind effect was notably minimised when the collector was covered. However, windy conditions meant a major impact on the SATS performance because the movement of the clouds generated fluctuations in the solar radiation values and therefore a consequent transient regime.

6.2.4 Solar woodchip dryer

SDMM programming tool was developed based on the woodchip dryer and the SATS experimental results. This tool simulated the solar woodchip dryer performance and estimated the amount of dried woodchip production in a period of time. The

predicted results obtained from the SDMM simulations with real weather data were satisfactorily validated with the corresponding experimental results.

SDMM simulation results revealed that the solar dryer prototype comprising the thick layer dryer had a low performance: the high drying efficiencies didn't compensate the negative effects of the high pressure drop. The daily and the annual SDMM simulation results in the thick layer dryer were poorer than in the thin layer dryer. The SDMM simulation results obtained from processing annual weather data from the location gave an estimation of the capacity for solar woodchip dryer. The solar dryer configuration comprising a SATS with a 3mm covered TPC and the thin layer can dry yearly 3,081kg of woodchip at 52% MC down to 30% MC. The annual solar dryer average efficiency for this case was 33%.

A small difference in the thermal performances of the SATS comprising a TPC meant a significant difference in the woodchip dry production. When TPC also has a glazing cover, the solar thin layer dryer performance was resulted notably more efficient. SATS comprised of a flat plate collector with a fabric absorber with glazing had a significant woodchip production in warm days.

The SDMM simulation results also indicated that the major woodchip production from the solar dryer operation was obtained during the spring and summer months, when days have long daylight. The solar dryer prototype was found ineffective during the cold season.

The employability of the solar woodchip dryer was limited because of its low annual production. Thus only small scale producers or owners may be interested in a solar application for drying or complementing the wood seasoning. The manufacturing cost of the solar dryer application was not high. However there were various designing factors that may increase the system costs and make the system hardly feasible for drying woodchips: controlling the woodchip feeding system and adapting the dryer prototype to the storing facility were the main drawbacks to be addressed when installing the solar dryer.

Scaling up the solar woodchip dryer prototype is advantageous for the global performance of both woodchip dryer and SATS. Scaling up usually implies higher production with better efficiencies in the processes. However the important drawbacks observed for the small prototype would be also reproduced in a large scale installation limiting the viability of the system. The dried woodchip production of the woodchip dryer should not depend on the weather conditions as it implies feeding control

problems and increases the costs of production. However the usage of a large scale solar dryer can report important saving costs in a woodchip dryer or storing installation, especially in remote places off the electrical grid. The power collected by a large PV installation can be stored and used more efficiently to power a fan. The solar air heater could provide heat to back up the main heating system. And a deep bed dryer, with optimal relation between layer thickness and pressure drop, can produce an adequate rate of dried woodchip.

A commercial application of the TPC like a Solarwall may have an important role for saving energy and reduce drying and storing costs when drying large volumes of woodchip in large installations. A solar wall installation can be used as a backup system for preheating drying air. A SWDM was developed to estimate the capacity of drying woodchip employing a solar woodchip dryer based on a solar wall installation.

6.3 Contribution to knowledge

This research involved the study of a novel solar woodchip dryer prototype for Scottish conditions by means of experimentation and modelling. The following points highlight the contribution to knowledge by this research:

This project studied the potential of using exclusively a solar energy application for drying woodchip. The exercise yielded inputs for better design and procedures for a dryer application powered only with solar energy.

This thesis also contributes to the knowledge of drying woodchips for fuel by analysing the performance of a small scale woodchip dryer operating with low temperatures and low air flow rates. The methodology followed in this work presented a rigorous analysis of the woodchip drying and modelling. The laboratory experiments provided detailed information of the woodchip drying characteristics for a range of drying conditions. Based on experimental results, the performance of the woodchip dryer was modelled with a general equation that defined the MC as a function of the key parameters that govern the process.

The SATS prototype utilised to preheat the drying air consisted of a PV driven fan and a solar air collector. This particular solar air heater was built and tested in the field under Scottish weather conditions during a year. The analysis of the SATS included the pneumatic and the thermal performance. Because of the nature of the PV driven fan electrical characteristics, the SATS performance can be simplified to a unique

operational regime in which both air flow and collector temperature rise can be estimated as function of solar radiation. The SATS performance was strongly affected by the pneumatic characteristics of the components that comprise the solar dryer. Thus the pneumatic analysis is fundamental to design and optimise the solar woodchip dryer. The thermal performance of the SATS was obtained for various solar air collectors and various weather conditions. The collector ΔT was modelled based on the experimental results using a simple linear equation. The effect of the environmental factors such as the wind was notable in the SATS performance, especially in the transient regime.

Based on the woodchip dryer and the SATS models, the SDMM tool was developed to predict the production of woodchip obtained from the solar dryer operating during a period of time. The SDMM simulation results were used to assess the different solar dryer configurations. However the annual dried woodchip production obtained from any solar dryer configuration was low. This limited the chances of developing a commercial application from the solar woodchip dryer prototype.

The viability study of the solar woodchip dryer prototype was not favourable: despite the manufacturing costs being relatively low, the annual production of dried woodchip was small. Moreover, the dryer feeding system and the adaption of the solar woodchip dryer to the storing facilities may increase the drying costs.

The SATS designed to pre heat the drying air was not suitable because the PV driven fan conditions the size of the dryer and furthermore implies a non-continuous production that depends on the weather conditions. However a solar thermal application such as TPC can bring important energy savings when used for backing up the heating system in a woodchip dryer installation.

A solar wall dryer tool was developed to assess the potential of using a TPC for drying woodchip in a large installation. The tool estimates the energy savings and the woodchip production when using a TPC application for drying woodchip at large scale.

6.4 Further work

The avenues for possible future research can be classified as follows:

6.4.1 Drying woodchip

The performances of the SATS and solar woodchip dryer depended on the woodchip dryer selected. Thus, it was found that the thick layer dryer had high drying efficiencies but operate with low flow rates while the thin layer introduced low pressure drop but the drying efficiencies were not high. Because of the operating condition of the solar dryer, there is an optimal design that maximises the woodchip dried production. For a given PV driven installation, there is a dryer geometry and an optimal woodchip layer thickness that optimises the drying rates and pressure drop for the working flow range.

6.4.2 SATS

The performance of various solar air collectors considered in this project were studied when working with the PV driven fan in the SATS. Thus it was not possible to compare the characteristics of the solar air collector performances when operating with different collector configurations. Knowing the thermal performance of the solar air collector for various air flow rates can be useful in order to develop a versatile tool to predict the solar dryer production as a function of the component characteristics.

The thermal performance of the SATS was modelled employing a proportional linear relation between ΔT and solar radiation. The model provided satisfactory results at any weather conditions. However the transient regime caused by sudden changes in solar radiation was not well described. The ΔT modelling code can be modified introducing a correction factor that considers the previous data. This factor should be estimated as a function of the collector time constant for both step increment and decrement in irradiance.

6.4.3 Solar woodchip dryer

The SDMM program is a tool that allows the estimation of the dried woodchip production for a period of time. The SATS is based on the model that describes the results of the solar dryer components performances. The dryer performance is easy to

obtain in a controlled lab conditions. However, although the SATS performance is also easy to obtain, in case of a major modification in the design of the solar dryer, new thermal results would have to be modelled. Thus the performance of the solar collector when working with a PV driven fan system should be calculated separately as a function of air flow rates and other parameters that may affect like wind and ambient temperature. The new SDMM would include a module that estimated the air flow in the system, considering the pressure drop of the collector and the dryer, and after it would calculate the thermal performance. In this way, changes in the PV driven fan and dryer design would be easily implemented in the SDMM.

The potential production of biomass in Scotland has not just been reduced to the usage of wood fuels but also includes the large production of seaweed that can be farmed in the coasts of the country. Seaweed like woodchip is a biomass source that can be used locally to produce heat, bring benefits to the local economy and have a positive impact in local biodiversity. A further work can open a new line of study towards the usage of solar energy in the process of drying seaweed for fuel in Scotland.

REFERENCES

- 4wire Ltd (2010). Wire Mesh Galvanized 6mm x 6 mm holes Retrieved on June 2010, from <http://www.4wire.co.uk/wire-mesh-galvanized-holes-14x14-36high-p-273.html>.
- A1 building supplies Ltd (2010). Plywood WBP Exterior 2440 x 1220 x 18mm L/O. Retrieved on June 2010, from http://www.a1building.co.uk/product_info.php?products_id=841.
- Abe, T. and Afzal, T. (1997), Thin-layer infrared radiation drying of rough rice. *Journal of agricultural engineering research* **67**(4): 289-297.
- Akpinar, E. (2006), Determination of suitable thin layer drying curve model for some vegetables and fruits. *Journal of Food Engineering* **73**(1): 75-84.
- Alakangas, E., Valtanen, J. and Levlin, J. E. (2006). CEN technical specification for solid biofuels—Fuel specification and classes, Elsevier. **30**: 908-914.
- Alonso, M. and Finn, E. J. (1974), *Campos y ondas*, Fondo Educativo Interamericano.
- Amos, W. (1998), *Report on Biomass Drying Technology*. National Renewable Energy Laboratory.
- Arulanandam, S. J., Hollands, K. G. T. and Brundrett, E. (1999), A CFD heat transfer analysis of the transpired solar collector under no-wind conditions. *Solar energy* **67**(1-3): 93-100.
- ASHRAE Standards (1977). *Methods of testing to determine the thermal performance of solar collectors*. ASHRAE . New York
- ASHRAE (1993) *ASHRAE Handbook: Fundamentals* (American Society of Heating, Refrigeration and Air-Conditioning Engineers) Atlanta GA, USA
- Augustus Leon, M., Kumar, S. and Bhattacharya, S. C. (2002), A comprehensive procedure for performance evaluation of solar food dryers. *Renewable and Sustainable Energy Reviews* **6**(4): 367-393.
- Ayensu, A. (1997), Dehydration of food crops using a solar dryer with convective heat flow. *Solar Energy* **59**(4-6): 121–126.
- Bala, B. and Woods, J. (1994), Simulation of the indirect natural convection solar drying of rough rice. *Solar energy* **53**(3): 259-266.
- BEG (2005). *Promoting and Accelerating the Market Penetration of Biomass Technology in Scotland*. Forum for Renewable Energy Development in Scotland, Scottish Executive.
- Betka, A. and Moussi, A. (2004), Performance optimization of a photovoltaic induction motor pumping system. *Renewable Energy* **29**(14): 2167-2181.

- Bione, J., Vilela, O. and Fraidenraich, N. (2004), Comparison of the performance of PV water pumping systems driven by fixed, tracking and V-trough generators. *Solar energy* **76**(6): 703-711.
- Björheden, R. (2006), Drivers behind the development of forest energy in Sweden. *Biomass and Bioenergy* **30**(4): 289-295.
- Blackburn, G. A. and Milton, E. J. (1997), An ecological survey of deciduous woodlands using airborne remote sensing and geographical information systems (GIS). *International Journal of Remote Sensing* **18**(9): 1919-1935.
- BP solar (2007). SX 310 module. Retrieved on June 2010, from <http://www.mrsolar.com/pdf/bp/BPSX310.pdf>.
- Brenndorfer, B. (1985), *Solar Dryers: Their Role in Post-Harvest Processing*, Commonwealth Secretariat.
- Brenndorfer, B., Kennedy, L. and Trim, D. (1985), *Solar dryers: their role in post-harvest processing*. London, The Commonwealth Secretariat.
- Buchberg, H., Catton, I. and Edwards, D. K. (1974), Natural convection in enclosed spaces-A review of application to solar energy collection. American Society of Mechanical Engineers.
- Buresch, M. (1983), *Photovoltaic energy systems*, McGraw-Hill.
- Buresch, M. (1983), *Photovoltaic energy systems: Design and installation*. New York, McGraw Hill.
- Calex Electronics Ltd. (2009), Materials Emissivity table, Retrieved on January 2011, from http://www.calex.co.uk/downloads/application_guidance/emissivity_tables.pdf.
- Castleman, J. (1994), *Fluidized bed combustion and gasification: a guide for biomass waste generators*. Prepared for Southeastern Regional Biomass Energy Program.
- Chamberlin, C., Lehman, P., Zoellick, J. and Pauletto, G. (1995), Effects of mismatch losses in photovoltaic arrays. *Solar energy* **54**(3): 165-171.
- Choundhury, C., Anderson, S. and Rekstand, J. (1988), A Solar Air Heater for Low Temperature Application. *Solar energy* **40**: 335-344.
- Clarage (2008). Temperature and altitude effects on fans. Clarage engineering data. Retrieved on May 2010, from http://www.clarage.com/clarage/pdfs/ED-1600_CLA.pdf.
- Cotton, R. (2005). *Woodfuel – Automated wood heating & woodfuel supply*. Northwoods, Wood Energy Ltd.
- Criqui, P. and Kouvaritakis, N. (2000). *World energy projections to 2030*, Inderscience. **14**: 116-136.
- Deans, J. and Weerakoon, A. (2008). The thermal performance of a solar air heater. V European Thermal-Sciences Conference. The Netherlands.

- DEFRA (2009). Guidance on how to measure and report your greenhouse gas emissions Retrieved on January 2011, from <http://www.defra.gov.uk/environment/business/reporting/pdf/ghg-guidance.pdf>
- Diamante, L. M. and Munro, P. A. (1993), Mathematical modelling of the thin layer solar drying of sweet potato slices. *Solar energy* **51**(4): 271-276.
- Ductingshop (2010). Uninsulated aluminium flexible ducting - 10m - 150mm. Retrieved on June 2010, from http://www.ductingshop.co.uk/ducting?gclid=CO_r_n7vIi6MCFQaRZgod8j_R_g.
- Duffie, J. A. and Beckman, W. A. (1991), *Solar engineering of thermal processes*. New York, Wiley.
- Duffie, J. A., Beckman, W. A. and McGowan, J. (1985), *Solar Engineering of Thermal Processes*. *American Journal of Physics* **53**: 382.
- Eckstein, J., Townsend, T., Beckman, W. and Duffie, J. (1990). Photovoltaic powered energy systems. Proceedings of the American Solar Energy Society, Austin, Texas, USA.
- Ekechukwu, O. and Norton, B. (1999), Review of solar-energy drying systems. III: low temperature air-heating solar collectors for crop drying applications. *Energy Conversion and Management* **40**(6): 657-667.
- Ekechukwu, O. V. (1999), Review of solar-energy drying systems I: an overview of drying principles and theory. *Energy Conversion and Management* **40**(6): 593-613.
- Ertekin, C. and Yaldiz, O. (2004), Drying of eggplant and selection of a suitable thin layer drying model. *Journal of Food Engineering* **63**(3): 349-359.
- Fagunwa, A., Koya, O. and Faborode, M. (2009), Development of an Intermittent Solar Dryer for Cocoa Beans. *Agricultural Engineering International: The CIGR EJournal*.(0).
- Forestry Commission (2010). Fact and figures: Fuel costs per kWh. Retrieved on January 2011, from <http://www.biomassenergycentre.org.uk/portal>
- Forward metals (2009). 1.5 mm aluminium sheet products Retrieved on June 2010, from http://www.forwardmetals.co.uk/acatalog/aluminium_sheet_1_5mm.html.
- Garg, H., Jha, R., Choudhury, C. and Datta, G. (1991), Theoretical analysis on a new finned type solar air heater. *Energy* **16**(10): 1231-1238.
- Garstang, J., Weekes, A., Poulter, R. and Bartlett, D. (2002), Identification and characterisation of factors affecting losses in the large-scale, non-ventilated bulkstorage of wood chips and development of best storage practices. First Renewables Ltd, London.
- Gawlik, K. (1999) National Renewable Energy Lab. Uses CFD to Develop Low-Cost, Solar collector. *Fluent software users* Retrieved on April 2010, from <http://www.fluent.com/solutions/articles/ja087.pdf>.

- Gigler, J., van Loon, W., van den Berg, J., Sonneveld, C. and Meerdink, G. (2000), Natural wind drying of willow stems. *Biomass and Bioenergy* **19**(3): 153-163.
- Gigler, J., Van Loon, W., Vissers, M. and Bot, G. (2000), Forced convective drying of willow chips. *Biomass and Bioenergy* **19**(4): 259-270.
- Gigler, J. K., Van Loon, W. K. P., Seres, I., Meerdink, G. and Coumans, W. J. (2000), Drying characteristics of willow chips and stems. *Journal of agricultural engineering research* **77**(4): 391-400.
- Grassie, T. (2006). Performance and modelling of a PV driven transpired solar air heater. EuroSun 2006 Glasgow.
- Grassie, T. (2007). Modelling the outlet temperature of a PV driven transpired solar air heater. SOLARIS, New Delhi.
- Grassie, T., MacGregor, K., Muneer, T. and Kubie, J. (2002), Design of a PV driven low flow solar domestic hot water system and modeling of the system collector outlet temperature. *Energy Conversion and Management* **43**(8): 1063-1078.
- Green, M. (2004), Recent developments in photovoltaics. *Solar energy* **76**(1-3): 3-8.
- Green, M., Emery, K., King, D., Hisikawa, Y. and Warta, W. (2006), Solar cell efficiency tables (version 27). *Progress in Photovoltaics* **14**(1): 45-52.
- Gregg, S. J., Sing, K. S. W. and Salzberg, H. W. (1967), Adsorption Surface Area and Porosity. *Journal of The Electrochemical Society* **114**: 279C.
- Gunnewiek, L., Hollands, K. and Brundrett, E. (2002), Effect of wind on flow distribution in unglazed transpired-plate collectors. *Solar energy* **72**(4): 317-325.
- Hastings, S. R. and Morck, O. (2000), *Solar air systems: a design handbook*, James & James.
- Helin, M. (2005). Wood as a fuel & drying of wood chips. Bioenergy production know-how to five European regions. North Karelia Polytechnic, Joensuu, Finland.
- Henderson, D., Junaidi, H., Muneer, T., Grassie, T. and Currie, J. (2007), Experimental and CFD investigation of an ICSSWH at various inclinations. *Renewable and Sustainable Energy Reviews* **11**(6): 1087-1116.
- Henderson, S. M. (1952), A basic concept of equilibrium moisture. *Agricultural Engineering* **33**(1): 29-32.
- Henderson, S. M. and Pabis, S. (1961), Grain drying theory I. Temperature effect on drying coefficient. *Journal of Agricultural Engineering Research* **6**(3): 169-174.
- Hollick, J. (1999), Commercial scale solar drying. *Renewable Energy* **16**(1-4): 714-719.
- Hollick, J. and Barnes, B. (2007). PV Thermal Systems; Capturing the Untapped Energy, AMERICAN SOLAR ENERGY SOCIETY; AMERICAN INSTITUTE OF ARCHITECTS.

- Hollick, J. C. (1999), Commercial scale solar drying. *Renewable energy* **16**(1-4): 714-719.
- Hottel, H. and Whillier, A. (1955). Evaluation of flat-plate solar collector performance. *Use of Solar Energy*, 3, 74-104.
- Houdson, B. (2006). Woodfuel – The Woodfuel Resource. IGNITE Woodfuel training program. Dumfries.
- Incropera, F., DeWitt, D., Bergman, T. and Lavine, A. (1996), Fundamentals of heat and mass transfer.
- Ion, I., V and Martins, J. G. (2006), Design, developing and testing of a solar air collector. Fascicle IV: Refrigerating technique, internal combustion engines, boilers and turbines.
- Jacobson, A., Kammen, D., Duke, R. and Hankins, M. (2000). Field performance measurements of amorphous silicon photovoltaic modules in Kenya, American solar energy society; american institute of architects.
- Junaidi, Haroon (2007). Optimized solar water heater for Scottish weather conditions. PhD thesis, Edinburgh Napier University
- Keey, R. B. (1972), Drying principles and practice, Pergamon Press.
- Kielder Forest products Ltd (2001) Commercial woodchip storage drying trials. DTI Sustainable energy programmes Retrieved on March 2010, from www.dti.gov.uk/renewables/publications/pdfs/bu100674.pdf.
- Kofman, P. and Spinelli, R. (1997), Recommendations for the establishment of short rotation coppice (SRC) based on practical experience of harvesting trials in Denmark and Italy. *Aspects of Applied Biology*
- Kofman, P. D. (2006). Quality wood chip fuel. Harvesting / Transportation. Sandyford. Dublin, COFORD. **6**.
- Kudra, T. and Mujumdar, A. S. (2002), Advanced drying technologies, Marcel Dekker New York.
- Kutscher, C. (1994), Heat exchange effectiveness and pressure drop for air flow through perforated plates with and without crosswind. *Journal of Heat Transfer, Transactions ASME* **116**(2): 391-399.
- Kutscher, C., Christensen, C. and Barker, G. (1993), Unglazed transpired solar collectors: heat loss theory. *Journal of Solar Energy Engineering* **115**: 182.
- Laitila, A. A. a. J. (2006). Harvesting and transport costs of forest energy. F. F. R. I. (Metla). Soria. Finland.
- Langmuir, I. (1918), THE adsorption of gases on plane surfaces of glass, mica and platinum. *Journal of the American Chemical Society* **40**(9): 1361-1403.

- Langridge, D., Lawrance, W. and Wichert, B. (1996), Development of a photo-voltaic pumping system using a brushless DC motor and helical rotor pump. *Solar energy* **56**(2): 151-160.
- Leon, M. and Kumar, S. (2007), Mathematical modeling and thermal performance analysis of unglazed transpired solar collectors. *Solar Energy* **81**(1): 62-75.
- Lewis, W. (1921), The Rate of Drying of Solid Materials. *Industrial & Engineering Chemistry* **13**(5): 427-432.
- Ljungdell, J. B. (2005). Bioenergy in Sweden, Swedish Energy Agency.
- Luikov, A. V. (1966), Heat and Mass Transfer in Capillary-porous Bodies.
- MacGregor, K. and Balmbro, D. (1984). Why North is best for solar heating of Buildings? Where is the best place in Scotland for solar space heating? *NorthSun 84: International Conference on Solar Energy at High Latitudes*, 76.
- Mallick, T., Eames, P., Hyde, T. and Norton, B. (2004), The design and experimental characterisation of an asymmetric compound parabolic photovoltaic concentrator for building facade integration in the UK. *Solar energy* **77**(3): 319-327.
- Matters, M. (2008). Solarflex, dryers and heaters. Retrieved on July, 2010, from <http://www.malnutrition.org/SolarFlex.pdf>.
- Matuska, T., Zmrhal, V. and Metzger, J. (2009). Detailed modelling of solar flat-plate collectors with design tool Kolektor 2.2. IBPSA, Glasgow.
- Mc Govern, R. (2007) Report on trial of farm grain dryer for woodchip moisture reduction. Retrieved on June 2010, from www.northernwoodheat.net/htm/Publications/FarmGrainDriers.pdf.
- Mc Govern, R. (2007). Trials of farm grain driers for woodchip moisture reduction. Harvesting / Transportation. Bucksburn.Aberdeen, SAC consuntalcy.
- Menges, H. and Ertekin, C. (2006), Mathematical modeling of thin layer drying of Golden apples. *Journal of Food Engineering* **77**(1): 119-125.
- Metals4u (2010). Stainless Steel Angle, 50 x 50 x 5mm angle 304. Retrieved on June 2010, from http://www.metals4u.co.uk/detail.asp?cat_id=77&prd_id=1912.
- Metwally, M. N., Abou-Ziyan, H. Z. and El-Leathy, A. M. (1997), Performance of advanced corrugated-duct solar air collector compared with five conventional designs. *Renewable energy* **10**(4): 519-537.
- Midilli, A. and Kucuk, H. (2003), Mathematical modeling of thin layer drying of pistachio by using solar energy. *Energy Conversion and Management* **44**(7): 1111-1122.
- Midilli, A., Kucuk, H. and Yapar, Z. (2002), A new model for single layer drying. *Drying Technology* **20**(7): 1503-1513.

- Mohamad, A. (1997), High efficiency solar air heater. *Solar energy* **60**(2): 71-76.
- Mohapatra, D. and Rao, S. (2005), A thin layer drying model of parboiled wheat. *Journal of Food Engineering* **66**(4): 513-518.
- Moumni, N., Youcef-Ali, S., Moumni, A. and Desmons, J. Y. (2004), Energy analysis of a solar air collector with rows of fins. *Renewable Energy* **29**(13): 2053-2064.
- Muneer, T. (2004), *Solar Radiation and Daylight Models*, Butterworth-Heinemann.
- Muneer, T., Maubleu, S. and Asif, M. (2006), Prospects of solar water heating for textile industry in Pakistan. *Renewable and Sustainable Energy Reviews* **10**(1): 1-23.
- Newborough, M. and Probert, S. (1990), Intelligent automatic electrical-load management for networks of major domestic appliances. *Applied Energy* **37**(2): 151-168.
- Odeh, N., Grassie, T., Henderson, D. and Muneer, T. (2006), Modelling of flow rate in a photovoltaic-driven roof slate-based solar ventilation air preheating system. *Energy Conversion and Management* **47**(7-8): 909-925.
- Page, G. (1949), Factors influencing the maximum rates of air drying shelled corn in thin layers. Unpublished MS thesis. West Lafayette, Ind.: Purdue University.
- Page, J. and Lebens, R. (1986), *Climate in the United Kingdom*. HMSO, London: 188.
- Pal, U. and Chakraverty, A. (1997), Thin layer convection-drying of mushrooms. *Energy Conversion and Management* **38**(2): 107-113.
- PAPST (2003). 3400 series tubeaxial fans. Retrieved on March 2010, from <http://www.newark.com/pdfs/datasheets/EBM/3400%20SERIES.pdf>.
- Parker, B., Lindley, M., Colliver, D. and Murphy, W. (1993), Thermal performance of three solar air heaters. *Solar energy* **51**(6): 467-479.
- Perry, R., Green, D. and Maloney, J. (1984), *Perry's chemical engineering handbook*. Chicago: RR Donnelley & Sons Company.
- Pottler, K., Sippel, C., Beck, A. and Fricke, J. (1999), Optimized finned absorber geometries for solar air heating collectors. *Solar energy* **67**(1-3): 35-52.
- Prabhanjan, D., Ramaswamy, H. and Raghavan, G. (1995), Microwave-assisted convective air drying of thin layer carrots. *Journal of Food Engineering* **25**(2): 283-293.
- Reeb, J. (2006), *Drying wood*. University of Kentucky Cooperative Extension Service, College of Agriculture **1**.
- RHG (2008). *Scotland's Renewable Heat Strategy: Recommendations to Scottish Ministers*. Renewable Heat Group. Scotland, Scottish Government.
- Rowell, R. M. (2005), Chemical Modification of Wood. *Handbook of Wood Chemistry and Wood Composites*: 381-420.

- Sabbath, M., Keener, H. and Meyer, G. (1979), Simulation of solar drying of shelled corn using the logarithmic model. American Society of Agricultural Engineers.
- SCHRI (2008). Accredited Installer July 2008. Retrieved on March 2010, from <http://www.energyagency.org.uk/admin/ktmllite/files/uploads/Latest%20Installer%20List.pdf>.
- Schubert, H. R. (1967), History of the British Iron and Steel Industry, Routledge and Kegan Paul.
- Scottish solar energy group (2001). Solar ventilation, examples: Burdiehouse, Edinburgh, Scotland.
- SDC (2005). Wood Fuel for Warmth. Sustainable Development Commission. Scotland, Scottish Executive.
- SFIC (2007), Scotland's Forest Industries. Edinburgh, Scotland, Scottish Enterprise.
- Sharaf-Eldeen, Y. I., Blaisdell, J. L. and Hamdy, M. Y. (1980), A model for ear corn drying. Transactions of the ASAE **23**(5): 1261-1265.
- Sharma, S., Saini, J. and Varma, H. (1991), Thermal performance of packed-bed solar air heaters. Solar energy **47**(2): 59-67.
- Singh, B., Putta Swamy, C. and Singh, B. (1998), Analysis and development of a low-cost permanent magnet brushless DC motor drive for PV-array fed water pumping system. Solar Energy Materials and Solar Cells **51**(1): 55-67.
- Smyth, M., Eames, P. C. and Norton, B. (2006), Integrated collector storage solar water heaters. Renewable and Sustainable Energy Reviews **10**(6): 503-538.
- Stein, J., Hydeman, P. E. and Mark, M. (2004), Development and testing of the characteristic fan curve model. ASHRAE Transactions: Symposia.
- Timo Tahvanainen, A. A. (2006). Storing of energy wood and wood fuel quality management. F. F. R. I. (Metla). Soria. Finland.
- Torul, T. and Pehlivan, D. (2002), Mathematical modelling of solar drying of apricots in thin layers. Journal of Food Engineering **55**(3): 209-216.
- Van Arsdel, W. B. and Copley, M. J. (1967), Food dehydration, vol. 2. Westport, Conn: AVI Publishing.
- Van Decker, G., Hollands, K. and Brunger, A. (2001), Heat-exchange relations for unglazed transpired solar collectors with circular holes on a square or triangular pitch. Solar energy **71**(1): 33-45.
- Van Dyk, E. and Meyer, E. (2004), Analysis of the effect of parasitic resistances on the performance of photovoltaic modules. Renewable Energy **29**(3): 333-344.
- White, F. (1986). Fluid mechanics, McGraw-Hill, New York.

Wickes (2010). Twin Wall Polycarbonate Sheet. Retrieved on June 2010, from http://www.wickes.co.uk/Twin-Wall-Polycarbonate-Sheet/invt/246000?source=123_4.

Yaldiz, O., Ertekin, C. (2003), Mathematical modeling of thin layer solar drying of sultana grapes. *Energy* **26**(5): 457-465

Yaldiz, O., Ertekin, C. and Uzun, H. (2001), Drying of eggplant and selection of a suitable thin layer drying model. *Food Engineering* **63**(4): 349-359.

Yeh, H., Ho, C. and Lin, C. (2000), Effect of collector aspect ratio on the collector efficiency of upward type baffled solar air heaters. *Energy Conversion and Management* **41**(9): 971-981.

Zhao, C. and Wang, D. (2006). Numerical Simulation Study on Transpired Solar Air Collector. ICEBO, Renewable Energy Resources and a Greener Future, Shenzhen, China.

Appendix A

List of VBA- Excel spreadsheets employed for data processing included in the CD attached with the thesis document.

Appendix A1. Drying test data processing

D:\\Appendix A\\Appendix A1_Drying test data processing.xls

Appendix A2. Drying model validation

D:\\Appendix A\\Appendix A2_Modelling drying test data processing.xls

Appendix A3. Mass and energy balance of a drying test

D:\\Appendix A\\Appendix A3_Mass and energy balance.xls

Appendix A4. Solar air thermal system

D:\\Appendix A\\Appendix A4_SATS.xls

Appendix A5. Solar dryer macro model

D:\\Appendix A\\Appendix A5_SDMM.xls

Appendix A6. Solar wall dryer model

D:\\Appendix A\\Appendix A6_SWDM.xls

Appendix A1: Drying data test processing

The **Appendix A1_Drying test data processing.xls** is an EXCEL spreadsheet that has been adapted using VBA tools to processes the drying data obtained from various tests. The analytical calculations of the drying characteristics of each test are calculated in **Module 1**. Calculations are based on the mass of the woodchip sample weighed in short intervals of time and the final mass of the dried woodchip sample. The considered drying parameters as drying rates, MC in wet basis and MC in dry basis are calculated during the tests period in each interval of time. The first data of the drying data series was the reference and had time equal to 0.

$$MC_{wet_basis} = \frac{W - W_{dried}}{W} \quad \text{Equation A1.1}$$

$$MC_{dry_basis} = \frac{W - W_{dried}}{W_{dried}} \quad \text{Equation A1.2}$$

$$Drying_rate = \frac{W_{i+1} - W_i}{\Delta T} \quad \text{Equation A1.3}$$

The main functions that describe *module 1* are:

- *Function read_variables (line 167)*: reads the main characteristics of each drying tests.
- *Function read_time (line 202)*: For each drying test, original time data is copied into adequate format for easy data processing.
- *Function read_weight (line 228)*: For each drying test, original mass data is copied into adequate format for easy data processing.
- *Function create_weight (line305)*: estimates the mass of woodchip at any time.
- *Function calc_mc_ratio (line 443)*: calculates the MC of the woodchip at any time.

The EMC dependence with temperature is obtained from observing the asymptotic values of the MC at the end of the tests at different drying conditions.

In order to compare the results of various drying tests conducted at similar testing conditions, it is necessary to set a common reference point of initial MC. For the first

woodchip sample is 57% MC and for the second woodchip sample is 52%. Thus, in **Module 2** the drying data is processed. The time equal to 0 corresponded to the data with the MC_0 . Based on this time reference and a new interval of time of half an hour, new drying data is generated by interpolation based on the original data. The variable of MR is calculated as a function of the MC at any interval of time, the value of MC_0 taken as a reference, the EMC.

$$MR = \frac{MC - MC_{eq}}{MC_0 - MC_{eq}} \quad \text{Equation A1.4}$$

The main functions that describe *module 2* are:

- *Function read_datas (line 195)*: reads the main characteristics of each drying tests.
- *Function read_time (line 202)*: processes the time data in each drying test.
- *Function calc_reference (line 276)*: calculates the time data considering the new MC_0 reference.
- *Function findpos (line 248)*: for a given time, finds the upper and lower data available in which the given time between is.
- *Function create_new_experiment (line 313)*: calculates through interpolation the new mass for a new point.
- *Function calc_value (line 366)*: interpolates the value of any variable for a given period of time included between two drying data points.

Appendix A2: Modelling drying test data

The Modelling drying test data is a VBA program developed to create the modelled drying data for a set of tests and facilitate the statistical study of the model using regression techniques.

The module **a_generate_curves** creates the modelled MR data and MC data based on a Page model equation previously calculated. This module generates the drying curves at different drying conditions of temperature and velocity in order to compare the modelled MR and MC data with the original MR and MC data. Equation A2.1 shows the Page equation model obtained from drying 57% MC woodchip in the thin layer dryer.

$$MR = \exp(-((0.15 \cdot V^2 - 0.036)(0.014 \cdot T^2 - 0.167 \cdot T + 5.92)) * t^{(18.06V^2 - 7.07V + 1.8)})$$

Equation A2.1

The main functions that describe module `a_generate_curves` are:

- *Function parameters (line 66)*: calculates the Page model equation parameters, k and n , as a function of temperature and drying velocity.
- *Function MR_page (line 97)*: estimates the MR for a given drying conditions and time.
- *Function times_MR (line 103)*: calculates the time of the process for a given MR.

Once obtained the new modelled curves, `b_expervsmodel` and `c_MCexpervsmodel` creates a graphics that compares the experimental and modelled data for MR and MC respectively. The regression analysis of the modelled data compared to the experimental data is developed in modules `d_Statistics` and `e_MC_Statistics`. Parameters such as R^2 , MBE, RMSE, skewness and kurtosis are estimated for each set of tests, presented with more detail in section 2.1.6.

The main procedure of module `b_expervsmodel` and `c_MCexpervsmodel` is:

- *Sub expervsmodel (line 13)*: presents the experimental and modelled data obtained from modelling the drying process.

The main statistical functions that are included in modules `d_Statistics` and in `e_MC_Statistics` are:

- *Function slope (line 73)*: calculates the slope of the best fit line when comparing the experimental and modelled MR or MC.
- *Function R2 (line 97)*: calculates the regression coefficient.
- *Function MBD (line 125)*: calculates the MBD.
- *Function RMSD (line 142)*: calculates the RMSD.
- *Function skew (line 159)*: calculates the skewness.
- *Function kurt (line 192)*: calculates the kurtosis.
- *Function sdev (line 223)*: calculates the typical deviation.

Appendix A3: Mass and Energy balance.

The Mass and energy balance tool is a VBA program developed to control the testing conditions and validate the results obtained from each drying woodchip test. This program processes all the data information acquired during the drying tests and finally models the amount of water evaporated in an interval of time. This program also calculates the heat gain by the air between different points of the woodchip dryer.

The modules **a_weight**, **b_velocity**, **c_temperatures** and **d_humidity** have been developed in order to process all the instrumentation data and convert them into measurements. All the data is presented with an identical interval of time and the same starting time.

The modules above described are built using common functions and procedures:

- *Function read_variables (line 55)*: for each variable considered in the mass and energy balance, the reference time is taken in the beginning.
- *Function read_time (line 66)*: copies the time data into an adequate format for easy data processing.
- *Function read_weight (line 92)*: copies the variable data into an adequate format for easy data processing.
- *Function calc_timsec2 (line 128)*: calculates the new times data considering the reference time and the time data of the each test.
- *Function create_variable (line 169)*: calculates for the values of the correspondent variable for a given time interpolating the upper and lower original values.
- *Function findpos (line 210)*: when interpolating, finds the interval of time or the position in the array of data in which the new time lies.
- *Function calc_value (line 238)*: calculates the value for any variable using the original data and the new reference time.
- *Function write_variable (line 257)*: writes the new variable data based on a new reference time.

The module **e_massbalance** calculates the psychrometric characteristics of the most relevant points of the woodchip dryer: Ambient air, drying air just before crossing the woodchip layer and the exhaust air. The Psychrometric characteristics are based on the measurements of temperature and relative humidity, considering that atmospheric

pressure was 101,325 kPa. The properties of interest to calculate are the enthalpy and the moisture in the air. For these estimations the following psychrometric equations ASHRAE (1993) were employed:

Estimation of the saturation pressure and water partial pressure.

The saturation pressure of water, $P_{\text{saturation}}$, in the air at atmospheric pressure of 101,325 kPa has been modelled by the ASHRAE (1993) employing a logarithmic equation that relates the saturation pressure as a function of the temperature :

$$\ln(P_{\text{saturation}}) = +C_1 + C_2T + C_3T^2 + C_4T^3 + C_5T^4 + C_6T^5 + C_7 \ln(T) \quad \text{Equation A3.1}$$

Where:

	(0 < T < 200 C)
C_1	$-5.80 \cdot 10^3$
C_2	-5.516
C_3	$-4.864 \cdot 10^{-2}$
C_4	$4.176 \cdot 10^{-5}$
C_5	$-1.445 \cdot 10^{-8}$
C_6	0.0
C_7	6.545

The partial water pressure, P_{water} , can be calculated as a function of the measured RH and the saturation pressure as in equation A3.2

$$P_{\text{water}} = RH \cdot 0.01 \cdot P_{\text{saturation}} \quad \text{Equation A3.2}$$

Fraction of mass water in a volume of wet air.

From the ideal gas law equation it is found that for the vapour of water:

$$P_{\text{water}} \cdot V_{\text{water}} = n_{\text{water}} \cdot RT \quad \text{Equation A3.3}$$

$$P_{\text{water}} \cdot V_{\text{water}} = \frac{m_{\text{water}}}{PM_{\text{water}}} \cdot RT \quad \text{Equation A3.4}$$

$$P_{\text{water}} \cdot V_{\text{water}} = m_{\text{water}} \cdot R_{\text{water}} \cdot T \quad \text{Equation A3.5}$$

And similarly for the air, it is shown the following relationship:

$$P_{air} \cdot V_{air} = m_{air} \cdot R_{air} \cdot T \quad \text{Equation A3.6}$$

Combining the previous equations, the fraction of mass water in the air is:

$$w = \frac{m_{water}}{m_{air}} = \frac{PM_{water}}{PM_{air}} \cdot \left(\frac{P_{water}}{P_{atm} - P_{water}} \right) \quad \text{Equation A3.7}$$

$$w = \frac{m_{water}}{m_{air}} = 0.62198 \cdot \left(\frac{P_{water}}{P_{atm} - P_{water}} \right) \quad \text{Equation A3.8}$$

Where: m_{water} is the amount of water that the volume of air contents.

m_{air} is the mass of air.

Estimation of the Entalphy

The enthalpy of the air, H, is calculated as the sum of the air and water enthalpy contributions:

$$H = H_{water} + H_{air} \quad \text{Equation A3.9}$$

$$H = m_{air} \cdot (h_{air} + w \cdot h_{water}) \quad \text{Equation A3.10}$$

The enthalpy of the water vapour, h_{water} , in the air is the sum of the contributions of latent heat and sensible heat, equation A3.12.

$$h_{water} = 2501 + 1.805 \cdot T \quad \text{Equation A3.12}$$

The latent heat of the air, h_{air} , is:

$$h_{aire} = C_p \cdot T \quad \text{where } C_p \text{ was considered constant: } C_p = 1.006 \text{ kJ/kg K.} \quad \text{Equation A3.13}$$

Then the enthalpy of the air was calculated as in equation A3.14

$$H = m_{air} \cdot (1.006 \cdot T + w \cdot (2501 + 1.805 \cdot T)) \quad \text{Equation A3.14}$$

Estimation of the Wet bulb temperature

The wet bulb temperature, T_{wet} , is calculated as a function of the air enthalpy at dry bulb temperature. The T_{wet} to calculate must satisfy the following conditions: firstly the enthalpy at T_{dry} is equal to the enthalpy at T_{wet} , equation A3.15. And secondly as the RH is 100%, therefore the P_{water_sat} is equal to $P_{saturation}$. This condition implies complexity in the calculation of the T_{wet} as it is required to resolve a non-linear system of 3 equations and 3 variables: T_{wet} , P_{water_sat} and the water content in the air, W_{sat} . For the resolution of the system, an iterative numerical analysis programme has been developed based on the mathematical numerical method of Newton – Raphson.

$$H = m_{air} \cdot (1.006 \cdot T_{dry} + w \cdot (2501 + 1.805 \cdot T_{dry})) = m_{air} \cdot (1.006 \cdot T_{wet} + w_{sat} \cdot (2501 + 1.805 \cdot T_{wet}))$$

Equation A3.15

$$P_{water_sat} = P_{saturation}$$

Equation A3.16

$$\ln(P_{saturation}) = +C_1 + C_2 T_{wet} + C_3 T_{wet}^2 + C_4 T_{wet}^3 + C_5 T_{wet}^4 + C_6 T_{wet}^5 + C_7 \ln(T_{wet})$$

Equation A3.17

$$w_{sat} = 0.62198 \cdot \left(\frac{P_{water_sat}}{P_{atm} - P_{water_sat}} \right)$$

Equation A3.18

The amount of water evaporated from the woodchip in an interval of time is therefore, as described in section 3.3.4:

$$W_{evaporated} = \sum \dot{m} \cdot (w_{outlet} - w_{inlet}) \cdot \Delta t$$

Equation A3.19

The increment of latent heat in the air due to the heating system can be also and compared to the amount of energy supplied by the heating, equation A3.19. Similarly it is calculated the difference between the air enthalpy before and after going through the wet woodchips, equation A3.20.

$$P_{input} \cdot \Delta t = \dot{m} \cdot \Delta t \cdot (h_{drying} - h_{ambient}) / 1000 \quad \text{Equation A3.20}$$

$$\dot{m} \cdot (h_{output} - h_{drying}) \cdot \Delta t = 0 \quad \text{Equation A3.21}$$

- *Function calc_points (line 76)*: calculates the psychrometric properties of the ambient air, dryer inlet and outlet air.
- *Function mass_balance (line 169)*: calculates the mass balance between the inlet and outlet air.
- *Function energy_balance (line 176)*: estimates the energy balance between 2 points of the dryer.
- *Function read_variables (line 196)*: reads the variables that intervene in the calculation of the mass or energy balance such as weight, temperature, air flow and relative humidity.
- *Function calc_prop (line 328)*: estimates the psychrometric properties of the air, such as water content in the air and enthalpy, for a given temperature and relative humidity data.
- *Function calc_psat (line 355)*: calculates the pressure of saturation as a function of temperature.

Appendix A4: SATS

The SATS program is a VBA program developed to process the SATS thermal test data. The analytical study of the thermal behaviour of each solar air collector is carried out using the module **a_SATS_flow_AT** that:

1. Transform the raw data from the data logger into temperature, irradiance and RH data: The downloaded data from the data logger are treated and presented as ambient, collector inlet and collector outlet temperatures, irradiance and ambient RH.

- *Function read_variables (line 375)*

2. In the analysis of the SATS only selected steady state points are considered. The criteria for the selection of data are presented in section 4.2.4.2.4. The interval time between two consecutive test data is 1 minute. As 5 minutes was the time interval of stability considered, 5 consecutive data must fulfil the condition presented in equation A4.

$$0.95 < \left| G_{T_i} / G_{T_{i-1\min}} \right| < 1.05$$

These points are employed to establish a relationship between ΔT and Irradiance values.

- *Function calc_points_collector1 (line 188)*

3. Estimate the air flow that circulates in the solar dryer system using the SATS air flow model developed in section 4.3.2.6. The air flow estimated is calculated exclusively as a function of the solar energy received by the PV panel. Equation A4.2 shows the air flow equation for the solar air dryer operating with a 2 mm diameter TPC no covered and a thin layer dryer.

The operation condition of the solar air dryer has its threshold in a minimum level of irradiance obtained experimentally. In the previous case $170\text{W}/\text{m}^2$.

$$Q = -1.7539 \cdot 10^{-4} \cdot G_T^2 + 0.397 \cdot G_T - 20.4 \quad \text{Equation A4.1}$$

- *Function read_variables (line 430)* in module **a_SATS_flow_AT**
- *Function flo2 (line 115)* in **module 2**.

4. The program estimates the modelled collector output temperature as a function of the irradiance, equations A4.2 and A4.3 for the previous example. The program also calculates the heat gain and efficiency for the selected points.

$$\Delta T = 0.0164 \cdot G_T + 3.8 \quad \text{morning data} \quad \text{Equation A4.2}$$

$$\Delta T = 0.0213 \cdot G_T \quad \text{afternoon data} \quad \text{Equation A4.3}$$

- *Function read_variables (line 461)* in module **a_SATS_flow_AT**
- *Function jate (line 164)* in **module 2**.

Appendix A5: SDMM

The SDMM program is a VBA program developed to estimate the amount of woodchip dried by the solar woodchip dryer during a period of time. The operation of the SDMM program is already detailed in section 5.2.2. The main module of the program, **a_main_program** simulates the solar woodchip dryer performance comprising a selected woodchip dryer and a selected STAS configuration.

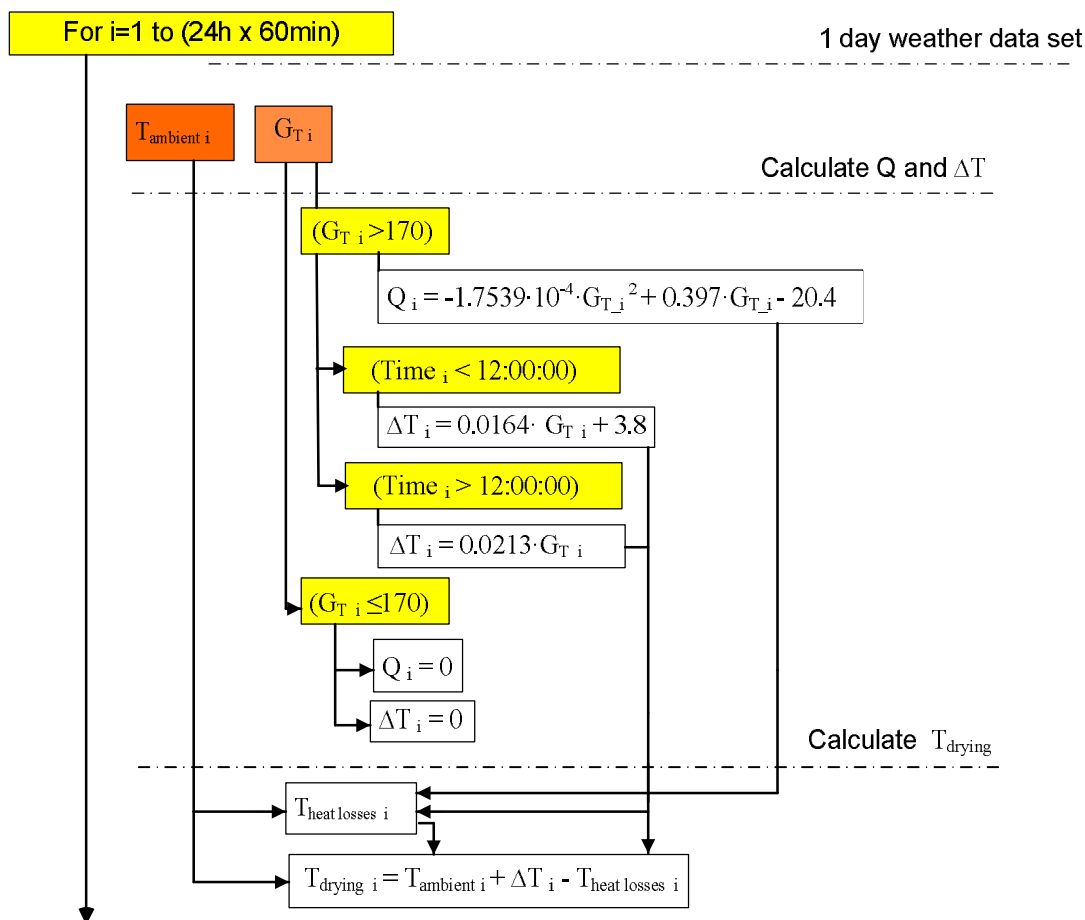
- *Sub collector_model (line 154)*: main routine in which the drying process is evaluated for any solar woodchip dryer for a given period of time.
- *Function read_all_data (line 419)*: reads the input weather data and copies it into an appropriate format in order to facilitate the calculations.
- *Function process_met_data (line 440)*: simulates the performance of a selected SATS calculating the collector outlet temperature and air flow.
- *Function write_collector_data2 (line 1041)*: writes the temperature and air flow data obtained from the SATS in an adequate format.
- *Function heat_losses (line 2101)*: calculates the drying temperature considering the heat losses of the ducting in the system.

Firstly the module **b_weather_data** process the weather data in an adequate format in order to facilitate the analysis. The weather data record created has the weather data of temperature and irradiance for 1 minute interval.

- *Function process_1990_data (line 108)*: reads annual input weather data and copies it into an appropriate format in order to facilitate the calculations.
- *Function process_weather_real (line 385)*: reads daily input weather data and copies it into an appropriate format in order to facilitate the calculations.

The **a_main_program** calculates the air flow in the solar woodchip dryer and the collector outlet temperatures for the period of time considered. The SATS thermal performance characteristics of each configuration is described in the module **c_collector_characteristics**. The drying conditions are estimated including the effect of the heat losses due to the ducting in the solar woodchip dryer. The amount of heat losses are estimated based on the analysis presented in section 4.5 where the drying temperature is calculated as a function of the convection and radiation losses from the duct to the ambient.

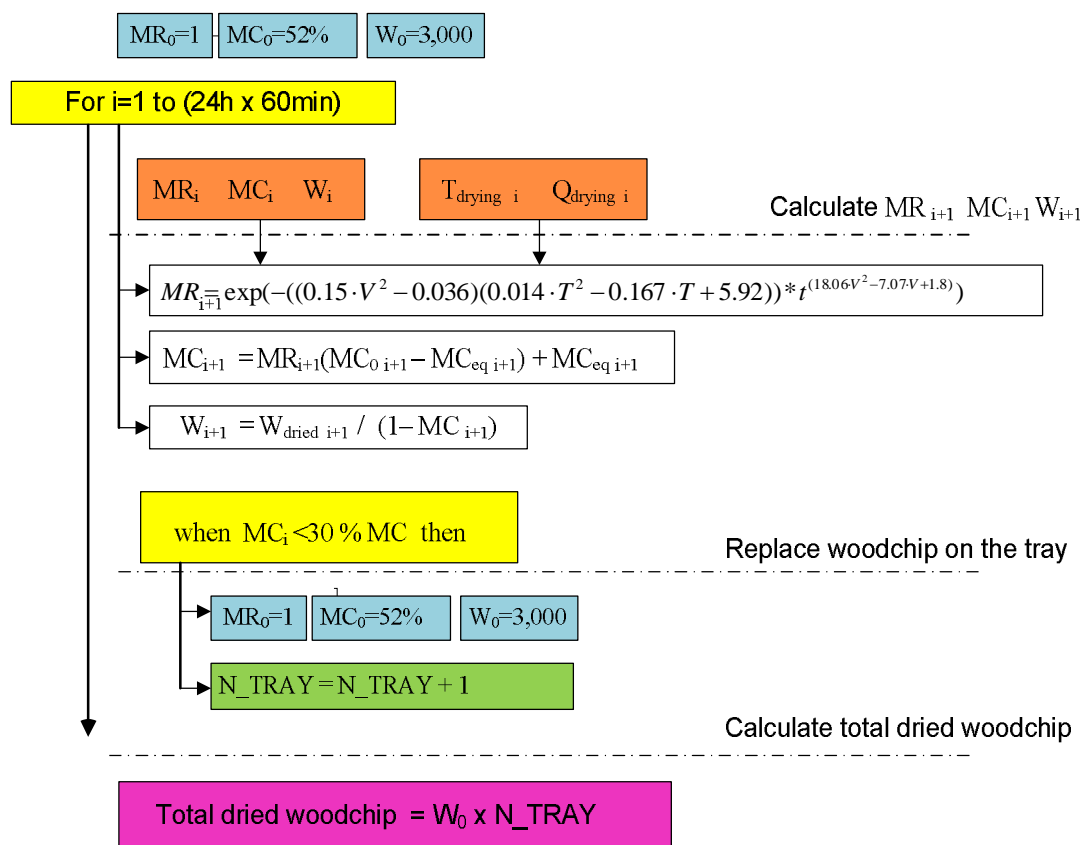
- *Function collector1flow (line 8)*: calculates the air flow in the SATS as a function of irradiance.
- *Function collector1tout (line 133)*: calculates the collector outlet temperature as a function of ambient temperature and irradiance.



The module **d_drying_model** simulates the drying process the array of drying condition data and estimates the amount of woodchip that can be dry in a maximum period of a day time.

- *Function process_dry_woodchip (line 92)*: simulates the drying process for a particular solar woodchip dryer configuration during 1 day.
- *Function parameters1 (line 398)*: calculates the k and n parameters of Page model equation in order to obtain the MR data.

The following chart illustrates the iterative calculations to estimate the amount of dried of woodchip dried in a day:



Appendix A6: SWDM

The SWDM tool is a VBA program developed to estimate the amount of woodchip dried by the solar woodchip dryer during a period of time. The solar thermal system is based on the solar wall performance and the deep bed dryer is considered to have a drying efficiency of 90%. The operation of the SWDM program is already detailed in section 5.6. The main module of the program is a **dryermodel** that indicates the main operations conducted by the program.

Firstly **b_ambient_data** module reads the annual weather data file and re-write the data into a record in order to facilitate the calculations.

- *Sub process_1990_data (line 118)*

c_Psychro_proper calculates all the psychrometric properties of the ambient air. The equations are employed for the calculations are presented in Appendix A2.

- *Sub process_psychro (line 73):* is the main routine.
- *Function function_wet (line 191):* calculates the humidity in the saturated air.
- *Function calc_psat (line 204):* calculates the saturation pressure for a given temperature.

- *Function calc_humrel (line 211)*: estimates the relative humidity by knowing temperature and water content in the air.
- *Function calc_enthalpy (line 229)*: calculates the enthalpy of the air from temperature and relative humidity values.
- *Function calc_wet (line 250)*: estimates the fraction of water in the air, knowing the enthalpy and dry bulb temperature.

d_power input is a unit that calculates the increment in air temperature due to a the action of the Solar wall plate, whose performance is described in section 5.6 in figure 5.13.

- *Sub process_power (line 72)*

e_heating point is a unit that calculates the increment in air enthalpy due to a the continuous action of a external heating source.

- *Sub process_heating (line 45)*

The following modules **e1_calc_td**, **e2_calc_wbt** respectively calculate the dry and wet bulb temperature of the drying air. All the calculations are based on the psychrometric equations previously described in Appendix A2.

- *Function calc_temp2 (line 8)* in module **e1_calc_td**.
- *Function calc_wbt (line 6)* in module **e2_calc_wbt**.

f_water_capacity calculates the maximum amount of water that can be evaporated when drying a product during a period of time with certain drying conditions already calculated. This magnitude is calculated in daily basis.

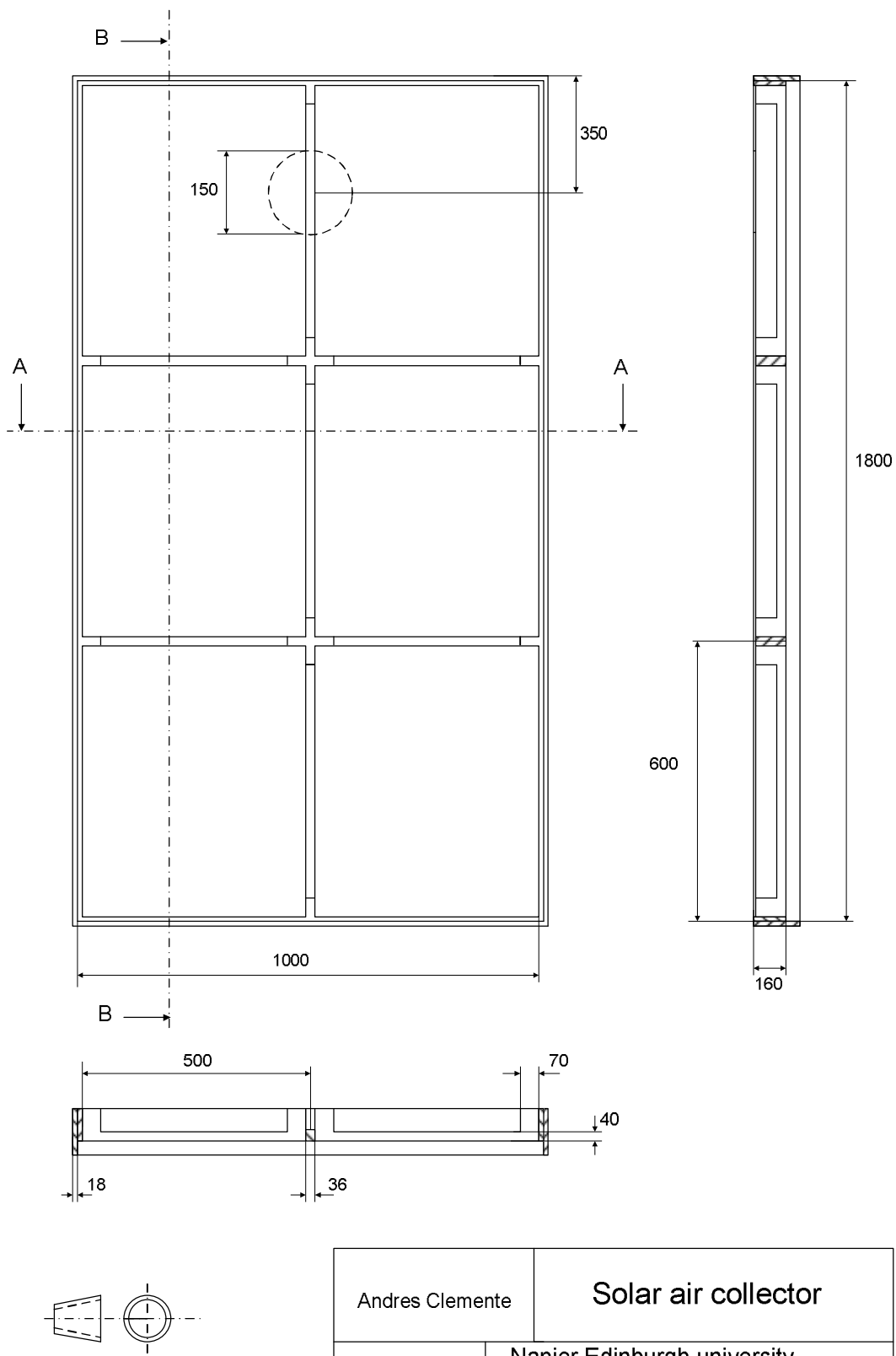
- *Sub water_capacity (line 48)*

Parallely, **g_energy_saving** estimated the amount of energy that is saved when using a solar wall installation and also estimates the energy used in the drying process.

- *Sub energy_saving (line 48)*

Appendix B

Solar air collector sketch:



Andres Clemente	Solar air collector
1 : 10	Napier Edinburgh university